

NUMERICAL MODELING OF COHESIVE SEDIMENT TRANSPORT AND BED MORPHOLOGY IN ESTUARIES

THÈSE N° 3266 (2005)

PRÉSENTÉE À LA FACULTÉ SCIENCES ET TECHNIQUES DE L'INGÉNIEUR

Institut des sciences de l'énergie

SECTION DE GÉNIE MÉCANIQUE

ÉCOLE POLYTECHNIQUE FÉDÉRALE DE LAUSANNE

POUR L'OBTENTION DU GRADE DE DOCTEUR ÈS SCIENCES

PAR

Célestin LEUPI

DIPET II de l'Université de Douala, Cameroun
et de nationalité camerounaise

acceptée sur proposition du jury:

Prof. M. Deville, Dr M. Altinakar, directeurs de thèse
Dr. J. Bühler, rapporteur
Dr E. Miglio, rapporteur
Prof. A. Quarteroni, rapporteur

Lausanne, EPFL
2005

Numerical modeling of cohesive sediment transport and bed morphology in estuaries

Célestin Leupi

Laboratoire d'Ingénierie Numérique-LIN
Faculté des Sciences et Technique de l'Ingénierie
Institut des sciences de l'énergie
Ecole Polytechnique Fédérale de Lausanne
1015 Lausanne, Switzerland

To my beloved son, Leupi Ngaha Célestin Junior,
and to my parents, Colette M. & Grégoire Ngaha.

Abstract

Two major lines of investigation have been pursued in this thesis: (1) More efficient, robust and realistic numerical techniques are designed for the simulation of complex turbulent fluid flows; (2) A new algorithm and its analysis is performed in the context of multiphasic fluid flow, for a cohesive fine-grained sediment (fluid mud) transport in estuaries.

Estuaries exist between marine and freshwater system where waters of different physical, chemical and biological composition meet, combine and disperse primarily due to tidal influences. In the present thesis, the behavior of cohesive sediment in estuaries is reviewed based on the existing literature. Basic theories and recent developments are introduced to describe the formation of fluid mud from a very dilute suspension and its motion down a natural river bed with complex bathymetry. The present work contributes to the numerical simulation of complex turbulent multiphasic fluid flows encountered in estuarine channels, with the aim of the better understanding of the underlying physical processes as well as predicting realistically the cohesive sediment transport and bed morphology in such a zone. The model is based on the mass preserving method by using the so-called Raviart-Thomas finite element on the unstructured mesh in the horizontal plane. In the vertical, the computational domain is divided into number of layers at predefined heights and the method uses a conventional conforming \mathcal{P}_1 finite element scheme, with the advantage that the lowermost and uppermost layers variable height allow a faithful representation of the time-varying bed and free surface, respectively. Concerning the modeling of turbulence, the research effort focuses on the turbulence two-equation $k - \varepsilon$ closure for the vertical parameterization of eddy viscosity. More precisely, a robust up-to-date algorithm is used for this issue. The new methodology is developed with the aim to account for more general relevant effects in the closure. The proposed model offers the capability to cope with the stiffness problem introduced by the large difference between the solid phase flow time scale and the hydrodynamic one, by using a sub-cycling strategy, whereas the splitting scheme is adopted with the aim of stability and the positivity of the relevant turbulent variables. The flexibility of the model and its performance are evaluated on several free-surface flow configurations with increasing complexity : homogeneous unsteady non-uniform flows in plane open channel flows, U-shaped (193°) curved open channel flow.

Concerning the cohesive sediment transport, most of the existing models in the literature assume the analogous transport characteristics with that of the coarse sediment and adopt the relevant developed sediment transport for the latter to treat the former. Moreover, these existing models do not account for the consolidation of the mud-bed. The present research effort focused on a novel methodology based on the realistic empirical relationships, which accounts for the mutually exclusive processes for re-suspension and/or erosion and deposition of fine sediment, whereas only a limited range of bed shear stresses is allowed for simultaneous erosion and deposition to occur. Hence, on this basis, the new model investigated the bed morphology evolution by taking into account of the fluidization and/or consolidation of the fluid mud, which was handled by modeling the bed in three layers: (i) the mud-bed layer, (ii) the partially consolidated bed and

(iii) the fully consolidated bed.

The prediction of deposition/re-suspension using these two different methods lead to a non negligible difference in the results. Therefore, investigation of the true mechanism of erosion/deposition processes for cohesive sediments and their implementation in the numerical model is very important. This suggests that a realistic prediction must account for the fresh mud-bed re-suspension once deposited, as well as the consolidation and/or fluidization of the mud-bed deposits.

Finally, the capability and improvements of the model are demonstrated, and its predicting performance is successfully evaluated by applying it to the simulation of the Po River Estuary (PRE) in Italy, which is the main source of river water discharge into the Northern Adriatic Sea. The analysis showed that the consolidation/fluidization process at the bed may have important influence on the prediction of bed morphology evolution. The three-layer approach used in this thesis is a first attempt to model these processes in detail within a numerical model.

Version abrégée

Deux axes principaux de recherche sont poursuivis dans cette thèse : (1) des techniques efficaces, robustes et réalistes sont développées pour la simulation des écoulements de fluides complexes et turbulents ; (2) un nouvel algorithme est développé et analysé dans un contexte d'écoulements multiphasiques, pour la simulation du transport de sédiments cohésifs (liquide vaseux) dans les estuaires, où l'eau chargée de sédiments de la rivière (avec différentes compositions physique, chimique et biologique) se mélange à l'eau salée de la mer, sous influence de marée.

Dans cette thèse, une revue est faite sur le comportement des sédiments de type cohésif dans les estuaires, à partir d'une littérature détaillée. Les théories de base et les récents développements sont introduits pour la description de la formation du liquide vaseux à partir du mélange en suspension et de son mouvement sur le fond du canal de la rivière naturelle avec une bathimétrie complexe. Le travail ci-présent est une contribution à la simulation numérique des écoulements multiphasiques complexes et turbulents que l'on rencontre dans les canaux estuariens dans l'optique d'une meilleure compréhension des processus physiques qui sont à l'origine, et de permettre ainsi des prédictions réalistes du transport de sédiments cohésifs et la formation du lit dans ces zones. Le modèle numérique garanti la conservation de masse et est construit sur la base d'une méthode des éléments finis de type Raviart-Thomas sur une grille non-structurée sur le plan horizontal. Dans la direction verticale, le domaine d'étude est sub-divisé en plusieurs couches prédéfinies et le modèle utilise la méthode conventionnelle des éléments finis de type \mathcal{P}_1 sur une grille conforme, avec l'avantage que l'épaisseur variable des couches du lit et de la surface libre permet une meilleure représentation de la forme du lit et de la surface libre qui varient en fonction du temps. En ce qui concerne la modélisation de la turbulence, les recherches sont focalisées sur le modèle $k - \varepsilon$ à deux équations de fermeture, pour la paramétrisation de la composante verticale de la viscosité turbulente. Plus précisément, un algorithme robuste récent est utilisé à cet effet. Une nouvelle méthodologie est proposée dans le but de tenir compte des plus importants aspects généraux qui jalonnent la fermeture. La méthode de sous-cyclage pendant l'intégration temporelle introduite dans le modèle proposé, permet de résoudre le problème de *raideur*, dû à l'existence d'une large différence entre les échelles caractéristiques de temps. En effet l'échelle caractéristique de temps de la phase solide est généralement très long par rapport à celui de l'hydrodynamique. D'autre part le modèle adopte la méthode d'intégration temporelle à pas fractionnés, afin d'obtenir et de préserver la positivité des variables de la turbulence et d'assurer la stabilité du schéma numérique. La flexibilité et les performances du modèle sont évaluées en l'appliquant pour la simulation des écoulements à surface libre suivant plusieurs configurations de complexités croissantes : les écoulements homogènes, instationnaires et non-uniformes dans les canaux ouverts droits et courbe à 193° .

S'agissant du transport de sédiments cohésifs, la plupart des modèles qui existent dans la littérature, utilisent par analogie aux les caractéristiques des sédiments de gros grains non-cohésifs, des modèles de transport adaptés à ces derniers pour modéliser des premiers. Par

ailleurs ces modèles ne traitent pas de la consolidation de la couche vaseuse du lit du canal. Ce travail de recherche focalise l'attention sur une nouvelle méthodologie basée sur le principe d'exclusion mutuelle dans les processus de re-suspension et/ou érosion d'une part, et de déposition d'autre part. Dans ce cas précis, il n'existe qu'une gamme limitée de contraintes de frottement qui permette un processus simultané de déposition et re-suspension. Ainsi donc, en se basant sur ce principe, le nouveau modèle tient compte de la constitution et du comportement du lit en tenant compte de la fluidification et/ou la consolidation du liquide vaseux, et entraîne ainsi la formation de trois couches sur le lit du canal qui sont: (i) la couche fraîche de vase, (ii) la couche partiellement consolidée et (iii) la couche complètement consolidée. La prédiction du processus de déposition/re-suspension sur la base des deux méthodes conduit à une différence non négligeable dans les résultats. Ainsi, l'investigation sur le mécanisme réel des processus d'érosion/érosion des sédiments cohésifs et de leur implémentation dans un modèle numérique, devient une nécessité. Ceci laisse entrevoir qu'une bonne prédiction doit tenir compte du processus de re-suspension, de même que la consolidation et/ou fluidisation de la couche de vase fraîchement déposée.

Finallement, la capacité et les améliorations du modèle sont proposées et ses performances sont évaluées avec succès pour la simulation de l'embouchure de l'estuaire du fleuve Po (PRE), qui est la principale source dans la partie Nord-Est de la Mer Adriatique. L'analyse montre que le processus de consolidation/fluidisation sur le lit pourrait avoir une influence importante sur la prédiction de l'évolution de la formation et de la morphologie du lit. L'approche abordée dans cette thèse, basée sur les trois composantes (type de couches) du lit, est une innovation en ce qui concerne la prise en compte avec détails, de ce type de phénomène dans un modèle numérique.

Preface

The present dissertation is the result of a research effort carried out in Laboratoire d'Ingénierie Numérique (LIN) of the School of Engineering (STI) in the Institute of Energy (IE) at the Swiss Federal Institute of Technology, Lausanne (EPFL). I wish to express my heartfelt thanks to Professor Michel O. Deville, Mustafa S. Altinakar and Alfio Quarteroni, for offering the chance to study simultaneously in LIN, LHE (Laboratoire d'Hydraulique Environnementale) at EPFL, and to interact with the MOX (Laboratorio di Modellistica e Calcolo Scientifico) at the Politecnico Milano in Italy. They provided me with a pleasant research environment, many discussions and continuous encouragement.

Prof. Michel O. Deville gave me the opportunity to come to EPFL within the LIN (former LMF) and he has always been confident in me, and I am very appreciative of his continuous support and guidance. This was the start of a very productive scientific interaction and the opening of a wonderful period in my life.

I am grateful to Prof. Walter H. Graf with special thanks to Prof. Mustafa S. Altinakar, who gave me their intelligent guidance. From the beginning of my thesis they interested me in research on environmental, river and lake hydraulics, during many fruitful discussions we have had.

I am specially indebted to Dr. Edie Miglio with whom I have learned a lot, not only about numerics. He gave me invaluable help for my research and helped me without reservation during my numerous visits to Milano.

Special thanks to Prof. Alfio Quarteroni and Prof. Fausto Saleri who gave me many fruitful assistances and to have provided me with an essential part of data for the Po River Estuary .

I would like to express my gratitude to the members of the jury, Prof. M. O. Deville, Prof. M S. Altinakar (NCCHE-Mississippi), Prof. A. Quarteroni (EPFL), Dr. J. Bühler (ETHZ), Dr. E. Miglio (MOX-Politecnico Milano) and the president of the jury Prof. C. Ancey (EPFL) for accepting to read my thesis and to be part of the jury.

I am also indebted to Professor Ebenezer Njeugna, for his support at the beginning of my research and especially to have been the first to interest me in the study of the hydro-sedimentary flows within estuaries. He enabled me to carry out a practical training course with the port of Douala located on the Wouri Estuary in Cameroon. Thanks to the General Manager of the "Port Autonome de Douala -PAD" and to all his/her collaborators of the division for the maritime field for their perfect collaboration.

Special thanks to Dr. Koen Blanckaert who provided me with some useful benchmark data and helpful advice during my research.

Many thanks to Mrs. Cathérine Vickenbosch and Annette Jaccard of the Service of orientation and council, mobility, social service at EPFL, for their support at the time of my arrival in Switzerland.

Many thanks to Mrs Birgitta Mergozzi (our secretary), Dr. Emmanuel Leriche, Dr. Ralph Gruber, Dr. Alain Drotz, Mr. Ali Tolou, Dr. Farid Moussaoui, Dr. Nicolas Fietier, Dr. Mark

Sawley and colleagues who gave me the ideal working atmosphere at LIN.

Dr. Emmanuel Leriche, Dr. Nicolas Fietier and Dr. Farid Moussaoui also provided helpful advice during my research.

Appreciation is expressed to my fellow doctoral students, especially to Mr. Roland Bouffanais, Nicolas Bodard, David Lojacono for their friendship and frequent discussions and for their helpful comments on the dissertation. Thanks to Mathieu Viallard, Vincent Keller and Vital Durand Matthieu for their friendship.

Thanks to the Swiss National Science Foundation (FNS:21-65095.01) for providing the funding that made this research possible.

I wish to express my gratitude to my understanding, supportive and patient girl friend, Hélène Nicole Kwédi Youmbi, to my beloved son Célestin Junior who gave me so much joy, pride and encouragement despite many sleepless nights, and to my junior sister and “My daughter according to the Bamiléké tradition ”, Anne Lydie Touani, for who this must be used as an example of courage and abnegation.

Finally, I would like to thank my dearest brothers and sisters of the “Famille Ngaha” for their continuous encouragement and support.

Contents

List Of Contents	xi
1 Introduction	1
1.1 Motivations	1
1.2 The scope and layout of the thesis	3
1.2.1 The scope the thesis	3
1.2.2 Organization of the contents	4
2 Physical description of environmental flows	7
2.1 Estuary: the theoretical background	7
2.1.1 Estuaries, their ecosystems and environmental flows	7
2.1.2 The distinctive nature of estuarine ecosystems	8
2.1.3 Relevant estuarine ecological processes	10
2.1.4 The imperative to protect and maintain estuaries	12
2.1.5 Estuary and multiphasic fluid-flow	13
2.2 Turbulence modeling	13
2.2.1 Why turbulence modeling	13
2.2.2 General properties	13
2.2.3 Turbulence and natural fluid flows	14
2.2.4 Correlations of fluctuations and turbulent quantities	15
2.3 The modeling of cohesive sediment	15
2.3.1 Cohesive sediment behavior and flocculation process	15
2.3.2 The cohesive-sediment transport modeling	16
2.3.3 Cohesive sediment transport and turbulence	18
2.4 Concluding remark	20
3 Mathematical modeling	23
3.1 Modeling of the geophysical flows	23
3.2 The Turbulent Navier-Stokes equations and the Boussinesq approximation	24
3.2.1 Hydrodynamics	26
3.2.2 The $k - \varepsilon$ turbulence closure	27
3.2.3 Boundary conditions for the hydrodynamics	29
3.2.4 Integral form of the free surface equation	32
3.2.5 Boundary conditions for the turbulence equations	34
3.3 Initial conditions	35
3.4 The hydrostatic approximation	35
3.4.1 Geophysical modeling and the scaling of the governing equations	35
3.4.2 3D Hydrostatic Shallow Water model	37
3.5 3D Non-hydrostatic model for variable-density flows	37

3.5.1	3D detailed description of free-surface flows	37
3.5.2	3D Reynolds Averaged Navier-Stokes equations for free-surface flows	38
4	Weak formulation and finite element approximation	41
4.1	Domain discretization	41
4.2	Weak formulation: functional spaces	42
4.3	Finite element approximation	42
4.3.1	Raviart-Thomas and P_1 finite element	42
4.3.2	Finite Element Approximation for the turbulence variables and scalars (heat, salt, sediment concentration)	43
4.3.3	The weak formulation	47
4.3.4	Semi-discrete system equations	48
5	Time discretization and approximate factorizations	55
5.1	Time discretization	55
5.1.1	Incremental scheme	56
5.1.2	The Stokes-like algebraic system equations	57
5.1.3	The inexact factorizations	58
5.1.4	The projection-correction method: the generalized Yosida method	59
5.2	Important features of the general algorithm	63
6	3D model for turbulent free-surface flows: Numerical Results	65
6.1	Validation of the model using benchmark test cases	65
6.1.1	Stability conditions and accuracy of the model	66
6.1.2	The model accuracy	66
6.1.3	Space and time accuracy	66
6.2	Constant density flows: numerical results	67
6.2.1	Finite element solver with hydrostatic pressure and $k - \epsilon$ turbulence model	70
6.2.2	Non-hydrostatic Pressure and $k - \epsilon$ Turbulence model	71
6.2.3	Concluding remark	82
6.3	3D model with non-hydrostatic pressure and modified $k - \epsilon$ model	83
6.3.1	Concluding remark	91
7	3D Modeling of Cohesive Sediment in Estuaries	99
7.1	3D model for turbulent and variable density fluid flows	99
7.2	Cohesive sediment transport in estuaries	100
7.2.1	The numerical modeling approaches	100
7.3	Solid phase flow modeling	100
7.4	Seabed morphology	104
7.4.1	Evolution of the non-consolidated layer using single function	104
7.4.2	Non-consolidated bed thickness using power law functions for mutually exclusive deposition and re-suspension	106
7.4.3	Consolidation process and consolidated bed layers	108
7.5	Prediction of discharges and bed morphology	110
7.5.1	The Po River Estuary and Adriatic Sea	110
7.6	Simulation of PRE: Numerical results	112
7.6.1	Numerical algorithms	112
7.7	Concluding remarks	129

8	General conclusions	139
8.1	Achievements	139
8.2	Turbulence modeling of variable density fluid flows	139
8.3	Cohesive sediment transport and bed morphology	139
8.4	Future prospects	141
	Bibliography	143

Chapter 1

Introduction

1.1 Motivations

The present research finds its motivation in the increasing need for efficient management of estuaries by taking into account the various conflicting environmental and socio-economical aspects. Estuaries exist between marine and freshwater system and they are the primary catchment drainage sites to the coastal ocean, where waters of different physical, chemical and biological composition meet, combine and disperse primarily due to tidal influences (where the freshwater charged with sediment from river meets the saline sea cold water). Many famous ports of the world are situated in estuaries. Estuaries, which are of great economical importance to society, pose challenging planning and management problems to engineers and scientists. As transitions between fresh river water and saline sea water the estuaries not only offer an ideal environment for the development of various natural habitats, but they also constitute a natural harbor and attract human settlements. This inevitable and conflicting juxtaposition of natural and human habitats creates a very fragile equilibrium which must be efficiently managed and conserved. In this fragile equilibrium, the transport of the cohesive sediment in the water column and the accompanying changes in the bed morphology of the estuary play an essential role in the dynamic equilibrium of estuaries. Fine cohesive sediments consisting of a mixture of clay, silt, fine sand, and occasionally some organic matter, enter in several ways into management of natural water bodies and into the design of water resources systems. The design of stable channels with cohesive sediment bed, the control of shoaling in estuarine waterways and the prevention of sediment pollution in coastal and estuarine zones are typical examples of cases where erosion and deposition of cohesive sediments play a dominant role. Generally the estuary harbors have a silty floor, and the navigation channels need to be regularly dredged for large ships to pass through shoals. The deposition of the sediment in navigation channels threatens the security of ships and the authorities in charge of the management of estuaries and harbors are often faced with frequent costly dredging operations with important environmental and economical consequences. Economic constraints dictate the construction of various coastal structures for coastline stabilization and for harbor functions, as well as the costly and frequent dredging of the estuary floor for maintaining safe navigation channels. On the other hand extreme care must be taken not to endanger rich natural environment and various habitats occupying the estuaries and to protect the coastal wetlands. Thus the development of the existing ports and improvement of estuaries channels, especially in the heavy shoaling area, are necessary. The efficient management of estuaries requires a sound understanding of the complex physical processes. The relocation with regard to short and long term morphology of dredged material placed on the seafloor at the open-water disposal sites can also be a problem (e.g. when the sediments are

contaminated). The interventions on the estuary bed must therefore be optimized. For example, two typical problems, with seemingly conflicting goals, often faced by coastal and estuary engineers are:

- prevention or reduction of the sediment deposition in harbor basins, channels, cooling water intakes, outlets of coastal power stations, etc;
- the favoring-deposition and reducing-erosion for the replenishment of beaches and protection of the foundations of marine structures. The knowledge of the transport of cohesive sediments is also necessary for improving water quality, and relocation of dredged sediments.

Improvements of ports and navigation channels will result in a change in original regimes of such an estuary such as shoaling patterns, circulation patterns, salinity intrusions etc. . . , and planning of such work requires therefore a knowledge of estuarine dynamics, sedimentation processes, sources of sediments, and location and amount of shoaling.

Nowadays, at many locations, offshore harbors are under construction to accommodate deep draft ships and to avoid shoaling problems. The construction costs of such facilities are very high, and therefore ports located in the vicinity of estuaries are still in use. Heavy shoaling in the lower section of estuaries act as navigational barriers, which have been insignificant in the past when vessels had shallow drafts.

Every year governments spend considerable amounts of money in estuarial development, maintenance, and management projects without necessarily being sure what their likely outcome and/or effectiveness will be.

The solution to many managerial problems in estuarine and coastal environments such as wetland protection and restoration, maintenance of navigation channels, dredging and relocation of dredged materials , contamination of sediments from anthropogenic sources, evaluation of the effects of man made construction works on siltation and turbidity maximum requires detailed information on sediment transport, turbidity levels and siltation rates. Laboratory scale models are quite costly and they cannot provide satisfactory answers to all questions. Field measurements are difficult to realize, cost considerable amounts of money and the results may contain too much noise for any general analysis. This suggests that adaptative management approaches launched from numerical modeling investigations are most appropriate for the better understanding and to obtain cost-effective results.

The modeling of sediment transport in coastal regions has great economic value, and robust and reliable numerical models with good predictive ability can provide invaluable information to both researchers and engineers interested in the modeling of complex estuary dynamics and hydrodynamics, driven by tidal forcing, wind action, density differences due to temperature, salinity, sediment concentration, freshwater and sediment input from the river, etc. Fluvial geomorphologists and sedimentation engineers recognize that there are complexities involved in dealing with fine-grained material bed streams. There is also a consensus that there is no universal approach for the solution of problems of managing or “re-naturalizing” streams in a cohesive bed material environment. As a result, general practices point toward the need for in-situ data collection and site-specific assessments. To effectively carry out these tasks, it is imperative that practitioners have a thorough understanding of the different physical processes that occur within streams bounded by fine-grained sediments.

This thesis attempts to present concise summary and discussion of the up-to-date knowledge on the fundamental aspects of cohesive sediment dynamics modeling and on the basic erosional and depositional processes modeling, together with some suggestions for future research needs.

Hence, the present work aims at the development of a numerical model for simulating the transport and fate of cohesive sediment in estuaries as well as for predicting the related changes in bed morphology resulting from erosion and/or re-suspension and deposition processes.

This thesis is based on current knowledge of cohesive sediment transport including new research and improvements to current knowledge, and future research directions. Moreover the present thesis points out not only the simplifications encountered in available literature, but also issues and topics not thoroughly understood.

1.2 The scope and layout of the thesis

1.2.1 The scope the thesis

The importance of the hydrodynamic behavior of cohesive sediments motivated extensive basic and applied research on the subject, particularly during the last thirty years. The current knowledge, although not yet complete, contributed to a substantial understanding of the overall dynamics of cohesive sediments, revealed the role of hydrodynamical and physico-chemical parameters on the process of erosion, transport and deposition and, led to the formulation of equations for the initiation, degree and rates of deposition and re-suspension. In this field, research has dual objectives of:

- understanding the basic processes,
- modeling the phenomenon.

Although these two objectives are expected to be strongly interrelated, scientists and engineers have frequently resorted to phenomenological models based primarily on intuition and empirical input with limited understanding of the dynamics of the processes involved. This has been the case in the modeling of the dynamics of the processes involved. The modeling of cohesive sediment transport in an estuary involves the numerical solution of basic conservation equations. In the present research, it is proposed to develop an integrated model of estuarine cohesive-sediment transport around an existing hydrodynamic module based on a novel method for solving three-dimensional ($3D$) shallow-water equations (SWE) with free surface (see [37], [90], [89]). The method uses a mass-preserving, unstructured finite element approach in the horizontal plane. In the vertical, the computational domain is divided into a number of layers at predefined heights and the model uses a conventional conforming finite element scheme. During the computation the layers may become empty or filled with water. The lowermost and uppermost elements of variable height allow a faithful representation of the bed and the time-varying free surface respectively. The model offers both hydrostatic and hydrodynamic pressure capabilities.

The developed hydrodynamic and sediment transport models should describe the fluid circulation, distribution of cohesive suspended sediment and sediment deposition patterns for non-homogeneous estuaries. The formulation of the models is based on the three-dimensional equations of conservation of mass and momentum. A suitable two-equation $k - \varepsilon$ turbulence model is introduced for the closure. By a similar procedure a set of advection-diffusion equations for the temperature, salinity, as well as the three-dimensional model for sediment transport is obtained. The Coriolis force, tidal forcing, wind action, resistance to flow at the bed, buoyancy effects due to temperature, salinity and sediment concentration, bed-level changes due to deposition and erosion are modeled for a realistic representation of the real world phenomena. In order to make the model as general as possible, free-water-surface fluctuations, irregular bed boundaries, near bed velocity profiles have been taken into account.

The estuarine sediment transport is divided into various processes such as the re-suspension during the flocculation process. Due consideration is made of the properties of sediment and related bed morphology.

Investigations on formation of multi-layer at the bed (the so-called *three-bed layer*) from consolidation and/or fluidization have not been undertaken in numerical model elsewhere. In this study, recent semi-empirical relationships collected from the wide review of the literature will be used to evaluate temporal variability of estuarine circulation patterns as well as the bed morphology deformation for a diurnal estuary. The understanding of circulation patterns specific to the systems will have important implications for determining the dynamics and fate of sediment transport within estuaries. A better understanding of the interaction of physical and biochemical processes will be very important for refining current remediation strategies and provide further information for designing new management techniques.

The research consists of the following tasks:

- Implementing a $k-\varepsilon$ turbulent closure scheme in the laminar hydrodynamic model by taking into account the influence of density stratification (due to salinity, suspended sediments and temperature differences) on the production and dissipation of turbulence;
- Developing a module for advection-diffusion based on linear, nonconforming finite elements for computing the suspended-sediment concentration, temperature and salinity;
- Developing a model for the simulation of the changes in bed morphology by considering a three-layer sediment bed. The upper layer is the fluid-mud with a non-Newtonian rheology due to high sediment concentration, the middle layer consists of partially consolidated sediments and finally the lowest layer is the consolidated sediment bed. The interactions with the water column (erosion and deposition) and the exchange mechanisms between the layers (processes of consolidation, liquefaction, fluidization) will be modeled using available recent physically-based semi-empirical models;
- Validation and verification of model will be obtained by using several benchmark data. Finally, the quantitative assessment of the model results will be done by applying it to the Po River Estuary in Italy on the Adriatic-Sea, for which field measurements are available.

1.2.2 Organization of the contents

The present dissertation was carried out during the author work thesis at the Swiss Federal Institute of Technology in Lausanne (Ecole Polytechnique Fédérale de Lausanne) from October 2001 to June 2005. The sequential organization of the chapters follows the chronological order of development of different ideas exposed here. It is important to note that many of the results contained in this thesis were published or submitted for publication to international journals. As summarized in the statement of the objectives of this thesis, two major lines of investigation have been pursued.

- Chapter 2: *Review of the literature on multiphasic fluid-flow in estuaries.*

This chapter focuses on the review on the behavior and modeling of the cohesive sediment (fluid mud) in estuaries from the existing literature, and fundamental theories have been reviewed. This chapter provides some illustrative examples of the rather wide range of situations concerned with the matter of variable density as well as some quantitative information about some salient features of variable density effects in turbulence.

- Chapter 3: *Mathematical modeling.*

This chapter is devoted to the mathematical modeling of the hydrodynamics, the turbulence closure, the advection-diffusion partial differential equations (PDEs) for the matter (salt, temperature and suspended sediment concentration) as well as the variable density. The suitable boundary conditions have been derived as well as the new methodologies for the numerical solutions.

- Chapters 4: *Weak formulation and finite element method.*

This chapter introduces the weak formulation and the finite element method (FEM). A spatial discretization is proposed for three-dimensional shallow-water equations (SWE) as well as the semi-discrete form of the partial differential equations system, using the non-hydrostatic system for the variable density fluid flow.

- Chapter 5: *Time discretization and the approximate formulation.*

This chapter deals with the time discretization and the approximate formulation. In this chapter, starting from the 3D turbulent incompressible Reynolds-Averaged Navier-Stokes (RANS) equations for the variable density fluid flow, a general mathematical framework for the factorizations of the algebraic system has been introduced. Particular attention has been paid to the enhancement of the robustness of numerical algorithms for the simulation of turbulent fluid flows. A robust fractional-step method is proposed for the turbulence model with the aim of preserving positivity of the relevant variables as well the stability of the scheme.

- Chapter 6: *3D model for turbulent free-surface flows: Numerical results.*

This chapter focuses on the validation of the turbulence hydrodynamic model using several complex turbulent flows, with the goal of providing more insight into some interesting features of the flow field and the turbulence. The relevant physical mechanisms and processes underlying these features and some illustrative examples of the rather wide range of situations concerned with the matter of variable density will be investigated.

- Chapter 7: *3D Modeling of Cohesive Sediment in Estuaries.*

This chapter deals with the cohesive sediment transport and bed morphology modeling. Hence some quantitative information about some salient features of variable density effects in turbulence will be provided. For the bed evolution modeling two approaches will be investigated: (i) The concept of turbidity accumulations modeling will be applied to fluid mud at the bottom using the recent advances in the calculation of erosion and deposition rates of fluid-mud. (ii) A bed multi-layers model based on the consolidation process using realistic empirical functions. Finally, in order to tackle a real case, the model is applied to investigate the suspended sediment concentration and the seabed evolution in the Po River Estuary in Italy.

- Chapter 8: *General conclusions.*

General conclusions are given in this chapter whereas future research topics are recommended.

Chapter 2

Physical description of environmental flows

2.1 Estuary: the theoretical background

Estuaries (see figure 2.1) transfer the water, sediments, nutrients and various pollutants collected from a river catchment to the coastal zones.

The physical, chemical, sediment, water quality and ecological processes within estuaries are exceedingly complex primarily due to their dynamic nature, complex mixing processes, stochastic influences, strong antecedent effects and the vast number of complex ecological linkages. There are many different definitions of estuaries (see Pierson *et al.* [107]):

- a semi-enclosed body water which has a free connection with the open sea water which is measurably diluted with fresh water derived from land drainage,
- as an inlet of the sea reaching into a river valley as far as the upper limit of tidal rise, usually being divisible into three sectors: (a) a marine or lower estuary, in free connection with the open ocean; (b) a middle estuary, subject to strong salt and fresh water mixing; (c) an upper or fluvial estuary, characterized by fresh water but subject to daily tidal action.

From a continental point-of-view, estuaries are the recipients of almost all of the runoff and groundwater flow yielded by catchment, where very little surface of groundwater flow enters the coastal ocean directly. It is the rivers that act as the primary drainage system of catchment, and, as the rivers enter the coastal zone, they become estuaries. During periods of high rainfall, groundwater systems are recharged for the rivers or by surface percolation and, during periods of low river flow, the same groundwater systems discharge to the river, water that is not returned to the atmosphere by evaporation or transpiration by plants flows downstream to the estuary. Consequently, estuarine systems are exceedingly vulnerable to catchment pollution. Conservative contaminants released within a catchment will eventually make their way downstream and contaminate the estuary. These include industrial contaminants, pesticides from agricultural activity and polluted runoff from urban drainage systems.

2.1.1 Estuaries, their ecosystems and environmental flows

Environmental flows describe fresh water flow (typically in-stream flow) that is maintained (or not allowed to be used for other, typically anthropogenic purposes) solely for environmental

reasons, to maintain the health and bio-diversity of a particular water-related entity, such as river, wetland, groundwater system or estuary. Any flow storage or diversion structure that alters the flow regime of a surface or groundwater system can influence the health of downstream aquatic ecosystems. Examples of anthropogenic influences on flow regime include:

- dams, and tidal gates (for many purposes including water supply, flood control and hydro-electricity)
- domestic water supply and water treatment works
- industrial water supplies
- irrigation water supply
- sewage treatment works (including possibly effluent re-use)
- catchment modifications (anything that alters the rainfall-run-off process); for example, clearing vegetation and introducing impervious catchment surfaces (roofs, roads and paving) will increase the quantity of surface runoff and reduce base flows.
- Channel modifications such as dredging, realignment and lining
- construction of in-stream obstructions and the creation of obstructions through sedimentation and debris buildup
- withdrawals from groundwater systems.

The flows diverted by these works may or may not be controlled and/or measured. Environmental flows are essential to the minimization of negative influences on health of aquatic ecosystems resulting from alterations to flow regime.

2.1.2 The distinctive nature of estuarine ecosystems

The significance of environmental flows on ecosystems has been the subject of intense investigation for many decades (see Arthington [1]). As consequence, the literature addressing environmental flows in rivers is large. Nevertheless, in spite of the significance of estuaries, the understanding of flow-related processes in rivers and streams is very limited.

It is important to highlight the fundamental differences between fluvial and estuarine flow systems particularly with climates. Much of environmental flow literature for rivers is focused on very low flow conditions. In fluvial systems, flow only occurs in a downstream direction and there are direct relationships between depth and flow velocity. In contrast, in estuaries there is no direct relationship between depth and flow velocity except under very high flow conditions. Flow depth is controlled primarily by ocean water levels and tides. Under moderate to low fresh water inflows within estuaries, alternating upstream and downstream flows (flood and ebb tides) are generated in response to tidal fluctuations in water level at the mouth. In river, only water mass type is under investigation and, whilst water quality issues are complex due to the intricate interactions of nutrients with in-stream biota, the scope of water quality investigations are generally focused on the location and intensity of nutrient or pollutant sources and their impact downstream. Within estuaries, water quality issues are far more complex than in river systems due to their internal mixing of fresh water and saline waters. Estuarine biota have differing tolerances to and dependencies on fresh and saline waters. Therefore, estuaries are inhibited by much more diverse biota than rivers with diversity supplemented by fluxes from both

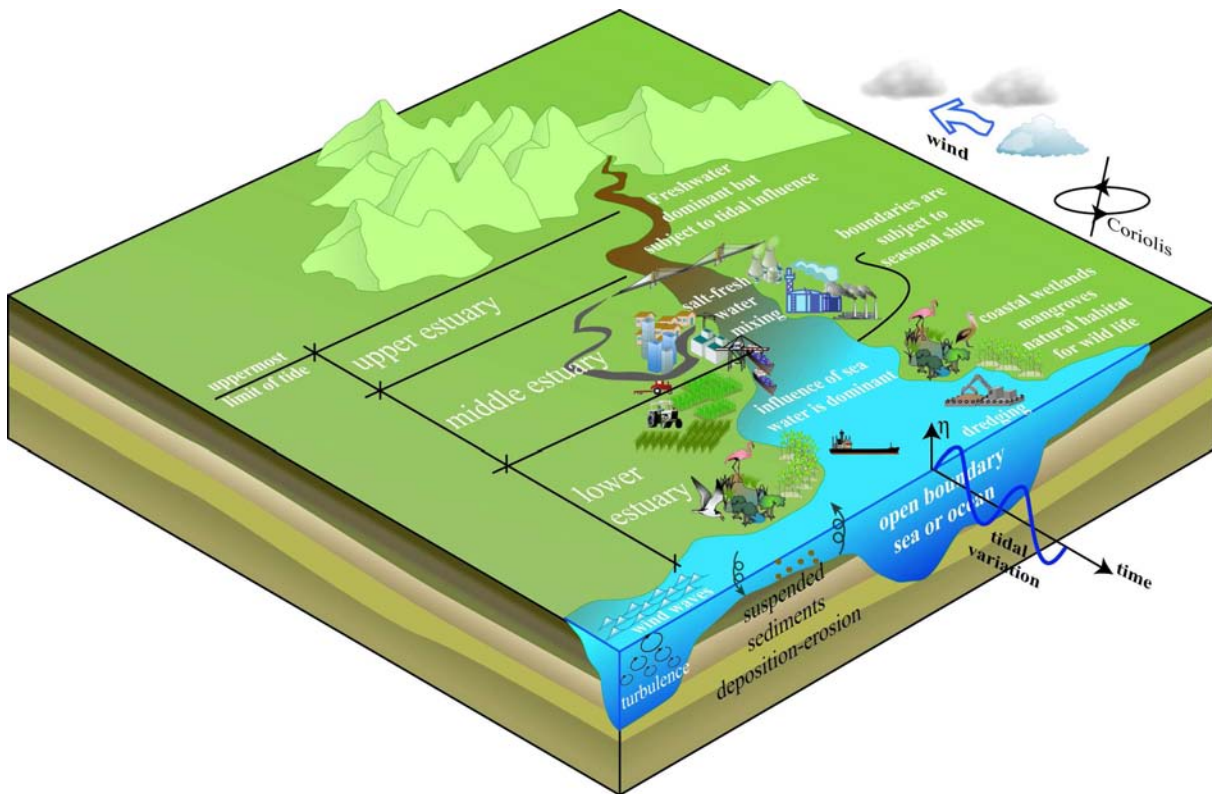


Figure 2.1: Schematic of an estuary showing division into different regions of waves, tides and shallow-water processes

fluvial and marine origin. This bio-diversity within estuarine systems makes ecological response to water quality impacts more difficult to predict. Nutrients and pollutants are dispersed by both tidal and fresh water inflows and relative importance of these dispersion processes will change in relation to the level of fresh water flow. In contrast with rivers, fresh water flow has an important impact on estuary mouth morphology at the ocean. Littoral drift along the coast due to wave action acts to close tidal entrances. Consequently, reduced fresh water flow can result in complete or partial closure of estuary entrances, which can lead to: (a) obstruct ships navigation channels, fish and crustacean migration; (b) alter estuarine flushing and water quality; and (c) alter the estuarine temperature and salinity gradient. As consequence it is not a simple issue to establish an appropriate amount of fresh water flow for an estuary, both technically (due to the many complex physical, chemical and biological processes in estuaries) and socio-economically (due to the many competing uses for water within and between estuarine water users and those that may exist upstream).

2.1.3 Relevant estuarine ecological processes

In a review of literature concerning fresh water flow management in riverine estuaries, Estevez [35] concluded: *Fresh water is an integral part of the definition of an estuary and so deserves primacy in all aspects of estuarine ecology, as a matter of first principles. Changes to inflows have harmed many estuaries in the world, and have the potential to harm more.* It is therefore emphasized that estuarine ecosystems are complex, highly valued and linked to other ecosystems, and there is a strong imperative to protect and maintain estuarine ecosystems. Furthermore, protecting estuaries from inflow-reduction impacts it is not a straightforward task, due to their complexity and the very limited knowledge of their ecological functioning. Hence, numerical simulation of transport and fate of cohesive sediments with the relevant bed morpho-dynamics may constitute an efficient tool for understanding the problems and for finding appropriate solutions.

Major ecological processes involving changes in fresh water inflows and bed erosion or deposition

Longley [77] has identified different functions of fresh water inflows when studying the ecological studies focusing on the effects of fresh water inflows to Texas bays and estuaries. He also examined the wider scientific literature and developed a list of impacts attributable to reduced fresh water inflows. The most significant impacts identified were:

- increased salinity and vertical stratification of water column,
- penetration of the salt-wedge farther upstream allowing intrusion of predators and parasites of estuarine species, and increased intrusion into groundwater and surface resources.
- increased frequency of benthic anaerobic conditions and decreased inputs of nutrient and organic matter used by estuarine species,
- loss of characteristic species and economically important seafood harvests.
- increases in erosion or deposition of delta areas resulting from the reduction or rise of sediment flux

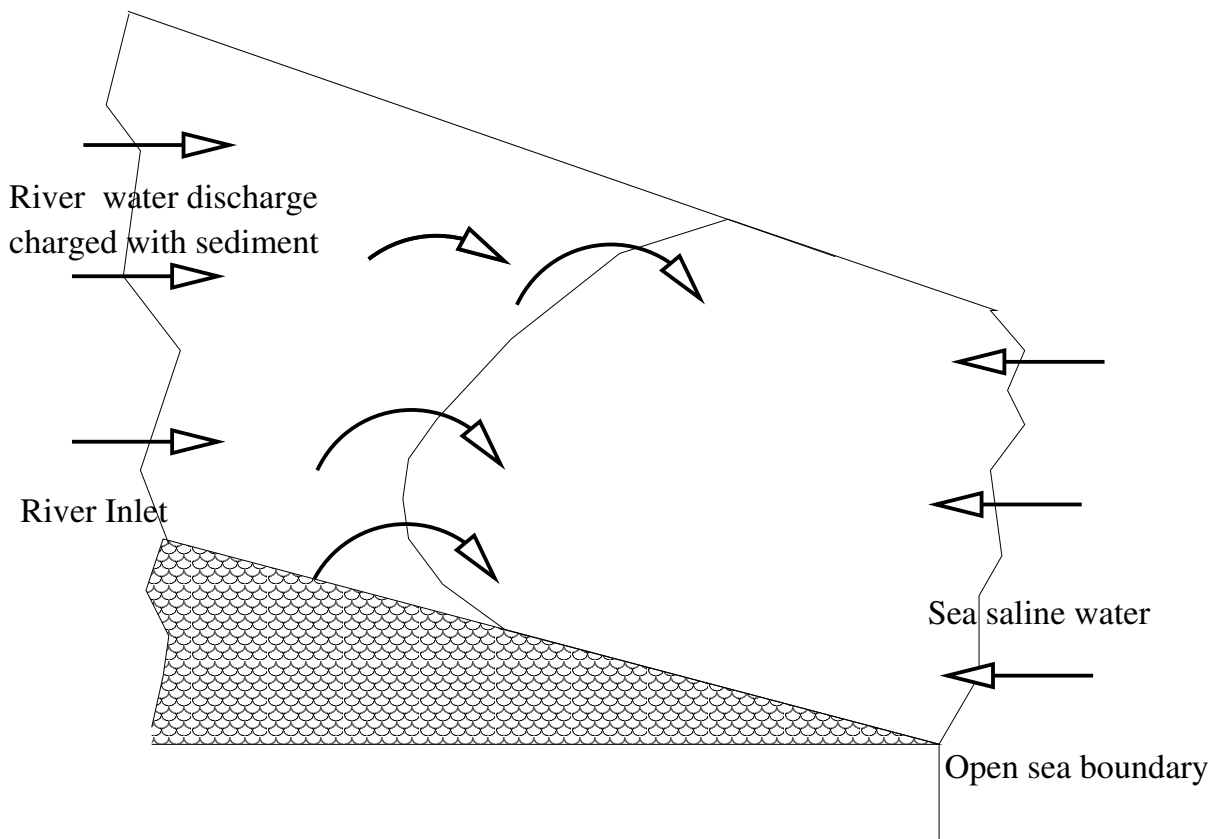


Figure 2.2: 2D vertical view of the salt and fresh-water mixture process

Salinity-mediated and temperature processes

Salinity is considered to be the *master factor* and the prominence of the complex salinity patterns in estuaries (see figure 2.2) that considered to have profound influence on the distribution of estuarine organisms (see Deeley and Paling [27]). Many complex follow-on impacts may occur as a result of these processes. The most notable concerns salinity impacts on the in-stream, loss of shelter and foraging areas for fauna, bank instability and multi-linked water quality reduction. Thus, the salinity regime of an estuary is fundamentally determinant for the distribution of its water quality and flow processes. However when assessing the role of salinity, it is clearly important to recognize the complexities introduced by taking into account environmental variables such as *temperature*.

Reductions in inflow-induced currents and vertical mixing

Processes involving changes in inflow-induced currents and the vertical mixing are the next most common. Three major processes involve these changes and concern: (a) the water quality changes induced by diminished vertical mixing (i.e. reduced turbulence level), (b) the direct physical impacts on eggs and larvae, specifically reductions in their suspension in the water column and their transport along the estuary, and (c) the loss of the physical-habitat component with higher water velocities induced by fresh water inflows. These processes would be most relevant to areas where tide-induced currents are least prevalent, i.e. in the upper reaches of

estuaries and/or in estuaries which have mouths that significantly restrict tidal exchange.

Reductions in flushing and channel-maintenance flows

These moderate-to-high inflow processes involve reductions in flushing or channel-maintenance inflows. This grouping is consistent with the understanding that episodes of high bed shear stress are required to flush or maintain estuary channels. Some processes here, involve the reduction of habitat quality by the reduced frequency of flushing inflows. These are probably most relevant to moderate-magnitude inflows. They specially concern reduced physical -habitat quality where hard substrates are coated by sediments or organic material for prolonged periods, and water-quality deterioration due to the accumulation of organic material and subsequent high biochemical oxygen demand. The other processes specially involves the reduced frequency of channel-maintenance fresh water inflows resulting in habitat contraction. This would be most relevant to high-magnitude inflows. Clearly, only water diversion schemes with large storage capacities and also the nature and amount of bed material being carried along the estuary would be capable of impacting such inflows. Estuaries with large volumes of such materials, which would reflect catchment geology and integrity, and/or estuary-bank stability, would be most prone to impacts arising from this process. Mouth closure (that is, severed marine-estuary connectivity) has many ramifications for the numerous fauna that migrate between the estuary and the ocean. Poor water quality may also result from reductions in tidal flushing.

Reductions input of river-borne nutrients and organic material

This moderate-and-high inflow process is consistent with the understanding that organic matter and nutrients (bound to sediments) primarily enter rivers from their catchment during major rainfall events, events which generate moderate-to-high inflows. In general only water diversion schemes with relatively large transfer and/or storage capacities compared with catchment yield would be capable of impacting such inflows.

Reduced dilution of pollutants

One process aggravation of pollutant problems, partially concerns the reduced dilution of pollutants arising from agricultural, industrial or urban sources. Reductions in inflow-induced currents and vertical mixing are also relevant to this process. Thus process is only relevant to polluted estuaries, particularly estuaries where tide-induced currents are least prevalent (i.e. in estuaries which have mouths that significantly restrict tidal exchange, and/or in the upper reaches of estuaries).

2.1.4 The imperative to protect and maintain estuaries

There is clearly an imperative to protect and maintain estuaries given combination of their high value and the vulnerability to the essential estuarine process to reductions in fresh water inflows. It is recognized that fresh water inflows fluctuate naturally and therefore the diverse processes would naturally stress estuaries. However, the key questions are:

- how far can the natural stressor be extended ?
- are there thresholds beyond which inflow-reduction impacts cause a noticeable escalation of channel bed morphology and/or biology risks ?

2.1.5 Estuary and multiphasic fluid-flow

Variable density fluid motions

The density ρ is defined as the ratio between the amount of mass M_a of a given body of fluid to its volume V_o , to distinguish among the various sources of density variations (see [19], [18]). It appears that two specific situations can be considered separately, according to whether (i) the *volume* of a constant mass fluid element varies or (ii) the *mass* of a given volume of fluid is changed. In this study we are concerned by the second one, with the *dilatation effects* that are observed when the volume of a fluid element changes due to the thermal expansion of the fluid. This volume variation, which results in a given amount of heat release to the fluid particle (by thermal convection, radiation, chemical reaction. . .) leads to buoyancy effects in non zero gravity situations.

In such geophysical applications density variations are small ($\pm 3\%$) and they are supposed to affect only the buoyancy terms (see [30]). Moreover the *Boussinesq approximation* is related to the density changes, and the density is supposed to depend on temperature (T), salinity (S) and sediment concentration (C_s). i.e. $\rho = \rho(T, S, C_s)$ (see more details in [80], [144]). In this work the biological aspect will not be taken into account, and we will focus on the transport of the pollutants or passive scalars (T, S, C_s) with the related variable density fluid flow as well as the formation of the delta on the bed.

2.2 Turbulence modeling

2.2.1 Why turbulence modeling

Navier-Stokes equations describe correctly the flow for all values of $R_e = \rho LV/\mu$ and ν (the Reynolds number and kinematic viscosity), where ρ is the density of the fluid, L and V a characteristic length and velocity respectively, and μ the dynamic viscosity of the fluid. The kinematic viscosity is defined by $\nu = \mu/\rho$. However, if ν becomes small (i.e. increased value of R_e), regularity of the solution is not preserved (i.e. the random fluctuations or turbulence effects appear). In numerical simulations today computers cannot handle as many grid points as are necessary to resolve small eddies. It is found that the smallest eddies are of order of magnitude of $\nu^{\frac{3}{4}}$, and the number of grid points (n) that is necessary to resolve these structures is

$$n \sim R_e^{\frac{9}{4}}$$

In applications with water (with $\nu = 10^{-6}$), $R_e \sim O(10^6)$, yielding $n \sim O(10^{13.5})$. It is not the motion of each and every small eddy which is interesting, but only the effect of turbulence on quantities of engineering significance is relevant. Thus, the idea is to calculate some sort of averaged flow field that is smoother than the actual flow, which drastically reduces the number of grid points required. The effects of small scale fluctuations are estimated by different *ad hoc* models, the derivation of which we will be concerned in the following chapters.

2.2.2 General properties

At a quick glance turbulent flow is characterized by chaotic movement of the fluid flow as opposed to the ordered structure of laminar flow. This occurs, when inertial forces are large compared to viscous forces so internal friction is no longer able to damp out chaotic fluctuations coming from in-ever present and inevitable-disturbance (e.g. at the inflow, boundary, etc. . .).

The transition from laminar flow to turbulence was first investigated on a systematic basis by Osborne Reynolds. To this end he introduced the dimensionless *Reynolds Number*. He observed from his experiments that

1. flow through a geometrically similar setup is physically similar, if and only if R_e is identical,
2. turbulence occurs, when R_e exceeds a specific value (depending on the geometry)

In the sequel, as starting point for a mathematical description we will take the Navier-Stokes equations for incompressible flow. A mathematical rigorous derivation from fundamental physical principals and conservation laws can be found in Pope [109] (see also Roland [124], Milosvav [95]).

2.2.3 Turbulence and natural fluid flows

There are hardly any situations in the dynamics of natural waters and the atmosphere that do not involve turbulent effects at some particular point, and therefore only little insight can be gained in the dominant processes if turbulence is not taken into account. The modeling of this phenomenon has attracted a great many researchers and more and more advanced models suitable for the description of large variety of geophysical flows evolved over the last decades. Due to its complexity, a general model embracing all aspects of turbulence is still out of reach. Nevertheless there has been an enormous progress in the understanding of turbulence. Nowadays Direct Numerical Simulations (DNS) and Large Eddy Simulations (LES) provide data that were previously obtained only by high-precision laboratory setups, and they have large impact on the development of new turbulence models. However in this thesis we shall not consider LES nor DNS modeling. Turbulence in atmosphere and in natural waters is extremely rich in scales and processes. Its modeling is notoriously difficult and even the most advanced second-order and third-order closures are known for their deficiencies ([11], [125]). Turbulence phenomena of geophysical interest are most often affected by the buoyancy of the fluid. Buoyancy introduces the notion of potential energy to the budget equations. This fact inherently complicates the description of turbulence.

Variable Density Fluid and Turbulence

As it is usual in fluid turbulence study, a statistical description is generally introduced to deal with the random character of this flow regime. In the sequel some kind of *mean motion* will be introduced, from which any actual flow realization departs by turbulent fluctuations. Thus, when the density changes, the following questions, at least arise:

- what are the effects of density variations on the mean flow field?
- what are the effects of density fluctuations on the statistical characteristics of the fluctuating motion?
- what are the specific turbulence mechanisms due to fluid density variations?

Dealing with *variable density turbulence* means that one is mainly concerned with (turbulent) density fluctuations. In low speed incompressible flows, pressure fluctuations cannot be taken as responsible for significant density fluctuations. Consequently, turbulent density fluctuations basically occur from temperature or concentrations fluctuations, obviously associated with velocity and vorticity fluctuations.

2.2.4 Correlations of fluctuations and turbulent quantities

In the framework of the Reynolds decomposition with mean and fluctuating quantities, the Reynolds Averaged Navier-Stokes Equations (RANS) for mean quantities contain unknown correlations. Numerous methods have been suggested to express these correlations as functionals of known mean parameters and thus to close the system of partial differential equations (PDE). Formally, well-known equations for their transport can be derived in a purely mathematical way (e.g. [143], [134]). More equations describing the turbulent transport quantities can be constructed by derivation from fluctuation terms of the Navier-Stokes equations. However, this introduces new unknown correlations and the number of equations easily increases beyond manageable limit. To arrive at a balance between the number of unknowns and the number of equations describing the transport of the turbulent fluxes, approximations for the unknowns correlations in terms of known flow properties have to be devised. The most advanced ideas with respect to geophysical and astrophysical modeling have been discussed and summarized for e.g. in [11] and [13]. The recent modeling approaches with respect to geophysical applications are summarized in a review article by Sander [125]). All closure schemes presume the knowledge of a number of turbulent length-scales. Many different ways to obtain estimates of these scales exist. Some authors obtain them analytically as functions of local flow parameters such turbulent Froude number (Fr), or the shear number (Sh) (see [12], [21]). This approach is particularly convenient for the sub-grid scale models LES. An alternative approach is to obtain the length-scales from the solution of differential equations. In that case, a differential equation can be formulated either directly for length-scale l or indirectly for related quantity such as the rate of dissipation, ϵ , of the turbulent kinetic energy k , or a turbulent frequency, ω , or for the product kl . Four different kinds of *closure schemes* are currently used:

- so-called *algebraic formulations*, the phenomenological approach with the formulation of mixing length;
- one-equation models;
- two-equation models;
- non-linear closure schemes.

Most of the three-dimensional models used in oceanography and physical limnology implement much simpler one or two-equation turbulence closures. One of the popular closure scheme which has recently attracted great attention in geophysical modeling is the two-equation $k-\epsilon$ model. It has originally been developed by Launder *et al.* [45], [55], and [62]. Some geophysical applications of this model have been described by Rodi [123]. The critical problem with this model is to guarantee the positivity of k and ϵ and the stability of the scheme in numerical computations.

However, in view of widely applicable description of turbulent scheme and in spite of several weaknesses, the two-equation models using two differential equations for both, the turbulent kinetic energy and its rate of dissipation, have proven to produce reasonable results.

2.3 The modeling of cohesive sediment

2.3.1 Cohesive sediment behavior and flocculation process

The deposition of the sediment in navigation channels may threaten the security of ships. The authorities in charge of the management of estuaries and harbors are often faced with frequent

costly dredging operations having important environmental and economical consequences. The relocation of the dredged material can also be a problem, especially when the sediments are contaminated. The interventions on the estuary bed must therefore be optimized [163]. Estuarine sediments play also an important role in the equilibrium of estuarine ecosystems. They contribute to biologic growth by delivering nutrients [42] and they also transport pollutants by absorption/dissorption. High concentration of suspended sediments inhibit photosynthesis by attenuating sunlight penetration into the water column [78]. The sediment-associated contaminants may become a major problem for living organisms [135]. The numerical modeling and simulation of the transport and fate of cohesive sediments and the related bed morpho-dynamics constitute an efficient tool for understanding the causes of sediment-related managerial problems and for finding appropriate solutions. Figure 2.3 shows the cohesive sediment structure within the estuary. Generally the estuary harbors have a silty floor, and the navigation channels need to be regularly dredged for large ships to pass through shoal. These fine sediments forming the bed material (in the order of micron) have relatively large ratios of surface area to volume. The electrochemical forces on the surface of the sediments lead to attraction between the particles. When fine particles collide with each other, the electrochemical force may cause them to bind together to form floc leading to the so-called flocculation process. The mechanism of flocculation considerably complicates the task of modeling the transport of cohesive fine sediments, such as the ones found in estuaries. The flocculation depends on the average diameter of the fine material, concentration of the solids, the level of turbulence intensity, and the salinity of the water. The floc consist of a skeleton formed by solid particles with the liquid filling the interstices. The density of the floc is, therefore, less than the density of the silt particles. The settling velocity of these flocculated sediments depend not only on the floc size and floc specific density but also on the concentration. The erosion and deposition mechanisms of cohesive sediments are also more complicated due to the presence of electrochemical forces, and consolidation of the deposited sediments. A bed made of consolidated cohesive sediments may resist relatively to large shear forces. However, once the failure occurs large chunks of sediment may be lifted from the bed. During the deposition, the consolidation of very fine particles takes place very slowly. Near the bed the depositing silt forms a layer with very high solid concentration. Such mud layers have a very small unit weight and a high degree of fluidity. They can be easily put into motion by relatively weak currents or wave action. With time such layers may loose their water and become consolidated.

2.3.2 The cohesive-sediment transport modeling

The cohesive sediment transport in an estuary involves the numerical solution of basic conservation equations for mass, momentum and turbulent energy. The Coriolis force, tidal forcing, wind action, resistance to flow at the bed, buoyancy effects due to temperature, salinity and sediment concentration, bed-level changes due to deposition and erosion should all be modeled for a realistic representation of the real world phenomena. In this respect, numerous research works have been carried out to establish well validated physical and mathematical descriptions of the behavior and fate of concentrated near-bed cohesive sediment suspensions and their interaction with the water column and the bed as well as the turbulence characteristics of sediment laden flow.

Van Rijn [115, 117] has developed a depth-integrated 2D model and a 3D model for non cohesive sediment transport. Only 3D model was used for simulating seabed evolution. Roberts [120] used a 2D depth-averaged model to investigate the fluid-mud. Ziegler and Nisbet [164] used a 2D model to study the transport of cohesive and non-cohesive sediments in Pawtuxet

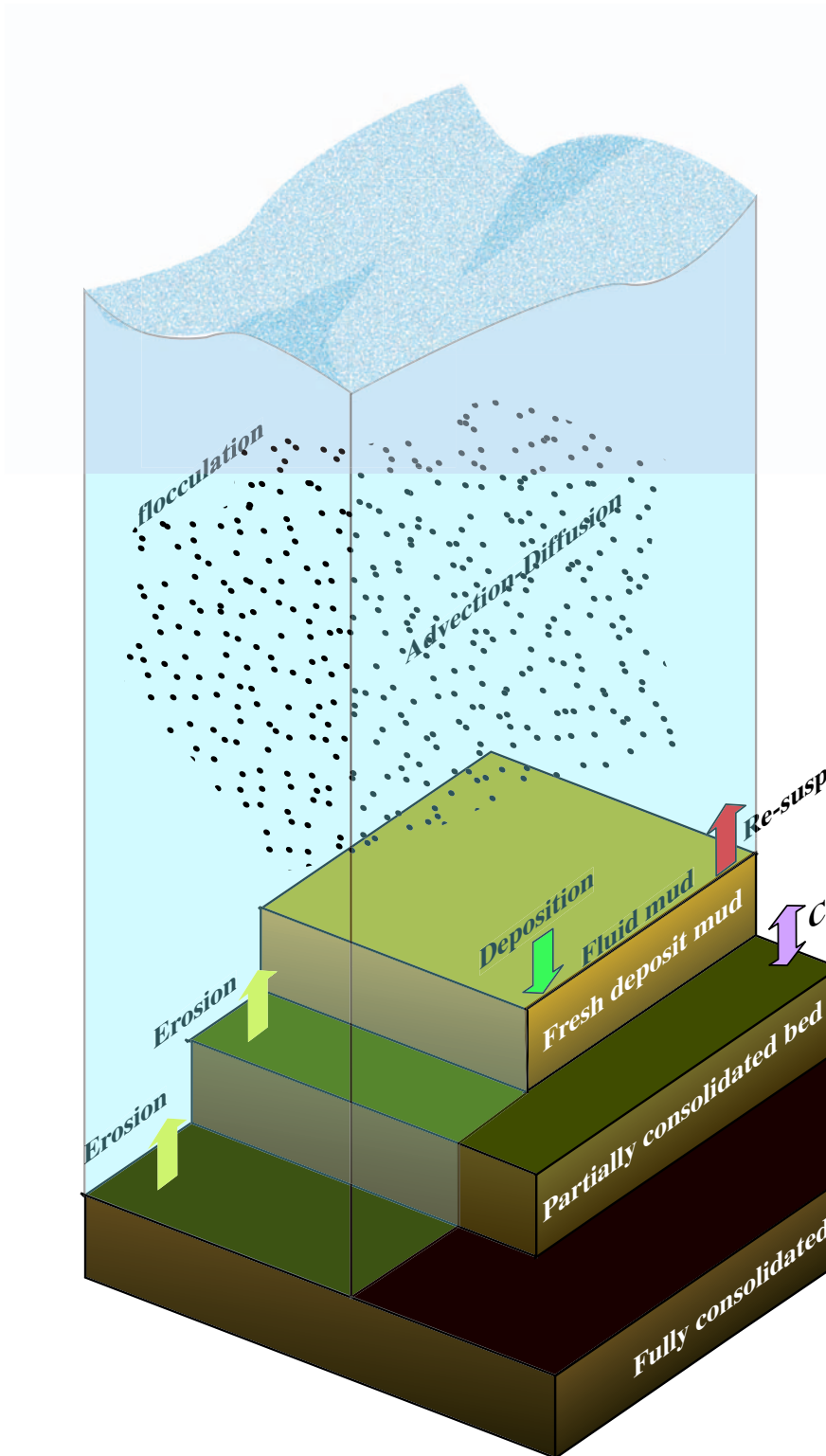


Figure 2.3: Bed structure and flocculation process within estuary

River in Rhode Island without simulating the seabed evolution. Guan *et al.* [43] used a 2D width-integrated model to compute sediment transport in Jiaojiang River Estuary in China. Lin and Falconer [73] used a 3D layer-integrated model to predict suspended sediment fluxes in the Humber Estuary, UK. Chen *et al.* [20] have successfully applied a three-dimensional finite difference model with hydrostatic pressure distribution for cohesive sediment transport by tidal currents and the resulting bed level changes to the Pearl River Estuary.

In the recent years several European research projects were launched on estuarine modeling within the framework of MARine Science and Technology (MAST). The MAST-COSINUS project aimed at establishing well validated physical and mathematical descriptions of the behavior and fate of concentrated near-bed cohesive sediment suspensions and their interaction with the water column and the sediment bed. One of the outcomes of this project was a *COupled Hydrodynamical Ecological model for Regional Shelf seas* called *COHERENS* [80]. The model COHERENS is composed of: a physical component with modules for currents, temperature and salinity; a microplankton module for simulating biological-ecological processes; a sediment module describing the deposition and resuspension of organic and inorganic material; an Eulerian and a Lagrangian particle tracer module for simulating the transport of contaminants (e.g. radioactive and non-radioactive waste material). The model does not however simulate the changes in bed morphology. Delft Hydraulics also developed an integrated 2D/3D model for simulating hydrodynamics and transport phenomena resulting from tidal and meteorological forcing. This model simulates also the variation of the bed morphology. The processes of consolidation, liquefaction, fluidization, erosion which determine the formation of the fluid-mud were studied by several researchers. Liu [76] derived several empirical functions for forecasting sediment deposition amounts in navigation channels. The unified theory of settling and consolidation proposed by Toorman [138] and the fluidization model of Yamamoto *et al.* [161] allow the computation of the density and/or stress history within the mud layer. The erosion of the consolidated sediment is generally used with an excess-shear type empirical relation in which the yield stress is a rheological property of the consolidated mud layer [44] and it is specified as a function of the density. Recently, van Kesteren *et al.* [145] proposed a geotechnical approach in order to take into account liquefaction and fluidization. Recent studies aim at parameterizing the structure of the mud using structural kinetics theory. This method was successfully applied to the modeling of the thixotropic behavior of mud [137] and to the formation of floc [155].

It is interesting to note that almost all of the models above assume a hydrostatic pressure distribution and use a finite difference or finite volume approach based on a topographically conform, sigma-transformed grid which, regardless of the depth, forces the same number of divisions in the water column. Most of the existing models are laminar (use simple algebraic expressions for parameterizing eddy coefficients), and they use varying degrees of parameterization in order to simplify the equations to be solved, whereas most of the exchange mechanisms are expressed by semi-empirical equations of state.

2.3.3 Cohesive sediment transport and turbulence

In the recent years considerable research work was carried out to establish well validated physical and mathematical descriptions of the behavior and fate of concentrated near-bed cohesive-sediment suspensions and their interaction with the water column and the bed as well as the turbulence characteristics of sediment laden flow. For estuarine flows the turbulence models should take into account the damping effect of vertical density stratification due to the presence of salt, and sediment as well as due to temperature differences. Casamitjana and Schladow [14] discussed the importance of a good turbulence modeling in the Eulerian approach used for pre-

dicting suspended sediment transport. Various researchers have numerically investigated the interaction between the turbulence and the sediment particles: Reynolds stress model [133], algebraic mixing-length model [64] and $k - \varepsilon$ two-equation model [142]. Olsen and Skoglund [103] calculated sediment concentration profiles in a sand trap using $k - \varepsilon$ turbulent model. Most of those models have considered only non-cohesive sediments for the sediment concentration profiles computation. In many models the settling velocity denoted by w_{ss} is taken as constant, whereas in reality it strongly depends on flocculation influenced by the turbulence intensity, salinity and temperature. Huang [49] proposed an expression of cohesive sediment settling velocity in which flocculation with effects of water temperature, settling distance sediment size and sediment concentration have been considered. Dyer [32] presented a conceptual model of the effect of shear and concentration on median floc settling velocity. The heuristic formulation of van Leussen and Corneliss [146], which relates flocculation and break-up to the dissipation rate of turbulent kinetic energy, was implemented with great success in the numerical estuary model by Malcherek *et al.* [81]. Tang [132] derived a function of critical shear stress for mixtures of cohesive and non cohesive sediments. Mehta and Srinivas [87] studied the entrainment between the water column and the fluid-mud.

Winterwerp and Kranenburg [156] derived an integral entrainment model by integrating the equation for kinetic turbulent energy over the water depth. Winterwerp and Kranenburg [157] proposed to model the entrainment of the fluid-mud as the entrainment of a dense fluid. Basoullet *et al.* [3] studied the sediment transport over an inter-tidal mud-flat and discussed about the field investigations and estimation fluxes within the “Baie De Marennes-Oleron” (France). Brenon and Le Hir [7–9] characterized the modeling of fine sediment dynamics in the estuaries, The changing position of the areas of maximum turbidity in estuaries, and the related processes of resuspension/settling and (de)flocculation are characterized with application made on the “Seine” estuary in France and the three-dimensional modeling of suspended cohesive sediment in the oriental Seine bay (Manche, France) has been studied. Some of these studies include also the (laser-reflectance) methodology used to investigate particle aggregate dynamics in experimental tidal flows. Such studies provide many insights into the complex relationships between floc size, tidal-velocity and suspended-sediment concentration, which may be useful in assessing the distribution of fines in ancient tidal deposit. The concept of turbidity accumulations modeling was applied successfully to fluid mud flows in the Loire estuary by Le Hir [65]. Le Hir *et al.* [66] applied *continuous modeling* concept to the highly concentrated suspended sediment. The results were compared successfully with the field measurements in a macro tidal estuary. Mallet *et al.* [82] discussed the use of numerical computation and statistical techniques to describe sedimentary circulation patterns in the mouth of the Gironde estuary in France. The mathematical modeling of the transport of fine particles and the mechanisms of the turbidity maximum stability have been applied to the Gironde Estuary by Sottolichio *et al.* [131]. Silva and Le Hir [128] discussed the rheological response of stratified muddy bed to water waves, while Roberts *et al.* [121] investigated the use of simple mathematical models to the effect of tidal currents and waves on the profile shape of inter-tidal mud-flats. Withehouse *et al.* [151] studied the influence of bed forms, flow, and sediment transport over inter-tidal mud-flats. The characterization of the inter-tidal flat-mud hydrodynamics has been discussed by Le Hir *et al.* [67]. A new set of equations and a new algorithm for computing erosion and deposition cohesive sediment transport has been proposed by Krishnappan [57] for the Fraser river (Canada). Chen *et al.* [20], using empirical functions specially developed for cohesive sediments have simulated successfully the Pearl River Estuary in China.

2.4 Concluding remark

Winterwerp and Kranenburg [158] discussed the interaction between suspended cohesive sediment and turbulence, and suggestions are made how to incorporate turbulence damping effects into standard turbulence models. The recommendations made resulting from their work exemplify the many uncertainties in quantifying cohesive-sediment dynamics, and the use of relatively simple turbulence modeling is recommended, because *more complex models do not perform any better by lack of proper calibration data in the case of sediment-laden flows*. They also discuss the dynamics of high-concentrated mud suspension, the flocculation processes and settling behavior of cohesive sediment. It should be emphasized that, although numerical hydrodynamic models are strongly based on the basic physics, sediment transport models rely heavily on the use of various empirical formula and are only numerical frameworks for interpolating and extrapolating full-scale field or laboratory measurements of “hydraulic sediment parameters”, such as threshold shears. Calibration of models against field and/or laboratory measurements is, therefore, of prime importance. Most of existing models of fine sediments transport assume the fine sediments behavior to be analogous to that of the coarse-grained sediment and consequently use transport theories developed for coarse sediment to treat the fine sediment. Among the many differences between the two types of sediments, the most crucial is the difference in the critical condition for initiation and cessation of sediment motion in a flowing medium. For the coarse-grained sediment, the critical conditions for initiation and cessation merge into a single criterion, i.e. the coarse sediments undergo simultaneous erosion and deposition while being transported under a constant bed shear stress. In the case of fine sediment, on the other hand, two distinct critical conditions (for deposition and erosion) were identified in literature (see Partheniades and Kennedy [106]; Partheniades *et al.* [105]; Ashish and Partheniades [2]; Lau and Krishnappan [61]). It should be pointed out that, for fine sediments, the simultaneous erosion and deposition is possible only for a certain range of bed shear stresses. Hence for shear stresses outside of this range, there could only be sediment deposition or erosion, but not both simultaneously. A true representation of the erosion and deposition of fine sediment is important for the cohesive sediment transport models. It is shown that if the simultaneous erosion and deposition is assumed, then the model will predict an enhanced dispersion of the contaminants whereas a mutually exclusion erosion and deposition will result in the preservation of comparatively high concentration of sediment bound contaminants over long distance from the source (see also [57]).

Recently Willis and Krishnappan [153] derived a new approach for numerical modeling cohesive mud in rivers and estuaries as well as recent advances in the calculation of erosion and deposition rates of cohesive sediment. Le Hir and Thouvenin [68] discussed the mathematical modeling of cohesive sediment and particle contaminants transport in the Loire estuary in France. Thorn and Parsons [136] investigations shown the possibility to model an estuary using quantitative relations from another one with the analogous characteristics.

In the present thesis, on the basis of the above mentioned literature the RANS equations will be solved in the framework of the SWE, and a suitable two-equation $k - \epsilon$ closure model is adopted to account for buoyancy effects encountered in multiphasic fluid-flows. Advection-diffusion equations will be written for the transport of scalar quantities such as salinity, concentration and temperature to account of the variable density fluid present in the estuaries. A new set of equations for the solid transport modeling respectively from (a) Chen *et al.* [20] (with simultaneous deposition and erosion) and (b) Krishnappan [57] (with mutually exclusive deposition and re-suspension power laws) will be incorporated in the model to investigate the suspended sediment concentration and seabed evolution, using the concept of turbidity accumulations mod-

eling (see [65]) and applying *continuous modeling* concept to the highly concentrated suspended sediment (see Le Hir *et al.* [66]), some empirical relationships investigated from experiments by Trimbak and Mehta [139] on the one hand, and on the other hand from the field observations by Migniot [93] in the Loire estuary, will be used for the bed consolidated-layers modeling in the Po River Estuary (PRE) in Italy.

Chapter 3

Mathematical modeling

In this chapter, starting from the three-dimensional incompressible Navier-Stokes equations, the mathematical modeling of free surface water flows is developed. Proper boundary conditions are introduced and some simplifying assumptions (hydrostatic and Boussinesq approximations) are presented. Finally $2D$ and $3D$ models are derived and discussed, while the closure turbulence equations and the suitable boundary conditions are introduced.

3.1 Modeling of the geophysical flows

In this chapter we will review the mathematical modeling of free surface flows for environmental applications. In particular we will discuss the validity of some hypotheses usually adopted in this context.

Many engineering and environmental flow problems involve the study of water motion in rivers, lakes and seas. They are characterized by the presence of a *free surface* and, in some cases, by a vertical scale much smaller than the horizontal one. For that reason they are commonly called *shallow water* flows. In this context a very common assumption is the hydrostatic approximation for the pressure distribution which is valid for *long waves* (small vertical accelerations). This approximation implies that the momentum equation in the vertical direction, z , is reduced to a static relation, *i.e.* the z derivative of the pressure is balanced by the gravity acceleration. In practical applications many $1D$ (depth and width averaged) and $2D$ (depth averaged) models based on this assumption are used. Nevertheless, in some situations the necessity of a detailed description of the $3D$ velocity field and/or the presence of short waves (or strong bathymetry gradients) demands the use of a $3D$ model. A $3D$ hydrostatic model is suitable for obtaining a three dimensional description of the velocity field (provided that a particular attention is paid to the calculation of the vertical velocity, as we will see in section 3.4.2) however to account for short waves one must resort to a more accurate model in which the hydrostatic assumption is removed.

In the sequel the Navier-Stokes Equations and the Boussinesq approximation are reviewed and discussed, with the boundary conditions to close the problem and to describe the motion of the free surface. The hydrostatic assumption is introduced and the SWE model based on this approximation is presented. Finally the $3D$ non-hydrostatic model is introduced.

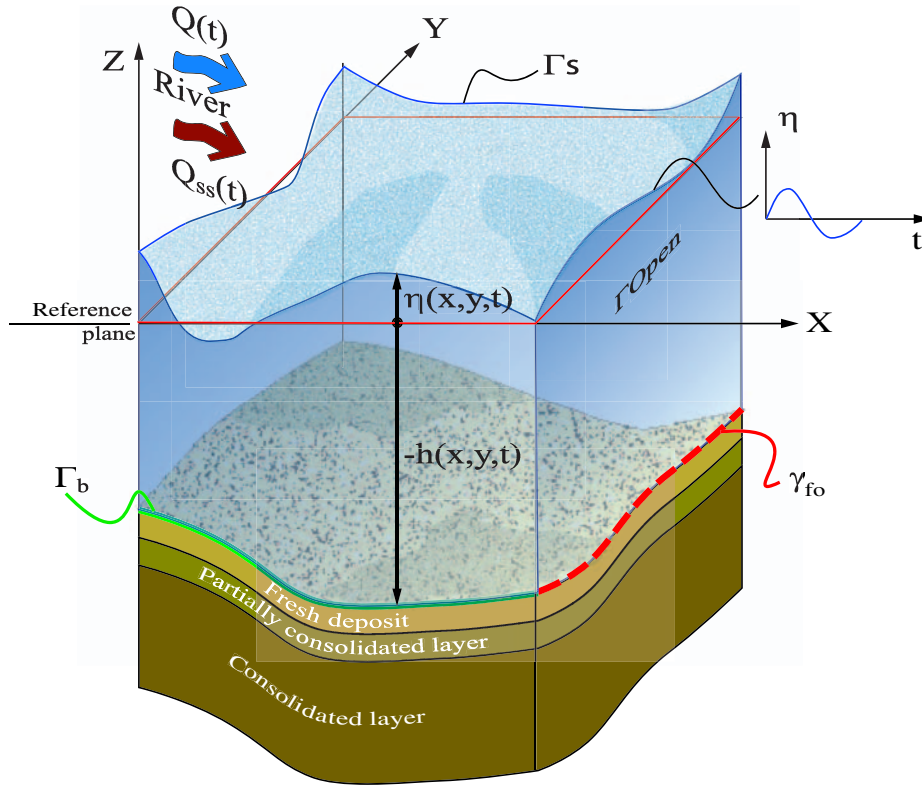


Figure 3.1: The computational domain $\hat{\Omega}(t)$

3.2 The Turbulent Navier-Stokes equations and the Boussinesq approximation

Let us refer to the Cartesian coordinate system (x, y, z) . We are interested in the description of the motion of a free-surface viscous incompressible fluid in a time-dependent 3D domain $\hat{\Omega}(t)$ (with $t > 0$). Let Ω be a fixed bounded region of $\hat{\Omega}(t)$ representing the domain of definition of the function $z = -h(x, y, t)$ which describes the bathymetry with respect to the reference level $z = 0$; Ω is such that for every t the projection on the xy plane of the volume occupied by the water at time t is contained in Ω . Finally the boundary of Ω will be denoted by γ_f .

It is worthwhile to notice that usually h does not depend on t . However, we will see in section 3.2.3 that there are problems where the bottom shape can change with time in a prescribed manner.

Moreover $z = \eta(x, y, t)$ is the function describing the free surface with respect to the reference level $z = 0$ (see fig. 3.1). The total depth of the fluid at point (x, y) at time t will be denoted by $H(x, y, t) = h(x, y, t) + \eta(x, y, t)$.

The domain which is occupied by the fluid at time t is then

$$\hat{\Omega}(t) = \{(x, y, z) | (x, y) \in \Omega, z \in (-h(t), \eta(t))\}. \quad (3.1)$$

The boundary of $\hat{\Omega}(t)$ is denoted by $\Gamma(t)$ and comprises three parts (see fig. 3.2):

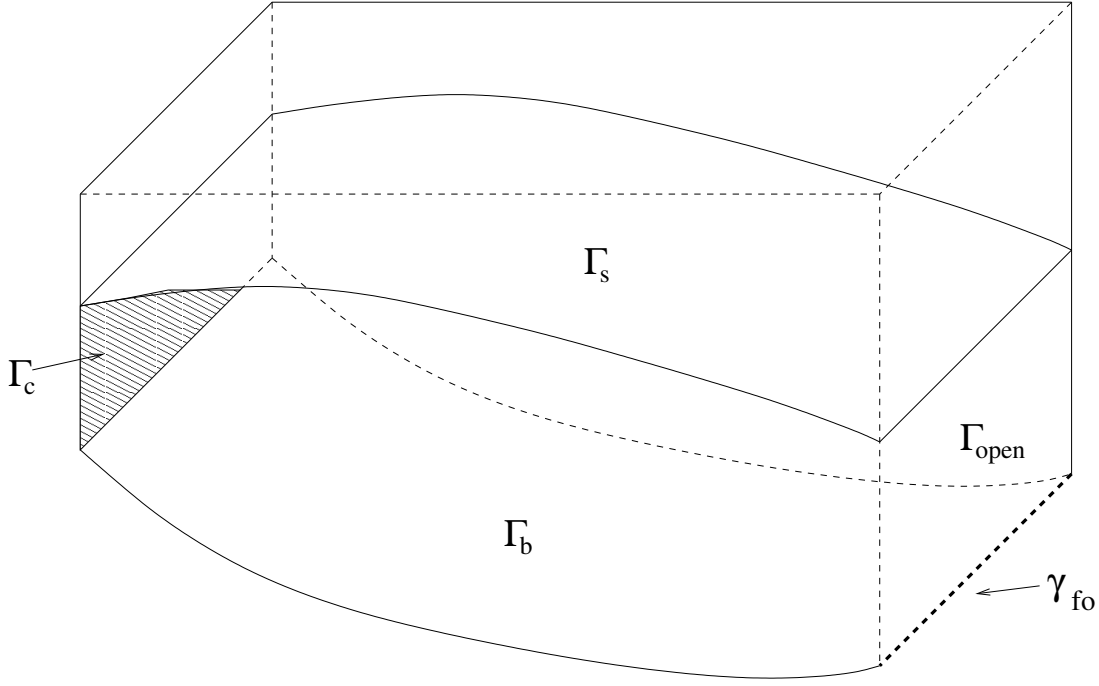


Figure 3.2: Notation for the boundary

1. the bottom topography $\Gamma_b(t) = \{(x, y, -h(t)) | (x, y) \in \Omega\}$;
2. the free surface $\Gamma_s(t) = \{(x, y, \eta(t)) | (x, y) \in \Omega\}$
3. the “lateral” boundary $\Gamma_l(t) = \{(x, y, z) | (x, y) \in \gamma_h, z \in (-h(t), \eta(t))\}$. This part of the boundary includes “vertical walls” (Γ_c) and fictitious water-water boundary, $\Gamma_{open} = \gamma_{fo} \times (-h(t), \eta(t))$, where γ_{fo} is the bold-dashed segment in figure 3.2.

Applying the Reynolds decomposition to turbulent flow (see [109], [124], [118]), an ensemble time-averaged mean value is well-defined for a variable Φ . From time-averaging procedure each instantaneous variable Φ is represented as a time-mean value, $\tilde{\Phi}$, and a fluctuation value Φ' , with the following properties :

$$\Phi = \tilde{\Phi} + \Phi' \quad , \quad \langle \Phi \rangle = \tilde{\Phi} \quad , \quad \langle \Phi' \rangle = 0 \quad (3.2)$$

where $\langle \Phi \rangle = \frac{1}{T} \int_0^T \Phi dt$ denotes the averaging procedure in which T is time-averaging period (this period T should be larger than the dominant turbulent scale, but smaller than the long periodic effects such as the tidal scale). This decomposition is applied to the dependent variables (such as velocity and pressure fields). When the Navier-Stokes equations are averaged the non linear term of the material time derivative generates a new tensor, the Reynolds turbulent stress, which in index notation is given by

$$\mathbf{R}_{ij} = -\rho \widetilde{\mathbf{V}'_i \mathbf{V}'_j} \quad (3.3)$$

here, V denotes the velocity field. This Reynolds stress is usually modeled via the Boussinesq eddy viscosity concept μ_T that is written

$$\mathbf{R} = -\frac{2}{3}k\mathbf{I} + 2\mu_T\bar{\boldsymbol{\tau}} \quad (3.4)$$

where $\bar{\boldsymbol{\tau}} = \left(\partial\tilde{\mathbf{V}}_i/\partial x_j + \partial\tilde{\mathbf{V}}_j/\partial x_i\right)/2$ is the mean strain rate tensor, \mathbf{I} is the identity tensor and μ_T is the turbulent dynamic viscosity. In the sequel, for the ease of notation, the mean turbulent quantities like the velocity and pressure fields will be used without tilde.

3.2.1 Hydrodynamics

The motion of the fluid is described by the following RANS valid for $\forall t > 0$ and $\forall (x, y, z) \in \hat{\Omega}(t)$, in which the physical viscosity $\nu = 10^{-6} [m^2/s]$ is neglected with respect to the turbulent viscosity :

$$\begin{cases} \nabla \cdot \mathbf{V} = 0 \\ \frac{D\mathbf{V}}{Dt} = -\frac{1}{\rho}\nabla p + \nabla_{xy} \cdot (\nu_h \nabla_{xy} \mathbf{V}) + \frac{\partial}{\partial z} \left(\nu_v \frac{\partial}{\partial z} \mathbf{V} \right) + \tilde{\mathbf{G}}_f \end{cases} \quad (3.5)$$

In the sequel we will use also the following notations : $\mathbf{V} = (u, v, w)$ is the 3D velocity vector. ν_h and ν_v represent respectively the horizontal and vertical eddy viscosity coefficients (see [122]), p is the mean pressure, $\tilde{\mathbf{G}}_f = (f_1 v, -f_2 u, -g)$ contains the gravity term $\mathbf{g} = (0, 0, -g)^T$ and the Coriolis term $\mathbf{f}_{xy} (f_1 = 2\Omega_m \sin\phi, f_2 = 2\Omega_m \cos\phi)^T$, in which Ω_m stands for the magnitude of the angular velocity of the Earth and ϕ for the angle of latitude. $\nabla_{xy} = \left(\frac{\partial}{\partial x}, \frac{\partial}{\partial y}\right)$ is the 2D nabla operator (the corresponding 3D operator is denoted by ∇).

$\left(\frac{D}{Dt} = \frac{\partial}{\partial t} + u\frac{\partial}{\partial x} + v\frac{\partial}{\partial y} + w\frac{\partial}{\partial z}\right)$ stands for the material derivative, and $\mathbf{v} = (u, v)$ is the 2D horizontal velocity vector.

As for variable density fluids some simplifying assumptions are usually made. First of all it must be noticed that density variations occurring in practical applications are relatively small ($\pm 3\%$) with respect to the average density. Due to this fact density variations are important only in those terms where they give rise to buoyancy forces and can be neglected in those terms where the density appears as a parameter describing the inertia of the fluid (see [31], [141]).

In particular in the momentum equation we must consider density variations in the term $\frac{1}{\rho}\nabla p$; moreover we suppose that the density can be written as the sum of a reference density ρ_0 and a local variable density $\delta\rho$, such that $\left|\frac{\delta\rho}{\rho_0}\right| \ll 1$, we have

$$\frac{1}{\rho} = \frac{1}{\rho_0 + \delta\rho} = \frac{1}{\rho_0 \left(1 + \frac{\delta\rho}{\rho_0}\right)} \approx \frac{1}{\rho_0} \left(1 - \frac{\delta\rho}{\rho_0}\right). \quad (3.6)$$

where ρ is the fluid density, $\rho_0 = 999.842594 [kg/m^3]$ is the reference water density at temperature $T = 4^\circ C$. As we will point out in section 3.5, the pressure can be split into two parts: an hydrostatic one $p_{h\rho_0} = \rho_0 g(\eta - z)$ deriving from the average density and a correction δp such that $p = p_{h\rho_0} + \delta p$; hence we have

$$\begin{aligned} -\frac{1}{\rho}\nabla p &\approx -\frac{1}{\rho_0}\nabla p + \frac{\delta\rho}{\rho_0^2}\nabla p = -\frac{1}{\rho_0}\nabla p + \frac{\delta\rho}{\rho_0^2}\nabla p_{h\rho_0} + \frac{\delta\rho}{\rho_0^2}\nabla(\delta p) \\ &= -\frac{1}{\rho_0}\nabla p - \frac{\delta\rho}{\rho_0}\mathbf{g} + \frac{\delta\rho}{\rho_0}g\nabla\eta + \frac{\delta\rho}{\rho_0^2}\nabla(\delta p). \end{aligned} \quad (3.7)$$

where \mathbf{g} is a vector containing the gravity acceleration. In the system of equations (3.5) the *Boussinesq approximation* is invoked, and this implies that the density ρ , is assumed to be constant, ρ_0 , except in the buoyancy term. Consequently the last two (second order) terms can be neglected, yielding

$$-\frac{1}{\rho}\nabla p = -\frac{1}{\rho_0}\nabla p + \frac{\delta\rho}{\rho_0}\mathbf{g}. \quad (3.8)$$

Moreover, the local variable density is supposed to depend only on temperature T , salinity S and concentration of a passive scalar C_s , *i.e.*, $\rho = \rho(T, S, C_s)$.

For T , S and/or C_s an additional equation must be specified as follows

$$\frac{D\Phi}{Dt} - \nabla_{xy} \cdot \left(\frac{\nu_h}{\sigma_\Phi} \nabla \Phi \right) - \frac{\partial}{\partial z} \left(\frac{\nu_v}{\sigma_\Phi} \frac{\partial \Phi}{\partial z} \right) = F_\Phi, \quad \text{for } \Phi = (T, S, C_s) \quad (3.9)$$

where Φ (here and in the following sections) may represent T, S or C_s and σ_Φ is a Schmidt turbulent number depending on the considered variable Φ .

A more suitable equation of state (see also [80], [144]) can be written as follows,

$$\begin{aligned} \rho_m = & \rho_0 + a_1 \cdot T + a_2 \cdot T^2 + a_3 \cdot T^3 + a_4 \cdot T^4 + a_5 \cdot T^5 \\ & + (a_6 + a_7 \cdot T + a_8 \cdot T^2 + a_9 \cdot T^3 + a_{10} \cdot T^4) S \\ & + (a_{11} + a_{12} \cdot T + a_{13} \cdot T^2) S^{3/2} + a_{14} \cdot S^2 \end{aligned} \quad (3.10)$$

$$\rho = \rho_m + \left(\frac{\rho_s - \rho_m}{\rho_s} \right) C_s$$

where ρ_m and ρ_s expressed in [kg/m³] are respectively the liquid mixture and sediment density, C_s is the sediment concentration, S and T are respectively the salinity and temperature of the fluid mixture (liquid+solid). The given coefficients in equation (3.10) can be found in the following table:

$a_1 = 0.06793952$	$a_2 = -0.009095290$	$a_3 = 0.0001001685$	$a_4 = -0.000001120083$
$a_5 = 0.000000006536332$	$a_6 = 0.824493$	$a_7 = -0.0040899$	$a_8 = 0.000076438$
$a_9 = -0.00000082467$	$a_{10} = 0.0000000053875$	$a_{11} = -0.00572466$	$a_{12} = 0.00010227$
$a_{13} = -0.0000016546$	$a_{14} = 0.00048314$		

Table 3.1: The coefficients of the equation of state (3.10)

The introduction of the closure relationship (3.4) brings the difficulty of turbulence modeling to the turbulent viscosity. this parameter will be related to the turbulent kinetic energy k and the dissipation rate ε on the basis of dimensional arguments, *i.e.* $\nu_T = c_\mu \frac{k^2}{\varepsilon}$, with c_μ a constant that will be calibrated on known homogeneous flows. Therefore, we have to compute k and ε through pdes which will be given in the sequel.

3.2.2 The $k - \varepsilon$ turbulence closure

One of the most difficult problems in such geophysical modeling is the adequate parameterization of the vertical exchange processes. In the present work, there are represented through the eddy coefficients ν_v, λ_v , which values are to be provided by a turbulence scheme. In view of widely applicable description of turbulent scheme, two-equation models using two differential

equations for both, the turbulent kinetic energy and its dissipation rate have proven to give good results [80].

Turbulence phenomena of geophysical interest are most often affected by the buoyancy of the fluid. Buoyancy introduces the notion of potential energy to the budget equations. This fact inherently complicates the description of the turbulence: at first, potential energy can be converted to kinetic energy in free convection. Next in stable situations potential energy can be gained from kinetic energy and a parallel energy cascade ending with the destruction of temperature fluctuations by thermal conduction is opened up. Besides this, the situation is further complicated by the fact that non-locally acting internal waves with properties completely different from turbulence can also contribute significantly to the fluctuating potential energy. In the present work the state-of-the-art $k - \varepsilon$ turbulence model will be introduced to be able to account for both the homogeneous and stratified flows. The turbulence equations read, (see also [63], [122], [96]).

$$\frac{Dk}{Dt} - \nabla \cdot \left[c_\mu \frac{k^2}{\varepsilon} \nabla k \right] = c_\mu \frac{k^2}{\varepsilon} P_d - \varepsilon - \lambda_v N^2 \quad (3.11)$$

$$\frac{D\varepsilon}{Dt} - \nabla \cdot \left[c_\varepsilon \frac{k^2}{\varepsilon} \nabla \varepsilon \right] = c_1 k P_d - \frac{\varepsilon}{k} [c_3 \lambda_v N^2 + c_2 \varepsilon] \quad (3.12)$$

The squared shear frequency or production term P_d is (see [80]):

$$P_d = \frac{1}{2} (\|\nabla \mathbf{V} + \nabla \mathbf{V}^T\|)^2 \quad (3.13)$$

where $\|\cdot\|$ is the 2-norm of the matrix. The constants are given: $c_1 = 0.126$, $c_2 = 1.92$, $c_\mu = 0.09$, $c_\varepsilon = 0.07$. In the above equations, N is the Brunt-Väisälä frequency, with the related following squared buoyancy N^2 (see [80]) expression,

$$N^2 = -\frac{\nu_v g}{\sigma_t \rho_0} \frac{\partial \rho}{\partial z} \quad (3.14)$$

Here $\sigma_t = 1$ is a constant, and the following expressions of eddy coefficients ν_v, λ_v should include the stability parameters to account for the turbulence damping in the stratified fluid flows (see Luyten et al. [79], COHERENS [80]):

$$\nu_v = S_u \frac{k^2}{\varepsilon} + \nu \quad , \quad \lambda_v = S_b \frac{k^2}{\varepsilon} + \lambda_b \quad (3.15)$$

$$S_u = \frac{0.108 + 0.0229\alpha_N}{1 + 0.471\alpha_N + 0.0275\alpha_{N^2}} \quad , \quad S_b = \frac{0.177}{1 + 0.403\alpha_N} \quad (3.16)$$

where $\lambda_b = 10^{-6}$, and the following stability coefficients α_N and c_3 can be expressed as,

$$\alpha_N = \frac{k^2}{\varepsilon^2} N^2 \quad (3.17)$$

$$c_3 = \begin{cases} -0.4 & \text{for } N^2 < 0 \\ 1 & \text{otherwise} \end{cases} \quad (3.18)$$

Richardson-number

The Richardson number is useful for classification of stratified flows depending on the stability of the water column. It can be defined according to the shear production and the buoyancy (see [104])

$$R_i = \frac{N^2}{\nu_v P_d} \quad (3.19)$$

3.2.3 Boundary conditions for the hydrodynamics

Free-surface

Consider now the system (3.5), at the free surface we impose a kinematic condition which states that the velocity of the fluid is equal to the velocity of the free surface itself

$$\frac{\partial \eta}{\partial t} + u \frac{\partial \eta}{\partial x} + v \frac{\partial \eta}{\partial y} = w, \text{ on } \Gamma_s(t). \quad (3.20)$$

This equation is able to describe the motion of the free surface of the fluid.

We need another equation that expresses a dynamic condition. If we neglect surface tension we have

$$p = p_a \quad (3.21)$$

where p_a is the atmospheric pressure and moreover

$$\nu_v \frac{\partial \mathbf{u}}{\partial z} = \mathbf{f}_1(\mathbf{W}) \quad (3.22)$$

where \mathbf{W} is the wind velocity vector and $\mathbf{f}_1(\mathbf{W})$ is a prescribed function. Typically $\mathbf{f}_1(\mathbf{W}) = \rho_a C_w |\mathbf{W}| \mathbf{W}$, where $|\mathbf{W}|$ denotes the modulus of the wind speed at the reference level above the mean free surface, ρ_a is the air density, and C_w is a constant whose value depends on the wind speed, such as:

$$C_w = \begin{cases} 1.2 \times 10^{-6}, & \text{if } |\mathbf{W}| \leq W_c, \\ 1.2 \times 10^{-6} + 2.25 \times 10^{-6} \left(1 - \frac{W_c}{|\mathbf{W}|}\right)^2, & \text{if } |\mathbf{W}| > W_c, \end{cases} \quad (3.23)$$

where $W_c = 5.6\text{m/s}$, as expressed in [26].

Bottom

On the bottom, the kinematic condition accounts for the presence of sinks and/or sources described by the known function $F_b(x, y, t)$ and for the bottom shape variation in time. Thus we have

$$\frac{\partial h}{\partial t} + u \frac{\partial h}{\partial x} + v \frac{\partial h}{\partial y} + w = F_b, \quad (3.24)$$

i.e.

$$w + u \frac{\partial h}{\partial x} + v \frac{\partial h}{\partial y} = \tilde{F}_b, \text{ on } \Gamma_b(t), \quad (3.25)$$

where $\tilde{F}_b = F_b - \frac{\partial h}{\partial t}$ accounts for the bottom shape functions that can be described from various values depending of the type of flow (see for instance [140], [89]):

1. The case of a draining vortex where there is no change in the bottom shape ($\frac{\partial h}{\partial t} = 0$) but there is a net flux through the bottom ($F_b \neq 0$) (see [140]). The same situation is encountered in the case of filtration of water in the ground (see for instance [91]).
2. The transport of sediment changes the shape of the bottom (hence $\frac{\partial h}{\partial t} \neq 0$ and $F_b = 0$) due to deposition or erosion.
3. The effect of a seaquake (see [84]) can be modeled through a sudden change in the bottom shape ($\frac{\partial h}{\partial t} \neq 0$).

The no-slip boundary condition is applied together with a zero normal velocity component to Γ_b . This second condition can be represented by :

$$w + u \frac{\partial h}{\partial x} + v \frac{\partial h}{\partial y} = F_b - \frac{\partial h}{\partial t} = \tilde{F}_b, \quad \text{on} \quad \Gamma_b(t) \quad (3.26)$$

where $F_b(x, y, t)$ and $\frac{\partial h}{\partial t}$ are known functions describing sinks and/or sources and the variation of the bottom shape, respectively.

At the bottom, with the no-slip boundary condition it is easily observed that viscous fluids have zero velocity at solid walls. The problem is that some assumptions used to derive the $k - \varepsilon$ equations are not fulfilled in these near wall regions and indeed the model fails. Consequently we can either modify the equations appropriately in these parts of the domain to be able to use the same boundary conditions at the same boundary anyway, or we can introduce a new boundary inside the original area where the model is assumed to be valid. Both approaches can be found in the literature.

- The so-called *Low-Reynolds-number-Models*, where the constants $c_\mu, c_1, c_2, c_\varepsilon$ are replaced with stability functions $f_\mu, f_1, f_2, f_\varepsilon$. These functions should be chosen in a way to reflect the right behavior of the flow near the wall. In the case of strong velocity gradient in the near-wall regions, adaptative refinement is required, and it might happen that all the refinement is done in this region alone. The resulting solution would be a dissatisfying level of accuracy in the interesting inner region.
- The so-called *wall law* or *wall function*, where an algebraic relation is developed between the velocity and the normal distance to the wall (see figure 3.3).

Analysis and comparison of different approaches can be found in [129].

In the sequel we will use the *wall function* to establish a nonlinear boundary condition at the interface between the inner domain and the boundary layer.

wall function

The figure 3.3 represents the region close to the wall b , where shear stress (see Eq. (3.32)) is defined according to the so-called *law of the wall*.

The *wall - functions* approximation is applied to the region closed to the rigid wall (see [62]), by assuming that no-slip flow condition prevails in the region close to the wall with the

universal logarithmic velocity distribution normal to the wall. The universal logarithmic velocity distribution can be applied in the boundary layer. (see figure 3.3)

$$\frac{\mathbf{V}_t}{\mathbf{V}_*} = \frac{1}{\kappa} \ln(\mathbf{E} \delta_n^+) \quad , \text{ with } \delta_n^+ = \frac{V_* \delta_n}{\nu} \quad (3.27)$$

where \mathbf{V}_* is a vector whose magnitude is the friction velocity, V_* , and whose direction is that of the projection, V_t , of the velocity at the first mesh point, A, near (on the plane parallel) to the wall. κ is von Karman universal constant, δ_n is the normal distance to the nearest wall (distance of point A), ν is the molecular viscosity of water, and \mathbf{E} is the wall roughness coefficient.

Remark 1 *It is worthwhile to notice that the coefficient \mathbf{E} in the above relation accounts for all flow regimes, either hydraulically smooth, rough, or transitional.*

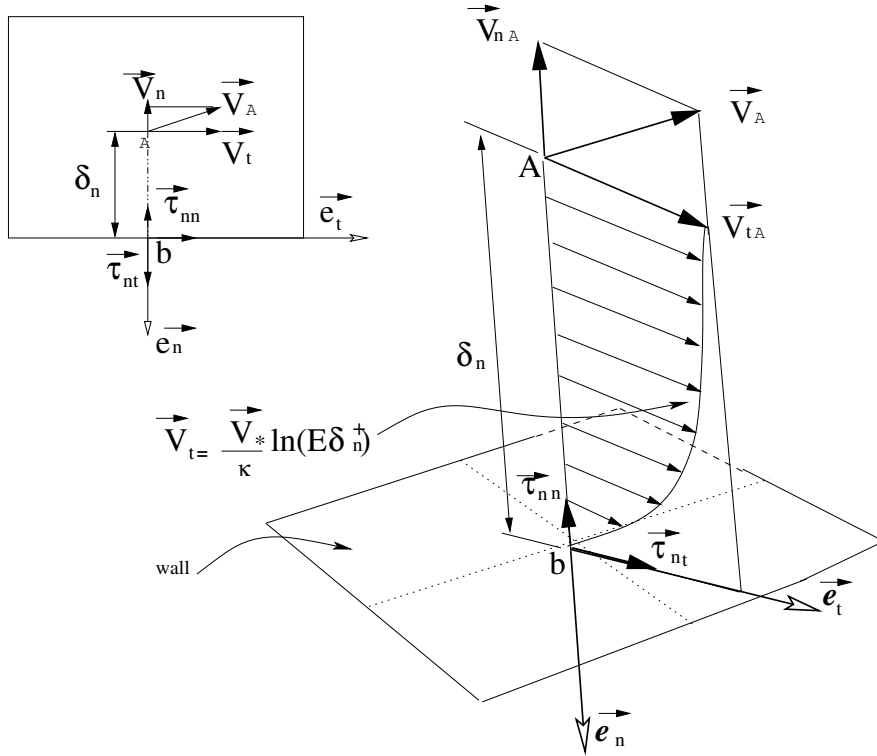


Figure 3.3: wall boundary

The wall roughness coefficient \mathbf{E} is adjusted according to the standard roughness (Wu *et al.* [159])

$$\mathbf{E} = \exp[\kappa(\mathcal{B} - \Delta\mathcal{B})] \quad (3.28)$$

where \mathcal{B} is an additive constant, $\Delta\mathcal{B}$ is a roughness function related to the standard roughness, k_s , such as (see [16]):

$$\Delta\mathcal{B} = \begin{cases} 0 & \text{for } k_s^+ < 2.25 \\ [\mathcal{B} - 8.5 + \frac{1}{\kappa} \ln k_s^+] \sin[0.4258(\ln k_s^+ - 0.811)] & \text{for } 2.25 < k_s^+ < 90 \\ \mathcal{B} - 8.5 + \frac{1}{\kappa} \ln k_s^+ & \text{for } k_s^+ > 90 \end{cases} \quad (3.29)$$

where $k_s^+ = \frac{V_* k_s}{\nu}$ is the roughness Reynolds number, $\kappa = 0.41$, and $\mathcal{B} = 5.2$.

Remark 2 *Strictly speaking the validity of the equation above is limited at the wall, but is extended to the cell center A close to the wall by approximation*

From Boussinesq concept and the definition of the shear stress one can find :

$$V_*^2 = \frac{\tau_{nt}}{\rho} = \nu_v \left[\left(\frac{\partial \mathbf{V}_t}{\partial n} \right) \right]_A \quad (3.30)$$

also the velocity gradient is computed by taking the derivative of the logarithmic law (3.27) and one can find that:

$$\left[\left(\frac{\partial \mathbf{V}_t}{\partial n} \right) \right]_A = \frac{V_*}{\kappa \delta_n} \quad (3.31)$$

From equations (3.31) and the eddy coefficients formulation the dynamic boundary condition becomes

$$\tau_{nt,b} = -\rho C_\mu^{\frac{1}{4}} k_A^{\frac{1}{2}} \frac{\kappa \mathbf{V}_{t,A}}{\ln(\mathbf{E} \delta_n^+)} \quad (3.32)$$

$$\mathbf{V}_* = C_\mu^{\frac{1}{4}} k_A^{\frac{1}{2}} \quad (3.33)$$

in which k_A represents the turbulent kinetic energy at the first vertical point from the bottom.

3.2.4 Integral form of the free surface equation

Let us now derive an alternative form of the equation describing the motion of the free surface. To this aim we integrate the first equation [i.e. (local) mass balance] of system (3.5) along the vertical coordinate

$$\int_{-h}^{\eta} \frac{\partial u}{\partial x} dz + \int_{-h}^{\eta} \frac{\partial v}{\partial y} dz + \int_{-h}^{\eta} \frac{\partial w}{\partial z} dz = \int_{-h}^{\eta} \frac{\partial u}{\partial x} dz + \int_{-h}^{\eta} \frac{\partial v}{\partial y} dz + w_s - w_b = 0, \quad (3.34)$$

where w_s and w_b are the vertical velocities on the surface and on the bottom. Using the Leibniz rule

$$\frac{\partial}{\partial s} \int_{a(s)}^{b(s)} f(x, s) dx = \int_{a(s)}^{b(s)} \frac{\partial f}{\partial s}(x, s) dx + f(b(s), s) \frac{\partial b}{\partial s} - f(a(s), s) \frac{\partial a}{\partial s} \quad (3.35)$$

we obtain

$$\begin{aligned} w_s - w_b &= - \int_{-h}^{\eta} \frac{\partial u}{\partial x} dz - \int_{-h}^{\eta} \frac{\partial v}{\partial y} dz = \\ &= - \frac{\partial}{\partial x} \int_{-h}^{\eta} u dz + u|_{\eta} \frac{\partial \eta}{\partial x} + u|_{-h} \frac{\partial h}{\partial x} - \frac{\partial}{\partial y} \int_{-h}^{\eta} v dz + v|_{\eta} \frac{\partial \eta}{\partial y} + v|_{-h} \frac{\partial h}{\partial y}. \end{aligned} \quad (3.36)$$

Using now (3.20) and (3.25) we finally have

$$\frac{\partial \eta}{\partial t} + \frac{\partial}{\partial x} \int_{-h}^{\eta} u dz + \frac{\partial}{\partial y} \int_{-h}^{\eta} v dz = \tilde{F}_b. \quad (3.37)$$

Remark 3 *In the above derivation we have implicitly assumed that the free surface is represented by a single valued function of x and y ; this fact implies that some phenomena, such as overturning waves, cannot be described. To describe overturning and breaking waves other methods could be used, such as e.g. the marker-and-cell (MAC) [46] [150], the volume of fluid (VOF) [48] and the level-set [53], [126]. The VOF and level-set methods do not use the integrated form of the continuity equations to find the free surface positions but they solve an additional advection equation to track the position of the particles on the free surface.*

Remark 4 *In some situations when the variations of the free surface are small the rigid lid approximation might be used, i.e. equation (3.20) is substituted by $w = 0$ on $\Gamma_s(t)$. This hypothesis avoids the solutions of a free surface problem and is widely adopted in ocean modeling (where even the bottom kinematic condition is simplified to $w = 0$ on $\Gamma_b(t)$) (see [75]).*

In this case integrating the continuity equation in the vertical direction and recalling that $w = 0$ on $\Gamma_b(t) \cup \Gamma_s(t)$ we obtain

$$\nabla \cdot \int_{-h}^0 \mathbf{u} dz = 0, \quad (3.38)$$

i.e. we have a non-local constraint in the system. For an analysis of this problem see [74] and [75].

Open sea

We have now to discuss the conditions on $\Gamma_l(t) = \Gamma_{Open}(t) \cup \Gamma_c(t)$. Let us first consider $\Gamma_{open}(t)$ (that we suppose to be vertical): this is a fictitious boundary used for computational purposes and on it the effect of the outside is taken into account. Typically we impose the elevation as a function of time *i.e.* $H(x, y, t) = H_0(x, y, t)$ where for all $(x, y) \in \gamma_{fo}$, H_0 is a prescribed function of t ; moreover the normal component of the velocity is set to zero on $\Gamma_c(t)$. Another approach has been proposed for the velocity by Huang and Lu [50], who have derived the velocity from the radiation condition (see also Yauw and Mellor [101]) using the observed data and according to the tidal wave propagating speed \sqrt{gh} . This form reads,

$$\frac{\partial \mathbf{v}}{\partial t} - c_i \nabla_{xy} \mathbf{v} = 0, \quad c_i = \sqrt{g H_{max} \frac{\delta \rho_m}{\rho_m}} \quad (3.39)$$

where $\mathbf{v} = (u, v)$ is the horizontal velocity vector, c_i is the baroclinic internal wave speed, H_{max} is the observed maximal flow total depth, $\delta \rho_m$ is the top-to-bottom fluid density difference.

Solid-wall

Here on the rigid boundary $\Gamma_c(t)$, the slip condition is applied and normal component of the velocity is set to zero for reflecting walls, and the no-slip boundary is applied for non reflecting walls.

Upstream

The given known functions describes the flow

$$Q = f(x, y, t) \quad (3.40)$$

$$\mathbf{V} = f(Q, H_{inl}) \quad (3.41)$$

where Q denotes a prescribed discharge, H_{inl} is the water depth at inlet.

3.2.5 Boundary conditions for the turbulence equations

Bottom

The production of the turbulent kinetic energy is merely due to the (turbulent) shear stress.

Since the velocity is equal to zero everywhere along the wall , $V_t = 0$ (no slip condition) and $V_n = 0$ (no flux across the wall), the production term or squared shear frequency can be rewritten,

$$P_d = \nu_v \left[\left(\frac{\partial V_t}{\partial n} \right)^2 + 2 \left(\frac{\partial V_n}{\partial \tau} \right)^2 \right] \quad (3.42)$$

The first and second terms denote respectively the turbulent energy production due to shear and the normal stress. The second term is too small compared with the first one, and can be neglected, and the squared shear frequency can be written as follows :

$$P_d = \nu_v \left[\left(\frac{\partial V_t}{\partial n} \right)^2 \right] \quad (3.43)$$

The link between the wall function and the k equation is achieved through the turbulent kinetic-energy production, the velocity gradient, and the shear velocity. Thus by combining Eqs. (3.27), (3.30)-(3.31), one can find the following final equations for the wall function :

$$\varepsilon_A = [P_d]_A = \frac{C_\mu^{\frac{3}{4}} k_A^{\frac{3}{2}}}{\kappa [\delta_n]_A} \quad (3.44)$$

$$k_A = \frac{V_{*b}^2}{C_\mu^{1/2}} \quad (3.45)$$

Following the approximation in which the effect of normal stress is neglected, a local energy balance exists and there is equilibrium between production and dissipation of turbulence, i.e., there is a local balance between the rate of turbulent energy dissipation, ε , and its production (squared shear production), P_d ([62], [124]). This yields :

$$\varepsilon_A = [P_d]_A = \nu_v \left[\left(\frac{\partial V_t}{\partial n} \right)^2 \right]_A \quad (3.46)$$

From Boussinesq concept and the definition of the shear stress one can find :

$$V_*^2 = \frac{\tau_{nt}}{\rho} = \nu_v \left[\left(\frac{\partial V_t}{\partial n} \right) \right]_A \quad (3.47)$$

Free-surface

At free-surface Dirichlet boundary conditions are respectively applied for k and ε as follows

$$k = \frac{V_*^2}{\sqrt{c_\mu}} \quad ; \quad \varepsilon = \frac{(k C_\mu)^{1.5}}{0.07 \kappa h} \quad (3.48)$$

or Neumann condition upon kinetic energy, $\frac{\partial k}{\partial z} = 0$, during flooding.

Solid or lateral wall

Here on the rigid boundary $\Gamma_c(t)$, Neumann condition is applied for the turbulence variables (i.e. zero normal derivative).

Open sea

The Robin boundary condition is applied and can be written as follows,

$$k = \zeta \frac{V_*^2}{\sqrt{c_\mu}} + (1 - \zeta) \frac{\partial k}{\partial n} \quad ; \quad \varepsilon = \zeta \frac{(kC_\mu)^{1.5}}{0.07\kappa h} + (1 - \zeta) \frac{\partial \varepsilon}{\partial n} \quad (3.49)$$

where $\zeta = 0$ during flooding and $\zeta = 1$ during ebbing.

Upstream

The given known functions describe the flow

$$k = 0.03V_{nx}^2; \quad \varepsilon = c_\mu \frac{k^{1.5}}{0.09h} \quad (3.50)$$

where V_{nx} stands for the velocity normal to the upstream surface.

3.3 Initial conditions

Using the initial values \mathbf{V}_0, η_0 , the initial conditions for velocities and free-surface are computed after running the model to reach the steady state.

The initial values of turbulent quantities : (see Versteeg and Malalasekera [147])

$$k = 1.5(0.06U)^2 \quad (3.51)$$

$$\varepsilon = \frac{c_\mu^{3/4} k^{3/2}}{0.09h} \quad (3.52)$$

where U is the known mean-value of uniform distribution velocity.

3.4 The hydrostatic approximation

3.4.1 Geophysical modeling and the scaling of the governing equations

In some geophysical applications the domain of interest is characterized by different geometric scales in the horizontal and in the vertical direction. In this section we will analyze the consequences of this geometrical anisotropy by deriving what is perhaps the most widely used approximation in geophysical modeling: *the hydrostatic relation*.

Let U, W, L, H be the scales for the horizontal and vertical velocities, for a characteristic horizontal length and for the depth. Performing a scaling procedure on the continuity equation we obtain that

$$\mathcal{O}\left(\frac{U}{L}\right) = \mathcal{O}\left(\frac{W}{H}\right). \quad (3.53)$$

The non-dimensional form of the vertical component of the momentum equation reads

$$\xi^2 \left(\frac{\partial w_*}{\partial t_*} + u_* \frac{\partial w_*}{\partial x_*} + v_* \frac{\partial w_*}{\partial y_*} + w_* \frac{\partial w_*}{\partial z_*} \right) = -\frac{\partial p_*}{\partial z_*} - \frac{1}{Fr^2} \frac{\rho}{\rho_0} + \frac{1}{Re} \left[\xi^2 \left(\frac{\partial^2 w_*}{\partial x_*^2} + \frac{\partial^2 w_*}{\partial y_*^2} \right) + \frac{\partial^2 w_*}{\partial z_*^2} \right], \quad (3.54)$$

where the subscript * denotes non-dimensional quantities, $\xi = H/L$ and

$$Fr = \frac{U}{\sqrt{gH}}, \quad Re = \frac{LU}{\nu}, \quad (3.55)$$

are the Froude and Reynolds numbers. Finally the time and the pressure has been scaled as follows $t_* = Ut/L$ and $p_* = p/(\rho_0 U^2)$.

Since in typical applications $Fr \simeq 0.1$ and the variation of ρ is small the gravitational term (as well as the pressure term) must always be retained. As for the other terms depending on the values of Re and ξ we can have the situation illustrated in the table 3.2. The symbol \times indicates that the corresponding term should be retained. The *hydrostatic approximation*

ξ	Re	vertical accelerations	vertical viscous term	horizontal viscous term	Corresponding model
$\ll 1$	small		\times		Primitive equations with vertical viscosity (PEV ²) see [74]
$\ll 1$	large				Hydrostatic approximation
$\gg 1$	small	\times	\times	\times	Full Navier-Stokes equations
$\gg 1$	large	\times			Primitive equations

Table 3.2: Different type of approximation

reduces the vertical momentum equation to a static relation, *i.e.*

$$\frac{\partial p}{\partial z} = -\rho g. \quad (3.56)$$

This approximation is equivalent to considering *long waves* in which the wave-length is large compared with the depth of the fluid (see [60]). The hydrostatic pressure p_h , under the Boussinesq approximation, can be easily obtained integrating (3.56) along the vertical coordinate between z and η and using (3.21)

$$p_h = p_a + g \int_z^\eta \rho dz = p_a + g\rho_0(\eta - z) + g \int_z^\eta \Delta\rho dz, \quad (3.57)$$

where $\Delta\rho = \rho - \rho_0$ and ρ_0 denotes an average density value. The terms $g\rho_0(\eta - z)$ and $g \int_z^\eta \Delta\rho dz$ are called *barotropic* and *baroclinic* pressure, respectively.

A similar scaling argument performed on the horizontal momentum equations shows that when $\xi \ll 1$ the horizontal viscous term are negligible with respect to the vertical ones.

3.4.2 3D Hydrostatic Shallow Water model

The first model that we introduce is a 3D model for a variable density fluid under the hydrostatic assumption where only the continuity equation is integrated along the vertical (see [149]). The system reads

$$\left\{ \begin{array}{l} \frac{D\mathbf{v}}{Dt} - \frac{\partial}{\partial z} \left(\nu_v \frac{\partial \mathbf{v}}{\partial z} \right) + g\nabla\eta + g\nabla \left(\int_z^\eta \frac{\Delta\rho}{\rho_0} dz \right) = \mathbf{f}_{xy}, \\ \frac{\partial\eta}{\partial t} + \nabla \cdot \int_{-h}^\eta \mathbf{v} dz = \tilde{F}_b, \\ \nabla_{xy} \cdot \mathbf{v} + \frac{\partial w}{\partial z} = 0, \\ \frac{D\zeta}{Dt} - \nabla \cdot \left[c_\zeta \frac{k^2}{\varepsilon} \nabla\zeta \right] = F_\zeta \quad \text{for } \forall \zeta = (k, \varepsilon) \\ \frac{D\Phi}{Dt} - \nabla_{xy} \cdot \left(\frac{\nu_h}{\sigma_\Phi} \nabla\Phi \right) - \frac{\partial}{\partial z} \left(\frac{\nu_v}{\sigma_\Phi} \frac{\partial\Phi}{\partial z} \right) = F_\Phi, \quad \Phi = (T, S, C_s), \\ \rho = \rho(T, S, C_s), \end{array} \right. \quad (3.58)$$

where the unknowns are $\mathbf{v}, w, \eta, k, \varepsilon, T, S,$ and C_s . Since w is not differentiated in time, no initial value for this unknown should be assigned. Moreover, w does not contribute to the energy conservation relation. It is worthwhile to notice also that the vertical velocity depends on t only implicitly through the variations of the other unknowns (for this reasons w is called *diagnostic* variable, in contrast u, v and η are called *prognostic*). In fact, from the computational point of view, the vertical velocity can be recovered a posteriori using the divergence free equation once the horizontal velocity is known, *i.e.*

$$\frac{\partial w}{\partial z} = \mathcal{D}, \quad (3.59)$$

where $\mathcal{D} = -\nabla \cdot \mathbf{v}$ is a known function. This computational approach has two main drawbacks:

- any inaccuracy in the calculation of \mathbf{v} will result in errors in the computation of w ;
- equation (3.59) is a first order differential equation thus it necessitates only one boundary condition at in flow. Since two boundary conditions involving w were prescribed, in particular (3.20) and (3.25), we have an *overdetermined* system. To overcome this problem usually only one of the boundary conditions is enforced. In the present work, this influencing boundary condition will be enforced at the bottom. This suggests that the flow in the channel is mostly influenced by gravity forces (*i.e.* Froude number less than 1 for fluvial regime), buoyancy and the flocculation (stratification). Consequently the bed behavior has a great influence on the free-surface evolution. One can refer to [98] for alternative approach.

3.5 3D Non-hydrostatic model for variable-density flows

3.5.1 3D detailed description of free-surface flows

Several 3D computations using the conventional hydrostatic pressure assumption and/or the shallow-water equations (SWE) assumptions have been successfully applied to many engineering problems, and their use has become standard practice in environmental impact studies in most

of geophysical flows such as estuarial and coastal regions. However in presence of steep bottom slopes (i.e. strong vertical accelerations), and when *short* waves must be considered this above approximation is no longer valid (see Whitham [152]). Moreover it is shown (see [10], [102]), that the hydrostatic system is ill-posed in presence of open boundaries. The 3D non-hydrostatic model is more suitable to obtain the description of the velocity field, in some situations where the necessity of detailed description of the 3D velocity field (e.g. the presence of short waves or strong bathymetry) demand the use of such a model. In this case attention must be paid to the detailed description of the vertical structure of the velocity and the density stratification of the fluid. In this section we present a 3D model for free-surface flows, in which the non-hydrostatic pressure is included in the momentum equations for incorporation in the surface elevation, for the variable density fluid flow.

3.5.2 3D Reynolds Averaged Navier-Stokes equations for free-surface flows

The key assumption is that the pressure p can be written as the sum of an hydrostatic term p_h and an hydrodynamic correction $p_c = \rho q$ such that:

$$p(\mathbf{x}, t) = p_h + p_c = p_a + g\rho_0(\eta - z) + g \int_z^\eta \Delta\rho dz + \rho q(\mathbf{x}, t) \quad (3.60)$$

From the computational point of view, it is shown that the splitting of the pressure is very attractive (see [89]). Using this pressure splitting we obtain the following 3D non-hydrostatic system

$$\left\{ \begin{array}{l} \nabla_{xy} \cdot \mathbf{v} + \frac{\partial w}{\partial z} = 0 \\ \frac{D\mathbf{v}}{Dt} - \nabla_{xy} \cdot (\nu_h \nabla_{xy} \mathbf{v}) + g \nabla_{xy} \eta + g \nabla \left(\int_z^\eta \frac{\Delta\rho}{\rho_0} dz \right) - \frac{\partial}{\partial z} \left(\nu_v \frac{\partial \mathbf{v}}{\partial z} \right) + \frac{1}{\rho_0} \nabla q = \mathbf{f}_{xy} \\ \frac{\partial \eta}{\partial t} + \nabla_{xy} \cdot \left(\int_{-h(x,y)}^{\eta(x,y)} \mathbf{v} dz \right) = \tilde{F}_b \\ \frac{Dw}{Dt} - \nabla_{xy} \cdot (\nu_h \nabla_{xy} w) - \frac{\partial}{\partial z} \left(\nu_v \frac{\partial w}{\partial z} \right) + \frac{1}{\rho_0} \frac{\partial q}{\partial z} = 0 \\ \frac{D\zeta}{Dt} - \nabla \cdot \left[c_\zeta \frac{k^2}{\varepsilon} \nabla \zeta \right] = F_\zeta \quad \text{for } \forall \zeta = (k, \varepsilon) \\ \frac{D\Phi}{Dt} - \nabla_{xy} \cdot \left(\frac{\nu_h}{\sigma_\Phi} \nabla \Phi \right) - \frac{\partial}{\partial z} \left(\frac{\nu_v}{\sigma_\Phi} \frac{\partial \Phi}{\partial z} \right) = F_\Phi \quad \text{for } \Phi = (T, S, C_s) \\ \rho = \rho(T, S, C_s) \end{array} \right. \quad (3.61)$$

In the present work the horizontal diffusion is parameterized through the uniform horizontal coefficient ν_h , using empirical relation from Elder [33]:

$$\nu_h = \zeta h u_* \quad (3.62)$$

where ζ it is a constant: e.g $\zeta = 0.1$ to 0.3 , u_* is a representative shear velocity. In this system (3.61) we have recovered the *prognostic* character of the vertical velocity. Thus we have a full

energy conservation principle in which all the three components of the velocity and the total pressure are taken into account. The system (3.61) is convective dominant. Hence the initial boundary value problem is well-posed also in presence of open boundaries. Using the linearized inviscid constant-density form of the above system of equations, it is shown that the three-dimensional non-hydrostatic system ensures that the gravity waves are treated accurately with an exact dispersion relation (see [89]). An analogous dispersion relation for the non-hydrostatic model in the rigid lid case has been studied by Marshall et al. [85].

Chapter 4

Weak formulation and finite element approximation

In this chapter a spatial discretization is proposed for the three-dimensional shallow-water equations (SWE) as well as the semi-discrete form of the partial differential equations system. This is an extension of the finite element method presented in [89,90], (see also [71]). This scheme is based on the combined use of Lagrangian linear finite element in the vertical direction, and the Raviart-Thomas finite element in the horizontal plane. In this chapter the non-hydrostatic system will be taken into consideration.

4.1 Domain discretization

Let us introduce some detailed figures for the computational uses. Figure 4.1 represents the physical domain. The physical three-dimensional domain is embedded in a parallelepiped composed of \mathcal{N} layers.

Remark 5 *In the sequel the subscript k will be used as an index to identify the k^{th} layer in the vertical direction, and this must not introduces any confusion with the “turbulent kinetic energy”.*

By I_k we identify the layer k whose thickness δz_k is fixed. A layer is said to be active if it is wet. By $I_{k+1/2}$ we identify the fictitious layer whose thickness $\delta z_{k+1/2}$ is a distance between the triangles located at mid-height of the layers k and $k+1$ (cf. figure 4.2). The number of active layers depends on the depth of the water column; therefore, it is not constant over the whole domain and can also change in time, to account for the variation of the free surface and bottom shape. In particular the thickness of the lowermost active layer (denoted by the index k_0) depends on the bottom shape, and the thickness of the uppermost active layer (denoted by the index \mathcal{K}) varie in space and time according to the free surface location. The horizontal projection of the domain Ω is discretized using an unstructured triangular mesh \mathcal{T}_h . The same mesh is placed in the middle of each layer. The vertical distance between the grids of the layers k and $k+1$ will be denoted by $\delta z_{k+1/2} = [\delta z_k + \delta z_{k+1}]/2$. It is important to emphasize that the mesh is the same on each layer. In a layer, as shown in figure 4.2, each triangular mesh element defines a three-dimensional prismatic element. The generic prism of the tridimensional grid will be denoted by P . The horizontal components of the velocity vector are defined at the middle of the edges of the triangular mesh elements, while the vertical components are associated

with the lower and upper horizontal faces of the element in the case of non-hydrostatic pressure assumption. The set of all prism in the finite element (F.E.) grid will be denoted by \mathcal{P}_h .

4.2 Weak formulation: functional spaces

The horizontal velocity is approximated combining the lowest order Raviart-Thomas element (\mathbb{RT}_0) in the xy plane (see [114], [90], [37]) with the \mathbb{P}_1 elements along the vertical direction. Let us introduce some functional spaces that will be used in this work. Let $\Omega \in \mathbb{R}^d$ and we have:

$$L^2(\Omega) = \left\{ \psi : \int_{\Omega} \psi^2 d\Omega < \infty \right\} \quad (4.1)$$

$$H^1(\Omega) = \left\{ \psi \in L^2(\Omega) : \partial_{x_i} \psi \in L^2(\Omega), i = 1, \dots, d \right\} \quad (4.2)$$

The following space of vectors have been introduced to derive the weak form of the 3D hydrodynamic model:

$$H_{0,c}(\text{div}; \Omega) = \left\{ \boldsymbol{\tau} : \boldsymbol{\tau} \in (L^2(\Omega))^2, \text{div } \boldsymbol{\tau} \in L^2(\Omega), \boldsymbol{\tau} \cdot \mathbf{n} = 0 \text{ on } \Gamma_c \right\} \quad (4.3)$$

where Γ_c denote the vertical solid wall.

4.3 Finite element approximation

4.3.1 Raviart-Thomas and P_1 finite element

For every integer $r \geq 0$ we denote by $\mathbb{P}_r(T)$ the space of polynomials of degree $\leq r$ on each triangle $T \in \mathcal{T}_h$ (see figure 4.1) and consider the Raviart-Thomas vector finite element space of lowest order (see [71], [90], [114]):

$$\mathbb{RT}_0(T) = (\mathbb{P}_0(T))^2 \oplus \mathbf{x}\mathbb{P}_0(T) = \left\{ \mathbf{v} = \begin{pmatrix} b \\ c \end{pmatrix} + a \begin{pmatrix} x \\ y \end{pmatrix}, a, b, c \in \mathbb{R} \right\}. \quad (4.4)$$

Let us introduce the following finite element spaces:

$$\mathbb{Q}_h = \left\{ \mathbf{q} \in H_{0,c}(\text{div}; \Omega) \mid \mathbf{q}|_T \in \mathbb{RT}_0(T), \forall T \in \mathcal{T}_h \right\},$$

$$U_h = \left\{ \psi \in L^2(\Omega) \mid \psi|_T \in \mathbb{P}_0(T), \forall T \in \mathcal{T}_h \right\},$$

$$W_{I_{1/2}^1} = \left\{ \varphi \in C^0([-h, \eta]) \mid \varphi|_{I_{k+1/2}} \in \mathbb{P}_1(I_{k+1/2}), \forall I_{k+1/2} \in \mathcal{I}_{1/2} \right\}, \quad (4.5)$$

$$W_{I_1^1} = \left\{ \zeta \in C^0([-h, \eta]) \mid \zeta|_{I_k} \in \mathbb{P}_1(I_k), \text{ with } \zeta|_{-h} = 0 \text{ and } \zeta|_{\eta} = 0, \forall I_k \in \mathcal{I}_1 \right\},$$

$$W_{I_1^0} = \left\{ \phi \in L^2(\Omega) \mid \phi|_k \in \mathbb{P}_0(p), \forall I_k \in \mathcal{I}_1 \right\},$$

$$X_p = \left\{ \chi \in L^2(\Omega) \mid \chi|_p \in \mathbb{P}_0(p), \forall p \right\}$$

Let us consider in figure 4.3 two triangles adjacent to the edge e_i , which belongs to the T_+^i and T_-^i , the following associated shape function $\boldsymbol{\tau}_i \in \mathbb{Q}_h$ can be defined as,

$$\boldsymbol{\tau}_i(\mathbf{x})|_T = \frac{\mathbf{x} - \mathbf{x}_j}{2|T|}, \quad \text{supp}(\boldsymbol{\tau}_i) = T_-^i \cup T_+^i \quad (4.6)$$

$$\operatorname{div} \boldsymbol{\tau}_i = \frac{1}{|T|}, \quad \boldsymbol{\tau}_i|_T \cdot \mathbf{n}_m = \frac{\delta_{im}}{|e_i|} \quad (4.7)$$

where \mathbf{x}_j is the coordinate of a generic Gauss point, $\operatorname{supp}(\tau_i)$ (a support of τ_i) is a generic edge of the two triangles $T_-^i \cup T_+^i$, $|T|$ and $|e_i|$ are respectively the area of the triangle T and the length of the edge e_i ; δ_{ij} is the Kronecker symbol. \mathbf{n}_m is the outward normal to the edge e_m . The shape functions, from their properties can guarantee the continuity of the normal flux to each edge of the triangle. Let us associate to the layer denoted by z_k and $z_{k+\frac{1}{2}}$, respectively the shape functions φ_k and $\varphi_{k+\frac{1}{2}}$, which have as geometrical support (z_{k-1}, z_{k+1}) for the first interval and $(z_{k-\frac{1}{2}}, z_{k+\frac{1}{2}})$ for the second interval. Denoting by N_{ed} and N_{el} respectively the number of (oriented) edges e_l and triangles T_j in the mesh, by k_0 and \mathcal{K} respectively the indices of bottom and uppermost layer, the approximation solutions for the variables can be written

$$\begin{aligned} \mathbf{v}_h(\mathbf{x}, z) &= \sum_{k=k_0}^{\mathcal{K}} \sum_{j=1}^{N_{ed}} (\mathbf{J}_j)_k \boldsymbol{\tau}_j(\mathbf{x}) \varphi_k(z), \quad \boldsymbol{\tau} \in \mathbb{Q}_h, \varphi \in W_{\mathcal{T}_{1/2}^1}, \\ \eta_h(\mathbf{x}) &= \sum_{j=1}^{N_{el}} \eta_j \psi_j(\mathbf{x}), \quad \forall \psi \in U_h, \end{aligned} \quad (4.8)$$

$$w_h(\mathbf{x}, z) = \sum_{s=1}^{N_{el}} \sum_{k=k_0}^{\mathcal{K}-1} (w_s)_k \psi_s(\mathbf{x}) \chi_{k+1/2}(z), \quad \psi \in U_h, \chi \in W_{\mathcal{T}_1^1},$$

$$q_h(\mathbf{x}, z) = \sum_{s=1}^{N_{el}} \sum_{k=k_0}^{\mathcal{K}-1} (q_s)_k \psi_s(\mathbf{x}) \chi_k(z), \quad \psi \in U_h, \chi \in W_{\mathcal{T}_1^0}$$

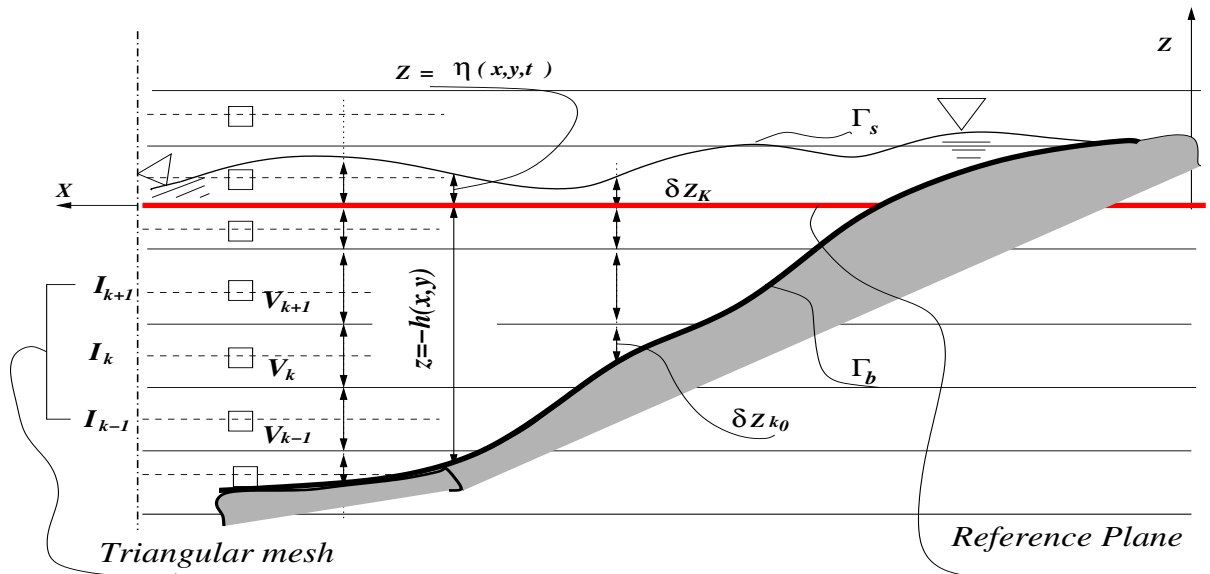
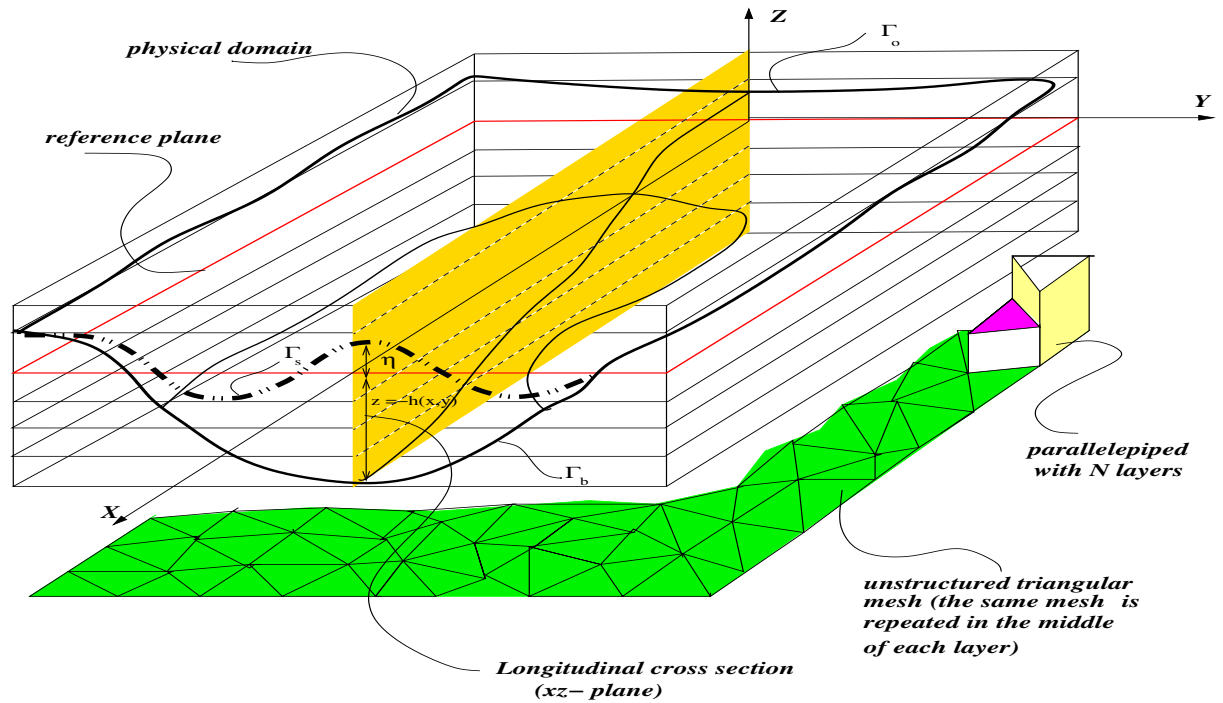
with $(\mathbf{J}_j)_k = \int_{e_l} \mathbf{v}_k \cdot \mathbf{n}_j d\sigma$

4.3.2 Finite Element Approximation for the turbulence variables and scalars (heat, salt, sediment concentration)

The approximate solutions for those variables can be written

$$\begin{aligned} k_h(\mathbf{x}, z) &= \sum_{k=k_0}^{\mathcal{K}} \sum_{j=1}^{N_{ed}} (k_j)_k \psi_j(\mathbf{x}) \varphi_k(z), \quad \psi \in U_h, \varphi \in W_{\mathcal{T}_{1/2}^1}, \\ \varepsilon_h(\mathbf{x}, z) &= \sum_{k=k_0}^{\mathcal{K}} \sum_{j=1}^{N_{ed}} (\varepsilon_j)_k \psi_j(\mathbf{x}) \varphi_k(z), \quad \psi \in U_h, \varphi \in W_{\mathcal{T}_{1/2}^1}, \\ \Phi_h(\mathbf{x}, z) &= \sum_{s=1}^{N_{el}} \sum_{k=k_0}^{\mathcal{K}-1} (\Phi_s)_k \psi_s(\mathbf{x}) \chi_k(z), \quad \forall \psi \in U_h, \forall \chi \in W_{\mathcal{T}_1^0}, \forall \Phi(T, S, C) = \text{scalars} \end{aligned} \quad (4.9)$$

Remark 6 *To simplify the algebraic form of the problem (and consequently reduce the computational cost), it is desirable to diagonalize the mass matrix. Therefore two kinds of lumping procedure are required: one for the φ -mass matrix, and the second one for the $\boldsymbol{\tau}$ -mass matrix.*



Longitudinal cross section and bathymetry (Plane $-xz$)

Figure 4.1: Computational domain

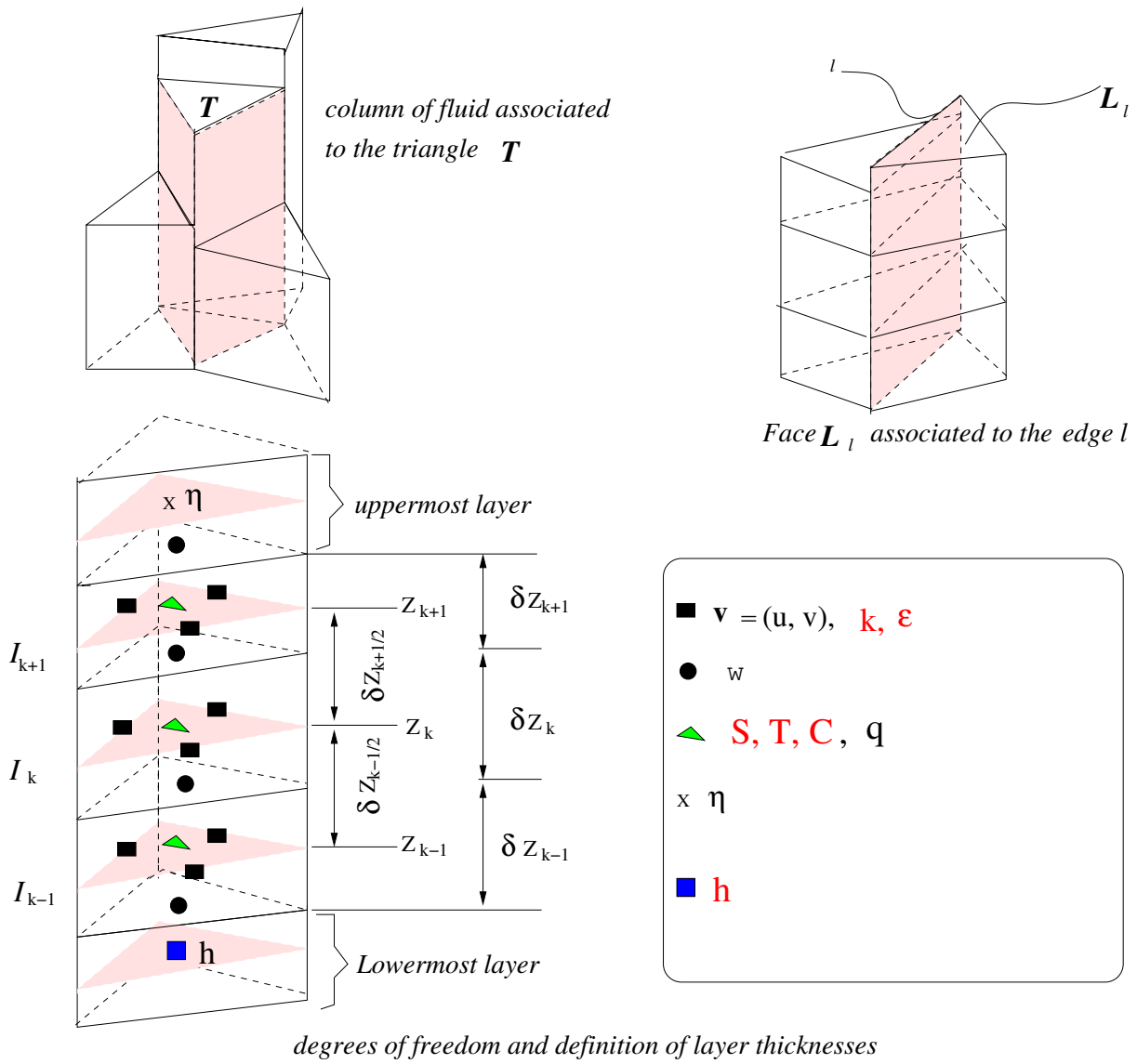
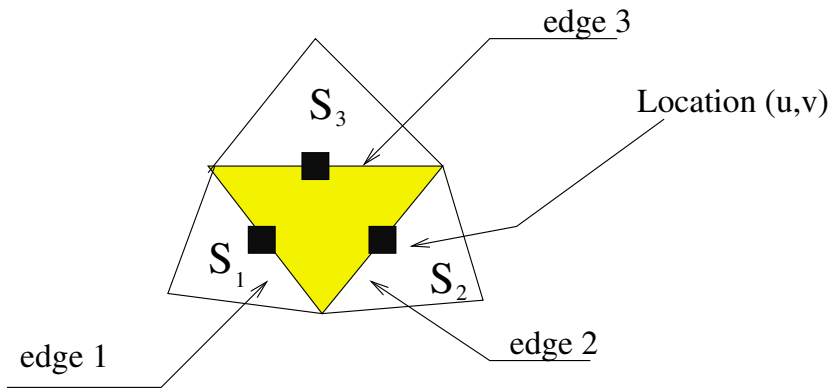
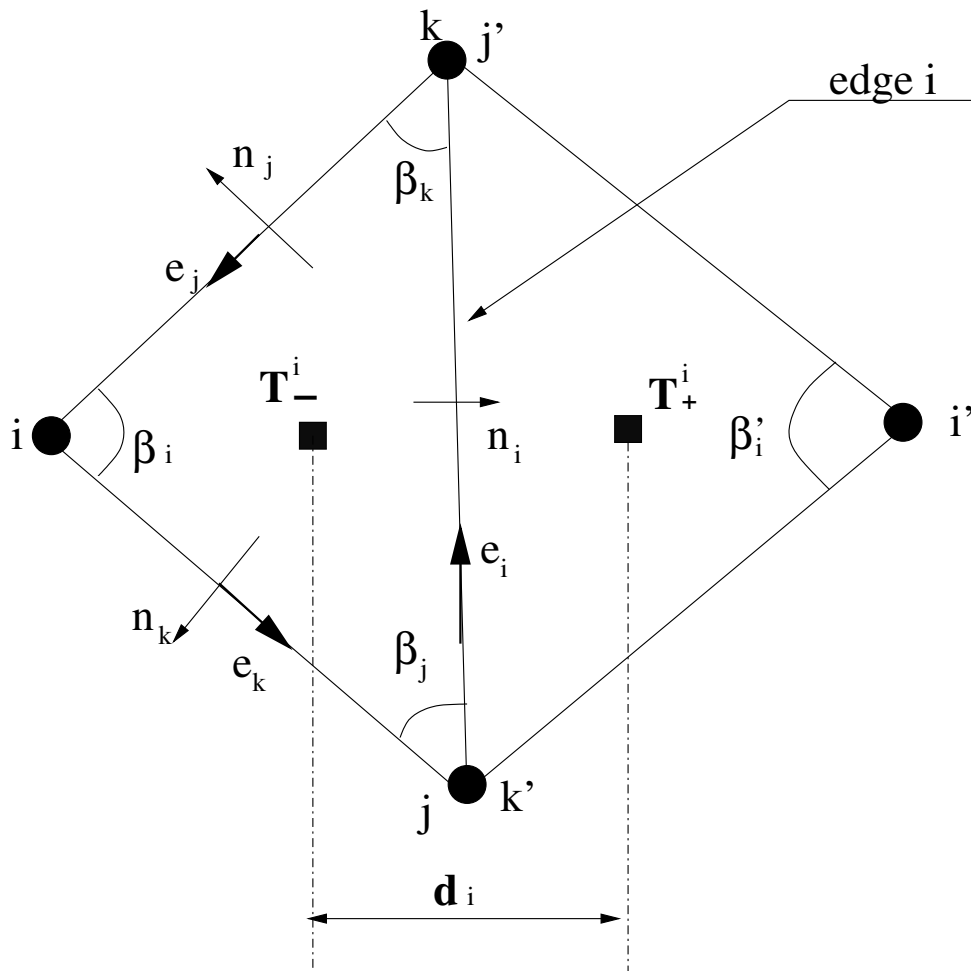


Figure 4.2: Space discretization



The element S and its neighbours



Notations for the shape functions

Figure 4.3: Sketches of adjacent triangles

For the first one, we can use the following quadrature formula,

$$\int_{z_{k-1}}^{z_{k+1}} \varphi_s \varphi_k dz \begin{cases} = 0 & \text{for } s \neq k, \\ = \frac{\delta z_{k+1/2} + \delta z_{k-1/2}}{2} = \Delta z_k & \text{for } s = k \end{cases} \quad (4.10)$$

For the second one, we can use the following quadrature formula,

$$\int_{\tau_i} (\boldsymbol{\tau}_i \boldsymbol{\tau}_r) d\mathbf{x} \begin{cases} = 0 & \text{for } i \neq r, \\ = \frac{d_i}{|e_i|} & \text{for } i = r \end{cases} \quad (4.11)$$

where d_i denotes the distance between the centers of the circumscribed circles to each of the two adjacent triangles T_-^i and T_+^i .

4.3.3 The weak formulation

First of all we suppose that the 3D domain $\widehat{\Omega}$ is made of the extension of Ω in the vertical direction z (extrusion). Thus any integral over the $\widehat{\Omega}$ can be written as follows

$$\int_{\widehat{\Omega}} (\dots) d\widehat{\Omega} = \int_{\Omega} \left(\int_{-\mathfrak{h}(x,y,t)}^{\eta(x,y,t)} dz \right) d\Omega \quad (4.12)$$

Using Gauss formula the variable density problem statement (3.61) becomes: Find $\mathbf{v}_h \in \mathbb{Q}_h \times W_{I_{1/2}^1}$, $w_h \in U_h \times W_{I_1^1}$, $q_h \in U_h \times W_{I_1^0}$, $\eta_h \in U_h$, $k_h \in U_h \times W_{I_{1/2}^1}$, $\epsilon_h \in U_h \times W_{I_{1/2}^1}$, such that

$$\int_{\partial p} w^{n+1} n_z dS = \int_{\partial p} \mathbf{v} \cdot \mathbf{n}_{xy} dS, \quad \forall p \in \mathcal{P}_h \quad (4.13)$$

$$\int_{\Omega} \frac{\partial \eta_h}{\partial t} \psi d\Omega + \int_{\Omega} \left(\nabla_{xy} \cdot \int_{-\mathfrak{h}}^{\eta} \mathbf{v} dz \right) \psi d\Omega = \int_{\Omega} \tilde{\mathbf{F}}_b \psi dz \quad \forall \psi \in U_h \quad (4.14)$$

$$\int_{\Omega} \int_{-\mathfrak{h}}^{\eta} \frac{Dw}{Dt} \psi \chi dz d\Omega - \int_{\Omega} \int_{-\mathfrak{h}}^{\eta} \varphi \nabla_{xy} \cdot (\nu_h \nabla_{xy} \mathbf{v}) \tau dz d\Omega - \int_{\Omega} \int_{-\mathfrak{h}}^{\eta} \frac{\partial}{\partial z} \left(\nu_v \frac{\partial w}{\partial z} \right) \psi \chi dz d\Omega \quad (4.15)$$

$$+ \frac{1}{\rho_0} \int_{\Omega} \int_{-\mathfrak{h}}^{\eta} \frac{\partial q}{\partial z} \psi \chi dz d\Omega = 0 \forall \psi \in U_h, \forall \chi \in W_{I_1^1}$$

$$\begin{aligned} \int_{\Omega} \int_{-\mathfrak{h}}^{\eta} \varphi \frac{D\mathbf{v}_h}{Dt} \cdot \boldsymbol{\tau} dz d\Omega &= g \int_{\Omega} \int_{-\mathfrak{h}}^{\eta} \varphi \eta_h \nabla_{xy} \cdot \boldsymbol{\tau} dz d\Omega, \\ &- \nu_v \int_{\Omega} \int_{-\mathfrak{h}}^{\eta} \boldsymbol{\tau} \cdot \frac{\partial \mathbf{v}_h}{\partial z} \frac{\partial \varphi}{\partial z} dz d\Omega + \int_{\Omega} \int_{-\mathfrak{h}}^{\eta} \varphi \mathbf{f}_{xy} \cdot \boldsymbol{\tau} dz d\Omega, \\ &+ \int_{\Omega} [(\rho_a C_w \|W\| W \cdot \boldsymbol{\tau} \varphi)|_{\eta} - u_m|_{-\mathfrak{h}} \cdot \boldsymbol{\tau} \varphi|_{\mathfrak{h}}] d\Omega, \\ &+ g \int_{\Omega} \nabla_{xy} \left(\int_z^{\eta} \frac{\rho - \rho_0}{\rho_0} dz \right) \cdot \boldsymbol{\tau} \varphi d\Omega + \frac{1}{\rho_0} \int_{\Omega} \nabla_{xy} q_h \cdot \boldsymbol{\tau} \varphi d\Omega, \\ &- g \int_{\Gamma_0 \cap \Gamma_b} \int_{-\mathfrak{h}}^{\eta} \varphi \eta_h \boldsymbol{\tau} \cdot \mathbf{n} dz d\gamma, \quad \forall \varphi \in W_{I_1^1} \end{aligned} \quad (4.16)$$

$$\begin{aligned}
& \int_{\Omega} \int_{-h}^{\eta} \psi \frac{D\Phi_h}{Dt} \chi dz d\Omega - \int_{\Omega} \int_{-h}^{\eta} \psi \left[\nabla_{xy} \cdot \left(\frac{\nu_h}{\sigma_{\Phi}} \nabla_{xy} \Phi_h \right) \right] \chi dz d\Omega \\
& - \int_{\Omega} \int_{-h}^{\eta} \psi \left[\frac{\partial}{\partial z} \left(\frac{\nu_v}{\sigma_{\Phi_h}} \frac{\partial \Phi_h}{\partial z} \right) \right] \chi dz d\Omega \\
& = \int_{\partial\Omega} \chi \left[\frac{\nu_h}{\sigma_{\Phi}} (\nabla_{xy} \Phi_h) \right] \psi \cdot \mathbf{n}_{xy} d\gamma - \int_{\partial\Omega} \chi \left[\frac{\nu_v}{\sigma_{\Phi_h}} \left(\frac{\partial \Phi_h}{\partial z} \right) \right] \psi \cdot n_z dS \\
& + \int_{\Omega} \int_{-h}^{\eta} \psi \mathbf{F}_{\Phi} \chi dz d\Omega
\end{aligned} \tag{4.17}$$

Turbulence equations read,

$$\begin{aligned}
& \int_{\Omega} \int_{-h}^{\eta} \psi \frac{Dk_h}{Dt} \varphi d\Omega dz - \int_{\Omega} \int_{-h}^{\eta} \varphi \nabla \cdot [\nu_e (\nabla k_h)] \psi d\Omega dz \\
& = \int_{\Omega} \int_{-h}^{\eta} \psi \left[c_{\mu} \nu_e P_d + \lambda_v H \left((-N)^2 \right) \right] \varphi d\Omega dz \\
& - \int_{\Omega} \int_{-h}^{\eta} \psi \left[\lambda_v H \left((N)^2 \right) + c_2 \varepsilon_h \right] \varphi d\Omega dz
\end{aligned} \tag{4.18}$$

$$\begin{aligned}
& \int_{\Omega} \int_{-h}^{\eta} \psi \frac{D\varepsilon_h}{Dt} \varphi d\Omega dz - \int_{\Omega} \int_{-h}^{\eta} \psi \nabla \cdot [\nu_e (\nabla \varepsilon_h)] \varphi dz d\Omega \\
& = \int_{\Omega} \int_{-h}^{\eta} \psi \left(c_1 k_h P_d + H \left((-N)^2 \right) \right) \varphi d\Omega dz \\
& - \int_{\Omega} \int_{-h}^{\eta} \psi \frac{k_h}{\nu_e} \left[c_2 \varepsilon_h + c_1 c_3 \lambda_v H \left((N)^2 \right) \right] d\Omega dz
\end{aligned} \tag{4.19}$$

where \mathbf{n}_{xy} , n_z are respectively the horizontal and vertical components of the normal vector \mathbf{n} , $|P|$ and $|T|$ denote respectively the volume of the prism (P) and the surface of the triangle of the prism. $\nu_e = \frac{k_h^2}{\varepsilon_h}$, and H is the Heaviside function defined as follows

$$H(x) = \begin{cases} = x & \text{for } x > 0 \\ = 0 & \text{otherwise} \end{cases} \tag{4.20}$$

4.3.4 Semi-discrete system equations

Let us define the various matrices related to the spatial discretization of Eqs.(4.13)-(4.19). The velocity mass matrix is obtained as;

$$\begin{aligned}
\mathbf{M}_v &= \int_{\Omega} \int_{-h}^{\eta} \boldsymbol{\tau}_i \varphi_l \sum_{k=k_0}^{\mathcal{K}} \sum_{j=1}^{N_{ed}} (\mathbf{J}_j)_k \varphi_k \boldsymbol{\tau}_j dz d\Omega \\
&= \sum_{j=1}^{N_{ed}} \sum_{k=k_0}^{\mathcal{K}} \boldsymbol{\tau}_j \varphi_l |\Omega|_j \int_{\Omega} \boldsymbol{\tau}_j \boldsymbol{\tau}_j d\Omega \int_{z_{k-1}}^{z_{k+1}} \varphi_k \varphi_k dz = \sum_{j=1}^{N_{ed}} \sum_{k=k_0}^{\mathcal{K}} \Delta z_k (\mathbf{J}_j)_k \frac{d_j}{|e_j|} |\Omega_j|
\end{aligned} \tag{4.21}$$

where the test functions φ and $\boldsymbol{\tau}$ are chosen as $\varphi = \varphi_l$ ($l = 1 \dots \mathcal{K}$) and $\boldsymbol{\tau} = \boldsymbol{\tau}_i$ ($i = 1 \dots N_{ed}$). Following the same line of reasoning, we can define the following matrices and right-hand side expressions

- horizontal velocity stiffness matrix K_v

$$\begin{aligned} \mathbf{K}_v &= \nu_v \int_{\Omega} \int_{-\mathfrak{h}}^{\eta} \tau_i \frac{\partial \varphi_l}{\partial z} \sum_{j=1}^{N_{ed}} \sum_{k=k_0}^{\mathcal{K}} \tau_j (\mathbf{J}_j)_k \frac{\partial \varphi_k}{\partial z} dz d\Omega \\ &= \nu_v \sum_{j=1}^{N_{ed}} \sum_{k=1}^{\mathcal{K}} |\Omega|_j (\mathbf{J}_j)_k \frac{d_j}{|e_j|} \frac{1}{\Delta z_k} \left(\frac{z_{k+1} - z_k}{\delta z_{k+1/2}} - \frac{z_k - z_{k-1}}{\delta z_{k-1/2}} \right) \end{aligned} \quad (4.22)$$

- “vertical” velocity mass matrix M_w

$$\begin{aligned} \mathbf{M}_w &= \int_{\Omega} \int_{-\mathfrak{h}}^{\eta} \psi_i \chi_l \sum_{s=1}^{N_{el}} \sum_{k=k_0}^{\mathcal{K}-1} (w_s)_k \chi_{k+1/2} \psi_s(\mathbf{x}) dz d\Omega \\ &= \sum_{s=1}^{N_{el}} \sum_{k=k_0}^{\mathcal{K}-1} |T|_j \Delta z_k (w_s)_k \chi_{k+1/2} \psi_s(\mathbf{x}) \end{aligned} \quad (4.23)$$

- “vertical” stiffness matrix K_w

$$\begin{aligned} \mathbf{K}_w &= \int_{\Omega} \int_{-\mathfrak{h}}^{\eta} \psi_i \chi_l \sum_{s=1}^{N_{el}} \sum_{k=k_0}^{\mathcal{K}-1} \left[\frac{\partial}{\partial z} \left(\nu_v \frac{\partial (w_s)_k \psi_s \chi_{k+1/2}}{\partial z} \right) \right] dz d\Omega \\ &= \sum_{s=1}^{N_{el}} \sum_{k=k_0}^{\mathcal{K}-1} |T|_s \Delta z_k \left[\frac{\partial}{\partial z} \left(\nu_v \frac{\partial (w_s)_k}{\partial z} \right) \right] \end{aligned} \quad (4.24)$$

- free surface mass matrix M_{η}

$$\mathbf{M}_{\eta} = \int_{\Omega} \psi_i \sum_{j=1}^{N_{el}} \psi_j d\Omega = \sum_{j=1}^{N_{el}} \eta_h \psi_j |T|_j \quad (4.25)$$

- turbulence variables mass matrix $M_{\zeta=(k,\varepsilon)}$

$$\mathbf{M}_{\zeta} = \int_{\Omega} \int_{-\mathfrak{h}}^{\eta} \tau_i \varphi_l \sum_{k=k_0}^{\mathcal{K}} \sum_{j=1}^{N_{ed}} (\zeta_j)_k \varphi_k \tau_j dz d\Omega = \sum_{j=1}^{N_{ed}} \sum_{k=k_0}^{\mathcal{K}} (\zeta_j)_k |\Omega|_j \Delta z_k \quad (4.26)$$

- turbulence variables stiffness matrix K_{ζ}

$$\begin{aligned} \mathbf{K}_{\zeta} &= \int_{\Omega} \int_{-\mathfrak{h}}^{\eta} \tau_i \left[\left(c_{\zeta} \sum_{j=1}^{N_{ed}} \sum_{k=k_0}^{\mathcal{K}} \tau_j \tau_j (\zeta_j)_k \frac{\partial \varphi_l}{\partial z} \frac{\partial \varphi_k}{\partial z} \right) \right] dz d\Omega \\ &= \sum_{j=1}^{N_{ed}} \sum_{k=1}^{\mathcal{K}} |\Omega|_j (\zeta_j)_k \left[c_{\zeta} \frac{d_j}{|e_j|} \frac{1}{\Delta z_k} \left(\frac{\varphi_{k+1} - \varphi_k}{\Delta z_{k+1/2}} - \frac{\varphi_k - \varphi_{k-1}}{\Delta z_{k-1/2}} \right) \right] \end{aligned} \quad (4.27)$$

with the following matrix (to account for the buoyancy)

$$\begin{aligned}
E_\zeta &= \int_{\Omega} \int_{-h}^{\eta} \boldsymbol{\tau} \left[\lambda_v H \left((N)^2 \right) + \sum_{k=k_0}^{\mathcal{K}} \sum_{j=1}^{N_{ed}} c_\zeta (\zeta_j)_k \tau_j \tau_j \varphi_k \right] \varphi d\Omega dz \\
&= \left[\sum_{j=1}^{N_{ed}} \sum_{k=k_0}^{\mathcal{K}} |\Omega|_j c_\zeta (\zeta_j)_k \frac{d_j}{|e|_j} \Delta z_k + \lambda_v H \left((N)^2 \right) \right]
\end{aligned} \tag{4.28}$$

- scalars mass matrix $M_{\Phi=(S,T,C)}$

$$\begin{aligned}
\mathbf{M}_\Phi &= \int_{\Omega} \int_{-h}^{\eta} \psi_i \chi_l \sum_{s=1}^{N_{el}} \sum_{k=k_0}^{\mathcal{K}} (\Phi_s)_k \chi_k \psi_s(\mathbf{x}) dz d\Omega \\
&= \sum_{s=1}^{N_{el}} \sum_{k=k_0}^{\mathcal{K}} |T|_s \Delta z_k (\Phi_s)_k \chi_k \psi_s(\mathbf{x})
\end{aligned} \tag{4.29}$$

- scalars stiffness matrix K_Φ

$$\begin{aligned}
\mathbf{K}_\Phi &= \int_{\Omega} \int_{-h}^{\eta} \psi_i \chi_l \sum_{s=1}^{N_{el}} \sum_{k=k_0}^{\mathcal{K}} \left[-\psi_j \nabla_{xy} \cdot \left(\frac{\nu_h}{\sigma_\Phi} \nabla_{xy} (\Phi_s)_k \chi_k \right) - \psi_k \frac{\partial}{\partial z} \left(\frac{\nu_v}{\sigma_\Phi} \frac{\partial (\Phi_s)_k \chi_j}{\partial z} \right) \right] dz d\Omega \\
&= \sum_{j=1}^{N_{el}} \sum_{k=k_0}^{\mathcal{K}-1} |T|_j \Delta z_k \left[-\nabla_{xy} \cdot \left(\frac{\nu_h}{\sigma_\Phi} \nabla_{xy} (\Phi_j)_k \right) - \frac{\partial}{\partial z} \left(\frac{\nu_v}{\sigma_\Phi} \frac{\partial (\Phi_s)_k}{\partial z} \right) \right]
\end{aligned} \tag{4.30}$$

and the following expressions

$$\begin{aligned}
\int_{\Omega} \int_{-h}^{\eta} D_{xy}^T \left(\frac{q}{\rho_0} \right) &= \sum_{s=1}^{N_{el}} \sum_{i=1}^{N_{ed}} \varphi_l \tau_i \nabla_{xy} \sum_{s=1}^{N_{el}} \sum_{k=k_0}^{N_{\mathcal{K}}} \frac{q_s}{\rho_0} \psi_s \chi_k dz d\Omega \\
D_z \left(\frac{q}{\rho_0} \right) &= \sum_{s=1}^{N_{el}} \sum_{k=k_0}^{\mathcal{K}-1} |T|_s \Delta z_k \left[\frac{1}{\rho_0} \frac{\partial q_s \psi_s \chi_k}{\partial z} \right]
\end{aligned} \tag{4.31}$$

- right hand side for horizontal velocity R_v [Eq. (4.16)]

$$\begin{aligned}
\mathbf{R}_v &= - \int_{\Omega} \boldsymbol{\tau}_i \left\{ \int_{-h}^{\eta} \varphi_l \mathbf{f}_{xy} dz - \varphi_l \left[(\rho_a C_w \|W\|W) |_{\eta} - \sum_{j=1}^{N_{ed}} \boldsymbol{\tau}_j \varphi |_{\eta} \right] \right\} d\Omega \\
&+ g \int_{\Gamma_0 \cap \Gamma_b} \int_{-h}^{\eta} \varphi_l \sum_{s=1}^{N_{ed}} \psi_s \sum_{j=1}^{N_{ed}} \boldsymbol{\tau}_j \cdot \mathbf{n} dz d\gamma + g \int_{\Omega} \int_{-h}^{\eta} \nabla_{xy} \left(\frac{\rho_s - \rho_0}{\rho_0} \right) \psi_s \chi_k dz d\Omega \\
&+ \frac{1}{\rho_0} \int_{\Omega} \int_{-h}^{\eta} \varphi_l \boldsymbol{\tau}_i \sum_{s=1}^{N_{el}} \sum_{k=k_0}^{N_{\mathcal{K}}} \nabla_{xy} q_s \psi_s \chi_k dz d\Omega \\
&= \sum_{s=1}^{N_{el}} \sum_{i=1}^{N_{ed}} \boldsymbol{\tau}_i \mathbf{f}_{xy} - \left[(\rho_a C_w \|W\|W) |_{\eta} - \sum_{j=1}^{N_{ed}} \boldsymbol{\tau}_j \varphi |_{\eta} \right] |\Omega|_i \\
&+ g \sum_{j \in \Gamma_0 \cap \Gamma_b} \sum_{s=1}^{N_{el}} \psi_k |\Omega|_j \boldsymbol{\tau}_j \cdot \mathbf{n}_j - \sum_{s=1}^{N_{el}} \sum_{k=k_0}^{N_{\mathcal{K}}} \nabla_{xy} \left(\frac{\rho_s - \rho_0}{\rho_0} \right) \psi_s \chi_k dz d\Omega \\
&+ \frac{1}{\rho_0} \sum_{s=1}^{N_{el}} \sum_{k=k_0}^{N_{\mathcal{K}}} \nabla_{xy} q_s \psi_s \chi_k
\end{aligned} \tag{4.32}$$

- right hand side for vertical velocity R_w [see eq. (4.15)]

$$R_w = \int_{\Omega} \int_{-h}^{\eta} \psi_i \chi_l \sum_{s=1}^{N_{el}} \sum_{k=k_0}^{\mathcal{K}-1} \frac{1}{\rho_0} \frac{\partial q_s \psi_s \chi_k}{\partial z} dz d\Omega = \sum_{s=1}^{N_{el}} \sum_{k=k_0}^{\mathcal{K}-1} \frac{1}{\rho_0} \chi_k q_s |\Omega|_s \tag{4.33}$$

- right hand side for free surface R_{η} [eq. (4.14)]

$$R_{\eta} = \int_{\Omega} \mathbf{F} \psi_s d\Omega = \sum_{s=1}^{N_{el}} \tilde{\mathbf{F}}_b \psi_s \tag{4.34}$$

- right hand side for turbulence equations R_{ζ} [eqs. (4.18), (4.19)]

$$R_{\zeta} = \int_{\Omega} \int_{-h}^{\eta} \tau_i \varphi_l c_{\zeta} P_d \sum_{j=1}^{N_{ed}} \sum_{k=k_0}^{\mathcal{K}} \tau_j \varphi_k dz d\Omega = P_d \sum_{j=1}^{N_{ed}} \sum_{k=k_0}^{\mathcal{K}} \frac{d_j}{|e|_j} \Delta z_k |\Omega|_j \tag{4.35}$$

- right hand side for passive scalars R_{Φ} [eq. (4.17)]

$$\begin{aligned}
R_\Phi &= \int_{\partial\Omega} \chi_l \psi_i \left\{ \sum_j^{N_{ed}} \sum_{k=k_0}^{\mathcal{K}} \left[\frac{\nu_h}{\sigma_\Phi} (\nabla_{xy} \Phi_h) \right] \psi_j \chi_k \cdot \mathbf{n}_{xy} \right\} d\gamma \\
&- \int_{\partial\Omega} \chi_l \psi_i \left\{ \sum_j^{N_{ed}} \sum_{k=k_0}^{\mathcal{K}} \left[\frac{\nu_v}{\sigma_{\Phi_h}} \left(\frac{\partial \Phi_h}{\partial z} \right) \right] \chi_k \psi_j \cdot \mathbf{n}_z \right\} dS + \int_\Omega \int_{-\mathfrak{h}}^\eta \mathbf{F}_\Phi \psi_s \chi_l d\Omega \\
&= \left\{ \sum_j^{N_{ed}} \sum_{k=k_0}^{\mathcal{K}} \left[\left(\frac{\nu_h}{\sigma_\Phi} (\nabla_{xy} \Phi_h) \right) \psi_j \chi_k \cdot \mathbf{n}_{xy} + \left(\frac{\nu_v}{\sigma_{\Phi_h}} \left(\frac{\partial \Phi_h}{\partial z} \right) \right) \chi_k \psi_j \cdot \mathbf{n}_z \right] \right\} \Delta z_k \\
&+ \sum_{k=k_0}^{\mathcal{K}} \sum_{j=1}^{N_{ed}} (\mathbf{F}_{\Phi_j})_k |T|_j \Delta z_k
\end{aligned} \tag{4.36}$$

Let us introduce some useful operators,

$$\begin{aligned}
D_{xy} I_v &= \int_\Omega \psi_s \left(\frac{\partial}{\partial x} \int_{-\mathfrak{h}}^\eta u + \frac{\partial}{\partial y} \int_{-\mathfrak{h}}^\eta v \right) d\Omega \\
&= \sum_{k=k_0}^{\mathcal{K}} \sum_{j=1}^{N_{ed}} \left[\frac{\partial}{\partial x} (\tau_{xj}) \varphi_k + \frac{\partial}{\partial y} (\tau_{yj}) \varphi_k \right] \Delta z_k |\Omega|_j
\end{aligned} \tag{4.37}$$

$$\begin{aligned}
G_{xy} \eta_h &= \int_\Omega \int_{-\mathfrak{h}}^\eta \varphi_l \tau_i \eta_h \nabla_{xy} \cdot \sum_{j=1}^{N_{ed}} \tau_j dz d\Omega \\
&= \sum_{k=k_0}^{\mathcal{K}} \sum_{j=1}^{N_{ed}} \varphi_k \tau_j \eta_h \left(\frac{\partial \tau_{xj} \varphi_k}{\partial x} + \frac{\partial \tau_{yj} \varphi_k}{\partial y} \right) \Delta z_k |\Omega|_j
\end{aligned} \tag{4.38}$$

where $\mathcal{D}_\rho(\mathbf{x}, z) = \int_z^\eta (\rho - \rho_0) / \rho_0 d\zeta$ is the approximation term of the density. The vertical integration operator is defined by $I_v \mathbf{v} = \int_{-\mathfrak{h}}^\eta \mathbf{v} dz$.

Considering a generic triangle, the external approximated pressure can be written

$$P_0 = \sum_{j=1}^{N_{el}} p_{0j} \psi_j(\mathbf{x}) \tag{4.39}$$

where p_{0j} are computed from the centers of the circumscribed circles of the two-adjacent triangles.

The Coriolis term, \mathcal{F} can be expressed as follows:

The approximation of the vector \mathbf{f}_{xy} can be written

$$\mathbf{f}_{xy}(\mathbf{x}, z) = \sum_{k=k_0}^{\mathcal{K}} \sum_{l=1}^{N_{el}} \left(\tilde{\mathbf{J}}_l \right)_k \boldsymbol{\tau}(\mathbf{x}) \varphi_k(z) \tag{4.40}$$

where $\left(\tilde{\mathbf{J}}_l \right)_k$ is the normal horizontal flux such that

$$\left(\tilde{\mathbf{J}}_l \right)_k = \overline{\mathbf{C}} [(\mathbf{v}_l)_k \cdot \mathbf{n}_l |e_l|] \tag{4.41}$$

where $(\mathbf{v}_l)_k$ is the horizontal velocity on the edge l in the k_{th} layer, while $\overline{\overline{\mathbf{C}}}$ is a following tensor

$$\overline{\overline{\mathbf{C}}} = \begin{bmatrix} 0 & f_1 \\ -f_2 & 0 \end{bmatrix} \quad (4.42)$$

Finally the Coriolis term can be defined using the lumping formulation

$$\mathcal{F} = \int_{T_{\uparrow}} \int_{z_{k-1}}^{z_{k+1}} \varphi_k \mathbf{f}_{xy} \cdot \boldsymbol{\tau}_l dx dz \approx \left(\tilde{\mathbf{J}}_l \right)_k \Delta z_k \frac{d_l}{|e_l|} \quad (4.43)$$

Thus the space discretization of the former partial differential equations generate a semi-discrete system of non linear ordinary differential equations (ODEs)

$$\left\{ \begin{array}{l} D_{xy} \mathbf{v} + D_z w = 0 \\ \frac{d}{dt} (M_{\eta} \boldsymbol{\eta}) + D_{xy} I_v \mathbf{v} = R_{\eta} \\ \frac{D}{Dt} (M_{\mathbf{v}} \mathbf{v}) + K_{\mathbf{v}} \mathbf{v} + D_{xy}^T \left(\frac{q}{\rho_0} \right) - g G_{xy} \eta = R_{\mathbf{v}} - g G_{xy} \mathcal{D}_{\rho} + \mathcal{F} - g G_{xy} P_0 \\ \frac{D}{Dt} (M_w \mathbf{W}) + K_w \mathbf{W} + D_z \left(\frac{q}{\rho_0} \right) = R_w \\ \frac{D}{Dt} (M_{\Phi} \Phi) + K_{\Phi} \Phi = R_{\Phi} \quad \text{for } \forall \Phi = (S, T, C) \\ \frac{D}{Dt} (M_{\zeta} \zeta) + K_{\zeta} \zeta = R_{\zeta} \quad \text{for } \forall \zeta = (k, \varepsilon) \end{array} \right. \quad (4.44)$$

where $\frac{d}{dt}$ is a Lagrangian derivative, $\frac{D}{Dt}$ is the material derivative.

Let us notice that the various mass matrices depend upon on time through the vertical integration where the upper limit is $\eta(x, y, t)$. This is a difficulty that we will address in the next chapter when we deal with the time discretization.

Chapter 5

Time discretization and approximate factorizations

In this chapter, starting from the three-dimensional turbulent incompressible Navier-Stokes equations for the variable density fluid flow, we introduce a general mathematical framework for the factorizations of the algebraic system with the non-hydrostatic pressure assumption. The fractional step schemes are widely adopted for the numerical solution of 3D free-surface flows. These schemes can be formally interpreted as deriving from inexact block factorizations of the matrix arising from the time discretization of the original system. In the sequel the generalized Yosida scheme (which is shown to behave well for large time-step [89], [37], [90]) that we intend to introduce, will be used to solve the RANS *pure hydrodynamics* equations. The fractional time step scheme proposed by Mohammadi and Pironneau [96] will be used to solve the turbulence equations.

5.1 Time discretization

Free-surface flows imply that the geometry evolves with time. In order to avoid a fully coupled problem with all difficulties associated with the resulting linear algebraic system, we assume that the geometry is given (and in fact it is frozen) at time level $t^n = n\Delta t$ and this constitutes the starting (or initial) condition to integrate the problem over the next step. Therefore the different mass matrices do not depend on time and may leave the time derivatives.

Remark 7 *The system (4.44) is convective dominant, and several different physical processes with different time scales lead to the stiff character of the problem. Thus to avoid instability problems (that could arise from the non-linear terms), we will use the characteristics method for the time integration, especially for the material time derivatives.*

Let us consider a discretization of the time interval $[0, T]$ into N subintervals $[t^n, t^{n+1}]$ with $\Delta t = t^{n+1} - t^n$ for $n = 0, 1, \dots, N - 1$. For the non-hydrostatic pressure case, applying the θ -projection method to the free surface (η) and the surface velocity field (\mathbf{v}) the following implicit time advancing scheme of the system (4.44) is reordered and the problem statement can be written: For each $n \geq 0$ find \mathbf{v}^{n+1} , \mathbf{w}^{n+1} , $\boldsymbol{\eta}^{n+1}$, $\boldsymbol{\zeta}^{n+1}$, $\boldsymbol{\Phi}^{n+1}$ such that

$$\left\{ \begin{array}{l} D_{xy} \mathbf{v}^{n+1} + D_z w^{n+1} = 0 \\ M_\eta \frac{(\eta^{n+1} - \eta^n)}{\Delta t} + \theta D_{xy} I_v \mathbf{v}^{n+1} = R_\eta^n - (1 - \theta) D_{xy} I_v \mathbf{v}^n \\ M_v \frac{(\mathbf{v}^{n+1} - \mathbf{v}(\mathbf{X}^n))}{\Delta t} + K_v \mathbf{v}^{n+1} + G_{xy} \left(\frac{q^{n+1}}{\rho_0} \right) - \theta g G_{xy} \eta^{n+1} = \\ R_v^n + (1 - \theta) g G_{xy} \eta^n - g G_{xy} \mathcal{D}_\rho^n + \mathcal{F}^n - g G_{xy} P_0^{n+1} \\ \\ M_w \frac{(\mathbf{W}^{n+1} - \mathbf{W}(\mathbf{X}^n))}{\Delta t} + K_w \mathbf{W}^{n+1} + D_z \left(\frac{q^{n+1}}{\rho_0} \right) = R_w^n \\ M_\Phi \frac{(\Phi^{n+1} - \Phi(\mathbf{X}^n))}{\Delta t} + K_\Phi \Phi^{n+1} = R_\Phi^n \quad \text{for } \forall \Phi = (S, T, C) \\ M_\zeta \frac{(\zeta^{n+1} - \zeta(\mathbf{X}^n))}{\Delta t} + K_\zeta \zeta^{n+1} = R_\zeta^n \quad \text{for } \forall \zeta = (k, \varepsilon) \end{array} \right. \quad (5.1)$$

In the above system $\mathbf{v}(\mathbf{X}^n) = \mathbf{v}(t^n, \mathbf{X}(t^n, t^{n+1}, (\mathbf{x}, z)))$.

The coordinate $\mathbf{X}(\tau; t, \mathbf{x})$ is the solution of the following problem (see [108], [112]):

$$\left\{ \begin{array}{l} \frac{d\mathbf{X}(\tau; t, \mathbf{x})}{d\tau} = \mathbf{V}(\tau, \mathbf{X}(\tau; t, \mathbf{x})) \quad \text{for } \tau \in (0, t) \\ \mathbf{X}(t; t, \mathbf{x}) = \mathbf{x} \end{array} \right\}. \quad (5.2)$$

From a geometric point of view $\mathbf{X}(\cdot) = \mathbf{X}(\cdot; t, \mathbf{x})$ is the parametric representation of the trajectories: $\mathbf{X}(\tau; t, \mathbf{x})$ is the position at time τ of a particle which has been driven by the field $\mathbf{V}(u, v, w)$ and that occupies the position \mathbf{x} at time t .

Problem (5.2) is a system of ordinary differential equations. For its discretization it is possible to use a backward Euler scheme, or a more accurate fourth-order Runge-Kutta scheme. Since (5.2) is non-linear, to compute $\mathbf{X}(t^{n+1}; t^n, \mathbf{x})$ we will use the velocity at time t^n . The total derivative for a generic variable Φ can be discretized as follows:

$$\frac{D\Phi}{Dt}(t^{n+1}, \mathbf{x}) \simeq \frac{\Phi(t^{n+1}, \mathbf{x}) - \Phi(t^n, \mathbf{X}(t^n; t^{n+1}, \mathbf{x}))}{\Delta t} \quad (5.3)$$

Remark 8 *Actually by using the temporal first order Euler scheme, the above characteristics method is found to be monotonic, and the stability is achieved accordingly.*

5.1.1 Incremental scheme

When the initial distribution of the hydrodynamic pressure is known, typically when we restart the simulation or when an analytical solution is available, the so-called *incremental* scheme becomes useful.

In this case the xy -gradient and the z derivative of the hydrodynamic correction at time t^{n+1} are split as follows

$$\nabla q^{n+1} = \nabla(q^{n+1} - q^n) + \nabla q^n \quad (5.4)$$

$$\frac{\partial q^{n+1}}{\partial z} = \frac{\partial(q^{n+1} - q^n)}{\partial z} + \frac{\partial q^n}{\partial z} \quad (5.5)$$

Hence at the algebraic level, one has a different right-hand side accounting for the gradient of hydrodynamic pressure at time t^n and moreover \mathbf{Q}^{n+1} represents now the increment of q . This implies that an initial condition q^0 is required for the hydrodynamic pressure. Moreover the presence of ∇q^n and $\frac{\partial q^n}{\partial z}$ in the correction-step is of great importance when the hydrodynamic correction becomes large compared to the hydrostatic pressure.

5.1.2 The Stokes-like algebraic system equations

The above overall ordinary differential equations system of the SWE is non-linear. The present work adopts a strategy of decoupling to avoid a fully coupled problem with all its difficulties. Therefore for the overall scheme we use the splitting between the “pure” hydrodynamic solver (first, second and third equations of system (5.1)), followed respectively by the scalars solver (fourth equation of system (5.1) and the turbulent solver (fifth equation of system (5.1)). Hence the hydrodynamic system of the ordinary differential equations (for dependent variables) are solved first, then using these values we solve advection-diffusion equations for scalars (S, T, C_s), and finally the turbulent quantities are computed with $\zeta = (k, \varepsilon)$.

The hydrodynamic model

At each time level t^{n+1} , using the θ projection method upon the free-surface equation, and the incremental scheme, the algebraic system of the ODEs can be written

$$\begin{bmatrix} \mathbf{A} & \widehat{\mathbf{G}} \\ \mathbf{D} & 0 \end{bmatrix} \begin{bmatrix} \boldsymbol{\Lambda}^{n+1} \\ \mathbf{Q}^{n+1} - \mathbf{Q}^n \end{bmatrix} = \begin{bmatrix} \tilde{\mathbf{R}} - \widehat{\mathbf{G}}\mathbf{Q}^n \\ 0 \end{bmatrix} \quad (5.6)$$

where $\boldsymbol{\Lambda}^{n+1} = (\mathbf{v}^{n+1}, \eta^{n+1}, \mathbf{W}^{n+1})^T$ is the unknown vector containing the discrete values of horizontal velocity, elevation and vertical velocity. $\widehat{\mathbf{G}} = (G_{xy}, G_z)$ and $\mathbf{D} = (D_{xy}, D_z)$ are the 3D gradient and divergence operators respectively.

The matrices \mathbf{A} , $\widehat{\mathbf{G}}$ and \mathbf{D}^T can be defined as follows

$$\mathbf{A} = \begin{bmatrix} \frac{1}{\Delta t} M_v + K_v & g\theta G_{xy} & 0 \\ -\theta D_{xy} I_v & \frac{1}{\Delta t} M_\eta & 0 \\ 0 & 0 & \frac{1}{\Delta t} M_w + K_w \end{bmatrix}; \quad \widehat{\mathbf{G}} = \begin{bmatrix} \frac{1}{\rho_0} G_{xy} \\ 0 \\ \frac{1}{\rho_0} G_z \end{bmatrix}; \quad \mathbf{D}^T = \begin{bmatrix} D_{xy}^T \\ 0 \\ D_z^T \end{bmatrix} \quad (5.7)$$

where M_v, M_η, M_w represent the mass matrices, K_v, K_w represent the stiffness matrices. G_{xy} and D_{xy} represent respectively the 2D horizontal gradient and divergence operator in the xy plane. G_z and D_z represent the algebraic counterpart of respectively \mathbf{G} and \mathbf{D} in the vertical direction. $\tilde{\mathbf{R}} = (\tilde{\mathbf{R}}_1, \tilde{\mathbf{R}}_2, \tilde{\mathbf{R}}_3)^T$ accounts for the boundary conditions and for the explicit terms of time derivatives, hence we can define

$$\begin{aligned} \tilde{\mathbf{R}}_1 &= \frac{M_v \Delta t}{v} (\mathbf{X}^n) - g(1 - \theta) G_{xy} P_0^{n+1} - g G_{xy} \mathcal{D}_\rho^n + \mathcal{F}^n \\ \tilde{\mathbf{R}}_2 &= \frac{M_\eta}{\Delta t} \eta^n - (1 - \theta) D_{xy} I_v \mathbf{v}^n \\ \tilde{\mathbf{R}}_3 &= \frac{M_w}{\Delta t} W^n (\mathbf{X}^n) \end{aligned} \quad (5.8)$$

5.1.3 The inexact factorizations

Let us consider \mathbf{A} the block matrix in (5.6), then assuming that the block \mathbf{A} is invertible, the following LU factorization of \mathbf{A} exists such that,

$$\begin{bmatrix} \mathbf{A} & \widehat{\mathbf{G}} \\ \mathbf{D} & 0 \end{bmatrix} = \begin{bmatrix} \mathbf{A} & 0 \\ \mathbf{D} & -\mathbf{D}\mathbf{B}\widehat{\mathbf{G}} \end{bmatrix} \begin{bmatrix} \mathbf{I} & \mathbf{B}\widehat{\mathbf{G}} \\ 0 & \mathbf{I} \end{bmatrix} \quad (5.9)$$

with $\mathbf{A}^{-1} = \mathbf{B}$.

Remark 9 *Unlike what happens with the classical differential projection schemes, it should be noticed that the proposed algebraic approach here, does not explicitly require to impose unphysical boundary conditions [89], [29]. On the other hand it should be noticed that all the physical-relevant boundary conditions have already been incorporated at this stage, and the actual form of matrices \mathbf{A} and \mathbf{D} in (5.6) does depend on them. Indeed no further conditions are needed.*

Starting from (5.9), we can introduce suitable inexact factorizations in order to reduce the computational effort [111].

Let us suppose that,

$\mathbf{B} = \mathbf{B}_1$ in the L-step, $\mathbf{B} = \mathbf{B}_2$ in the U step, one can obtain the following approximation matrix

$$\begin{bmatrix} \mathbf{A} & 0 \\ \mathbf{D} & -\mathbf{D}\mathbf{B}_1\widehat{\mathbf{G}} \end{bmatrix} \begin{bmatrix} \mathbf{I} & \mathbf{B}_2\mathbf{D}^T \\ 0 & \mathbf{I} \end{bmatrix} = \begin{bmatrix} \mathbf{A} & \mathbf{A}\mathbf{B}_2\widehat{\mathbf{G}} \\ \mathbf{D} & \mathbf{D}(\mathbf{B}_2 - \mathbf{B}_1)\widehat{\mathbf{G}} \end{bmatrix} \quad (5.10)$$

- one can easily find that the mass conservation is fully unperturbed if $\mathbf{B}_2 = \mathbf{B}_1 = \mathbf{B}$,
- equations concerning the vector \mathbf{A} are unperturbed if $\mathbf{B}_2 = \mathbf{A}^{-1}$, and $\mathbf{B}_1 = \mathcal{H} \neq \mathbf{B}_2$.

A candidate for the matrix \mathcal{H} can be found by observing that

$$\mathbf{A} = \begin{bmatrix} \frac{1}{\Delta t}M_v + K_v & g\theta G_{xy} & 0 \\ -\theta D_{xy}I_v & \frac{1}{\Delta t}M_\eta & 0 \\ 0 & 0 & \frac{1}{\Delta t}M_w + K_w \end{bmatrix} = \frac{1}{\Delta t} \begin{bmatrix} M_v & 0 & 0 \\ 0 & M_\eta & 0 \\ 0 & 0 & M_w \end{bmatrix} + \mathcal{B} \quad (5.11)$$

and we can also write

$$\mathbf{A} = \frac{1}{\Delta t}\mathcal{M} + \mathcal{B} = \frac{1}{\Delta t}\mathcal{M} \left(\begin{bmatrix} \mathbf{I} & 0 & 0 \\ 0 & \mathbf{I} & 0 \\ 0 & 0 & \mathbf{I} \end{bmatrix} + \Delta t\mathcal{M}^{-1}\mathcal{B} \right) \quad (5.12)$$

Hence a convenient choice of \mathcal{H} (see [89], [111]) is given by

$$\mathcal{H} = \Delta t\mathcal{M}^{-1} \quad (5.13)$$

5.1.4 The projection-correction method: the generalized Yosida method

Let us introduce first some useful explicit terms used by the finite element approximation:

- Terms of external pressure: $G_{xy}P_0^{n+1}$.

Applying the Gauss-Green formulation, the discretized form of the pressure term 4.39 reads

$$G_{xy}P_0^{n+1} = \sum_{l=1}^3 \sum_{z_{k-1}}^{z_{k+1}} p_0^{n+1} (\Delta z_k)_l d_l \approx \sum_{l=1}^3 (\Delta z_k)_l \left(p_{0T_+^l}^{n+1} - p_{0T_-^l}^{n+1} \right) \quad (5.14)$$

- Terms of density: $G_{xy}\mathcal{D}^n$.

Let the function

$$\mathcal{D}_\rho^n(\mathbf{x}, z) = \int_z^{\eta^n} \frac{\rho^n - \rho_0}{\rho_0} d\zeta \quad (5.15)$$

$$\mathcal{C}^n = \int_{\mathcal{T}} G_{xy} \mathcal{D}_\rho^n \cdot \boldsymbol{\tau} \varphi dz d\mathbf{x} \quad (5.16)$$

Assuming that density is constant for a prism and using the trapezoidal rule for a basic triangle \mathcal{T}_j in a layer s , the function \mathcal{C}^n can be written

$$\mathcal{C}_{s,\mathcal{T}_j}^n \approx \frac{1}{\rho_0} \sum_{k=s}^{\mathcal{K}} \frac{z_{k+1} - z_k}{2} \left(\Delta \rho_{k+1,\mathcal{T}_j}^n + \Delta \rho_{k,\mathcal{T}_j}^n \right) \quad (5.17)$$

where $\Delta \rho_{k,\mathcal{T}_j}^n = \rho_{k,\mathcal{T}_j}^n - \rho_0$.

Using the Gauss-Green formula in Eq. (5.16), Eq. (5.17) reads

$$\begin{aligned} \int_{\mathcal{T}_l} \int_{z_{k-1}}^{z_{k+1}} \varphi_k \nabla \mathcal{C}^n \cdot \boldsymbol{\tau}_l d\mathbf{x} dz &\approx (\mathcal{C}_{k-1,T_+} - \mathcal{C}_{k-1,T_-}) \int_{z_{k-1}}^{z_{k-1/2}} \varphi_k dz \\ &+ (\mathcal{C}_{k,T_+} - \mathcal{C}_{k,T_-}) \int_{z_{k-1/2}}^{z_{k+1/2}} \varphi_k dz \\ &+ (\mathcal{C}_{k+1,T_+} - \mathcal{C}_{k+1,T_-}) \int_{z_{k+1/2}}^{z_{k+1}} \varphi_k dz \end{aligned} \quad (5.18)$$

with the following integral expressions

$$\begin{aligned} \int_{z_{k-1}}^{z_{k-1/2}} \varphi_k dz &= \frac{\delta^2 z_{k-1}}{8\delta z_{k-1/2}} \\ \int_{z_{k-1/2}}^{z_{k+1/2}} \varphi_k dz &= \Delta z_k - \frac{1}{8} \left(\frac{\delta^2 z_{k-1}}{\delta z_{k-1/2}} + \frac{\delta^2 z_{k+1}}{\delta z_{k+1/2}} \right) \\ \int_{z_{k+1/2}}^{z_{k+1}} \varphi_k dz &= \frac{\delta^2 z_{k+1}}{8\delta z_{k+1/2}} \end{aligned} \quad (5.19)$$

Hence by using the value of \mathcal{H} as in (5.13) the approximated values of \mathbf{v}^{n+1} and q^{n+1} can be computed by means of the following sequence of steps

$$\text{L-step: } \begin{cases} \mathbf{A}\tilde{\Lambda}^{n+1} = \mathbf{R} - \widehat{\mathbf{G}}\mathbf{Q}^n \\ \mathbf{D}\tilde{\Lambda}^{n+1} - \mathbf{D}\mathbf{B}\widehat{\mathbf{G}}\tilde{\mathbf{Q}}^{n+1} = 0 \end{cases} \quad (5.20)$$

$$\text{U-step: } \begin{cases} \Lambda^{n+1} + \mathcal{H}\widehat{\mathbf{G}}(\mathbf{Q}^{n+1} - \mathbf{Q}^n) = \tilde{\Lambda}^{n+1} \\ \mathbf{Q}^{n+1} - \mathbf{Q}^n = \tilde{\mathbf{Q}}^{n+1} \end{cases} \quad (5.21)$$

We observe that

$$\mathcal{H}\widehat{\mathbf{G}} = \Delta t \begin{bmatrix} \frac{1}{\rho_0} M_{\mathbf{v}}^{-1} G_{xy} \\ 0 \\ \frac{1}{\rho_0} M_w^{-1} G_z \end{bmatrix}; \quad \mathbf{D}\mathcal{H}\widehat{\mathbf{G}} = \Delta t \frac{1}{\rho_0} \left[D_{xy} M_{\mathbf{v}}^{-1} G_{xy} + \frac{1}{\rho_0} D_z M_w^{-1} G_z \right] \quad (5.22)$$

Using the so-called *Generalized Yosida Method* (GYM), the L and U-step can be rewritten as L-step:

Hydrostatic step

$$\begin{cases} \left(\frac{1}{\Delta t} M_{\mathbf{v}} + K_{\mathbf{v}} \right) \tilde{\mathbf{v}}^{n+1} & + \theta g G_{xy} \tilde{\eta}^{n+1} = \frac{1}{\Delta t} M_{\mathbf{v}} \mathbf{v}^n (\mathbf{X}^n), \\ & - (1 - \theta) g G_{xy} \eta^n - \frac{1}{\rho_0} G_{xy} P_0^{n+1} - g \mathcal{C}^n, \\ & + \mathbf{F}^n - \frac{1}{\rho_0} G_{xy} \mathbf{Q}^n; \\ -g D_{xy} I_v \tilde{\mathbf{v}}^{n+1} + \frac{1}{\Delta t} M_{\eta} \tilde{\eta}^{n+1} & = \frac{1}{\Delta t} M_{\eta} \tilde{\eta}^n \end{cases} \quad (5.23)$$

Determination of an intermediate vertical velocity

$$\left(\frac{1}{\Delta t} M_w + K_w \right) \tilde{\mathbf{W}}^{n+1} = \frac{1}{\Delta t} M_w \mathbf{W}^n (\mathbf{X}^n) - \frac{1}{\rho_0} G_z \mathbf{Q}^n; \quad (5.24)$$

Determination of an intermediate pressure

$$-\Delta t \frac{1}{\rho_0} [D_{xy} M_{\mathbf{v}}^{-1} G_{xy} + G_z M_w^{-1} D_z^T] \tilde{\mathbf{Q}}^{n+1} = - \left(D_{xy} \tilde{\mathbf{v}}^{n+1} + D_z \tilde{\mathbf{W}}^{n+1} \right) \quad (5.25)$$

U-step:

$$\mathbf{Q}^{n+1} = \tilde{\mathbf{Q}}^{n+1} \quad (5.26)$$

$$\begin{cases} \left(\frac{1}{\Delta t} M_{\mathbf{v}} + K_{\mathbf{v}} \right) \mathbf{v}^{n+1} & + \theta g G_{xy} \frac{1}{\rho_0} \eta^{n+1} = \left(\frac{1}{\Delta t} M_{\mathbf{v}} + K_{\mathbf{v}} \right) \tilde{\mathbf{v}}^{n+1} \\ & + \theta g G_{xy} \frac{1}{\rho_0} \tilde{\eta}^{n+1} - (1 - \theta) g G_{xy} \frac{1}{\rho_0} \eta^n \\ & - \frac{1}{\rho_0} G_{xy} (\mathbf{Q}^{n+1} - \mathbf{Q}^n) \\ -D_{xy} I_v \mathbf{v}^{n+1} & + \frac{1}{\Delta t} M_{\eta} \eta^{n+1} = D_{xy} I_v \tilde{\mathbf{v}}^{n+1} + \frac{1}{\Delta t} M_{\eta} \tilde{\eta}^{n+1} \end{cases} \quad (5.27)$$

$$\left(\frac{1}{\Delta t}M_w + K_w\right)\mathbf{W}^{n+1} = \frac{1}{\Delta t}M_w\tilde{\mathbf{W}}^{n+1} - G_z(\mathbf{Q}^{n+1} - \mathbf{Q}^n) \quad (5.28)$$

This GYM extends to the free-surface flow Yosida method for the Navier-Stokes Equations (see [111]). The method of solution requires to solve

1. the hydrostatic step (5.23)-(5.24);
2. the system (5.25) in order to compute the intermediate pressure;
3. the hydrodynamic correction (5.27);
4. the tridiagonal system (5.28) in order to compute the vertical velocity at time step t^{n+1} .

Remark 10 *The nature of advection-diffusion equations for scalars is similar to that of the turbulence equations, and the following solver will be considered to be closer to the one used for computing the scalars (S, T, C_s) with some modifications. More precisely the turbulence equations right-hand sides as well as the sediment concentration one, contains non-linear terms with the source of difficulties in modeling, and will be subject of our attention in the following paragraphs and in chapter 7.*

The turbulence model

In a typical case of the problems that we want to solve, we are facing the situation where a fluid enters a domain, moves through the domain in turbulent motion and exits again at one or more outflows. The aim here is to develop a closed set of equations together with appropriate boundary conditions, which govern the turbulent fluid flow. It should be pointed out that the turbulence equations are generally convection dominated. The critical problem in the turbulence modeling is the stability of the scheme as well as preserving the positivity of the turbulent kinetic energy, k , and its rate of dissipation, ε . For $k - \varepsilon$ turbulence modeling, Mohammadi and Pironneau [96] analyzed some properties of this model and proposed two methods that could allow to enforce those properties.

- A semi-implicit multi-step scheme using an auxiliary system
- A semi-implicit multi-step scheme in k and ε only.

In this work we basically follow the second approach for the $k - \varepsilon$ turbulence modeling. Here we will analyze some properties of the derived Stokes operator which will be used. More precisely we will consider the existence, uniqueness and positivity of the solution, as well as the stabilization of the scheme.

Existence and uniqueness of the solution

We know no existence or uniqueness results for the $k - \varepsilon$ system itself. Some attempts concentrate on a simpler model, which is formulated in the transformed functions $\psi = \varepsilon^2/k^3$, $\theta = k/\varepsilon$ and contains some simplifications. For this system an existence result has been found (see [96]), but *uniqueness* is still an open problem.

The quasi-implicit form

The right-hand sides (RHS) of the turbulence equations contain the non-linear terms. On the other hand the physical instabilities introduced by density gradient in multiphase flows could generate instabilities in the numerical scheme. To avoid such the inconvenient, the present thesis adopts the quasi-implicit time discretization for the linearization of the RHS-sink terms in the turbulence equations [see Eq. (4.28)]. For example, to illustrate our point, the time discretization of the rate of dissipation in the RHS of the kinetic energy PDE Eq. (4.18) (a similar procedure holds for the rate of dissipation PDE Eq. (4.19)), is represented by the following expression: $\lambda_v H \left((N^2)^2 \right) + \varepsilon^n \frac{k^{n+1}}{k^n}$ (see [80]). Thus the relevant matrices of stabilization become

$$\begin{aligned} E_k &= \int_{\Omega} \int_{-\mathfrak{h}}^{\eta} \tau_i \left[\lambda_v^n H (N^2)^n + \sum_{k=k_0}^{\mathcal{K}} \sum_{j=1}^{Ned} c_1 \tau_j \varphi_k \right] \frac{\varepsilon^n}{k^n} \varphi_k d\Omega dz \\ E_{\varepsilon} &= \int_{\Omega} \int_{-\mathfrak{h}}^{\eta} \tau \left[\left(c_3 \lambda_v^n H (N^2)^n + \sum_{k=k_0}^{\mathcal{K}} \sum_{j=1}^{Ned} c_2 \tau_j \tau_j \varphi_k \right) \frac{\varepsilon^n}{k^n} + c_1 k^n P_d^{n+1} \right] \varphi d\Omega dz \end{aligned} \quad (5.29)$$

Hence diagonal terms in stiffness matrix are boosted and the stability of the scheme is improved. Moreover, to enforce the accuracy of the solution, a high order fourteen points Gaussian quadrature formula is implemented for evaluating the source term at the right-hand sides of the turbulence equations Eqs. (4.18) and (4.19).

Fractional-step algorithm: Mohammadi and Pironneau

The main idea of this algorithm proposed by Mohammadi and Pironneau (see [96]), is to split the system of equations into a convection step and a diffusion step. At each time level t^{n+1} we obtain the following algebraic system equation

$$\begin{bmatrix} \mathbf{A}_k & E_k \\ E_{\varepsilon} & \mathbf{A}_{\varepsilon} \end{bmatrix} \begin{bmatrix} \mathbf{k}^{n+1} \\ \varepsilon^{n+1} \end{bmatrix} = \begin{bmatrix} \mathbf{R}_k \\ \mathbf{R}_{\varepsilon} \end{bmatrix} \quad (5.30)$$

where $\mathbf{A}_k = \frac{1}{\Delta t} \mathbf{M}_k + \mathbf{K}_k$; $\mathbf{A}_{\varepsilon} = \frac{1}{\Delta t} \mathbf{M}_{\varepsilon} + \mathbf{K}_{\varepsilon}$.

One can find the following LU factorization,

$$\begin{bmatrix} \mathbf{A}_k & E_k \\ E_{\varepsilon} & \mathbf{A}_{\varepsilon} \end{bmatrix} = \begin{bmatrix} \mathbf{A}_k & 0 \\ E_{\varepsilon} & (\mathbf{A}_{\varepsilon} - E_{\varepsilon} \mathbf{B}_{1k} E_k) \end{bmatrix} \begin{bmatrix} \mathbf{I} & \mathbf{B}_{2k} E_k \\ 0 & \mathbf{I} \end{bmatrix} \quad (5.31)$$

in which E_k and E_{ε} come from the quasi-implicit temporal discretization Eq.(4.28) [80].

Here the algorithm is split into two fractional steps: (i) the convection step which only contains the zero-order terms; (ii) the diffusion step for the others.

Convection step:

Here $\mathbf{A}_k^{-1} = \mathbf{B}_{1k}$ contains only the zero-order terms of the matrix \mathbf{A}_k

$$\begin{cases} \mathbf{A}_k \tilde{\mathbf{k}}^{n+1} = R_k \\ E_{\varepsilon} \tilde{\mathbf{k}}^{n+1} - (\mathbf{A}_{\varepsilon} - E_{\varepsilon} \mathbf{B}_{1k} E_k) \tilde{\varepsilon}^{n+1} = R_{\varepsilon} \end{cases} \quad (5.32)$$

Diffusion step:

In this step $\mathbf{A}_k^{-1} = \mathbf{B}_{2k}$ contains only the diffusion terms of the matrix \mathbf{A}_k

$$\begin{cases} \mathbf{k}^{n+1} + \mathbf{B}_{2k} E_k \boldsymbol{\varepsilon}^{n+1} = \tilde{\mathbf{k}}^{n+1} \\ \boldsymbol{\varepsilon}^{n+1} = \tilde{\boldsymbol{\varepsilon}}^{n+1} \end{cases} \quad (5.33)$$

At each time step the convective step is solved first using the Galerkin characteristics method for the convection terms. Finally the diffusion step is solved and the θ projection method can be adopted for e.g. Crank Nicolson with $\theta = 1/2$ (see Rappaz *et al.* [113], Fletcher [36]) by means of improving the time accuracy.

Positivity of k and ε , stability of the turbulence scheme

Here the zero order terms have been split into their positive and negative parts. For the stability purpose, the positive terms are treated explicitly, while the negative terms are treated implicitly (see also [80]).

It is worthwhile to notice that for a generic prism P , the computation of production, kinetic energy and its dissipation rate takes into account all the neighbors contribution. Moreover, by using an upwind scheme (characteristics Galerkin method), the conservative form of the scalar equations and the fractional step algorithm can enforce preservation of the positive k , ε , as well as the mass balance and the stability of the scheme.

Remark 11 *The advection-diffusion equations for the passive scalars such as heat, salt and solute concentration are similar to the turbulence equations. Thus the same solver will be used for their solutions with a little adaptation for the sources, sinks and boundary conditions.*

5.2 Important features of the general algorithm

The some important features of the overall solution method can be summarized as follows,

- The velocity field is described using lowest order Raviart-Thomas finite elements to account of the discontinuity into the solution (see free-surface position), while the linear \mathcal{P}_1 Galerkin F. E. M is used in the vertical direction.
- The linear systems are solved by means of conjugate gradient method in its stabilized version namely the Bi-CGSTAB using Krylov accelerators (see Quarteroni and Valli [112]).
- In this study the so-called *Eulerian-Lagrangian Galerkin (ELG)-weak method* is adopted to guarantee a high degree of mass conservation of model, i.e. in the finite element context, the Eulerian-Lagrangian method combines the characteristics method with a Galerkin finite element weak formulation, and the Eulerian grid is transported backward in time to construct the Lagrangian grid. This method has better conservation properties.
- Moreover, because the spatial and temporal discretization are combined as result of the Lagrangian tracking, the temporal discretization error is reduced markedly. In effect, the Eulerian-Lagrangian methods perform the temporal discretization of the total derivative by tracking a fictitious fluid particle during each time. Thus for example, the truncation error for a first-order Eulerian-Lagrangian is proportional to the second total derivative of Eulerian solution. Hence the accuracy is enforced in the numerical integration (see Morton *et al.* [97], Benqué *et al.* [4]).

- The principal advantage of the *ELG* method is that, owing to the Lagrangian (i.e. non-local) nature of the advection step, the CFL restriction is eliminated, since there is no limitation in theory on time step size in the Eulerian Lagrangian scheme. In practice however, large time step introduces large errors in the approximation of the trajectories, specifically in the location of the departure points at the foot of the characteristics lines. Thus, for accuracy reason, the implicit time marching scheme is used for the free-surface discretization (see second equation in system 5.1), and the time-step size, Δt , needs to be limited. This effectively places a limit on how large the time step can be (this is none the less, much less restrictive than that imposed by Eulerian schemes), by means of Courant-Friedrichs-Levy (CFL) restriction. This is found numerically to be

$$\Delta t \leq 15 \frac{\Delta x}{\sqrt{\frac{\tau_0}{\rho_m}}} ; \quad \delta\tau < \frac{\Delta t}{10} \quad (5.34)$$

where $\delta\tau$ stands for the characteristics parametric sub-scale time step size, and τ_0 is the bottom shear stress magnitude.

- The model uses the conservative scheme, which is particularly desirable for scalar transport. The characteristics method taking the hyperbolic nature of the advection operator into account was implemented via the *ELG method*. This method is suitable for the relatively large time step and can enforce the preservation of the $k - \varepsilon$ positivity as well as the stability of the scheme.
- The model overall accuracy is found to be of first order in time and second-order in space.

Chapter 6

3D model for turbulent free-surface flows: Numerical Results

This chapter deals with the validation of the turbulent hydrodynamic model, whereas some test cases have been carried out to :

- check the validity of the model developed, by simulating the constant or variable density fluid flow
- provide insight in some interesting features of the flow field and the turbulence and the relevant physical mechanisms and processes underlying these features.
- provide some illustrative examples of the rather wide range of situations concerned with the matter of variable density, and to bring out some numerical computations carried out for simulating open channel fluid flows including a suitable $k - \epsilon$ turbulence closure for stratified fluid flows.
- apply the acquired knowledge in an engineering sense, mainly by evaluating, improving and developing suitable and efficient numerical scheme.

6.1 Validation of the model using benchmark test cases

Detailed experimental data for testing the solver are limited. However in order to check the validity of the model developed, the computation was carried out for simulating open channel flows and the computed results were compared with the experimental measurements from laboratory flumes. Hence three cases of uniform and non-uniform unsteady flows in open channels will be used to test our model. The data for straight-uniform open channel flow test case were taken from Istiarto [54], those of non-uniform open channel flow were taken from Qu [110], while those of curved open-channel flow test case were taken from Blanckaert [5]. The data for Qu's experiment have been measured by an electromagnetic measuring system (PROline Promag), while other experimental data have been carried out with detailed velocity and turbulence measurements in laboratory flumes at the Laboratoire d'Hydraulique Environnementale (LHE) in the Ecole Polytechnique Fédérale de Lausanne (EPFL), Switzerland, using a specially designed Acoustic Doppler Velocity Profiler (ADVP). The ADVP is capable of measuring instantaneous profiles of three components of velocity simultaneously at a sampling frequency of 33 Hz. Using these velocity measurements, the profiles of turbulence characteristics, and the components of Reynolds stress tensor were also computed.

The test results will be compared to experimental data for the steady open channel flow which is the suitable case (see [54]), curved open channel flow (see [5]) and for the unsteady open channel flow (see [110]), for the water surface profile along the channel and the vertical distributions of the velocity, eddy viscosity, and shear stress.

6.1.1 Stability conditions and accuracy of the model

The most important requirements on numerical methods for solving RANS arise from the goal of producing an accurate realization of a flow that contains a wide range of length scales. Time accuracy for the advection-diffusion equations (e.g. turbulence equations or closure equations) requires a small time step and it is important to know whether the time-advance method is stable for the time step demanded by accuracy. The most common description of the accuracy of a time and spatial discretization method is its order, the numbers that describe the rates at which the discretization errors decrease as the time step and/or grid size goes to zero.

6.1.2 The model accuracy

To compute the decay of the homogeneous turbulence convected by a uniform flow, some analytical solutions have been used (see [96]) for the steady open channel flow (see [54], [71]) :

$$k = k^0 \left(1 + (c_a - 1) x \frac{\varepsilon^0}{k^0} \right)^{\frac{1}{1-c_a}} \quad (6.1)$$

$$\varepsilon = \varepsilon^0 \left(1 + (c_a - 1) x \frac{\varepsilon^0}{k^0} \right)^{\frac{c_a}{1-c_a}} \quad (6.2)$$

where x is the longitudinal coordinate, $c_a = 2.06$ is a constant, k^0 and ε^0 are respectively the initial values of the turbulent kinetic energy and its rate of dissipation. The channel is $38[m]$ long, the width is $B = 2[m]$ and the flow depth is $h = 0.183[m]$. The discharge is $Q = 0.25[m^3/s]$, the bed roughness is $k_s = 0.0042[m]$, and the bed slope is set to $S_0 = 0.000624$. Computations were conducted using 100 layers. Several layers of thickness $\delta z_b = 0.002[m]$ have been used at the bed (see figure 6.1) in order to take into account the boundary layer effects at the bottom.

Figures 6.3 and 6.2 show the good agreement between computed and analytical solutions.

6.1.3 Space and time accuracy

The order of the spatial accuracy of the model is investigated through the above analytical solutions (for the temporal accuracy and following the Taylor hypothesis on frozen turbulence, we used the same Eqs. (6.1) and (6.2) in which x is replaced by t). One can determine the observed order of spatial accuracy on the space increment by calculating (see Michler et al. [88]),

$$p(\Phi) = \log \left(\frac{\|\Phi^n - \Phi^{n+1}\|_2}{\|\Phi^{n+1} - \Phi^{n+2}\|_2} \right) / \log(2) \quad (6.3)$$

where $p(\Phi)$ denotes the observed order of spatial accuracy for the computed turbulence variable $\Phi = (k, \varepsilon)$ on different mesh sizes (denotes by $n, n+1, n+2$), and the differences are measured in the L_2 -norm. The computations were performed on different sequences of mesh sizes (to determine the spatial order accuracy) and on different time-step sizes (to determine the temporal accuracy). The error between the exact solution Φ_e and numerical solutions $\Phi = (k, \varepsilon)$ is calculated using a high order Gaussian quadrature formula to compute the following L_2 norm,

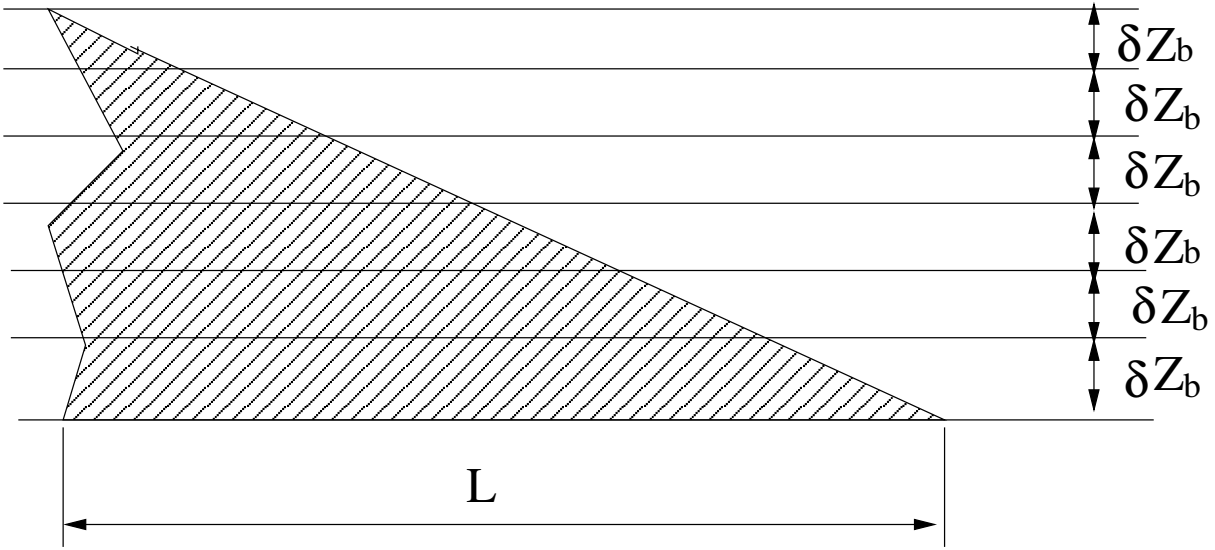


Figure 6.1: Subdivision of channel bed between several layers of thickness δz_b

$$\|e\| = \|\Phi_e - \Phi\| = \left[\int_{\hat{\Omega}} |\Phi_e - \Phi|^2 d\hat{\Omega} \right]^{\frac{1}{2}} \quad (6.4)$$

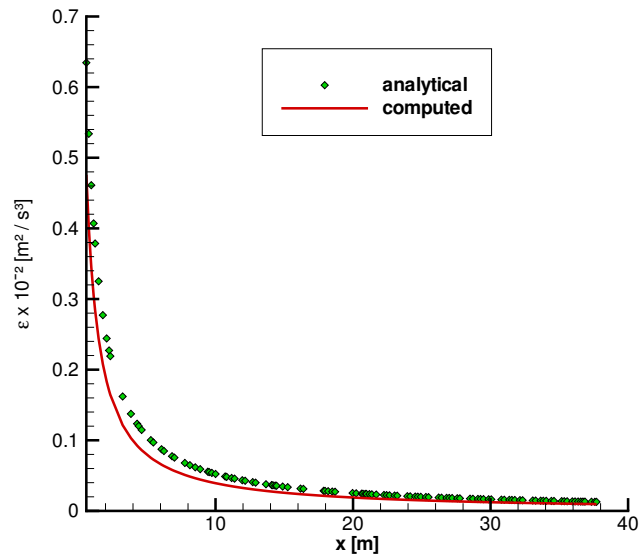
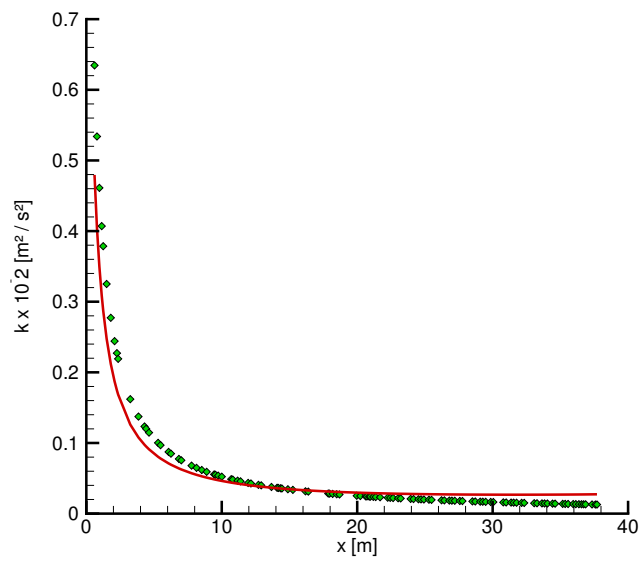
Table 6.1 shows the observed order of spatial accuracy, where C_A represents the ratio between the maximum and minimum diameters of the circumscribed triangles (d_{max}^T, d_{min}^T) of the $2D$ -horizontal unstructured mesh. During computations, the coarse $2D$ unstructured mesh (for $n = 0$ in table 6.1) has 300 elements and 117 nodes, while the finest mesh (for $n = 7$ in table 6.1) has 5044 elements and 2733 nodes.

Figure 6.5 shows the expected spatial accuracy behavior, i.e., second-order space accuracy. This figure indicates a convergence of the scheme for k and ϵ . It is observed that ϵ equation behaves better, while for a specific error tolerance, both solutions do not depend on the mesh size.

Table 6.2 shows the observed order of temporal accuracy, where C_T is a constant. The time characteristic-Galerkin for the turbulence model uses first order explicit backward Euler scheme to preserve the monotonicity of the scheme. The time discretization is expected therefore to be first-order accurate. Consequently the coupled system can be at most first order time accurate as confirmed in figure 6.4, in which we use the finest mesh corresponding to the last line of table 6.1.

6.2 Constant density flows: numerical results

Some numerical tests of various complexity have been conducted with the aim of outlining the good properties of the model. It is worthwhile to mention that several layers of thickness δz_b have been used at the bed (see figure 6.1) to resolve the boundary layer effects at the bottom.

Figure 6.2: Computed ϵ versus analytical solutionFigure 6.3: Computed k versus analytical solution

n	$C_A = \frac{d_{max}^T}{d_{min}^T}$	$k [m^2/s^2]$	$\epsilon [m^2/s^3]$	$p(k)$	$p(\epsilon)$
0	0.90537	0.09444869	0.0005053	1.7523201	1.1594802
1	0.45084	0.06473693	0.0007306	1.5348852	1.6964046
2	0.22551	0.04930999	0.0012773	1.8440260	1.8364252
3	0.11437	0.02277905	0.0027249	1.9016979	1.7976704
4	0.05586	0.01535665	0.0030808	1.9556649	1.9763579
5	0.02833	0.00823566	0.0033009	1.9997129	1.9980793
6	0.01406	0.00649211	0.0033198	2.0018692	2.0930549
7	0.00713	0.00648377	0.0033198	2.0018511	2.0919611

Table 6.1: Spatial order accuracy

n ($\Delta t = \sqrt{C_T}$ [s])	C_T	$k [m^2/s^2]$	$\epsilon [m^2/s^3]$	$p(k)$	$p(\epsilon)$
0	0.2	0.0098023	0.0004865	0.460602294	0.470819844
1	0.15	0.0018911	0.0012081	0.965543241	0.976251193
2	0.1	0.0257790	0.0021249	0.976235828	0.996778353
3	0.08	0.0394728	0.0029808	0.996763275	1.032926204
4	0.06	0.0583956	0.0031808	1.011424351	1.033425036
5	0.05	0.0643692	0.0033198	1.073921159	1.054290358
6	0.02	0.0647604	0.0033585	1.073049571	1.068591611
7	0.01	0.0648377	0.0033874	1.079972414	1.079981914

Table 6.2: Temporal order accuracy

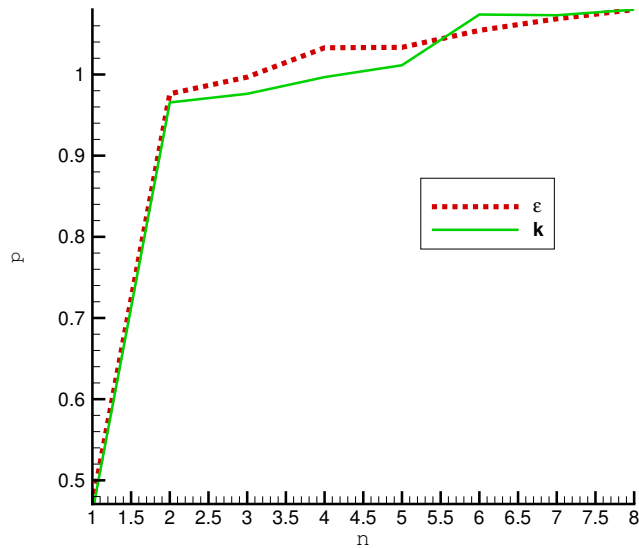


Figure 6.4: Observed order p of temporal accuracy versus different mesh sizes

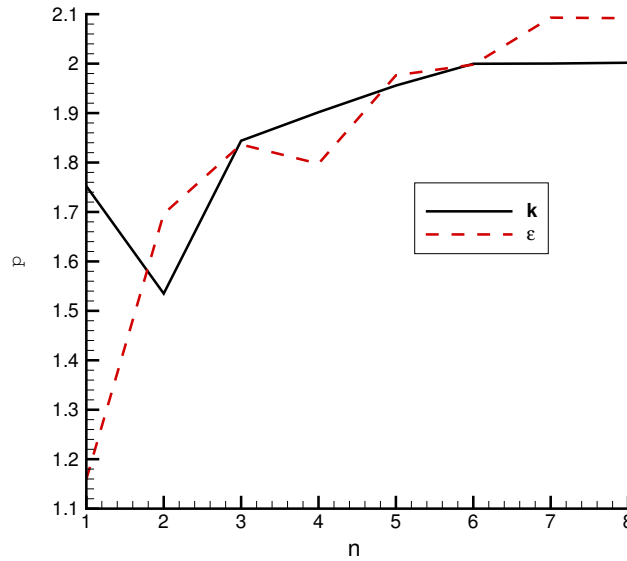


Figure 6.5: Observed order of spatial accuracy p versus different time step sizes

6.2.1 Finite element solver with hydrostatic pressure and $k - \epsilon$ turbulence model

This section deals with the numerical computations using the 3D model introduced in section (3.4.2), which is used for simulating the constant density fluid flow under the hydrostatic assumption. Note that the height of the free surface at the outflow section is prescribed.

Test I: Quasi-uniform flow

The channel layout and dimension is shown in figure 6.6-A. The discharge is set to $Q = 0.25[m^3/s]$, the bed slope $S_0 = 0.000624$. The rough bed is characterized by an equivalent roughness height, $k_s = 0.0042[m]$. The flow depth at the outflow (downstream end of the flume) is $0.183[m]$. The experimental data are available for the flow case (see Istiarto [54]). The horizontal grid is composed of 5044 elements and 2733 nodes, and the vertical is divided into 50 layers. The bottom is divided into fifteen lowermost layers of equal thickness $\delta z_b = 0.002[m]$ (see figure 6.1). The time step is set to $0.1 [s]$, and the computation is performed till a steady state is reached. The model produces the logarithmic velocity distribution as expected for uniform flows. Figure 6.6-B shows the water surface. Figure 6.7 shows the steady state distributions of the velocities at selected sections and compares the computed and measured distributions of the velocity, the eddy viscosity, and the shear stress at half reach of the channel, $x = 19.040[m]$. The water surface shows a decreasing flow depth in the first 8-meter reach. Further downstream the flow depth gradually increases towards the specified depth of $h = 0.183[m]$ at the outlet boundary. Within the downstream half channel-reach, $x \geq 20[m]$, a nearly uniform flow-depth is observed, showing less than $1 [mm]$ difference between the two ends of this channel reach. The computed eddy viscosity profile compares favorably with the experimental one as shown in figure 6.7. The eddy viscosity goes to zero near the free-surface, increases with the depth and presents a maximum around the mid-depth, and then, decreases towards zero near the bed. The

shear stress profile is linearly distributed with the depth, from zero at free surface to maximum near the bed. The computed solutions agree quite well with the experiments.

Test II: Unsteady open-channel flow

The channel layout and dimensions are shown in figure 6.8 as well the specified triangular hydrograph for the discharge. The channel is 18[m] long, the width is $B = 0.60[m]$. The rough bed has an equivalent roughness height, $k_s = 0.0058[m]$. The flow depth at the outflow (downstream end of the flume) is 0.13[m]. The experimental data (velocities, water depth, shear stress and eddy coefficient) are available for the flow case (see [110]). The grid is composed of 3216 elements and 1802 nodes and the vertical is divided into 30 layers and the time step is $\Delta t = 0.1[s]$. The bottom is divided into fifteen lowermost layers of equal thickness $\delta z_b = 0.002[m]$ (see figure 6.1).

Figure 6.9 shows at two stations $x = 10.78[m]$ and $x = 14.08[m]$, the comparison between computed solution and measured time variation of flow depths. The model produces the surface undulation as expected for the non-uniform flow.

Figure 6.10 shows the comparison between computed and measured distributions of the velocity, the eddy viscosity, and the shear stress at two stations $x = 10.78[m]$ and $x = 14.08[m]$ at time $T=350[s]$. The computed velocity distribution and eddy viscosity profile compare favorably with the experiments. The eddy viscosity goes to zero near the free-surface, increases with the depth with a maximum around the mid-depth, and decreases towards zero near the bed. The shear stress profile is linearly distributed with the depth and from zero at the free surface goes to maximum near the bed. Figure 6.11 shows good agreement between computed and measured kinetic energy and its rate of dissipation at the selected sections. A good agreement is found between the computed and measured flow fields.

6.2.2 Non-hydrostatic Pressure and $k - \varepsilon$ Turbulence model

Several numerical models using the hydrostatic pressure have been successfully applied to the free surface flows modeling in most of geophysical flows. However in the presence of complex flows with complicated bathymetry (such as the natural rivers), it is useful to resort to a more accurate model in which the hydrostatic assumption is removed.

In this subsection we present the numerical results obtained for the case of unsteady non-uniform flows. The 3D model introduced in section (3.5) is used for simulating the constant density fluid. Computations with and without hydrostatic pressure are compared for the same trench to test the validity of the conventional pressure assumption.

Numerical results

To check the validity of the developed model, the computations were carried out against well-known flows with the increasing complexity, using a high quality and high spatial resolution data set. In the spatial discretization, the lowest layer thickness δz_b (see figure 6.1) is chosen such that, the adjacent grid point (first vertical grid point) should lie within the rough turbulent boundary layer, i.e. $30\nu/u_* < \delta_n = \delta z_b/2 < 100\nu/u_*$. In the wall region, the shear stress can be assumed constant, $u_* \approx 0.1U$, where U is a flow mean velocity (see [40]), δ_n is a normal vertical distance of the first vertical mesh point from the bottom.

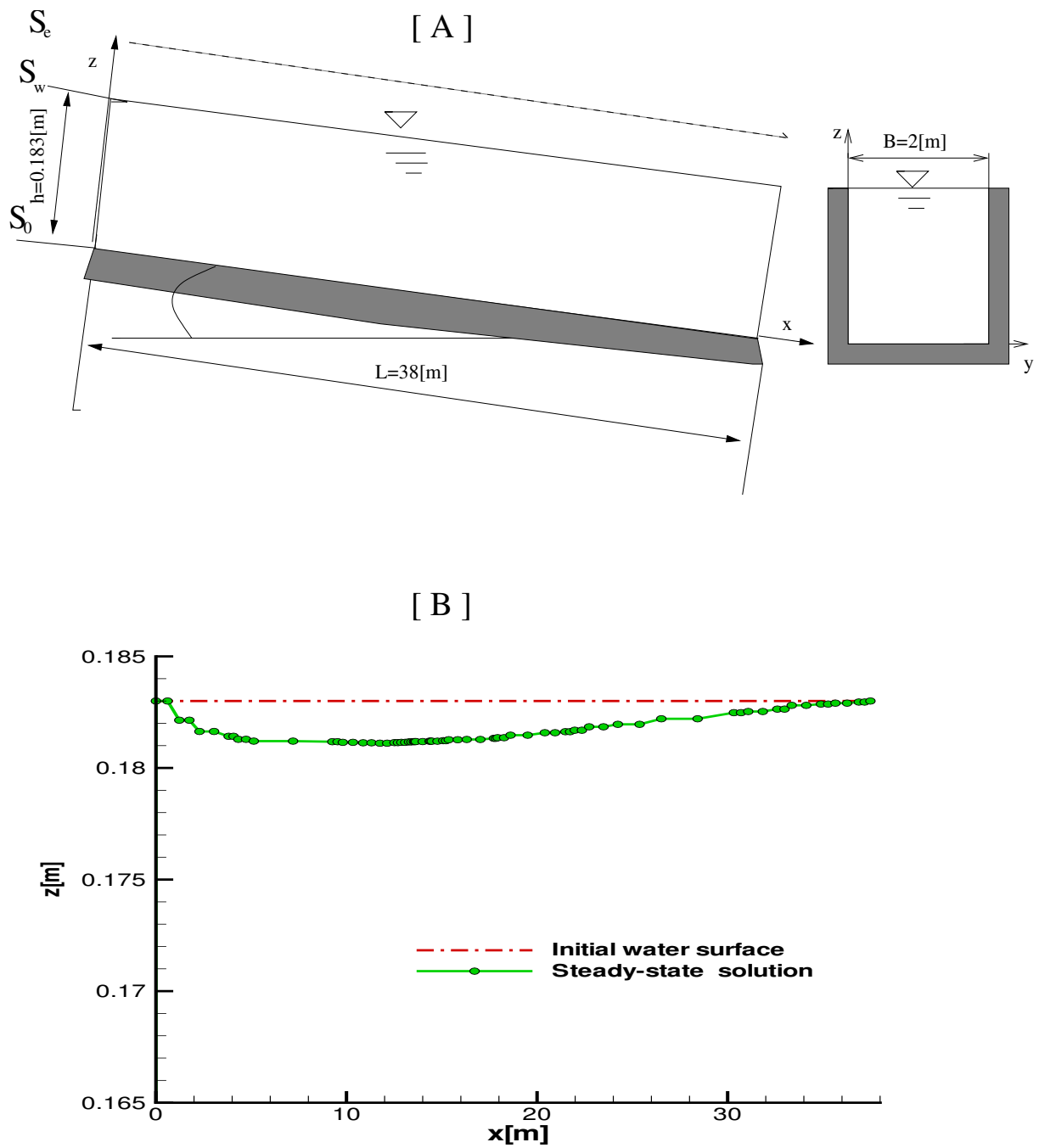


Figure 6.6: Test I: A) Sketch of the experimental installation; B) Steady state and initial water surface

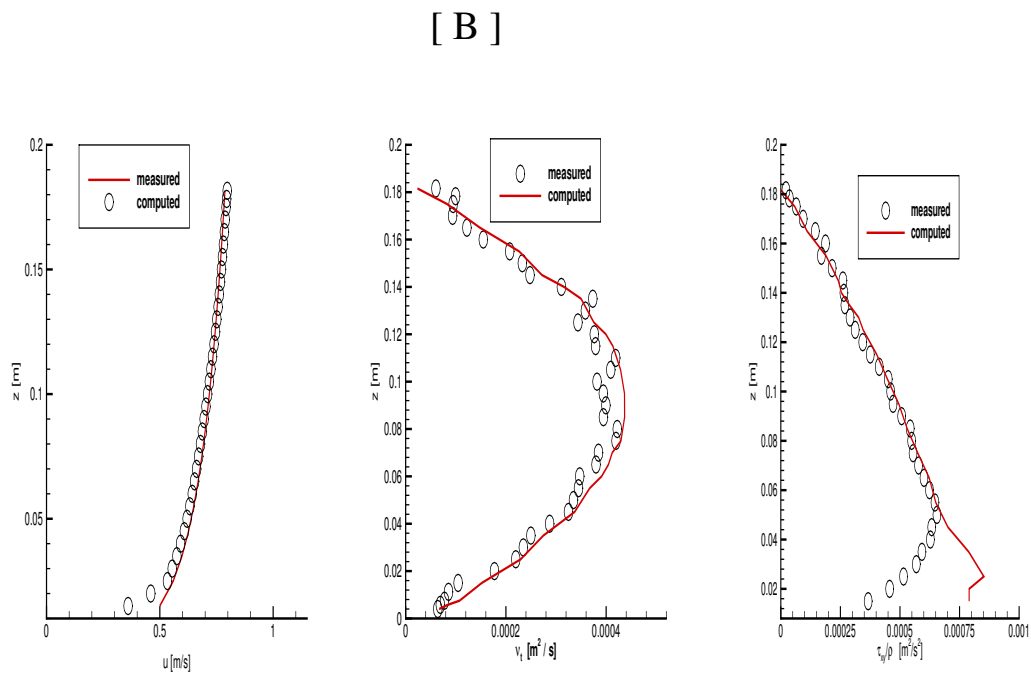
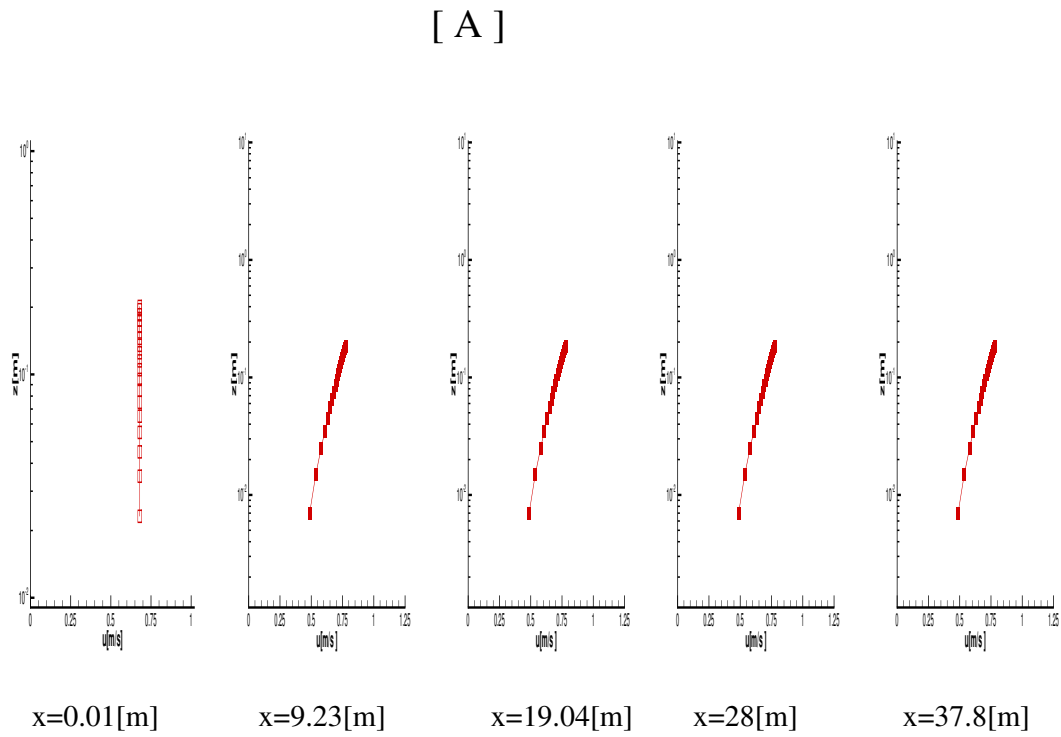


Figure 6.7: Test I: Computations versus experiments at the selected sections: A) linear distribution of the velocity; B) profiles of the velocity, eddy viscosity and shear stress

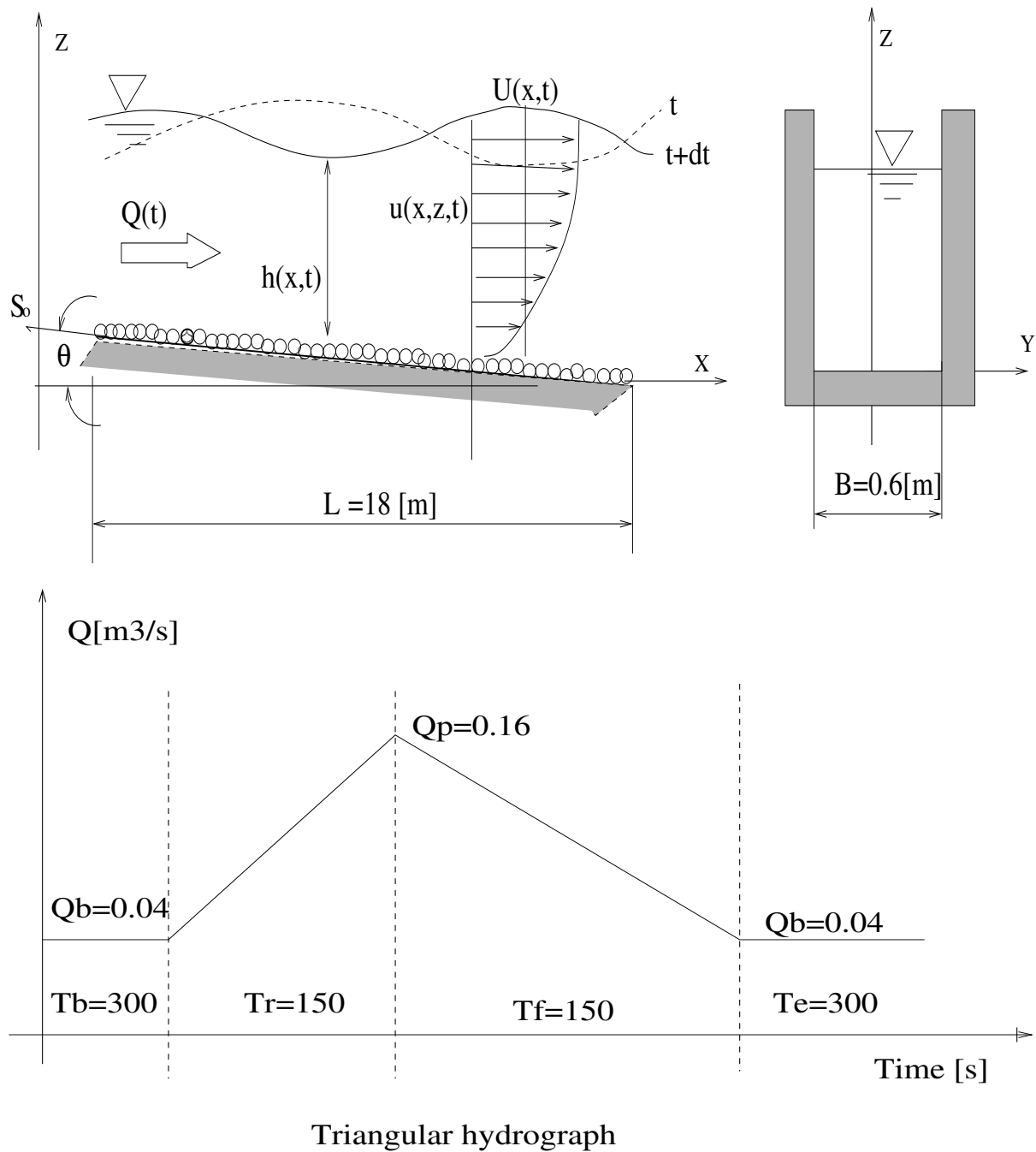


Figure 6.8: Test II: Sketch of the experimental installation and the corresponding triangular hydrograph

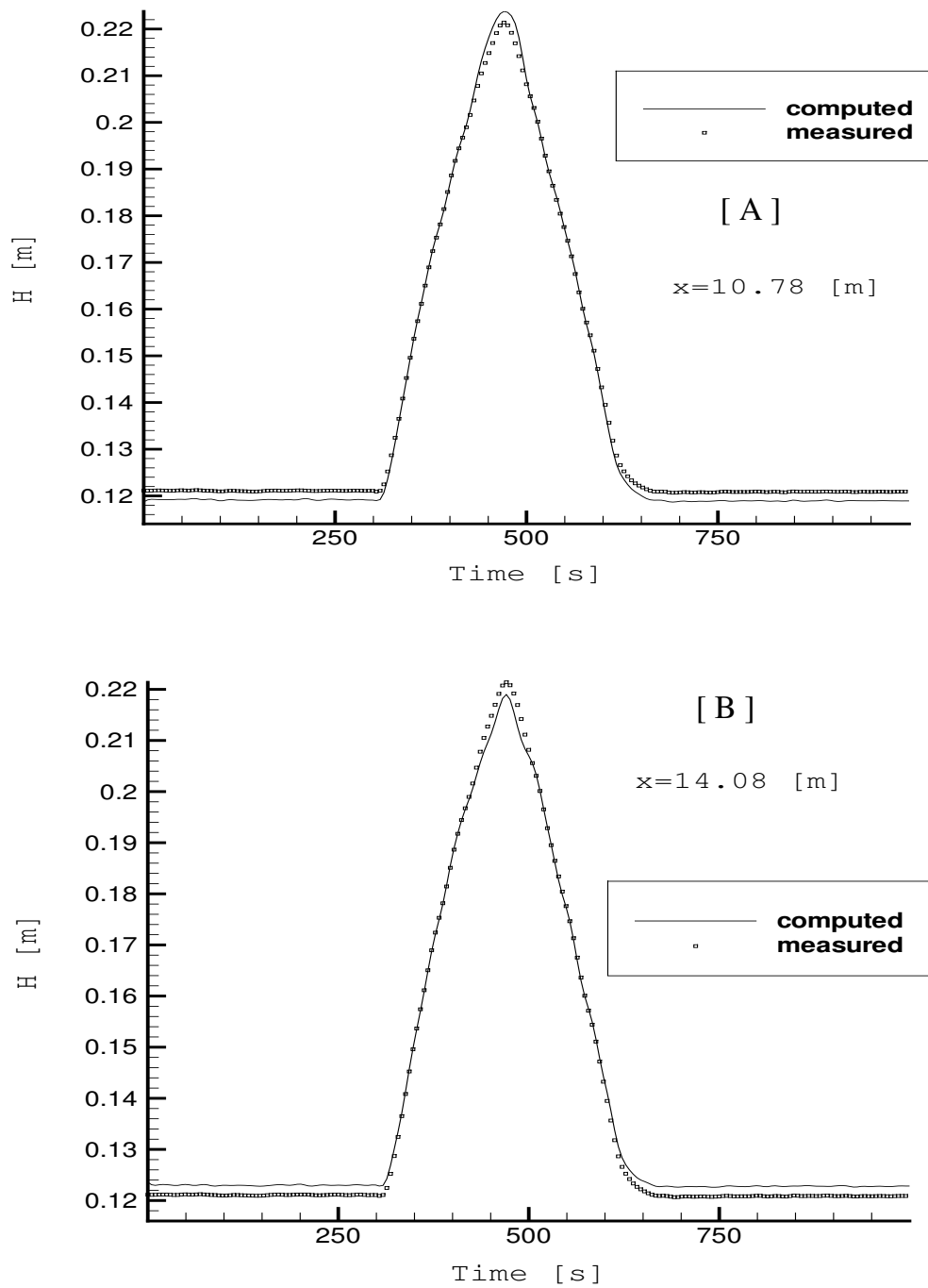


Figure 6.9: Test II: Comparison between computed and measured time variation of depth at the selected sections : A) $x=10.78$ [m] ; B) $x=14.08$ [m]

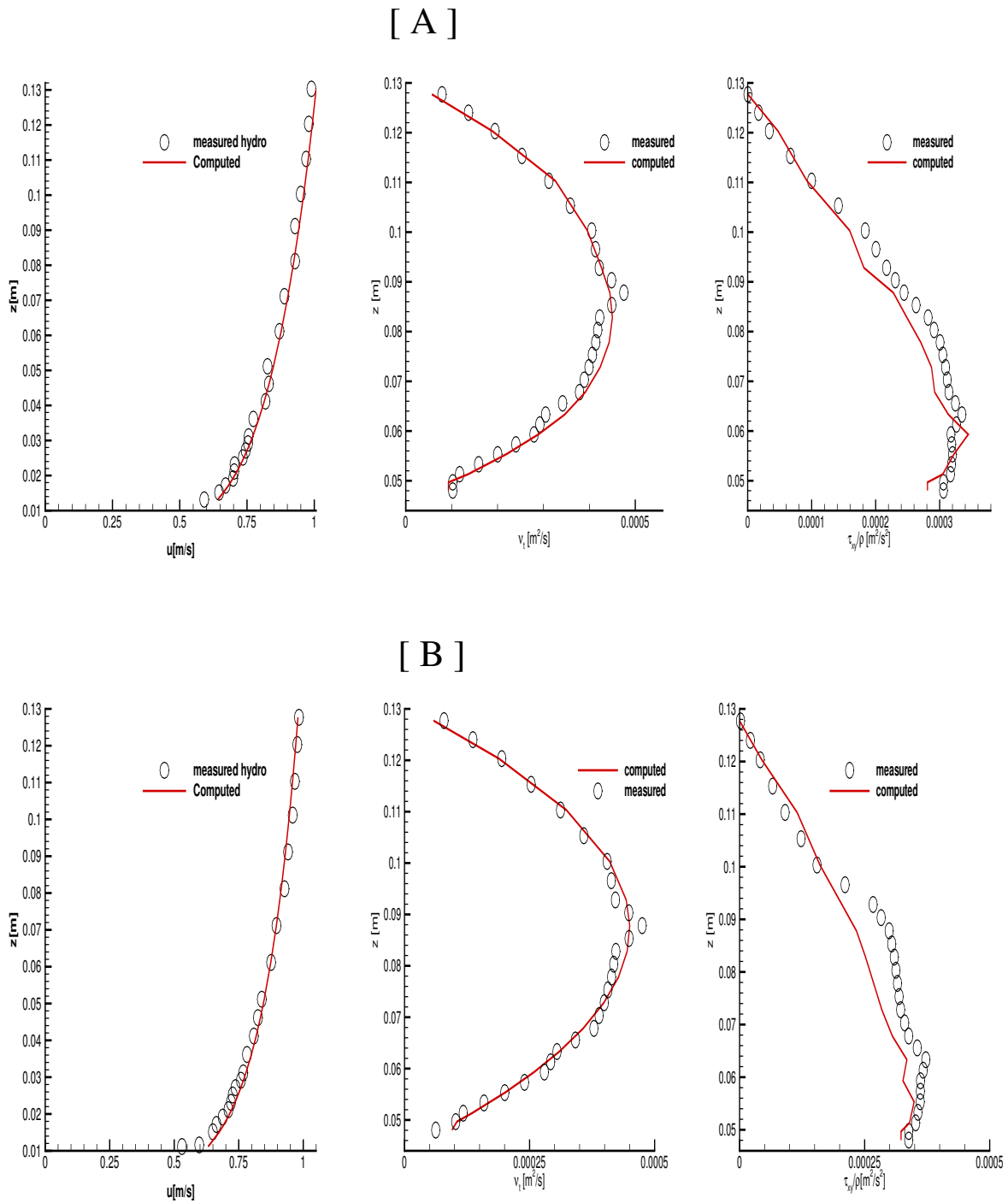


Figure 6.10: Test II: Computations versus experiments at time $T=350$ [s]: A) $x=10.78$ [m]; B) $x=14.08$ [m]

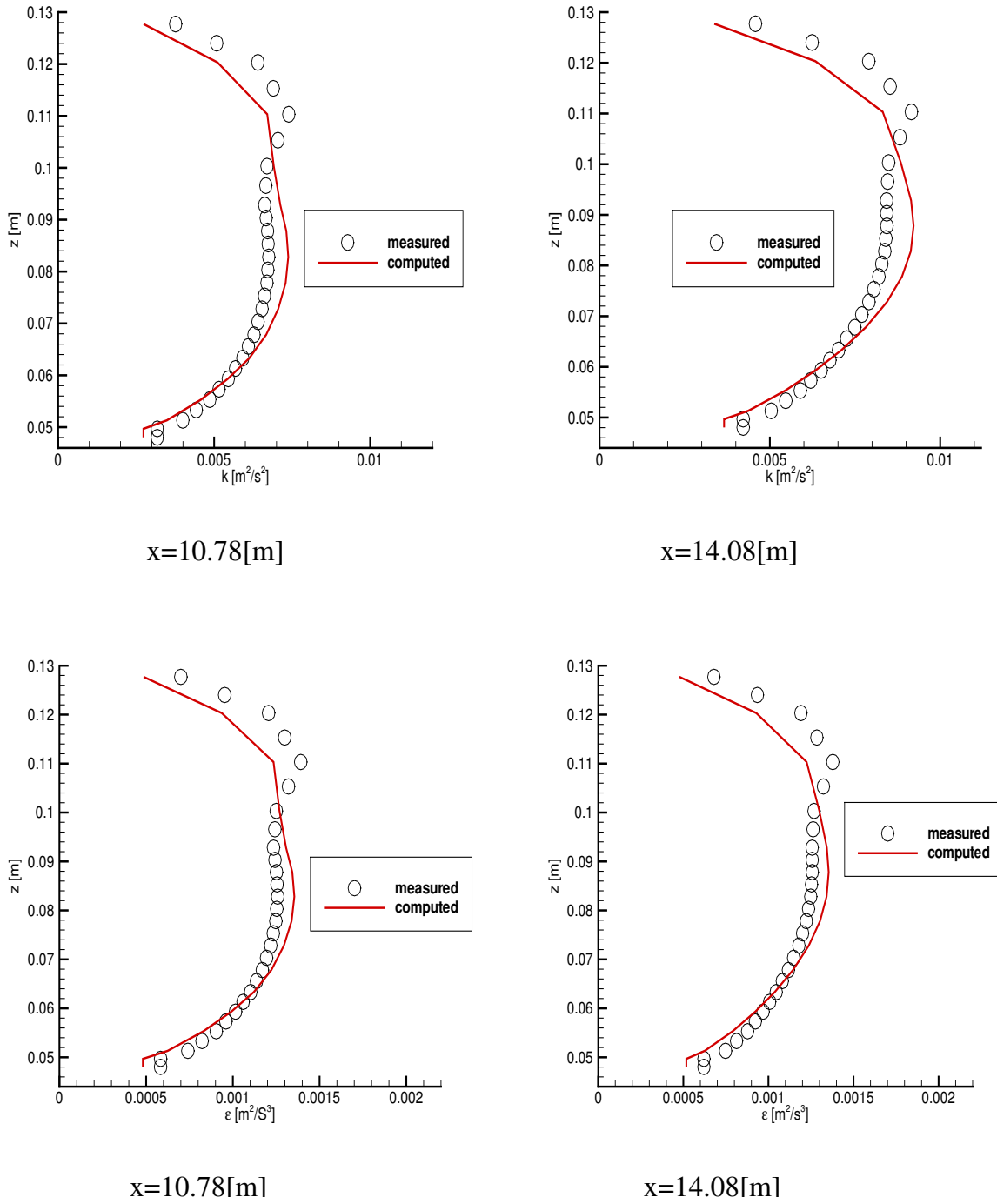


Figure 6.11: Test II: Computed k and ϵ versus experiments at the selected sections

Test III: Unsteady and non-uniform open-channel flow

The channel layout and dimensions as well as the given discharge hydrograph are shown in figure 6.8. The channel is 18[m] long, the width is $B = 0.60[m]$. The rough bed has an equivalent roughness height, $k_s = 0.0058[m]$. The flow depth at the outflow (downstream end of the flume) is 0.13[m]. The experimental data are available for the flow case (see [110]). The 2D horizontal unstructured mesh is composed of 30000 elements and 18000 nodes. The mean diameter of the circumscribe is about $d^T = 0.08[m]$ and the time step is set to $\Delta t = 0.1[s]$. Computations were conducted using 30 layers in the vertical direction, with several layers of thickness $\delta z_b = 0.002[m]$ at the bottom.

Error between modeled depth and Experiments

Error estimation is conducted between the computed flow depth (H_c) and experiments (H) at the selected sections $x = 10.78[m]$ and $x = 14.08[m]$, using the following expression

$$Error(H(t)) = (H(t) - H_c(t)) \quad (6.5)$$

Figure 6.12 shows the error between computations and flow depth values and experiments at time $T = 350[s]$. The error is found to be less than 0.0006[m], which confirms the good accuracy of the numerical model.

computations versus experiments

Figure 6.13 shows the comparison between computed and measured distributions of the velocity, eddy viscosity, and shear stress at two stations $x = 10.78[m]$ and $x = 14.08[m]$ using both the hydrostatic and non-hydrostatic pressure in order to test the validity of conventional hydrostatic pressure assumption.

The computed velocity, eddy viscosity and shear stress profiles of the well developed flow at $T = 700[s]$ compare favorably with the experiments. The eddy viscosity goes to zero near the free-surface, increases with the depth with a maximum around the mid-depth and decreases towards zero near the bed. Satisfactory results have been produced with and without non-hydrostatic pressure. Computations agree well with experiments for the kinetic energy, its rate of dissipation and shear stress at the selected sections. However, as shown in figure 6.14 the non-hydrostatic pressure solution produces little improvement for this problem. In such a problem, the additional computational expense may be kept to minimum by using hydrostatic pressure. The non-hydrostatic pressure is more computationally expensive method, and must be used (full 3D) where these considerations are particularly significant.

Test IV: Sharp and curved open channel: discussions

The channel layout and dimensions are shown in figure 6.15. The discharge is set to $Q = 0.089[m^3/s]$, the bed slope $S_0 = 0.000624$. The rough bed is characterized by an equivalent roughness height, $k_s = 0.0022[m]$. The flow depth at the outflow (downstream end of the flume) is 0.159[m]. The experimental data are available for the flow case (see Blanckaert [5]). The grid is composed of 50000 elements and 30000 nodes on the xy plane. Figure 6.16 shows the horizontal unstructured mesh with mean grid size of about $d^T = 0.05[m]$, while the time step size is set to $\Delta t = 0.1 [s]$. Computation is performed until the flow is well developed at $T=1300 [s]$, using 60 layers, with several layers of thickness $\delta z_b = 0.002[m]$ at the bottom (see figure 6.1). Here V_n and V_s represent respectively the span wise and longitudinal velocity components

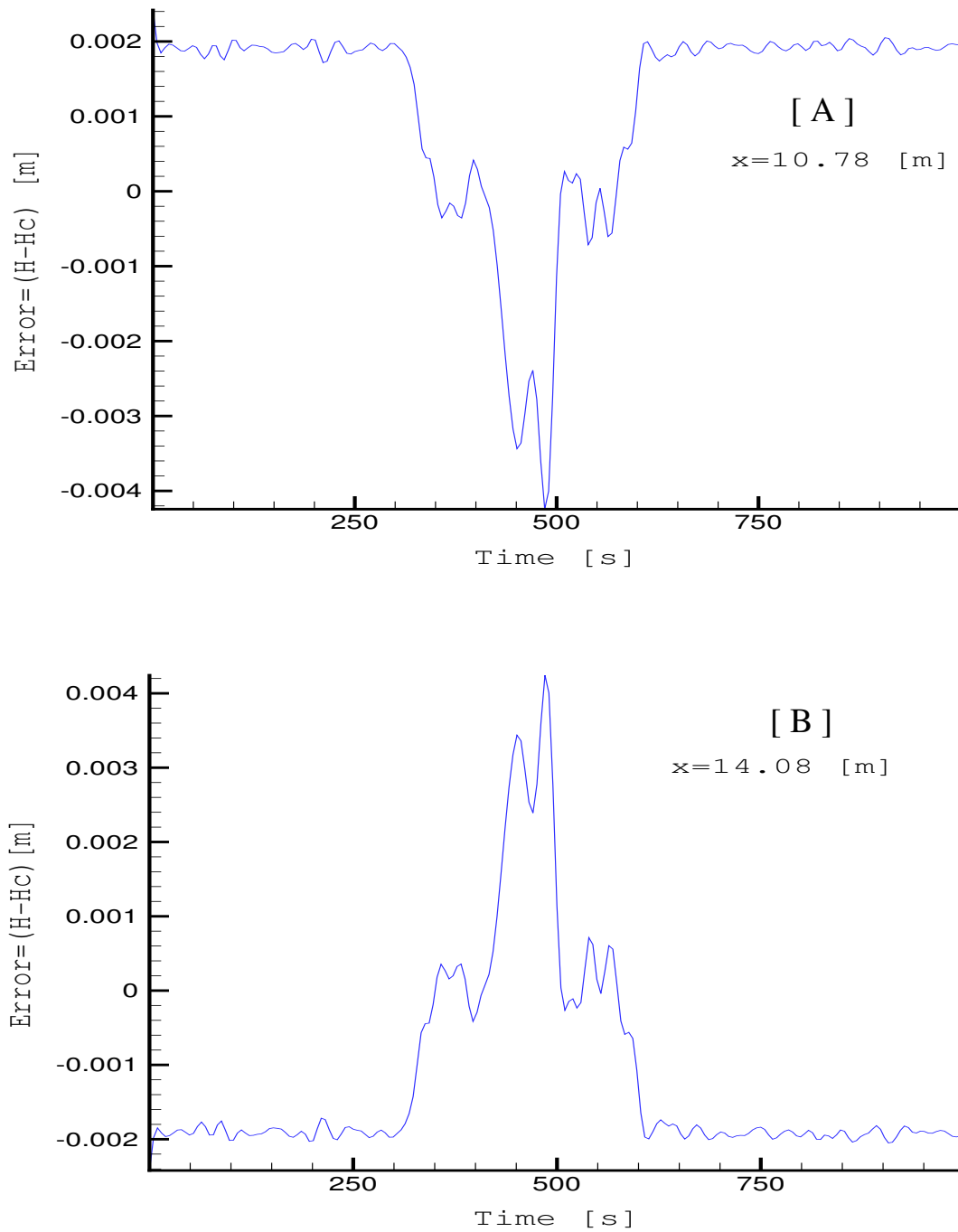


Figure 6.12: Test III: Error with time between computed flow depth and experiments at the selected sections

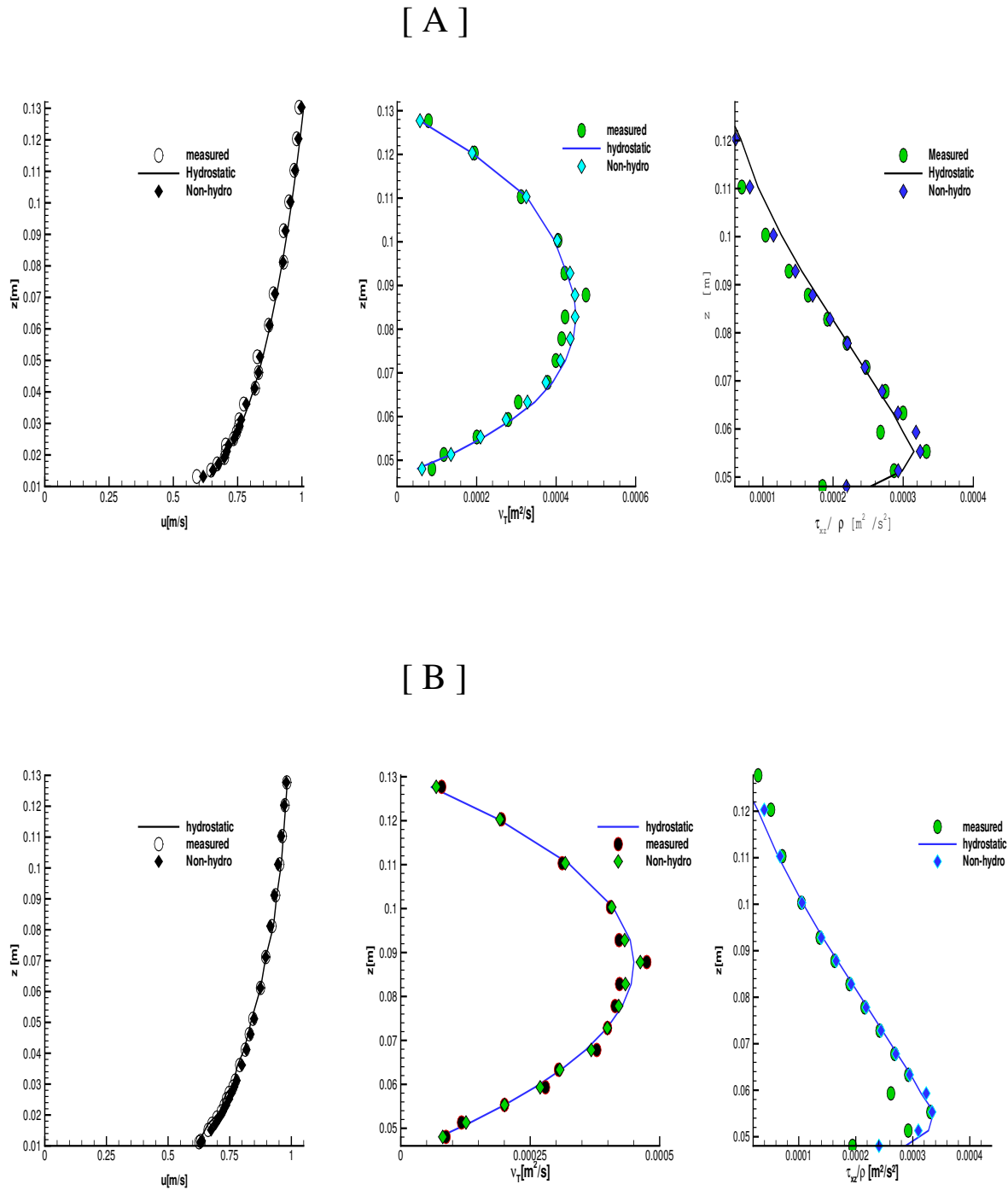
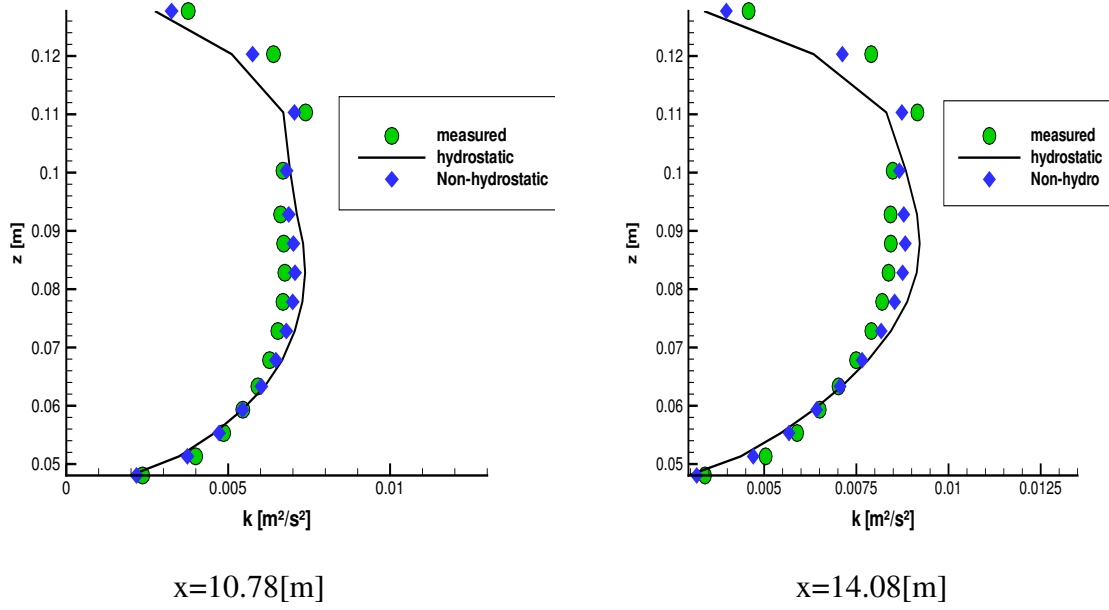


Figure 6.13: Test III: Comparison at time $T=700[s]$ between hydrostatic solution (-), Non hydrostatic solution (\diamond) and experiments (\circ) at the sections : A) $x=10.78 [m]$; B) $x=14.08 [m]$

[A]



[B]

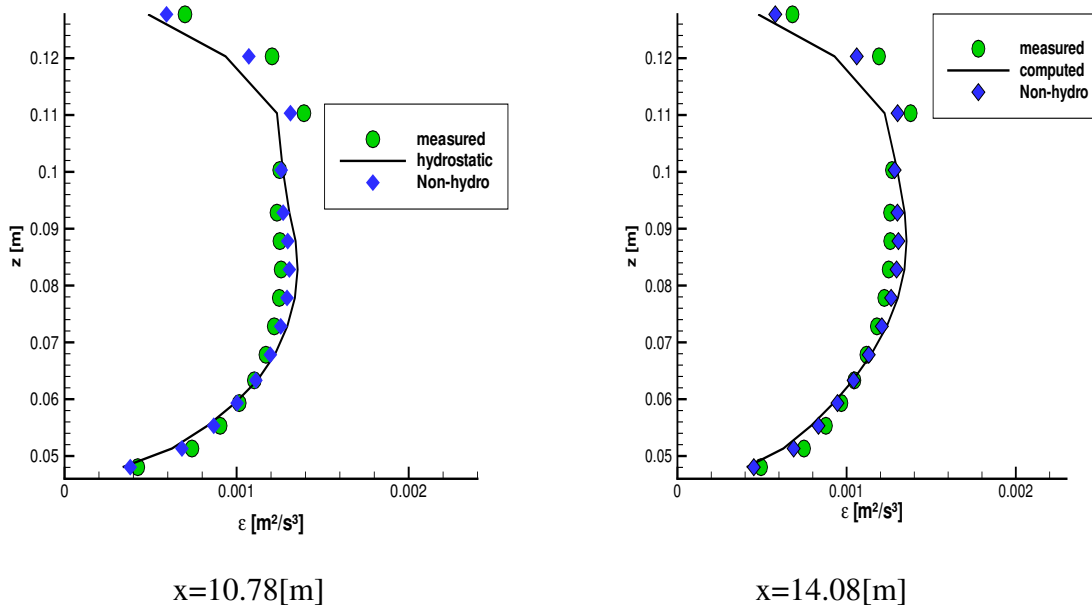


Figure 6.14: Test III: Non-hydrostatic and hydrostatic solutions versus experiments at the selected sections: A) kinetic energy; B) the rate of dissipation

(see figure 6.15). Computations were conducted with the hydrostatic pressure assumption for different cross-sections with the increasing curvature, to determine the conditions where the non-hydrostatic pressure component becomes significant.

Computations predict the bulk flow features, while the water surface profile is under-estimated at the outer bank, and over-estimated at the inner bank.

Figure 6.17 shows the results in the cross-section at $\alpha = 120^\circ$, where H_0 denotes the average water depth. The conventional hydrostatic pressure is found to perform poorly, while non-hydrostatic pressure solution behaves well with the increasing curvature. This might be resulting from the incorporation of the free-surface movement rather than rigid-lid approximation. This suggests that, in curved channel flows, the pressure-driven secondary effects are important and the computation of free surface must be more improved to account of the damping effects of free surface.

In figures 6.18 and 6.19, both hydrostatic and non-hydrostatic solutions show only one secondary flow circulation rotating clockwise from inner bank to outer bank, i.e. the weak secondary currents are not predicted. The maximum under prediction in the secondary current for each vertical examined in this cross-section is in between 25 and 95% for non-hydrostatic solution, while the hydrostatic one is in between 30 and 105%. According to some analysis (see also Ye and McCorquodale [162], Wilson et al. [154]), these results suggest that this model can be considered to perform well compared to other models. Figure 6.19 shows the center of vortex position, that is located at about $z = 0.25[m]$ for the hydrostatic solution, $z = 0.35[m]$ for the non-hydrostatic solution while experiments is located at $z = 0.4[m]$.

Figure 6.20 shows the cross-wise longitudinal velocity component at the section $\alpha = 120^\circ$, and the hydrostatic solution is over predicted, while the non-hydrostatic solution is closer to the experiments. The computed maximum primary velocity is offset towards the channel center relative to the outside of the bend, leading to the under prediction in secondary currents strength. This suggests that the turbulence-driven secondary effects are non-linear. The anisotropic stress caused by walls and the junction region is not captured by the model. This could rely on the reduced momentum transfers towards the outer region of the bend with the consequence on the position of the maximum longitudinal velocity. Consequently, as shown by Gatski et al. [39], the related weaker turbulence-driven secondary motion cannot be reproduced by linear and isotropic eddy-viscosity turbulence models. However the major flow features such as the presence and rotational sense of the major secondary currents are reproduced and agree well with experiments. Moreover the non-hydrostatic pressure influence is found to be more significant with the increasing curvature region. Therefore, although being more expensive, it becomes useful for such flows where its influence is thought to be significant. This suggests that the pressure-driven secondary currents are relatively important in the accurate description of the velocity field, and the anisotropic turbulence models being useful for improving the flow field prediction.

6.2.3 Concluding remark

In the present subsection the validation of the 3D finite element solver for the Reynolds-averaged Navier-Stokes equations with the state-of-art $k - \varepsilon$ turbulence closure is successfully conducted. The tests were performed in order to validate the model against well-known flows with the increasing complexity, using a high quality and high spatial resolution data set. Computations with hydrostatic and non-hydrostatic pressure are compared for the same trench to test the validity of the conventional hydrostatic pressure assumption. For the curved open channel, as expected, the model does not reproduce the weaker secondary current in the straight part

of the channel. The non-hydrostatic pressure influence is found to be more significant with the increasing curvature region, and this suggests that the non-hydrostatic pressure (which is the computationally expensive part of the scheme) may be useful and well suited when a 3D description of flow field is needed or where its influence is thought to be significant. The model predicts reasonably the complex major features and their consequences on the 3D flows. However, further study is needed to improve the general applicability of the model. The following subsection will be focused on the non-uniform anisotropic turbulence-driven secondary motion.

6.3 3D model with non-hydrostatic pressure and modified $k - \varepsilon$ model

In this subsection, we are dealing with the presence of complex flows (short waves and/or strong bathymetry) where the full 3D description of the velocity field is required. In such a problem the non-hydrostatic pressure as well as the anisotropic features of the turbulence closure are required. The modeling water flow system with curved or meandering open channel is a subject of significant importance in large number of hydraulic and environmental flows, and the physical phenomena characterizing such flows is important for environmental hydraulic engineering. In such complex flows, the main flow while passing bend ways generates secondary currents and superelevation of the water surface due to the centrifugal forces and the gravity force. These secondary flows play an important role on the channel flow and for environmental study. Numerical models using the standard linear $k - \varepsilon$ turbulence with isotropic eddy viscosity appear to be deficient in predicting moderately and strongly complex turbulent curved flows. The 3D model introduced in section (3.5) is used for simulating the constant density fluid and the model is applied for simulating a 193° curved open channel.

Turbulence modeling

The turbulent eddy coefficients in the governing equations are determined by the turbulence modeling. For many situations, due to its relative simplicity, the $k - \varepsilon$ turbulence model is widely used with reasonable accuracy. Cokljat and Younis [22], showed that the standard $k - \varepsilon$ model based on an isotropic eddy viscosity assumption appears to be deficient in predicting flow of complex turbulent shear layers such as the common hydraulics flows with significant streamline curvature and free surface. In the present study we assume that, the streamline curvature mainly affects the horizontal plane and the vertical direction is mostly influenced by the free surface damping effects. According to experiments analysis [6], effects of the center-region cell in moderately to strongly curved flow can only be modeled if one takes due account of the deformation of downstream velocity profiles and the feedback between the downstream velocity and the center-region cell. To account for the anisotropic effects of the turbulence structure, the present study introduces new terms into the linear model formulation of the state-of-the-art $k - \varepsilon$ turbulence model. Hence, algebraic formulations are introduced into the eddy coefficient computed from the previous $k - \varepsilon$ turbulence modeling as follows,

$$\nu_t = c_\mu \frac{k^2}{\varepsilon} \quad ; \quad \nu_v = \zeta_v \nu_t \quad ; \quad \nu_h = \zeta_h \nu_t \quad (6.6)$$

in which ν_t is the isotropic turbulent viscosity calculated from previous $k - \varepsilon$ model in Eqs.(4.18) and (4.19). The streamline curvature effect ζ_h derived by Leschziner and Rodi [69] is expressed as

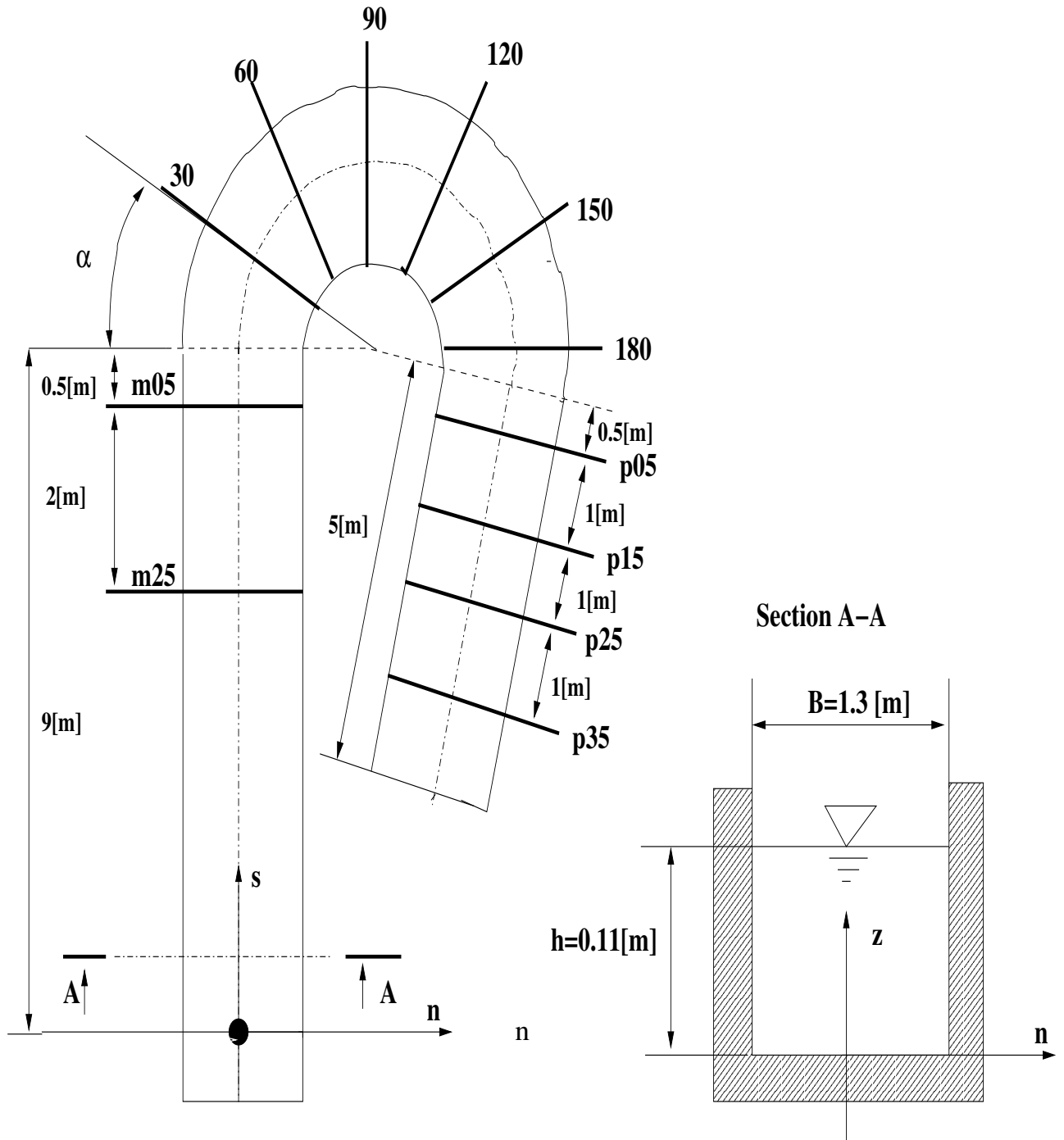


Figure 6.15: Test IV: Sketch of the 193° curved channel experimental installation

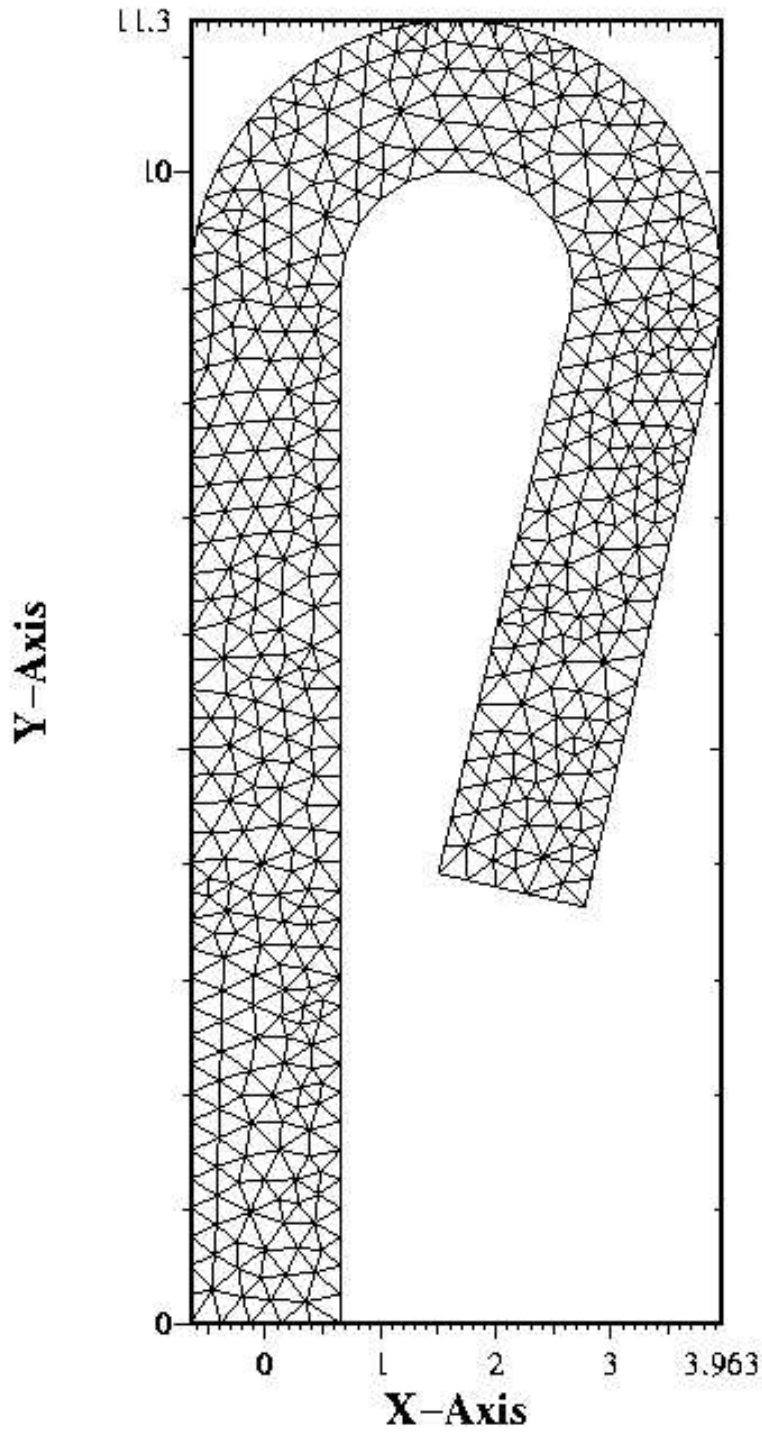


Figure 6.16: Test IV: The 2D unstructured triangular mesh for the 193° curved open-channel

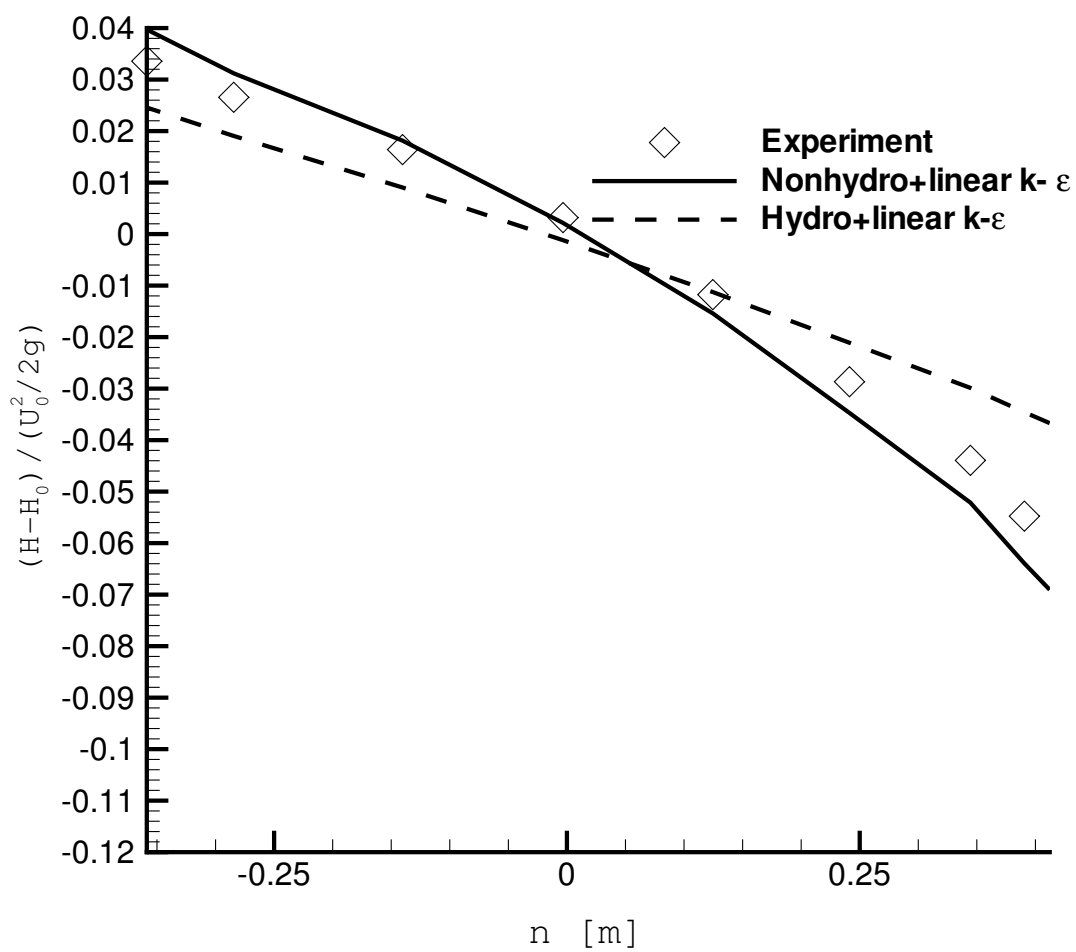


Figure 6.17: Test IV: Experiments versus computed free-surface solutions at section $\alpha = 120^\circ$ using linear $k-\epsilon$ turbulence model : Experiment (\diamond) ; Hydrostatic (dashed line) ; Non-hydrostatic (solid line)

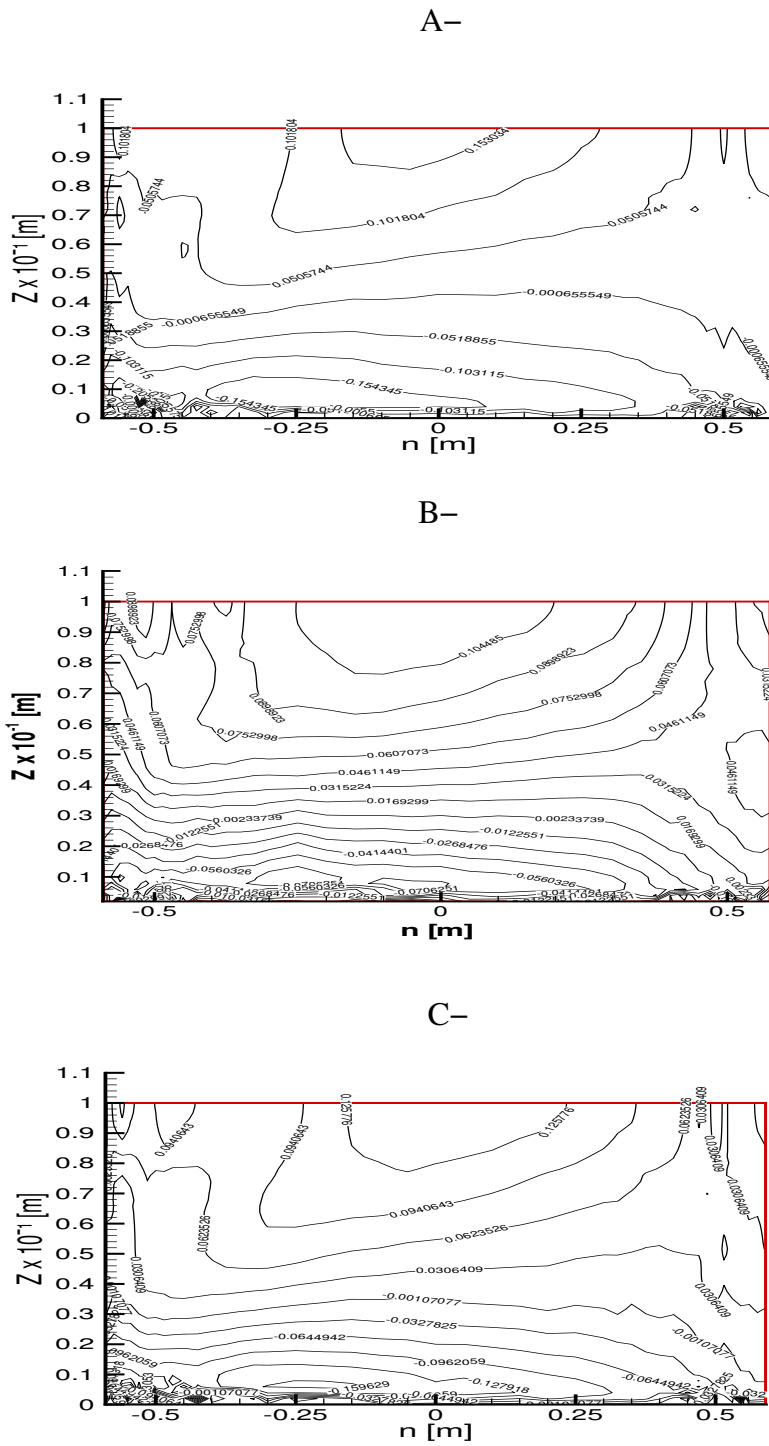


Figure 6.18: Test IV: Experiments versus computed solutions of the transversal velocity component V_n of cross-stream at section $\alpha = 120^\circ$: A) Experiment ; B) Hydrostatic ; C) Non hydrostatic

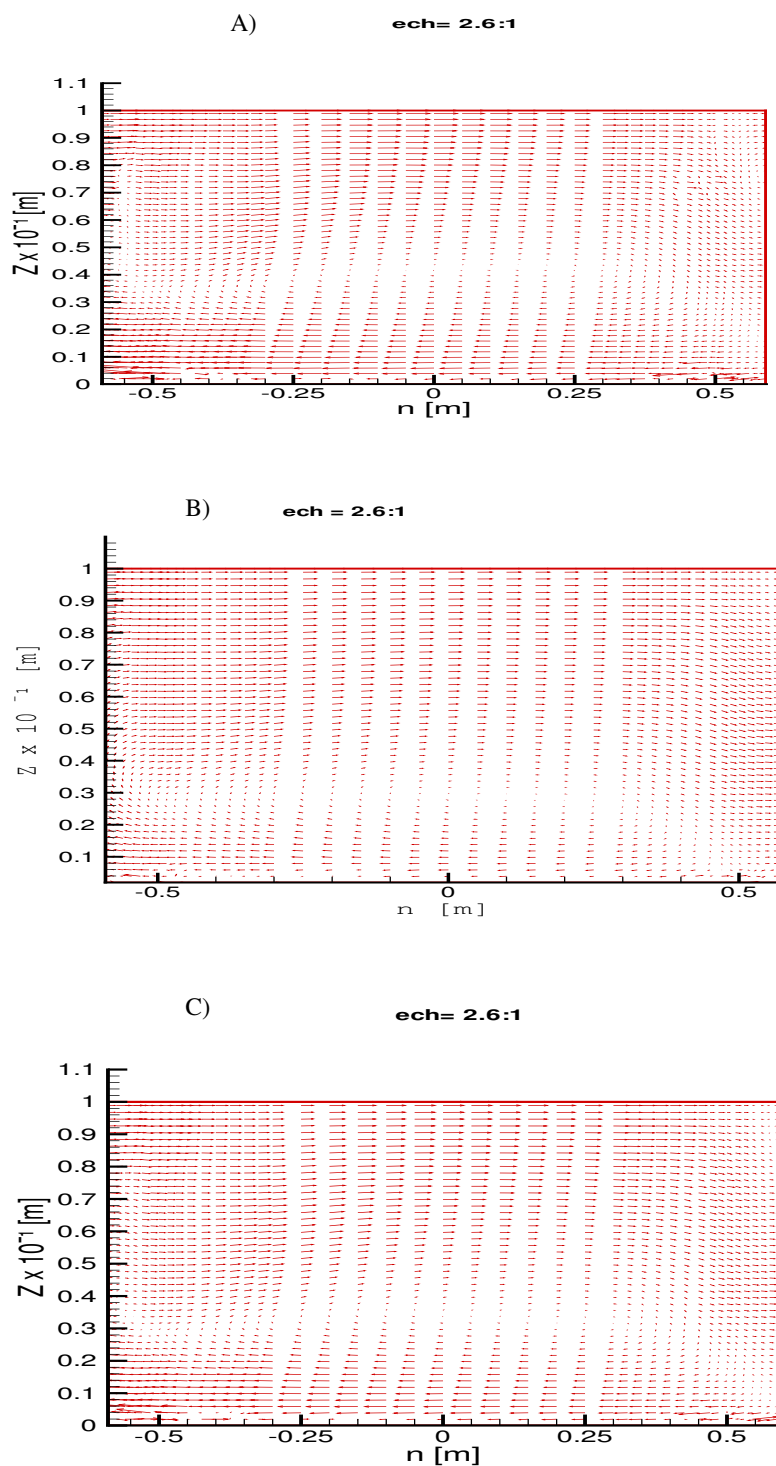


Figure 6.19: Test IV: Experiments versus computed solutions of the of cross-stream velocity V_n vector at section: $\alpha = 120^\circ$: A) Experiment ; B) Hydrostatic ; C) Non hydrostatic

$$\zeta_h = \frac{1}{1 + 0.57 \frac{k^2}{\varepsilon^2} \left(\frac{\partial V_s}{\partial n} + \frac{V_s}{R} \right) \frac{V_s}{R}} \quad (6.7)$$

The influence of the free surface and the bottom, derived by Naot and Rodi [99] is expressed as

$$\zeta_v = \frac{C_v^2}{(C_v + 0.15\alpha_2)(C_v + 0.2\alpha_2)} \quad (6.8)$$

and

$$C_v = 1.5 - 0.5\alpha_1 \quad ; \quad \alpha_1 = \left(\frac{L}{z_1} \right)^2 \quad ; \quad \alpha_2 = \left(\frac{L}{z_2} \right)^2 \quad ; \quad z_1 = \left\langle \frac{1}{z} \right\rangle^{-1/2} \quad (6.9)$$

$$z_2 = \left\langle \frac{1}{(H-z)^2} \right\rangle^{-1/2} + 0.31662L \quad ; \quad L = \left(\frac{C_\mu^{3/4}}{k} \right) \frac{k^{3/2}}{\varepsilon} \quad (6.10)$$

where V_s = downstream velocity component, R = local radius of curvature of streamline, n = normal distance from the wall, L = dissipation length, z_1, z_2 = root-mean-squared reciprocal distances from the solid walls and free surface, respectively.

Test V: simulation of 193° open channel

Numerical results

The channel layout, dimensions, grid and the characteristics of the flow are given in Test IV at the previous subsection [see figures (6.15) and (6.16)]. Figure 6.21 shows good agreement between computations and experiments, in which H is a water depth and, H_0 , denotes the average water depth at the selected cross-sections (m05, $\alpha = 90^\circ$, and p25).

Figures 6.22, 6.23 and 6.24 compare favorably the measured and computed solutions of respectively the cross-stream downstream velocity (V_s) and transversal velocity (V_n) components at the selected sections $\alpha = 90^\circ$, m05, $\alpha = 30^\circ$, $\alpha = 150^\circ$, and p25. In such flow problem, the secondary currents are produced from two sources : those which are generated by the lateral pressure gradient with the embedded background turbulence due to the advective momentum transport by the cross-stream circulation, and those which are bed form induced. The prediction accuracy of the two former sources will be determined from both the free-surface calculation method and the turbulence modeling, whereas the latter source will depend on the roughness refinement and the turbulence representation.

Sotiropoulos and Patel [130], and Wilson et al. [154] advocate that, in case of flow with roughness and cross-sectional uniformity, an anisotropic representation of turbulence is necessary for an accurate description of most three-dimensional turbulent flows.

In this simulation some important features and processes underlying the full 3D computation of such complex flow have been taken into account.

Experimental data analysis has shown (see [5]) the important role of advective momentum transport by the cross-stream circulation in the distribution of downstream velocity and bottom shear stress. The use of Lagrange-Galerkin method for computing the advection terms helps the model to better describe the effect of cross-stream circulation in a dynamical way as well as the vertical structure of the fluid flow.

In this model the isotropic eddy-coefficients from linear $k - \varepsilon$ turbulence model have been modified to account for the anisotropic effects of the curvature and the embedded turbulence-driven secondary motion. Due to the super-elevation of the water surface the non-uniform inward pressure gradient is not in equilibrium with the non-uniform outward centrifugal force. This non-equilibrium leads to a negative feedback of downstream velocity which relies on the kinetic energy restitution. The center-region behavior is mainly influenced by the vertical gradient of centrifugal force and the distribution of downstream velocity is influenced by the secondary circulation. The non-hydrostatic pressure is included in the momentum equations for incorporation in the surface elevation, and its correction provide the local continuity. This leads to the more improved description (in the dynamic way) of the advective momentum transport with the consequence on the free surface elevation. The consequence (as expected from experiments) on the computations, is that the upper part of the flow is pushed toward the outer bank while the lower part of the flow towards the lateral inner bank. In the straight part of the channel the outer-bank weaker secondary currents are not captured, due probably to the fact that such mechanism relies on strong anisotropy of turbulence, and in those areas the computed solutions of the longitudinal velocity component is over predicted (at sections $m05$ and $p25$ in figures 6.22 and 6.24). In the curved part they rely both on the critical value of the curvature and background turbulence. Besides the classical helical motion, a weaker and smaller outer-bank secondary flow in the curvature region is under-predicted and observed (see figure 6.23). This suggests that, in case of channel flow with uniform roughness and cross-section, the pressure-driven secondary motion is relatively more important with the increasing strong curvature. Therefore the effects of secondary circulation upon the downstream velocity V_s distribution are observed and the maximum velocity shifts in outward direction such that the vertical profiles are flattened.

At the sections $\alpha = 90^\circ$ and $\alpha = 150^\circ$ (located in the strong curved region) the maximum downstream velocity core remains towards the outer bank, however computations is under predicted and its width occupies the channel center (see figures 6.23 and 6.24). Experiments show a relatively large band near to the right hand bank. This seems to be the reason of the strong secondary currents in these regions (see sections $\alpha = 90^\circ$ and $\alpha = 150^\circ$). Compared to the experiments, the computed solutions perform well and reproduce successfully the downstream velocity, secondary circulations as well as the related weakness secondary circulation with increasing curvature. The nearer outer-region behavior is influenced by the vertical gradient of centrifugal force (which changes sign near the water surface). Figure 6.25 compares with good agreement the computed solutions and experiments for the vertical velocity component at the sections $\alpha = 90^\circ$ and $\alpha = 150^\circ$. The under prediction in secondary flows strength may result in the computed maximum primary velocity core being offset towards the channel center relative to the outside of the bend. The maximum under prediction in the secondary current for each vertical examined in one cross section ranged from 20 to 65% with the present model. In such complex flow, the use of distributed heterogeneous roughness and the non-linear turbulence model might help to predict more accurately the secondary motion with its inherently three-dimensional effects and local bed features.

6.3.1 Concluding remark

In the present test case a full 3D semi-implicit F.E.M. solver with the non-hydrostatic pressure is applied for simulating a 193⁰ open channel. More insight about the processes underlying the interesting features of the flow field such as multi-cellular patterns of the secondary circulation due to the curvature influence on the lateral free surface gradient and embedded turbulence have been evaluated successfully. The use of Euler scheme of order $O(\Delta t)$ with Lagrange-Galerkin

method for computing the advection terms helps the model to preserve the monotonicity of the solution and to better describe the vertical structure of the fluid flow. The incorporation of the free-surface movement instead of the rigid-lid approximation, and the use of non-hydrostatic pressure (suitable for short waves) better accounts for a wave-like oscillation of the pattern of secondary motion embedded in background turbulence. Using modified algebraic expression of eddy coefficients, the relevant modified $k - \varepsilon$ turbulence accounts for anisotropic turbulence effects in such flows. Even under predicted, the outer-bank weaker secondary circulation has been successfully captured with the increasing curvature. Validation of the full 3D model is performed by applying the model against well-known flow cases. This suggests that a simplified approach of the turbulence modeling with modified algebraic expressions to account of the anisotropic effects, may give slight improvement in the three-dimensional velocity distribution depending on the cross-section location. It is well known that overestimation of the linear model is due to the adoption of a straight-flow downstream velocity component profile, thereby neglecting the feedback between the latter profile and the center-region cell (de vriend [25]). This suggests that the effects of the center-region cell in moderately to strongly curved flow can only be modeled if one takes due account of the deformation of downstream velocity profiles, and the feedback between the downstream velocity and the center-region cell. Thus, by incorporating these terms into the linear model formulation, we have developed the so-called *anisotropic model*. Moreover, without information about spatial distribution of the roughness this model can accurately predict presence and rotational sense of secondary currents in curved open channel with realistic cross-sectional shape, and the examined turbulence characteristics being useful for the natural rivers modeling.

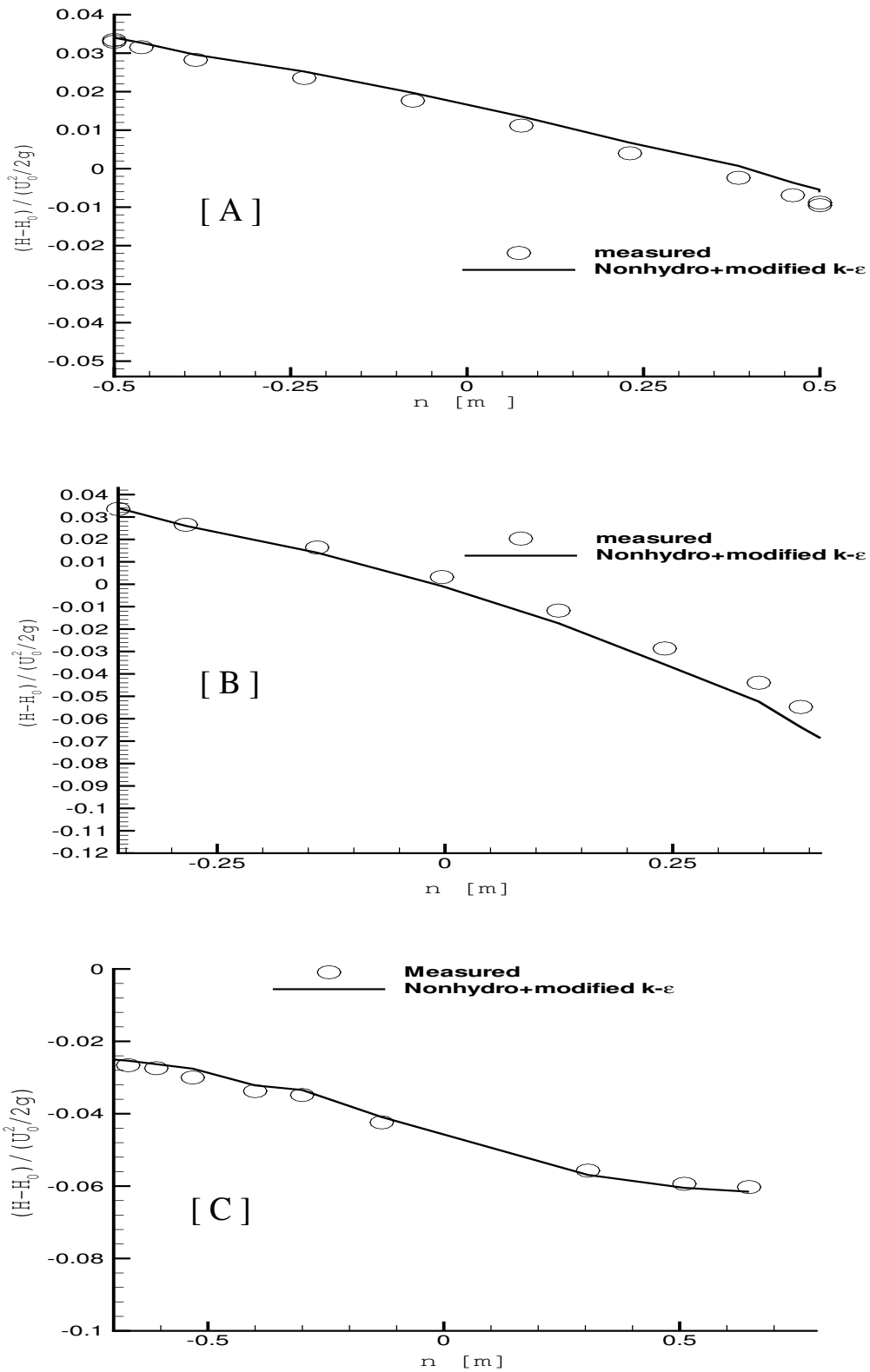


Figure 6.21: Test V: Experiments versus computed free-surface solutions at the selected cross-sections : A) section m05 ; B)section $\alpha = 90^\circ$; C)section p25

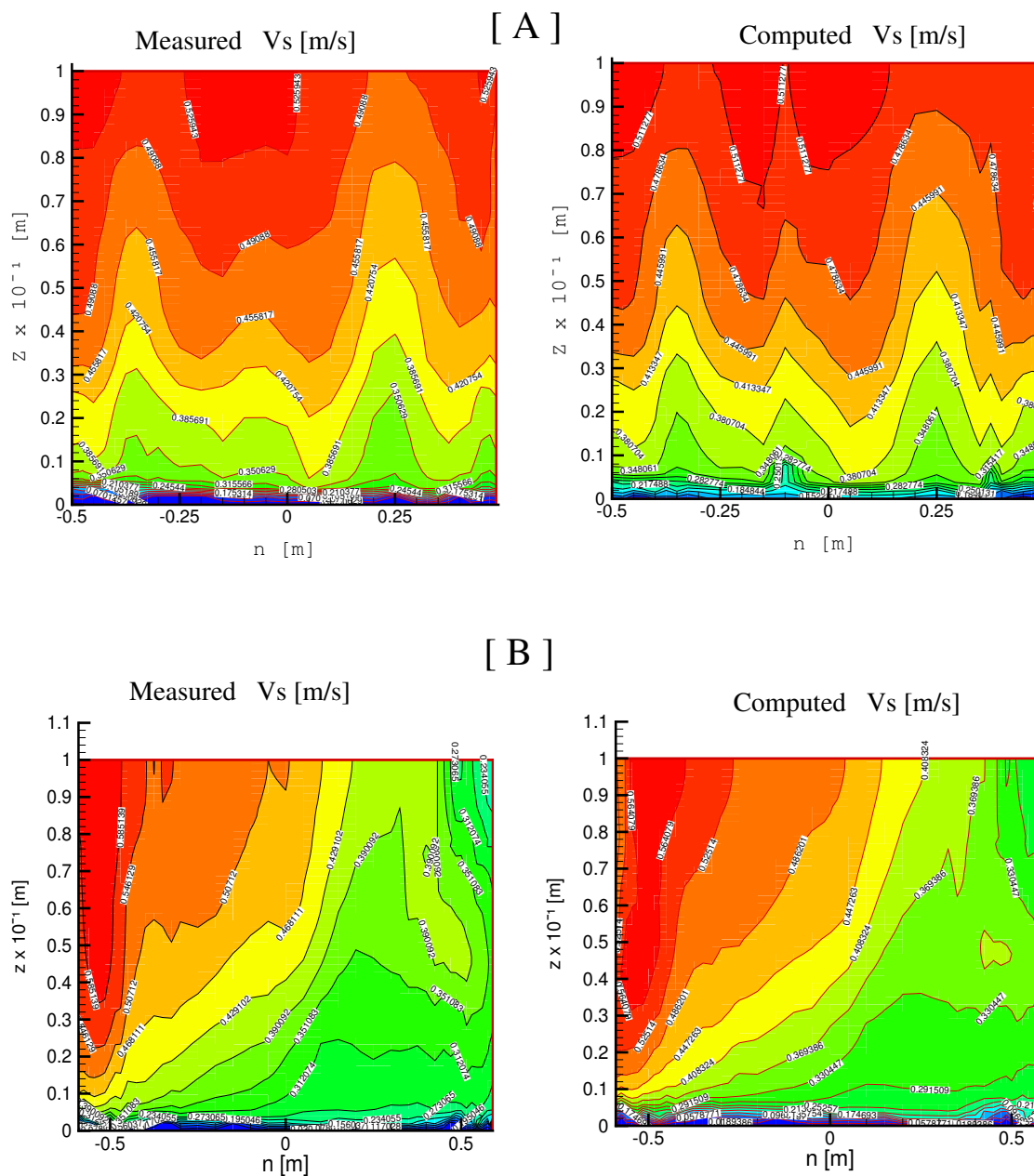


Figure 6.22: Test V: Measured and computed Iso contours of the of the downstream velocity component V_s at the selected sections: A) section m05; B) section $\alpha = 30^\circ$

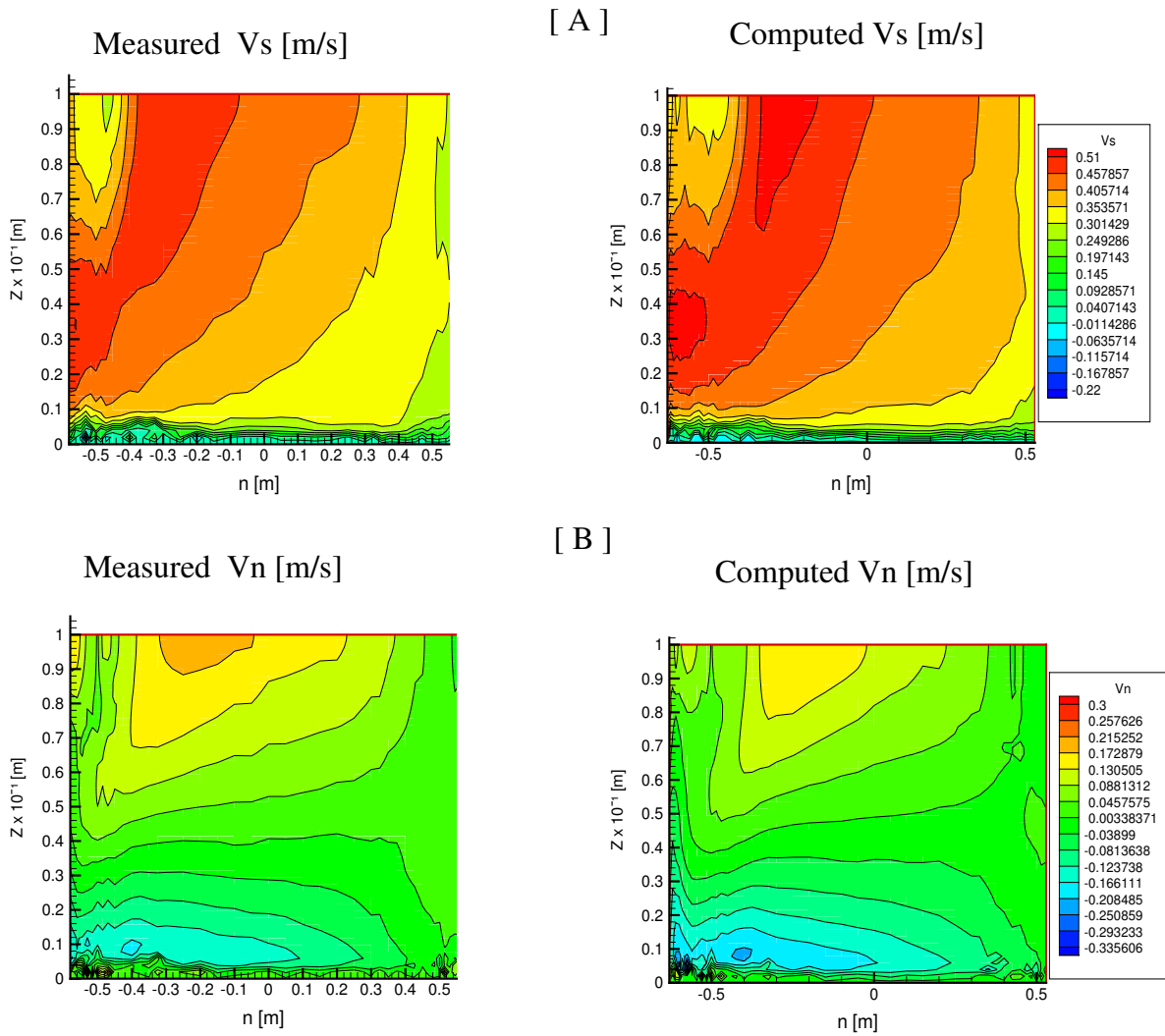


Figure 6.23: Test V: Iso contours at the section $\alpha = 90^\circ$ of : A) downstream velocity component V_s ; B) transversal velocity component V_n

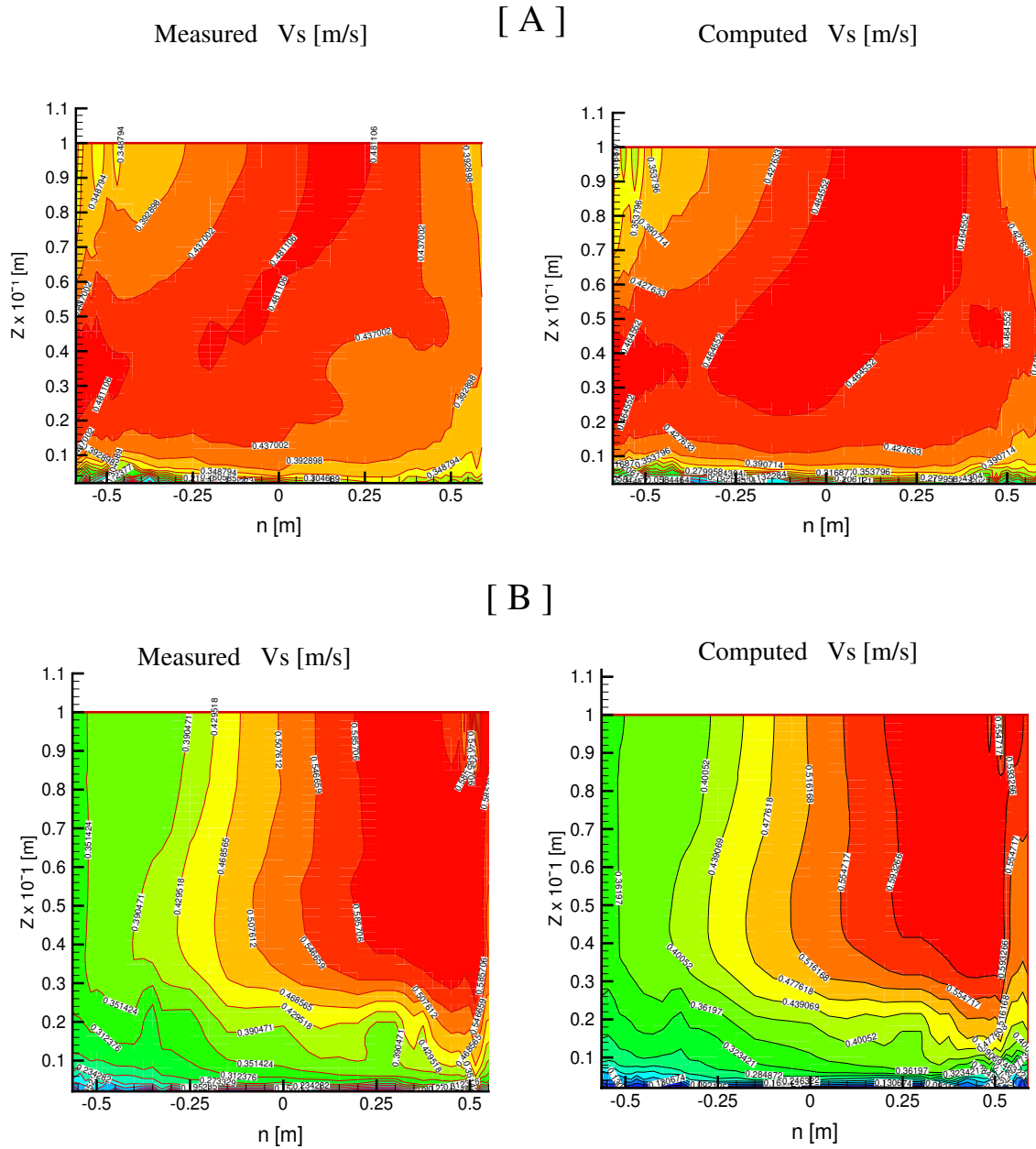


Figure 6.24: Test V: Measured and computed Iso contours of the of the downstream velocity component V_s at the selected sections: A) section $\alpha = 150^\circ$; B) section p25

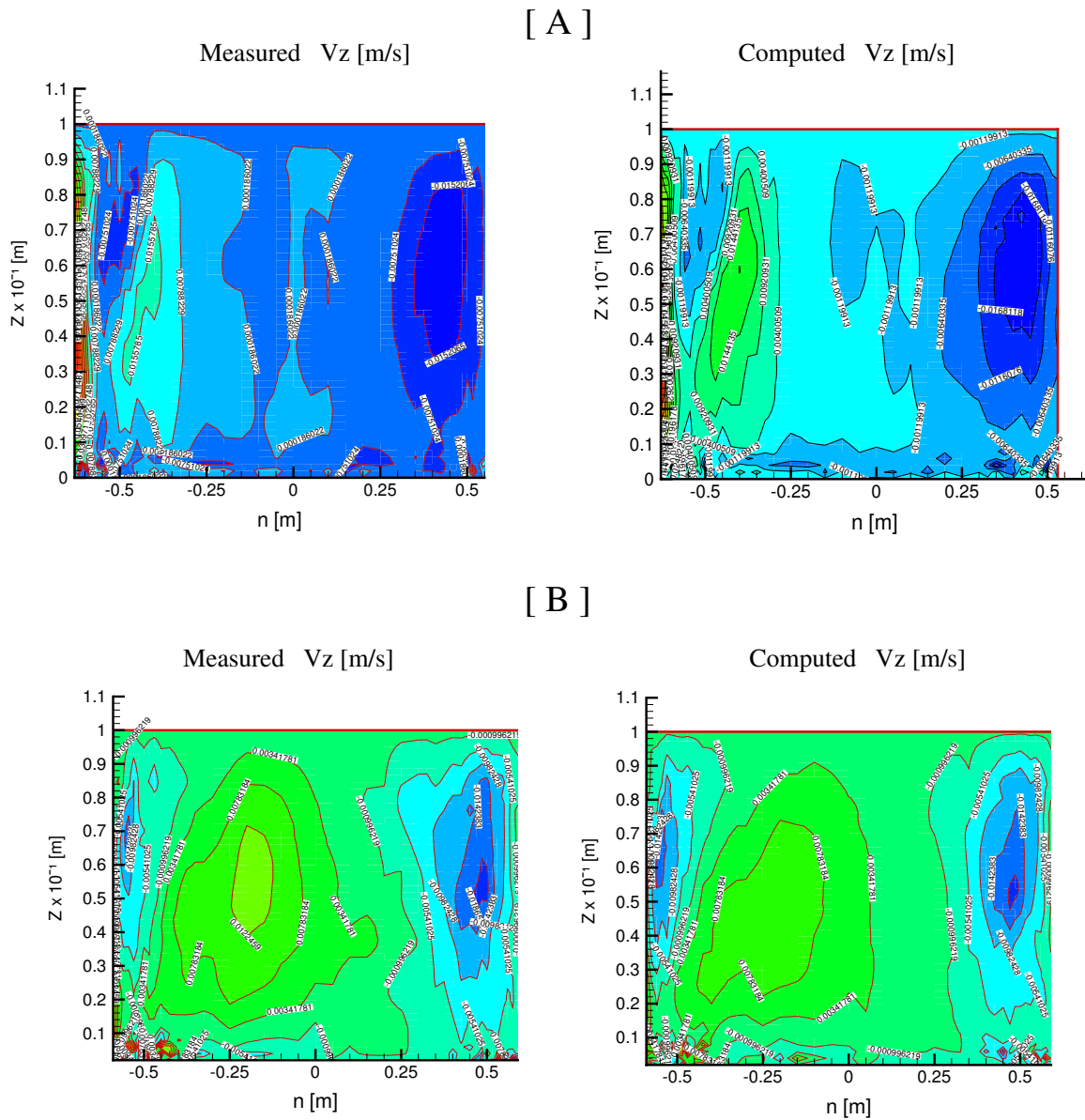


Figure 6.25: Test V: Measured and computed Iso contours of the vertical velocity component V_z of cross-stream at the selected sections: A) section $\alpha = 90^\circ$; B) section $\alpha = 150^\circ$

Chapter 7

3D Modeling of Cohesive Sediment in Estuaries

This chapter deals with the cohesive sediment transport and bed morphology modeling. In this chapter quantitative information about some salient features of variable density effects in turbulence will be provided. For the bed evolution modeling two approaches will be investigated: (i) the concept of turbidity accumulations modeling will be applied to fluid mud at the bottom using the recent advances in the calculation of erosion and deposition rates of fluid-mud; (ii) the three-bed layers modeling based on the consolidation process, using realistic empirical functions. In order to treat a real case and therefore demonstrate the feasibility of the method, the model is applied to investigate the suspended sediment concentration and the seabed evolution in the Po River Estuary in Italy.

7.1 3D model for turbulent and variable density fluid flows

In the present work the three-dimensional numerical model is implemented for simulating sediment transport by taking into account the effects of cohesiveness between sediment as well as the mutual influence of turbulence on flocculation process (buoyancy). From field observations (Odd and Rodger [100]), we know that a layer of fluid mud will start to flow along the flat bed of an estuary as a result of imposed hydrostatic head caused by the increase of the water surface slope after slack tide. On the other hand, from the scale analysis in table 3.2, one could easily find that the SWE-model is suitable for the estuaries modeling. Thus in the sequel the 3D-system of PDEs in section (3.4.2) will be used in the framework of hydrodynamic fluid flow modeling with an ODE system from (5.1).

An efficient splitting scheme is employed to solve hydrodynamic, turbulence, suspended sediment transport, heat, salinity and bed morphology. The splitting method partitions a time step into fractional steps according to physical phenomena. In the first step hydrodynamics is solved, followed by turbulence closure, then the advection-diffusion equations for passive scalars (temperature, salinity, suspended sediment concentration) are solved in the third step and finally the bed morphology is computed at the fourth step using empirical functions specially developed for cohesive sediments. This model will be applied to investigate the suspended sediment concentration and the seabed evolution in the Po River Estuary in Italy. The computed results will be compared to the field measurements for validating the model.

7.2 Cohesive sediment transport in estuaries

7.2.1 The numerical modeling approaches

Most of the existing models in the literature assume analogous transport characteristics with that of the coarse sediment and adopt sediment transport that were developed for the latter to treat the cohesive sediment. A contrario, it is shown that there are fundamental differences in the transport characteristics of these two types of sediments (see [58], [86]).

For suitable modeling of an estuary, there are different parameters that require quantification, such as sediment settling velocity, incipient shear stress of cohesive (and/or non-cohesive) sediments (see figure 7.1). Up to now some natures of silt movement have been revealed and many study works which include field measurement, theoretical analysis and simulation tests have been carried out (see Chapter 1). The new model proposed in this thesis used novel realistic empirical relationships of deposition and erosion or re-suspension of fine sediment in the laboratory flumes derived from experiments and observations. This formulation will take into account the differences in the critical conditions for erosion or re-suspension and deposition of fine sediment and allows simultaneous erosion and deposition to occur only for a limited range of bed shear stresses. In this thesis the cohesive sediment transport in estuaries relies on the numerical solution of basic conservation equations of mass, momentum and turbulent energy. The Coriolis force, tidal forcing, wind action, resistance to flow at the bed, buoyancy effects due to temperature, salinity of sea-water and sediment concentration, bed-level changes due to deposition and erosion will be modeled for a realistic representation of the phenomena.

In figure (7.1), the settling velocity is denoted by w_{ss} , $d\rho/dz$ denotes the vertical density gradient, and dh/dt stands as the water depth gradient due to the formation of delta at the bed. In the present work, silty sediment erosion, deposition, re-suspension and seabed evolution will be taken into account as well as the consolidated bed layer in the 3D cohesive sediment numerical model. Thus the new set of equations and new algorithm proposed by Krishnappan and Engel [58] and the model developed by Chen *et al.* [20] will be applied for computing erosion and deposition of cohesive sediment transport in the Po River Estuary in Italy. Finally the validation of the model and its application will be therefore carried out.

Remark 12 *It should be pointed out that this model uses Boussinesq's assumption, i.e. relation between Reynolds shear stress and the gradient of velocity can be connected with eddy viscosity coefficient. The turbulence modeling should account for the buoyant effects introduced by multiphasic fluid-flow. To avoid the spurious numerical oscillations (due also from the physical instabilities), some stability functions (S_u and S_b) have been used in the chapter 3, when computing the eddy coefficients to take into account the damping of the turbulence [79]. On the other hand in Eq. (4.18) and (4.19), the source terms have been discretized explicitly while the sink terms have been discretized using the quasi-implicit forms, and consequently the nonlinear terms have been linearized [80].*

7.3 Solid phase flow modeling

Due to their different particle sizes, sediments may not have the same physical and chemical characteristics. Usually the sediments with particle size less than 30 [μm] is classified as silty sand [92]. Gravity force is predominant for coarse sand particle, while for fine or silty sand with sediment size less than 100 [μm] (specially for less than 30 [μm]), viscous effect around particles becomes significant. The transport of sediment particles by flow can be in the form of bed-load (coarse particle size) or suspended load, depending on the size of bed particles and the flow

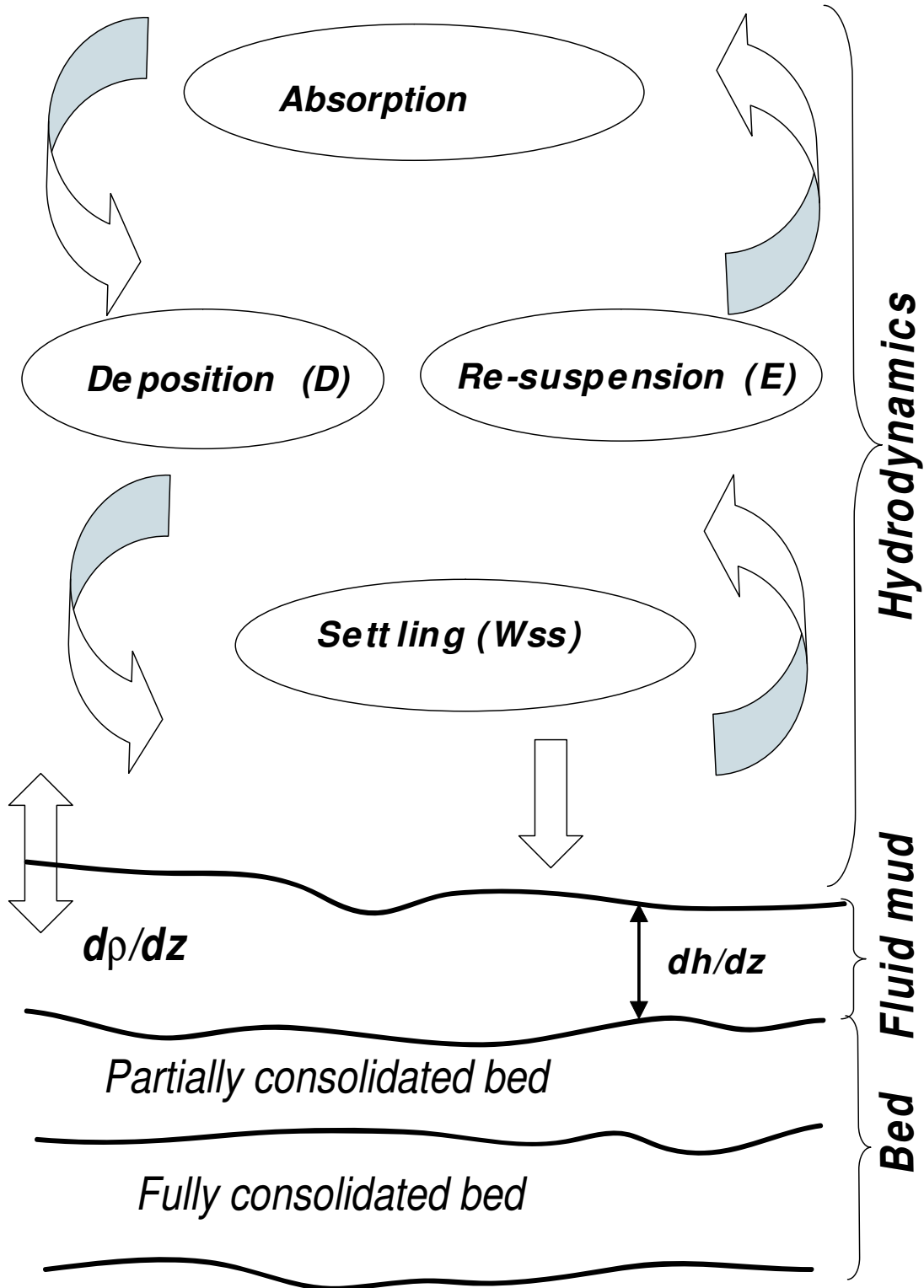


Figure 7.1: Cohesive sediment transport processes within the estuaries

conditions. In Po River Estuary sediments are mainly silty particles with medium diameter of the sediments being about 0.064 [mm] [148].

The bed morphology evolution Δz must be defined to close the so-called *integrated continuity equation* Eq. (3.37). From equation (4.34) we assume that,

$$\int_{\Omega} \tilde{\mathbf{F}}_b d\Omega = \int_{\Omega} \int_0^{T_s} \frac{\partial h}{\partial t} \psi dt d\Omega = \Delta z |\Omega| \quad (7.1)$$

where T_s represents the solid flow time scale (which is in general much higher than the hydrodynamic time scale). The following lines deal with the parameterization of the bed morphology for the sediment transport. This bed evolution accounts for three processes including the bed fresh deposit layer, Δz , the partially consolidated and the fully consolidated bed.

Advection-diffusion equation for suspended sediment concentration

A cohesive sediment model is conducted using combined semi-empirical functions to predict the seabed sediment deposition and erosion rates. As a reminder, the advection-diffusion equation for the suspended sediment transport reads

$$\frac{DC_s}{Dt} - \nabla_{xy} \cdot (\nu_{h,s} \nabla C_s) - \frac{\partial}{\partial z} \left[(\nu_{v,s}) \frac{\partial C_s}{\partial z} \right] = F_s + \omega_{ss} \frac{\partial C_s}{\partial z} \quad (7.2)$$

where C_s [kg/m³] is the sediment concentration, $\nu_{h,s}$ and $\nu_{v,s}$ [m²/s] are respectively horizontal and vertical mixing coefficients, ω_{ss} [m/s] is the settling velocity of sediment particles, F_s [m³/s] is the net flux of suspended sediment. The horizontal processes not resolved by the model can be parameterized by the diffusion coefficient using empirical relations from Elder [33] and Shirou [127]:

$$\nu_{h,s} = \frac{\nu_h}{\sigma_s} \quad (7.3)$$

where $\sigma_s = 1$ is the turbulent Schmidt's number, and ν_h is the horizontal parameterization of eddy coefficient in Eq. (3.62). The vertical diffusion coefficient of sediment particles ($\nu_{v,s}$) is related to the diffusion of fluid momentum

$$\nu_{v,s} = \zeta_s \phi \nu_v \quad (7.4)$$

Based on the experimental data of Coleman [23], the factor ζ_s was found to be in the range of 1 to 3, and We chose $\zeta_s = 1$.

Yalin and Finlayson [160] analyzed measured flow velocity profiles and observed that the local velocity gradient in a sediment-fluid mixture is larger than that in a clear flow. This suggests that the damping effects should be taken into account for the velocity distribution of the flow-carrying sediment in suspension. The damping factor for local concentration ϕ reads [116]:

$$\phi = 1 + \left[\frac{C_s}{C_s^0} \right]^{0.8} - 2 \left[\frac{C_s}{C_s^0} \right]^{0.4} \quad (7.5)$$

For concentration smaller than 1%, one can take a value of $\phi = 1$.

The settling (fall/rise) velocity of the flocculated granule is expressed from Stokes function [119] as follows

$$\omega_{ss} = D_{50}^2 g \frac{(\rho_m - \rho_0)}{18\nu C_h \rho_0} \quad (7.6)$$

where D_{50} is the sediment medium diameter. The Chezy's coefficient C_h can be expressed as a function of the relative roughness [40] such that

$$C_h = \sqrt{8g} \left[2 \cdot \log \left(\frac{a_f}{k_s/R_h} \right) \right] \quad (7.7)$$

where R_h [m] is the hydraulic radius of the channel flow, $a_f = 12.7$ is a given coefficient, k_s [m] is the bottom roughness.

The suspended cohesive sediment in seawater usually have flocculated structures. It should be pointed out that the settling velocity of the flocculated granule is much larger than that of the particles in dispersive state [92]. The smaller the sediment particle diameter size is, the stronger the flocculation ability may be. To express such effects, Migniot [92] used a flocculation factor L such that,

$$L = \frac{\omega_{L50}}{\omega_{D50}} \quad (7.8)$$

where ω_{L50} is flocculation limited settling velocity and the ω_{D50} is the sand particle velocity without flocculation.

A function ω_L has been derived by Huang [49] for sediment velocity combined with water temperature, settling distance, particle size and sediment concentration:

$$\omega_L = \omega_{ss} \left[1 - \left(\frac{L-1}{L} \right) e^{-KC_0Z_b} \right], \quad L = 7.25 D_{50}^{-2} \quad (7.9)$$

where $K = 0.012$ is constant, C_0 is the initial sediment volumetric concentration, Z_b is the settling distance.

Bottom conditions

To solve Eq. (7.2), the boundary conditions and the physical parameters associated with the sediment and flow properties must be known. The boundary conditions are given as the sediment concentration at the river upstream intake and the sediment exchanges at the water surface, open boundaries and seabed. The vertical sediment exchange, noted F_s is defined by the net flux of the sediment which reads

$$F_s = D - E; \quad D = \omega_{ss}C; \quad E = -\nu_{v,s} \frac{\partial C}{\partial z} \quad (7.10)$$

This net flux of the sediment in the vertical direction expressed as the difference of downward sediment flux, D , and the upward sediment flux, E . The net vertical sediment transport is assumed to be zero at the water surface boundary, resulting in $F_s = 0$. At the seabed the net flux sediment is considered as the difference of the deposition to the bed, noted D_b , and the sediment entrainment from the bed, noted as E_b .

Remark 13 *It is worthwhile to mention that the boundary conditions at the bottom, are determinant for the net flux calculation and the related deposition on the bed. In the present work we will use two approaches for simulating the sediment exchanges in the lowermost layer: (i) Uniform critical conditions for erosion and deposition [28], [20]; (ii) Two different power law functions for deposition and re-suspension from the mutually exclusive processes proposed by Krishnappan and Engel [58].*

7.4 Seabed morphology

7.4.1 Evolution of the non-consolidated layer using single function

The seabed mud-fluid layer is modeled using semi-empirical functions to predict deposition and erosion rates [20]. In the sequel, h is indeed as it was introduced in chapter 3, the height in between the bottom and the xy reference plane.

For uniform sediments, the deposition rate is proportional to the concentration and can be expressed as the production of the settling velocity and sediment settling probability that accounts for the turbulent parameter and physical features of the bed sediments

$$D_b = \alpha_s \omega_{ss} C \quad (7.11)$$

where α_s is the probability of the sediment settling with the range of 0 up to 1.

The entrainment rate from seabed is assumed to be a function of flow parameters and physical features of bed sediments:

$$E_b = \begin{cases} 0 & \text{for } \tau_b \leq \tau_{b,cr} \\ -\nu_{v,s} \left(\frac{\partial C}{\partial z} \right)_{z=a} = \alpha_s \omega_{ss} C_a & \text{for } \tau_b > \tau_{b,cr} \end{cases} \quad (7.12)$$

where C_a the near-bed equilibrium reference concentration at level $a = 0.01h$ above the bottom (value with water depth averaged) reflects the capacity to carry sediment by current. Under currents based on field measurement and flume tests and based on energy considerations, Dou *et al.* [28], (also [20]) derived function of reference concentration for silty particles at level $a = 0.01h$ above seabed such that:

$$C_a = \alpha \frac{\rho \rho_s}{\rho_s - \rho} \left(\frac{n_s^2 u_a^3}{h^{4/3} \omega_{ss}} \right) \quad (7.13)$$

in which u_a is the current velocity at level a ; $\alpha = 0.0067$ is a constant coefficient; n_s [$\text{m}^{-1/3}/\text{s}$] is the Strickler coefficient defined as $n_s = R_h/C_h$, and R_h [m] is the hydraulic radius [40].

$\tau_{b,cr}$ is the critical erosion bed shear stress. τ_b is the bed shear stress which is expressed as follows

$$\tau_b = \nu_v \sqrt{\left[\left(\frac{\partial u}{\partial z} \right)^2 + \left(\frac{\partial v}{\partial z} \right)^2 \right]} \quad (7.14)$$

Based on the information obtained from field measurements and experiments, Tang [132] derived a function for incipient bed sediment motion velocity for the sediment particle size ranging (see [132]) from 1 [μm] to $1.25 \cdot 10^5$ [μm], such that

$$u_{b,cr} = \vartheta \bar{u}_{b,cr} = \left[3.2 \left(\frac{\gamma_s - \gamma}{\gamma} \right) g D_{50} + \frac{\xi}{\rho^* D_{50}} \right]^{\frac{1}{2}} \quad (7.15)$$

in which $u_{b,cr}$ is the bottom sediment incipient velocity; $\bar{u}_{b,cr}$ is the vertical averaged critical velocity and

$$\vartheta = \frac{\left(\frac{m+1}{m} \right)}{\left(\frac{h}{D_{50}} \right)^{1/m}} ; \quad m = 0.47 \left(\frac{H}{D_{50}} \right)^{0.06} \quad (7.16)$$

where $\gamma_s = \rho_s g$, and $\gamma = \rho g$ are the voluminal weight of respectively sediment and water (Graf and Altinakar [41]), ρ_s is the sediment density. $\xi = 2.9 \cdot 10^{-5}$ [kg/m] and $\rho^* = 102$ [kgs^2/m^4] are the given coefficients related to viscous effects.

The critical shear stress can be expressed as follows:

$$\tau_{b,cr} = \frac{1}{77.5} \left[3.2 (\gamma_s - \gamma) D_{50} + \frac{\xi}{D_{50}} \right] \quad (7.17)$$

The non-consolidated bed layer (fresh deposit mud), Δz , can be calculated using the following expression Dou *et al.* [28], and Chen *et al.* [20]:

$$\Delta z = \frac{\alpha_s \omega_{ss}}{\gamma_0} (C - \beta C_a) \Delta \tau \quad (7.18)$$

in which γ_0 is the dry sediment density, β is a coefficient and $\Delta \tau$ is the solid flow time step. The sediment dry density can be derived from the water content as a fraction of total mass or as a ratio of water mass to solid mass. The dry density γ_0 , is the ratio of the dry mass (M_d), to the total volume (V_T) of water-saturated, and it can be calculated from the corrected water content (W_d), and porosity (Φ):

$$\gamma_0 = \left(\frac{\Phi}{W_d} \right) \rho_m \quad (7.19)$$

ρ_m is the pore fluid density. The porosity Φ , is the ratio of pore-water volume to total volume and can be written:

$$\Phi = 100 \left[\frac{(\rho_g - \rho_b)}{(\rho_g - \rho_m)} \right] \quad (7.20)$$

where ρ_b is the bulk density, ρ_g is the grain density in [kg/m³].

The grain density can be determined from the dry mass and dry volume such that

$$\rho_g = \frac{(M_d - M_{sal})}{\left[V_d - \left(\frac{M_{sal}}{\rho_{sal}} \right) \right]} \quad (7.21)$$

where $\rho_{sal} = 2.257$ [kg/m³] is the density of salt, S [ppt] is a pore-water salinity; $M_{sal} = S M_m$ is the mass of salt in the pore fluid, and $M_m = (M_T - M_d) / (1 - S)$ is the salt-corrected mass of the seawater. $V_d = \frac{C_s}{\rho_s} V_T$ is the volume of dry mass, with C_s a sediment mass-concentration in [kg/m³].

The bulk density, ρ_b , is the density of the saturated sample and can be calculated from total water-saturated mass M_T and its volume V_T , such that $\rho_b = M_T / V_T$.

The difference between total water-saturated mass M_T and dry mass M_d is taken as uncorrected water mass, and the measured wet and dry masses must be corrected. Therefore the wet and dry water contents, W_d and W_m (in percent), are given respectively by

$$W_d = 100 \left[\frac{(M_T - M_d)}{(M_d - S M_T)} \right]; \quad W_m = 100 \left[\frac{(M_T - M_d)}{((1 - S) M_T)} \right] \quad (7.22)$$

where $M_m = (M_T - M_d) / (1 - S)$ is the salt-corrected mass of pore-water
In Eq. (7.18), the coefficient, β , is defined as:

$$\beta = \begin{cases} 1 & C > C_a \\ 1 & C \geq C_a \text{ and } \tau_b > \tau_{b,cr} \\ \frac{C}{C_a} & C \leq C_a \text{ and } \tau_b \leq \tau_{b,cr} \end{cases} \quad (7.23)$$

7.4.2 Non-consolidated bed thickness using power law functions for mutually exclusive deposition and re-suspension

For a true representation of the erosion and deposition of the fine cohesive sediment, Lau and Krishnappan [61] have shown that these two processes are mutually exclusive for a certain range of shear stresses. This information is very useful for the good representation of the consolidated bed, since the consolidation process depends on the real quantity of deposited sediment and its concentration at the bottom. From experiments, Krishnappan and Engel [58] have studied the behavior of the Fraser river (Canada) that is found to be similar to that of the cohesive sediment [57].

Computations will take into account the novel algorithm of Lau and Krishnappan using power law functions for deposition and erosion of sediment at the bed, while some empirical laws from Migniot [92,93], will be used for the consolidation process.

Transport power law functions

For fine sediments, the simultaneous erosion and deposition is possible only for a certain range of bed shear stresses. For shear stress outside of this range, there could only be sediment deposition or sediment erosion, but not both simultaneously. The shear stress at which the concentration in suspension becomes zero is termed the critical shear stress for deposition (τ_{cd}). From experiments of Krishnappan and Engel [58], its value was estimated to be $\tau_{cd} = 0.05$ [N/m^2], while the critical shear stress for erosion (i.e. shear stress for which there is no deposition) was calibrated at $\tau_{ce} = 0.12$ [N/m^2]. It should be pointed out that the critical shear stress for erosion for the sediment is almost two and a half times the critical shear stress for deposition. From the power law relationship between the fraction deposited and the ratio of bed shear stress to the critical shear stress for deposition, the fraction deposited, f_d , can be expressed as follows ([57]),

$$f_d = \begin{cases} 1 - 0.26 \left(\frac{\tau_b}{\tau_{cd}} - 1 \right) & \text{for } \left[1 < \frac{\tau_b}{\tau_{cd}} < 10.5 \right] \\ 1 & \text{for } \frac{\tau_b}{\tau_{cd}} < 1 \\ 0 & \text{for } \frac{\tau_b}{\tau_{cd}} > 10.5 \end{cases} \quad (7.24)$$

For complete re-suspension a shear stress 25 times larger than the critical shear stress for deposition was found. The fraction of sediment re-suspended, f_e , can be expressed as follows:

$$f_e = \begin{cases} 0.29 \left(\frac{\tau_b}{\tau_{cd}} - 2.4 \right)^{0.4} & \text{for } \left[2.4 < \frac{\tau_b}{\tau_{cd}} < 25 \right] \\ 0 & \text{for } \frac{\tau_b}{\tau_{cd}} < 2.4 \\ 1 & \text{for } \frac{\tau_b}{\tau_{cd}} > 25 \end{cases} \quad (7.25)$$

Mass balance of sediment in control segment

In the algorithm proposed by Lau and Krishnappan, sediment concentration is calculated using the mass balance of sediment in a control segment located next to the bottom layer (which comprises the three layers shown in figure 7.1). Sediment entering the control segment can be: (i) from the upstream and (ii) from tributary inflows. Let us refer to figure 7.2, the amount of

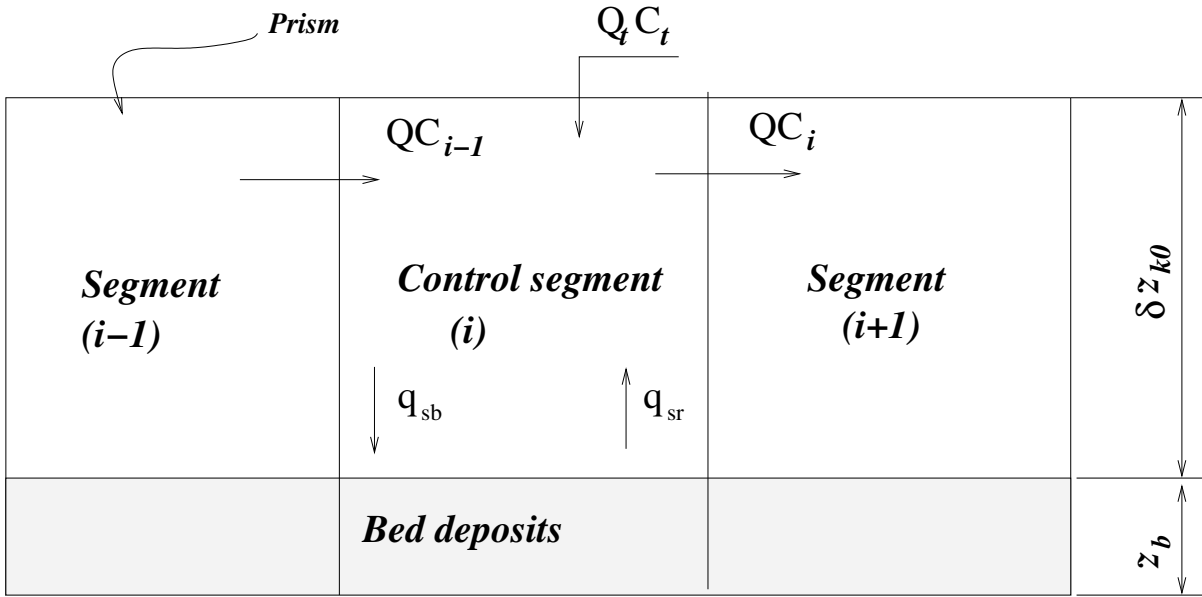


Figure 7.2: Schematic representation of control segment sediment (lowermost prism) mass balance

upstream sediment (q_{su}) entering the control segment (lowermost prism) during time interval $\Delta\tau$ can be expressed as:

$$q_{su} = Q_t V_{st}^{i-1} + Q_t V_{st} \quad (7.26)$$

where V_{st}^{i-1} is the volume of water-saturated (pore water) in the upstream segment (prism), V_{st} is the of water-saturated in the tributary inflow to the control segment (prism next to the lowermost prism in the water column), Q is the flow rate of the control segment and Q_t is the tributary inflow rate (figure 7.2). In figure 7.2, δz_{k0} represents the height of the lowermost prism (lowermost active layer), and z_b denotes the thickness of the total deposition on bed.

Sediment deposition and resuspension

Out of the incoming upstream sediment, q_{su} [kg], a portion will deposit depending on the prevailing flow conditions. The sediment quantity coming from the upstream segment will be subjected to the deposition only when the shear stress in the control segment is lower than that in the upstream segment. If the shear stress in the control segment is equal to or greater than that of the upstream segment, then the sediment arriving from the upstream segment would have gone through the deposition process already and would have reached the steady state concentration. Therefore, this sediment has to be routed straight through the control segment. The amount that would deposit in the control segment, q_{sd} [kg], can be therefore calculated from the following expression,

$$\begin{aligned} q_{sd} &= QV_{st}^{i-1}f_d + Q_tV_{st}f_d & \text{if } \tau_b^i \leq \tau_b^{i-1} \\ q_{sd} &= Q_tV_{st}f_d & \text{if } \tau_b^i > \tau_b^{i-1} \end{aligned} \quad (7.27)$$

The amount of sediment that remains in suspension q_{ss} [kg] becomes

$$\begin{aligned} q_{ss} &= (QV_{st}^{i-1} + Q_tV_{st}^t)(1 - f_d) & \text{if } \tau_b^i \leq \tau_b^{i-1} \\ q_{ss} &= Q_tV_{st}^t(1 - f_d) & \text{if } \tau_b^i > \tau_b^{i-1} \end{aligned} \quad (7.28)$$

Remark 14 *It should be pointed out that the bed evolution modeling needs a long period of simulation (e.g. one year simulation for solid phase flow time scale, and a daily tidal time scale for hydrodynamics). Thus when using the sub-cycling scaling during simulation, the solid phase flow time step can be equivalent to $\Delta\tau = N \Delta t$, with $N > 0$ being a natural number.*

Sediment can also be re-suspended from deposits that occurred in previous time steps. This resuspended amount can be calculated by keeping track of the amounts of deposited sediment and the shear stresses at which the depositions took place. For a given shear stress, the sediment re-suspension can be calculated with the appropriate τ_{cd} value as follows:

$$q_{sr} = q_{sd}^n f_e \quad (7.29)$$

where q_{sr}^n is the value of total resuspended sediment, q_{sr} [kg], at the previous time step.

The suspended sediment concentration in the control segment at the end of the current time step reads

$$C_s = \frac{(q_{sr} + q_{ss})}{V_T} \quad (7.30)$$

The amount of sediment left behind the control segment (i) at the end of the current time step must be updated such as:

$$q_{sd*}^i = q_{sd}^n (1 - f_e) + \delta_{i,k} (q_{sd})^k \quad (7.31)$$

where q_{sd*}^i is the updated value of the sediment deposit at the segment (i), $\delta_{i,k}$ takes a value of unity if ($i = k$) and zero if ($i \neq k$, with $k \in [1, 5]$ the indices of the k^{th} face of the prism).

The concentration of the deposited sediment C_{sd} , can be expressed as follows

$$C_{sd} = \frac{q_{sd}}{V_T} \quad (7.32)$$

7.4.3 Consolidation process and consolidated bed layers

The consolidation process is a function of the consolidation of the stationary suspension and the partially consolidated component of the bed, by the packing of the bed, the force of cohesion of the particles and the reduction thickness of the bed with time. It is considered that the consolidation starts after the process of formation of the layer of the bed is complete, at which time the thickness of the layer of the bed would be maximum (see [42], [86]). Experiments revealed that after a certain time of consolidation T_{dc} , of a certain value T_{dc1} , the stationary suspensions (layers of mud coldly deposited) undergo a reversal in re-suspension just like (it is opposed to the drive when $T_{dc} < T_{dc1}$), when they are subjected to an excess of constraint of friction (Hayter [47]). The profile of the bed has two categories of layers of various thicknesses with a specific density, friction resistance and duration of stability. According to the experiment of Migniot [92,93], this duration of stability accounts for the consolidation.

According to Mehta's experiments [139], [86] the mass of dry sediments in the stationary suspension for which ($T_{dc} = T_{dc1}$), is built-in in the partially consolidated layer of the bed, and will go up in suspension when it is subjected to an excess of constraint of friction. Standardized relations were established between the average density of dry sediments, $\tilde{\rho}_g$, (realized on the depth) and the time of consolidation, and make it possible to determine this density in the consolidation process as follows,

$$\frac{\tilde{\rho}_g}{\tilde{\rho}_{g\infty}} = 1 - \alpha \exp[-\lambda R_{dc}]; \quad R_{dc} = \frac{T_{dc}}{T_{cd\infty}} \quad (7.33)$$

where $\tilde{\rho}_{g\infty} \in [110, 130]$ is the final average density of the consolidated layer of the bed, and a value of $\tilde{\rho}_{g\infty} = 119.92$ [kg/m³] is valid (Migniot [93]). $T_{dc\infty} = 8$ [days] corresponds to the limiting value of the time of consolidation determined by Krone experiments [59] (see also [2]). $\alpha = 0.845$ and $\lambda = 6.58$ are empirical constants. The profile of sediments dry density for the natural consolidation of the mud at the bed can be expressed as follows

$$\frac{\rho_g(z_b)}{\tilde{\rho}_g} = \beta_s Z_\Delta^\delta; \quad Z_\Delta = \frac{E_b^j - z_0}{z_0} \quad (7.34)$$

in which β_s and δ are the empirical constants. E_b^j is the thickness of layer according to the nature of the deposit with $j = 1, \dots, 3$ (fresh mud layer, partially consolidated layer or fully consolidated layer), and $z_0 = 30 k_s$ is the bottom thin layer [143].

The thickness of the fully consolidated layer

From experiments, Mehta [86] drew up a table (7.1) of values of coefficients valid for the fine and cohesive sediments as follows

Table 7.1: Time of consolidation

T_{dc} (hours)	β_s	δ
2	0.36	-1.40
5	0.48	-0.72
11	0.62	-0.45
24	0.66	-0.50
≥ 48	0.80	-0.29

It can be found in table (7.1), that for values $T_{dc} < 48$ hours the parameters β_s and δ vary with time (this confers difficulties of making use of the formula 7.34 in this interval), since one does not have information for intermediate times. A contrario for $T_{dc} \geq 48$ hours, these parameters are found to be constant. This suggests that the formula in Eq. (7.33) is suitable for this interval (i.e. for the fully consolidated layers), and the consolidated bed thickness can be calculated from Eq. (7.34).

The thickness of the partially consolidated layer

The speed of decantation decreases with the increase in concentration (Migniot [94]), and the concentration of partially consolidated deposits vary slightly compared to the fully consolidated layer. Compressing (cohesion between particles) is also influenced by the conditions of sedimentation, in particular the initial thickness. According to experiments carried out in laboratory (see Trimbak and Mehta [139]), any increment ΔE_b , of the concentration involves a corresponding change of layer of deposit on the bed according to the following relation

$$\Delta E_b = \frac{H}{\rho_g(z)} \Delta C_s \quad (7.35)$$

where $\Delta C_s = C_s^{n+1} - C_s^n$ is the fraction of concentration of deposit on bed, and ΔE_b is the thickness of the partially consolidated bed.



Figure 7.3: Map of the Po River Estuary (PRE) and overview of the area of study

7.5 Prediction of discharges and bed morphology

In this section, flow field and cohesive sediment transport in the Po River Estuary (PRE) will be simulated. PRE is located in the east of the Adriatic Sea along the direction North West-North East (NW-NE) as shown in figure 7.3.

7.5.1 The Po River Estuary and Adriatic Sea

The Po River Estuary is the main source of the river water discharge into the Northern Adriatic. The river plume hugs the western side of the basin as aided by the dominant cyclonic circulation [15]. Along with wave re-suspension, the plume is responsible for the formation of 35 [m] thick mud wedge that extend from Po Delta to Gargano subaqueous delta, 500 [km] further south. During summer the Po River Estuary generally spreads over the entire northern sub-basin as a thin surface layer 5 [m] (Cushman-Roisin *et al.* [24]). The Adriatic Sea forms the northernmost part of the Mediterranean Sea. It is a relatively shallow almost rectangular basin bordered to the north by the Alps, to the west by the Apennines and on the east by Dinaric mountain chain. This temperate warm sea is more than 800 [km] long in NW-NE direction and has an average width of about 200 [km]. The Adriatic Sea is often divided into three geographical regions,

namely the Northern, Middle and Southern Adriatic basins. The Northern Adriatic, which is the area lying north of the 100 [m] isobath, has a wide continental shelf, sloping gently south and quite shallow. The middle Adriatic comprises the three trenches of the middle Adriatic Pit, with a maximum depth of 270 [m] and is bounded by the 170 [m] deep Palagruza Sill. The southern Adriatic extends from the Palagruza Sill to the Strait of Otranto, including the South Adriatic Pit, which is at its deepest point around 1200 [m] (see Cattaneo *et al.* [15]).

Application to the Po River Estuary

Po River (Padus River in ancient times) flows 652 kilometers from West to East across northern Italy, from Mount Monviso (in the Cottian Alps) to the Adriatic Sea near Venice. It has a drainage area of 75,000 square kilometers. The axis of PRE is east longitude 12.05° and north latitude $44^\circ 96667$. The 75000 [km²] river catchment of the Po is bounded at the North by the Alps with peaks over 4500 [m], and at the South-West by the Apennines mountain chain with peaks generally less than 2000 [m] (more than a third of the drainage area (30800 [km²]) can be considered mountainous (Ketter and Syvistki [56]). It is the longest Italian river and goes through many important Italian towns, including Turin and (indirectly) Milan. In Milan it enters the town as a net of channels called navigli, creating a very characteristic area. Near the end of its course, it creates a wide delta (with hundreds of small channels and 5 main ones called Po di Maestra, Po della Pila, Po delle Tolle, Po di Gnocca and Po di Goro). The vast valley around the Po is called Pianura Padana and is so efficiently connected by the river that the whole valley became the main industrial area of the country.

Characteristics of Po River

The tidal regime is that of a irregular diurnal micro-tidal type with the mean diurnal range form 0.80 [m] for the spring tide and 0.30 [m] for the neap tide. The M_2 main tidal component is taken into account in this study. High water levels in the North Adriatic Sea can be caused by storms coming from the south-east, the Sirocco wind, associates to depressional fields, which move towards the East and the mean wind speed is 30 – 50[km/h] (see [17]). These events can determine oscillations with periods of 22 hours and maximum amplitudes often exceeding 1 meter. The data recorded by the tide gauge (of *Porto Corsini*) showed that during 1999, the maximum value of the sea level rise recorded was 1.67 [m], caused by both the astronomical and the meteorological effects (see [38]). The prevailing wind and waves, which determine the main components of the solid coastal transport in the area are those from the North-east (locally called *Bora*) and the South-east (*Sirroco*). The typical characteristics for waves can be summarized as follows:

- Waves range: main orientation of the waves is $30 - 45^\circ$ and $120 - 145^\circ$.
- Maximum energetic wave $H_s = 4$ [m], with a wave period of 8 – 9 [s].
- Mean $H_s = 1.5 - 2$ [m], with a wave period of 5 – 6 [s].

The PRE has two flood periods, June (freshet caused by snow melting) and November (corresponding to precipitation maxima), and two low water periods, January and August (Marchi *et al.* [83], Cattaneo *et al.* [15]). The average discharge of the PRE is 1.5×10^3 [m³/s], measured at Pontelagoscuro (near Ferrara) 90 [km] from the coast and just before the apex of delta. Downstream of Pontelagoscuro, the Po forms a delta consisting of five major distributaries (see figure 7.3): the Maestra, Pilla, Tolle, Gnocca and the Goro drain, respectively 2%, 65%, 12%,

13%, 8% of the discharge. Salinity values for the station upstream reaches a maximum value of 8-20 [g/l] or 8-20‰ correlated with the tide cycles, while simultaneously, salt percentage measured downstream show high salt content, up to 25-35 [g/l] or 25-35‰ (see [34]).

The PRE is characterized by its high level of engineering; Comprehensive and contemporary evaluations of physical, chemical and toxicological endpoints have been performed on sediments of the PRE. The particle-size composition along the PRE showed a relatively uniform distribution of fine sand, a progressive downstream decrease of coarse sands and a corresponding increase of fine materials [148]. The major sediments class is silty sand (with clay) in which the average sediments size is less than 63 [μm]. Hundred detailed measurements of sediment dynamics at each distributary channel have been taken. There is hardly any top set aggradation, most of sediment load is funneled to the offshore, about 16×10^6 tonnes/year, causing a high rate of fore-set propagation into the shallow northern part of Adriatic Sea, while bed-load contributes only 2.5-5% of the total sediment output and high suspended sediment concentration (SSC). The monthly suspended sediment load were measured for the main distributary channels during six years field study (Kettner and Syvitski [56]), and may reach 300-400 [mg/l] in the main river stream (Panaro-Pilla) and in Tolle branch, while it is around 150 – 300[mg/l] in secondary distributaries at South-Pilla and South-Tolle (see figure 7.4).

7.6 Simulation of PRE: Numerical results

To simulate the tidal currents and sediment transport in PRE, a large area was selected as the modeled domain called *PRE-SD* shown in figure 7.3, and the 2D horizontal plane mesh in figure 7.4. The north upstream boundary has been set far upstream the five open boundaries as shown in figure 7.4. The available field data for the model calibration were mostly provided by the *MOX (Modeling and Scientific Computing)*, *Department of Mathematics, Politecnico of Milano* and the *Istituto di ricerca Sulle Acque, CNR, Milan, Italy*. In this model, the horizontal unstructured mesh of simulated area has been divided into 3185 triangles in each horizontal layer, and 2172 nodes with the mean space step size ranging from $d^T = 6.2$ to 46.08 [m] (where d^T denotes the diameter size of the circumscribed triangle). The vertical is divided into 30 layers. To account of the boundary layer effects the bottom is divided into several thin layers of thickness $\delta z_b = 0.5$ [m] (see figure 7.6).

The PRE bathymetry is shown in figure 7.5. The simulation period is from 14.00 of 1st of May to 14:00 of 2nd May 1999 for hydrodynamic calibration. The forcing is neap tide in wet season. There are seven tide gauges and seven tide stations and water open boundaries were controlled by tidal levels and sediments concentrations located at *NV*, *NT*, *ST1*, *ST2*, *SP1*, *SP2*, *SP3* (see figure 7.4). The boundary conditions are specified in chapter 3.

7.6.1 Numerical algorithms

For seabed evolution, a long period simulation need to be conducted. Generally, the smaller the time step, the higher the accuracy. However for a small time step, the simulation will require much more computational time.

Remark 15 *The present thesis uses a decoupling between pure hydrodynamic, turbulence module, passive scalars module and finally the solid phase flow (bed morphology) that solved in this order (see figure 7.7). Thus the model offers a capability to cope with the stiffness problem introduced by the large difference between the solid phase flow and hydrodynamics time scale.*

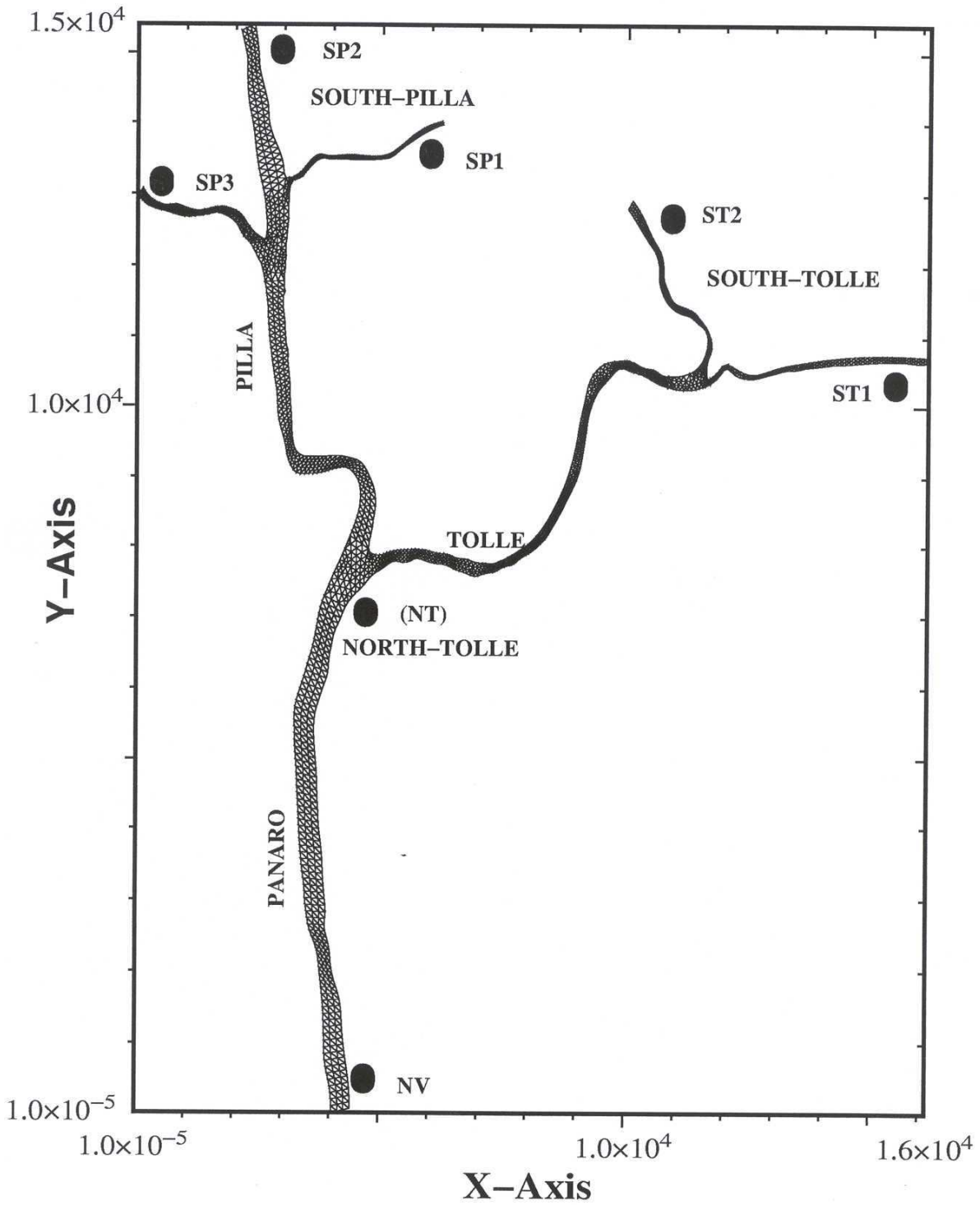


Figure 7.4: 2D-Horizontal Mesh of the domain of study and tidal gauges location in the Po River Estuary

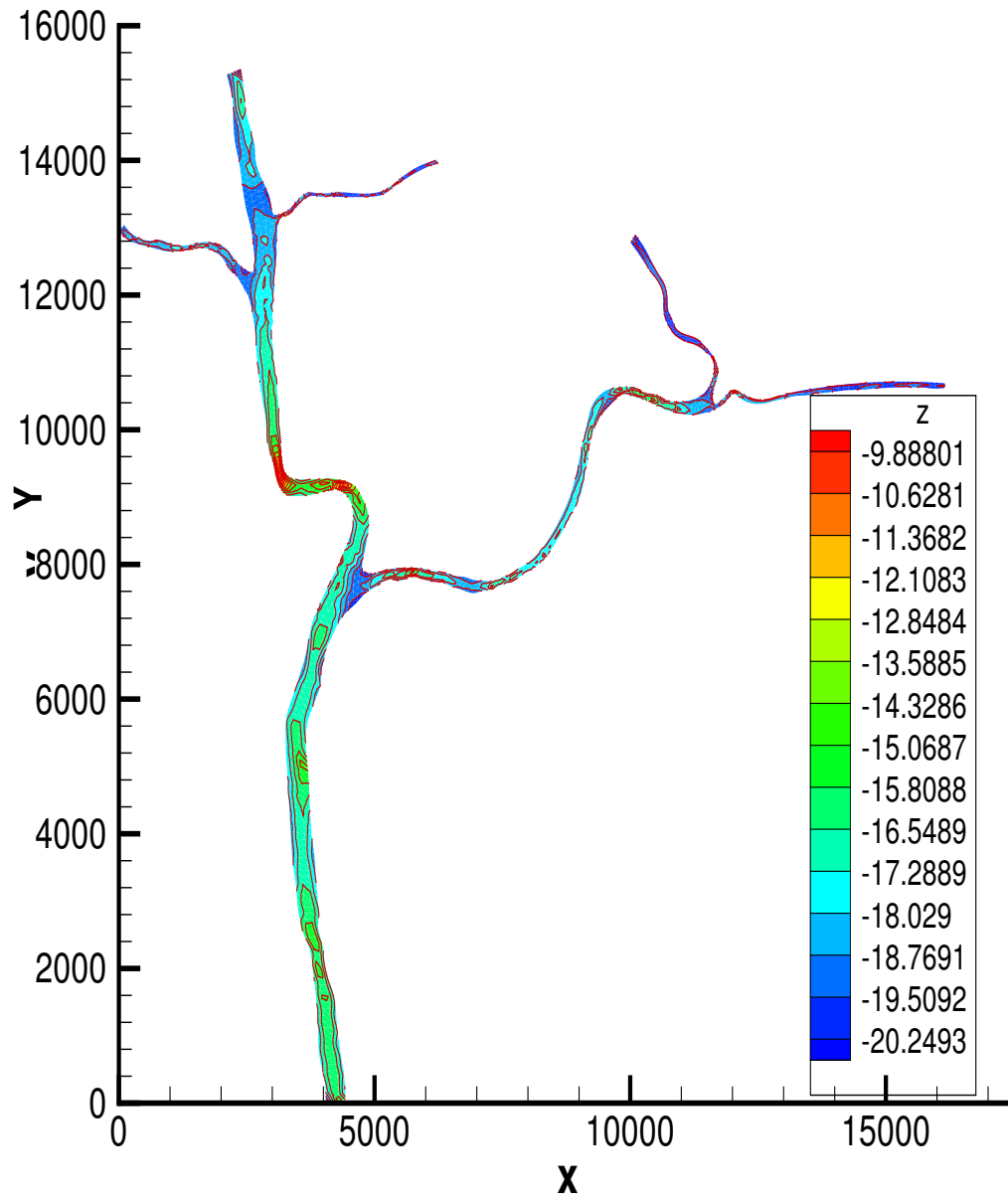


Figure 7.5: The bathymetry in [m] of the domain of study of the Po River Estuary

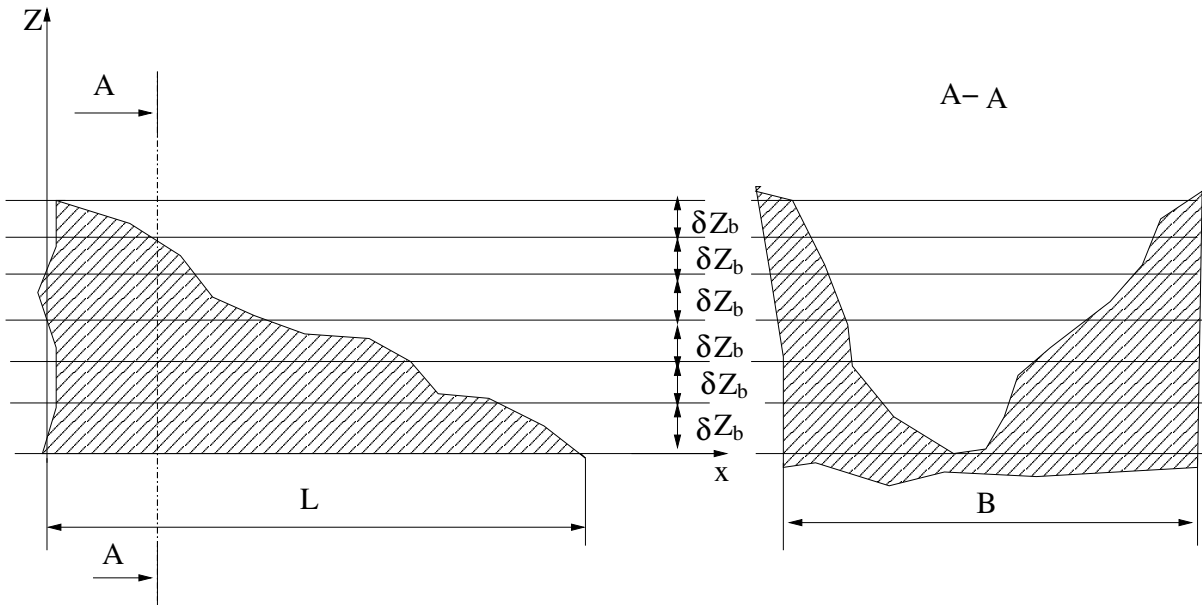


Figure 7.6: Sketch of the channel bed subdivided into several layers: L is the length and B is the width of the cross section of the channel

It is well known that the $k - \epsilon$ turbulence model needs small time steps, while the bed morphology (solid phase flow) needs a long time simulation. The model uses the sub-cycling strategy in the mind of saving computation time. Therefore several time steps have been set as shown in the flow chart of figure 7.7: $\delta t = 60[s]$ for the pure hydrodynamic [see sections 5.1.4-5.1.4], one day ($\Delta \tau = 24$ [hours]) for the solid phase flow (transport of sediment) [sections 7.4.1, 7.4.2, 7.4.3]. It is worthwhile to notice that the time step for passive scalars, Δt , is a multiple of $\delta t = 60[s]$ [Eq. 4.17].

conducted and the accuracy of numerical results were compared.

Figure 7.8 shows the comparisons of the computed and observed flow discharge at the tide gauge North-Tolle (NT) during one year, from January to December 1999. The observed discharge is greater at November corresponding to precipitation maxima. The model predicts well the total water discharge (the model does not account for meteorological conditions such as precipitation, and this could explain the discrepancy between computations and observations during this period).

Figure 7.9 shows the comparisons of the computed and observed tidal elevations during the flood at different tide stations. As indicated, the model predicts the tidal elevations with good accuracy. The figures 7.10, 7.11, 7.12, 7.13, 7.14 and 7.15 show the comparisons of the computed and observed flow velocity magnitude at different tide stations and different vertical layers position at respectively free-surface, $0.8H$, $0.6H$, $0.4H$ and $0.2H$. Good agreement is found between computed and observed velocity distributions and the largest discrepancy is found at the stations ST1 and ST2 near the open boundary at the South-Tolle1 (ST1) (this may be due to the conjugate effects of wave and curvature effects on the flow in the so-called *Tolle* channel branch).

Figure 7.16 shows a typical ebbing flow pattern and flooding pattern in a section of the domain of study. The hydrodynamics computations have shown the ability of the model. Thus based on these verifications, a long morphological simulation is performed to predict the seabed

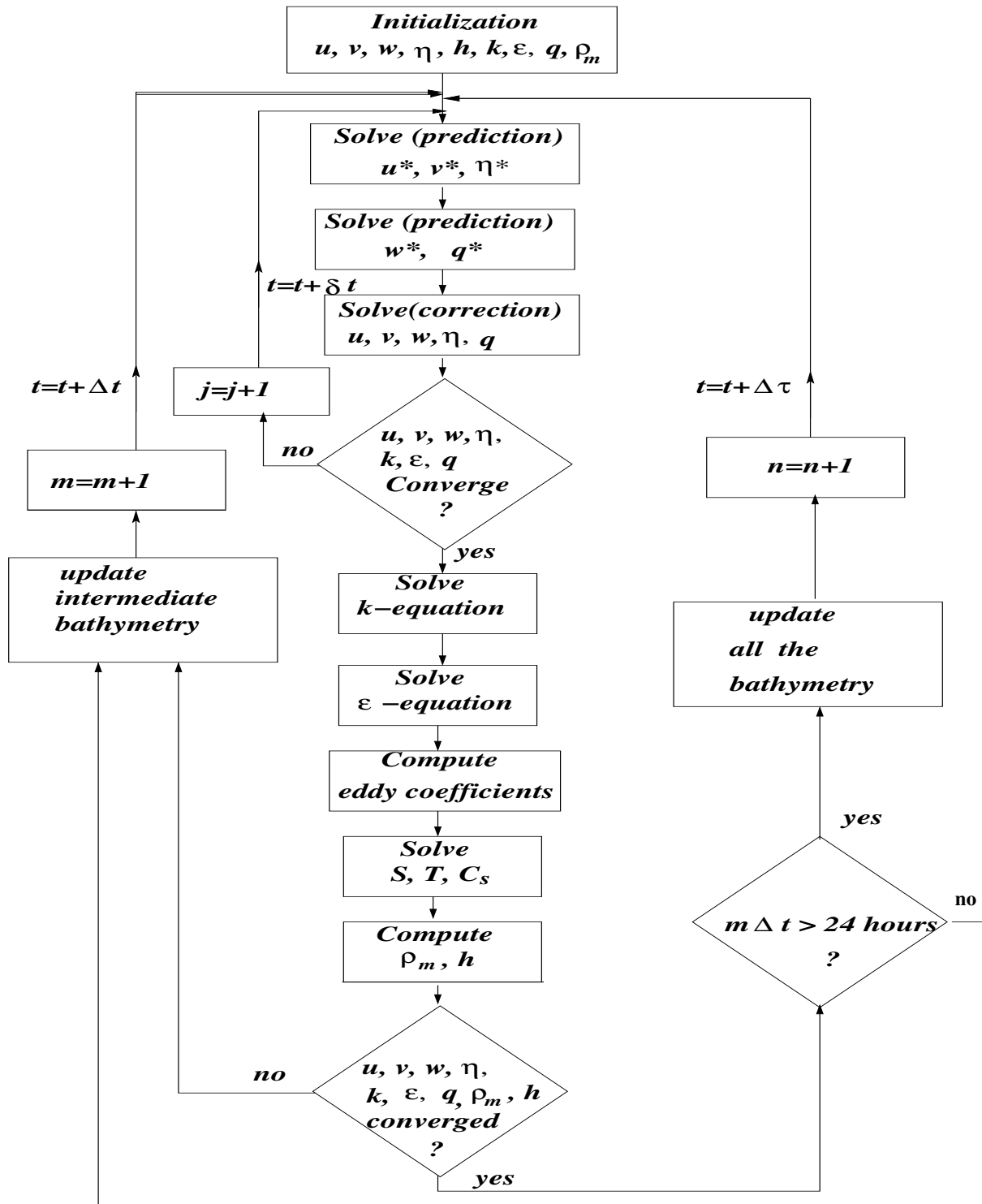


Figure 7.7: The flow chart of over all iterative procedure of the computations

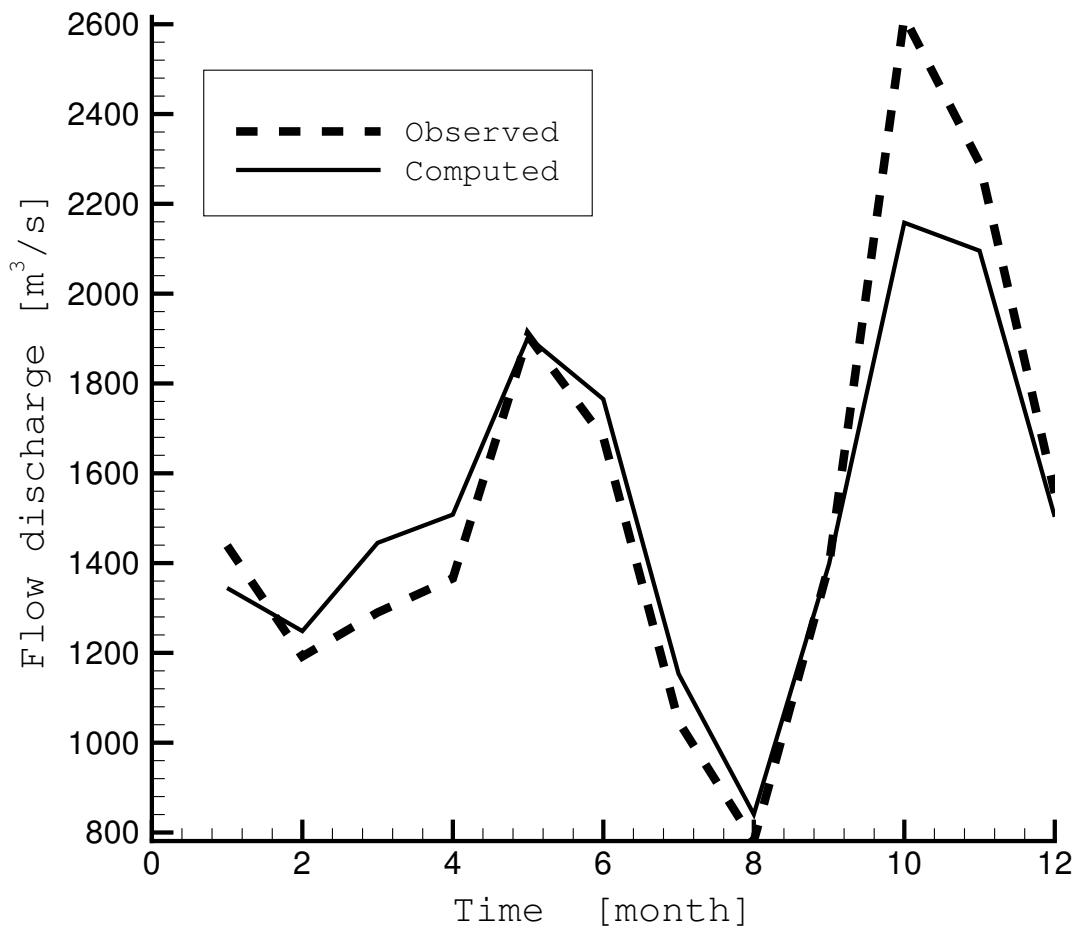


Figure 7.8: Comparison of the one year computed and observed flow discharge in Po River Estuary

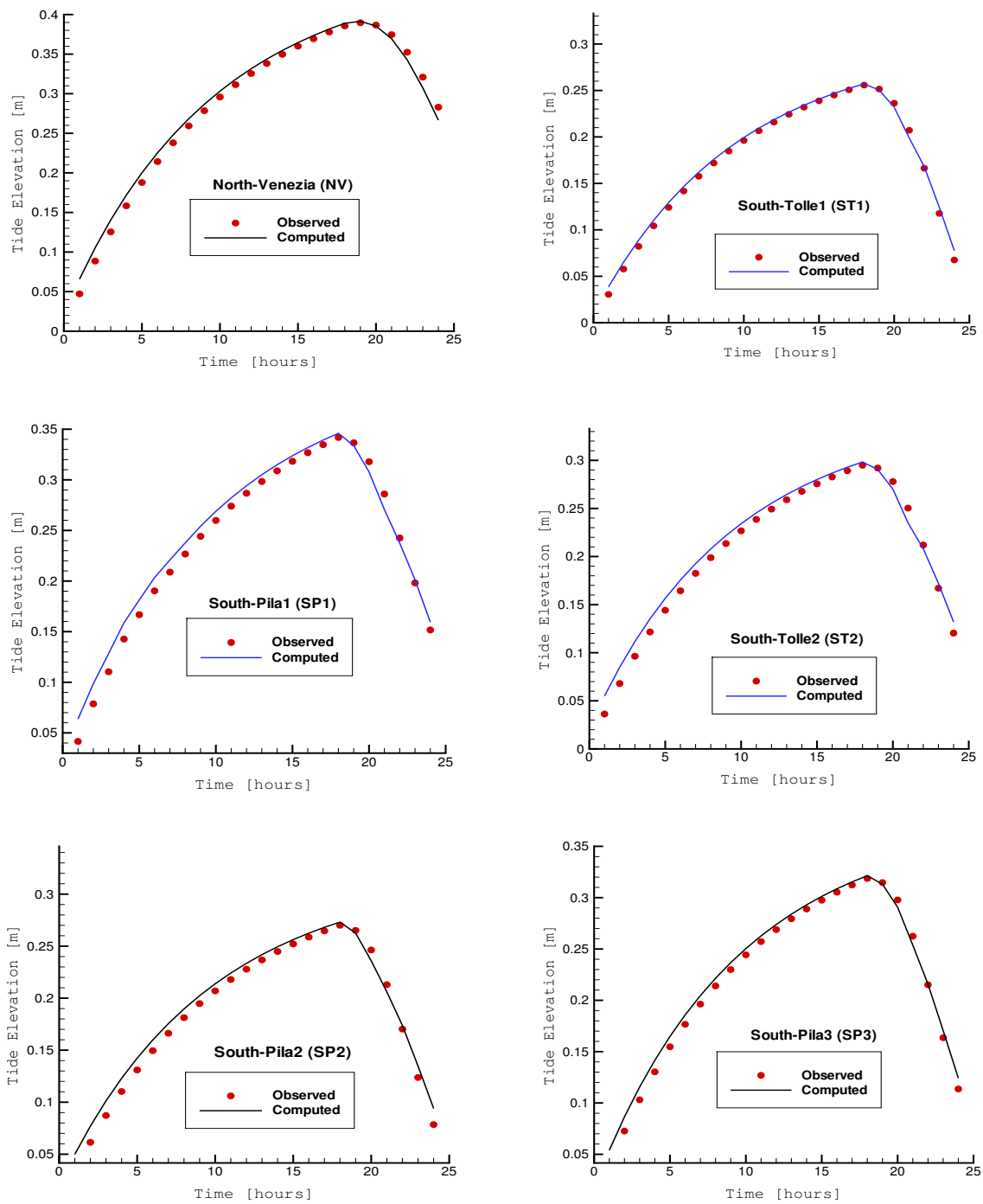


Figure 7.9: Comparison of the computed and observed tidal elevations at different locations in Po River Estuary (see fig. 7.4)

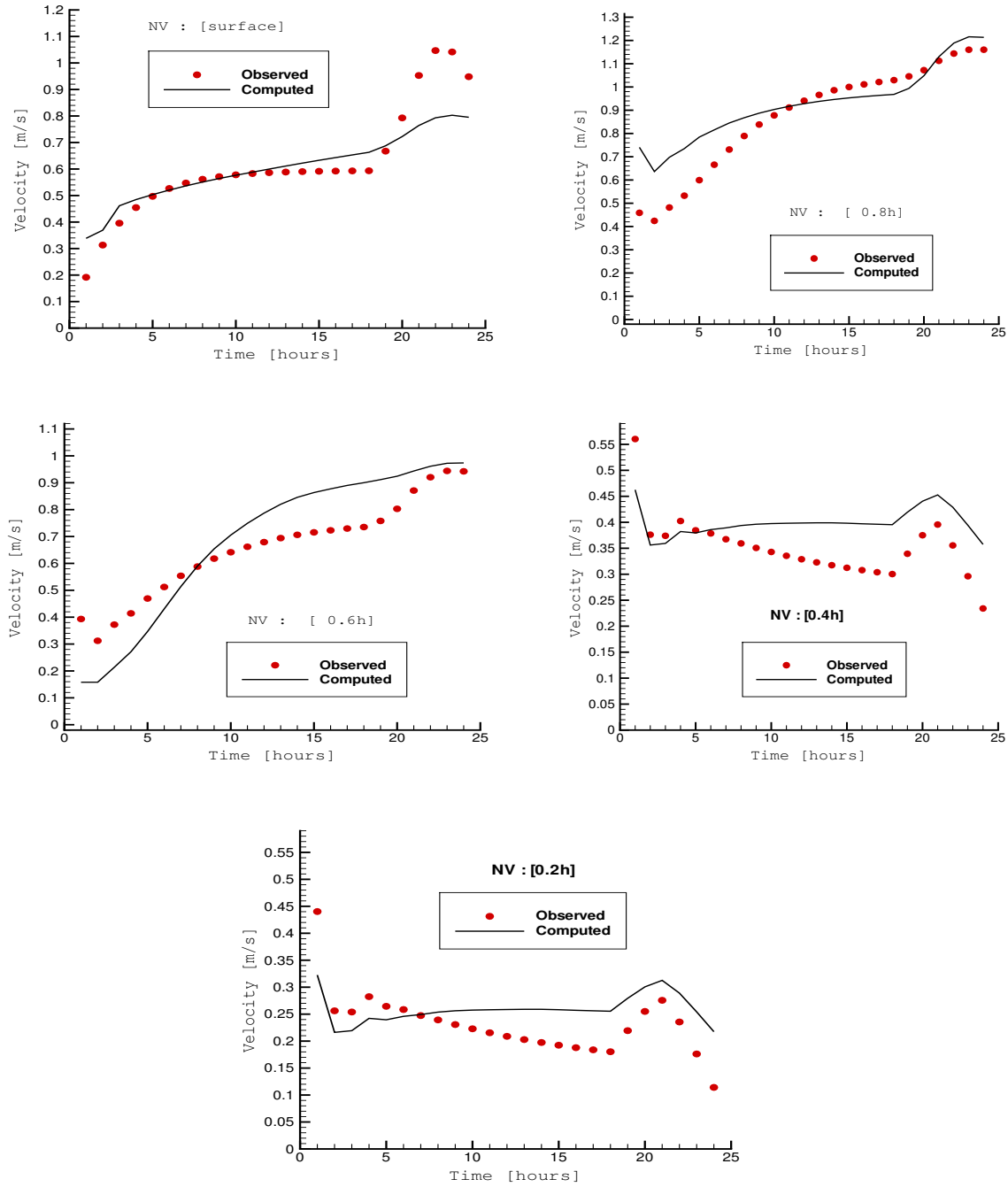


Figure 7.10: Comparison of the computed and observed current velocities at North-Venezia (NV) station in Po River Estuary (see fig. 7.4)

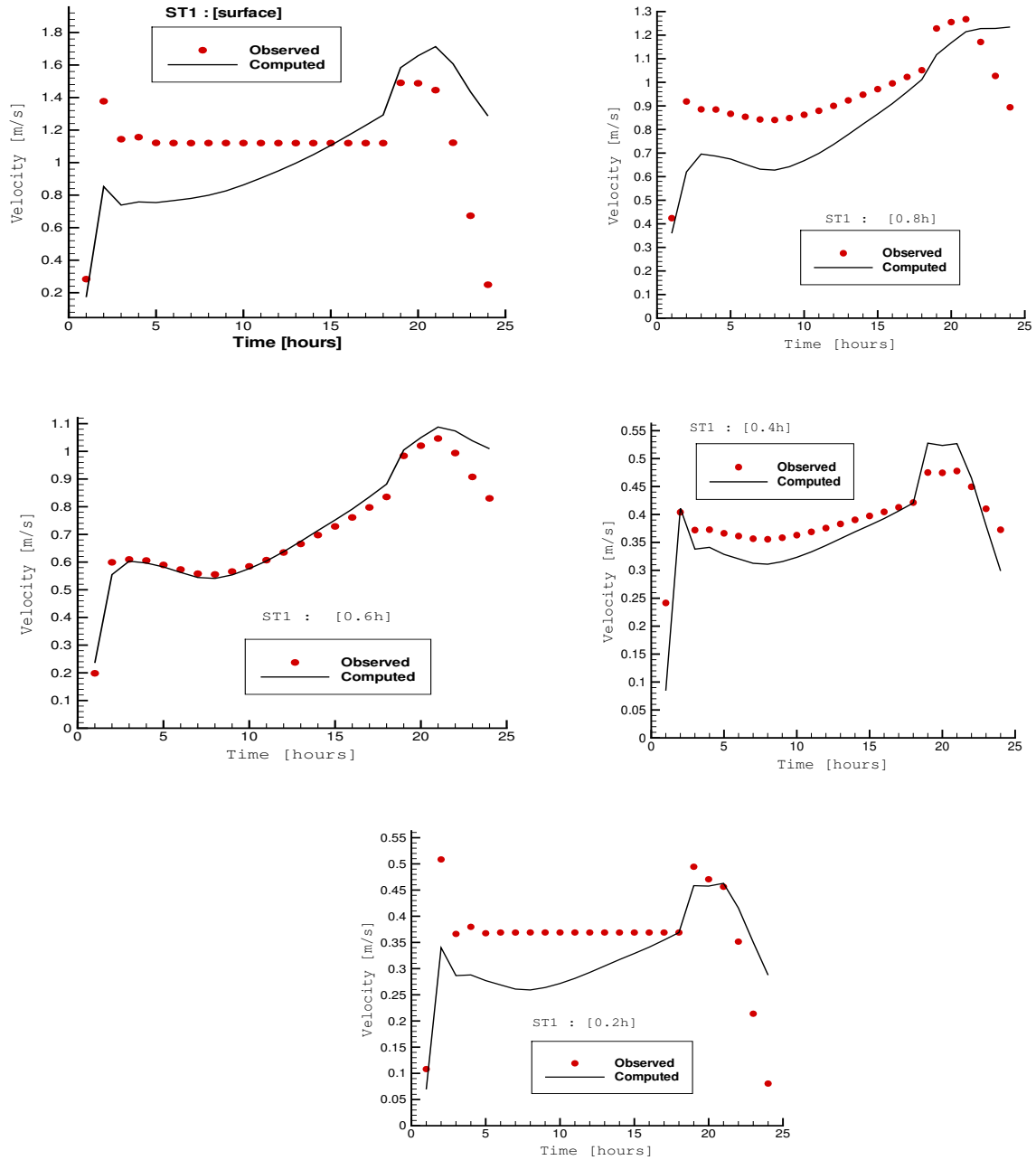


Figure 7.11: Comparison of the computed and observed current velocities at South-Tolle1 (ST1) station in Po River Estuary (see fig. 7.4)

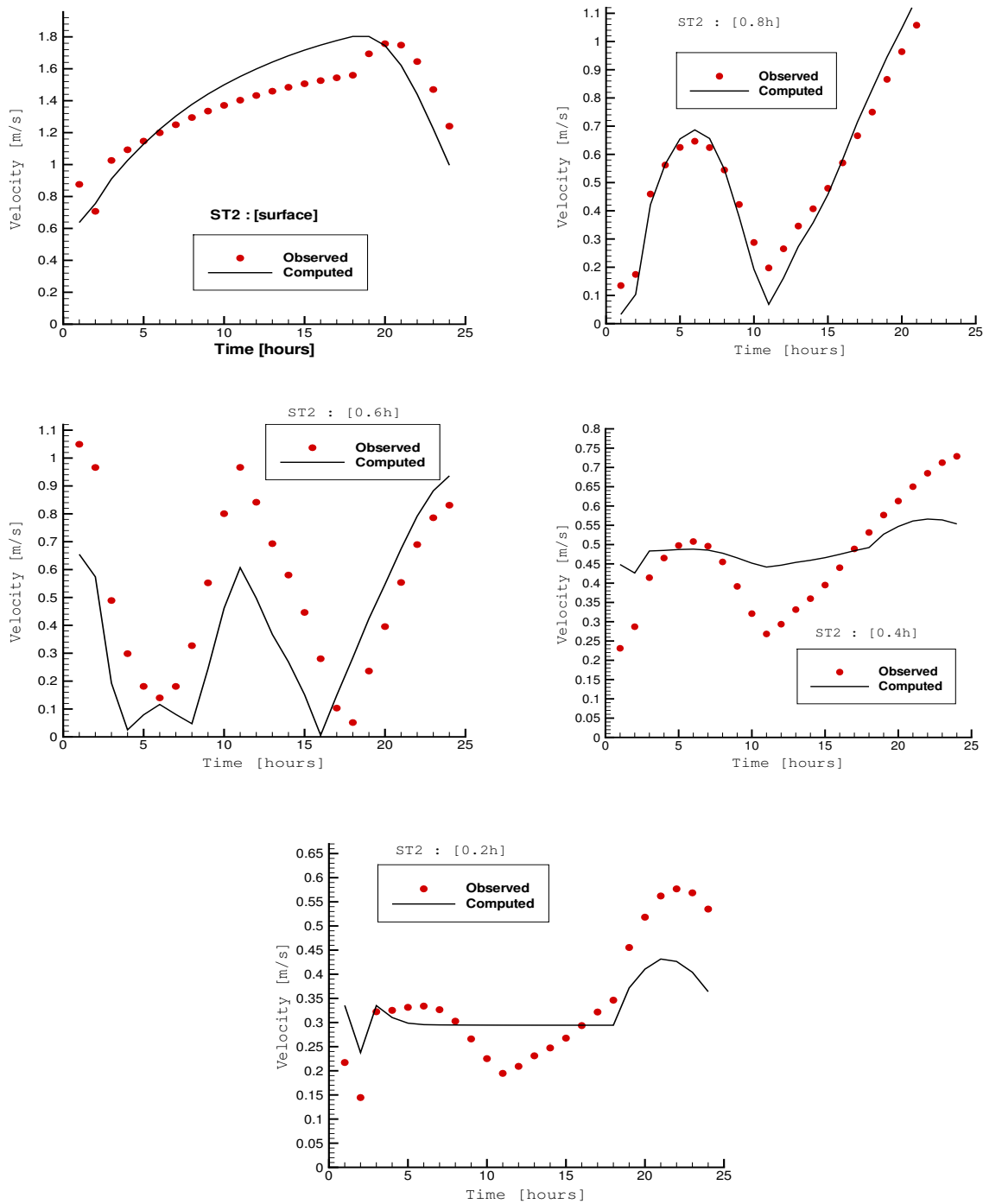


Figure 7.12: Comparison of the computed and observed current velocities at South-Tolle2 (*ST2*) station in Po River Estuary (see fig. 7.4)

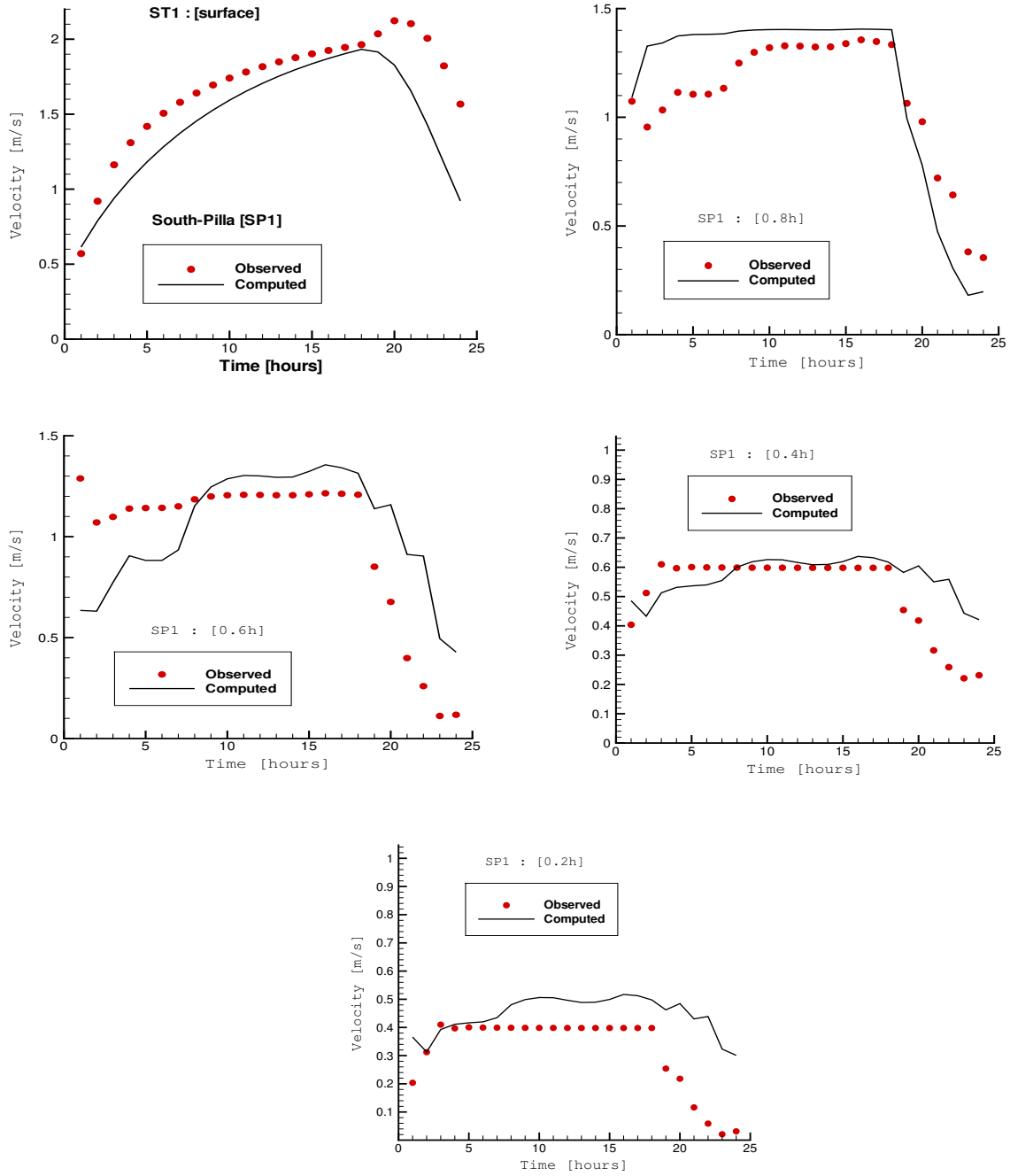


Figure 7.13: Comparison of the computed and observed current velocities at South-Pilla1 (SP1) station in Po River Estuary

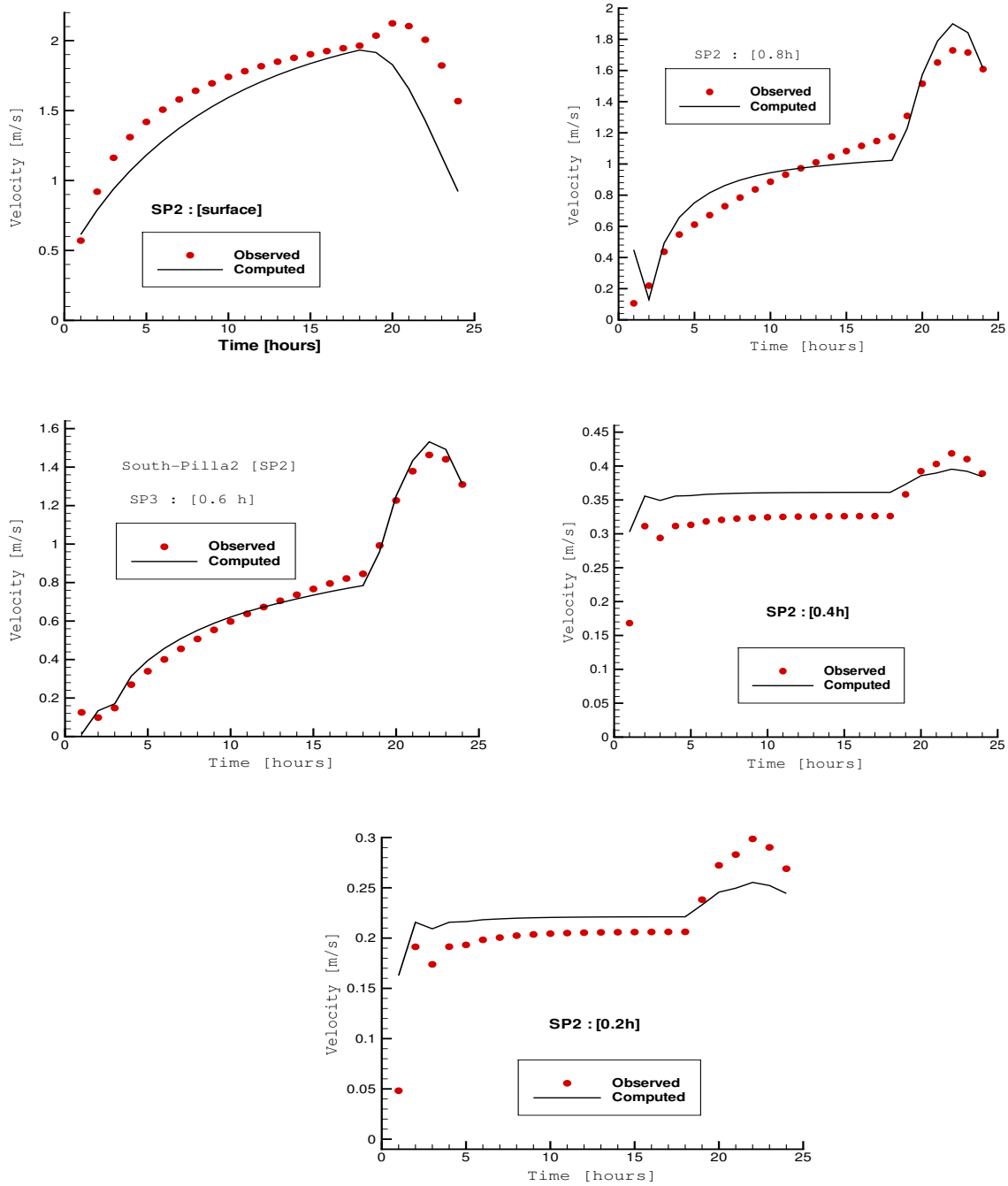


Figure 7.14: Comparison of the computed and observed current velocities at South-Pilla2 (SP2) station (see fig. 7.4)

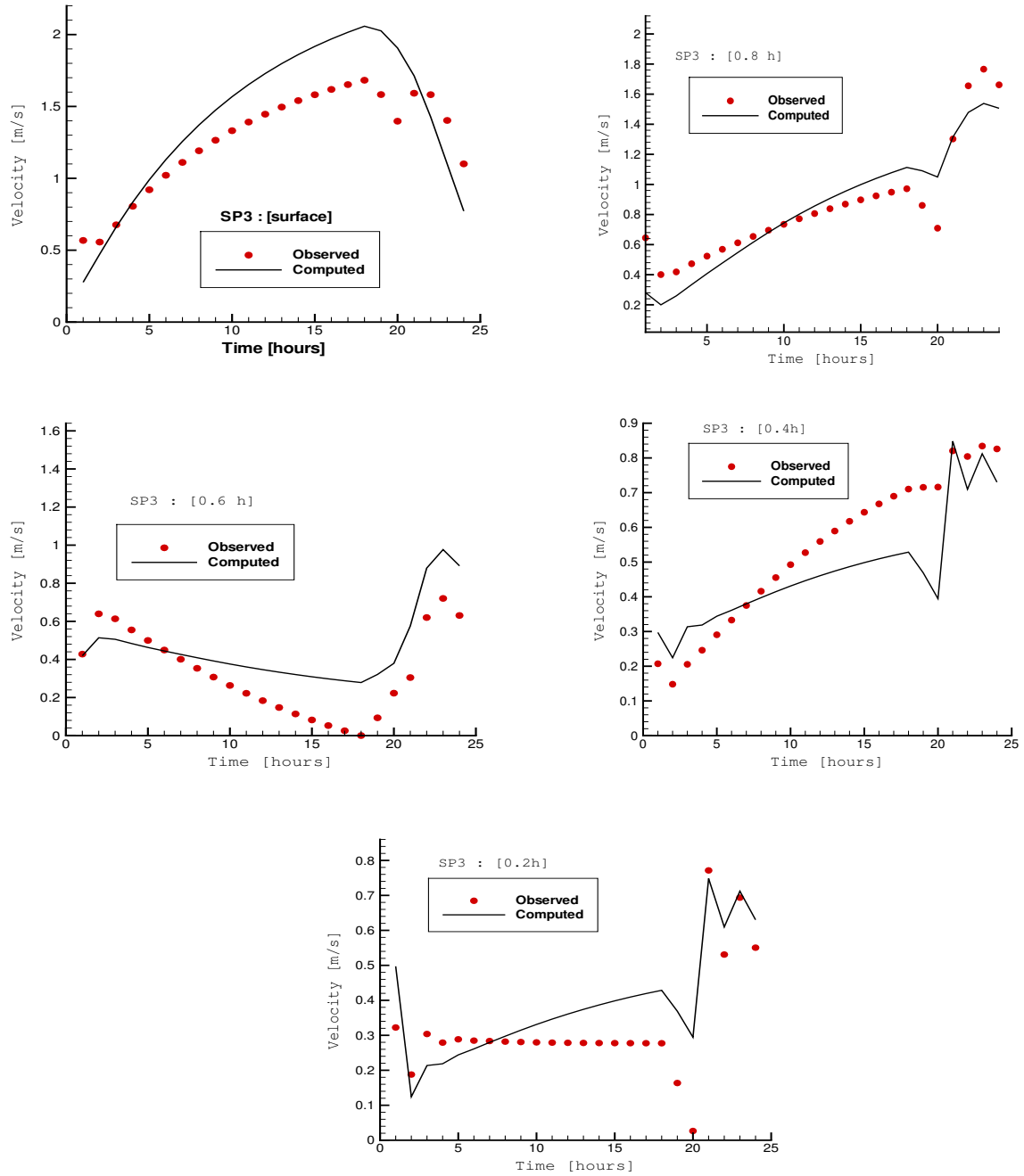
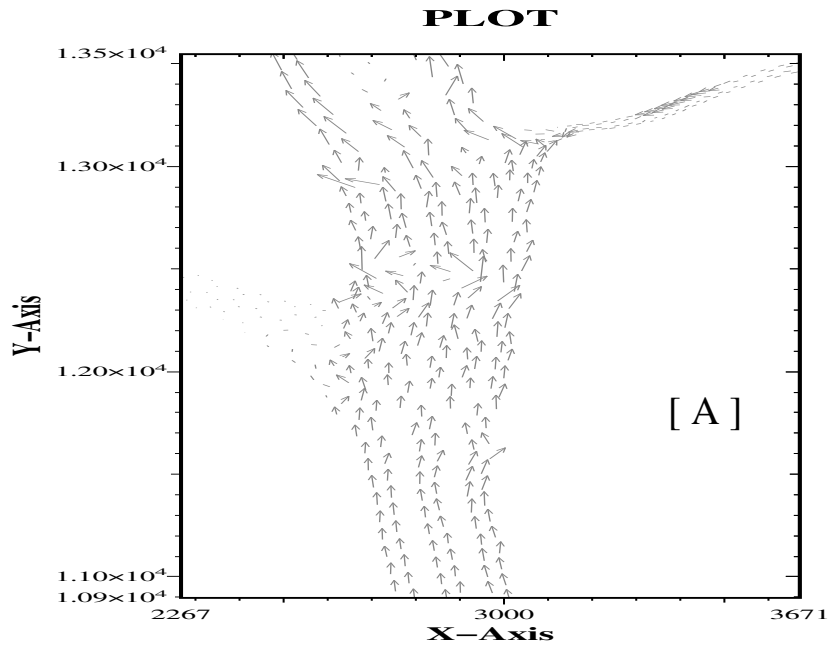


Figure 7.15: Comparison of the computed and observed current velocities at South-Pilla3 (*SP3*) station in Po River Estuary (see fig. 7.4)

Thu Apr 28 19:51:32 2005



Thu Apr 28 19:50:27 2005

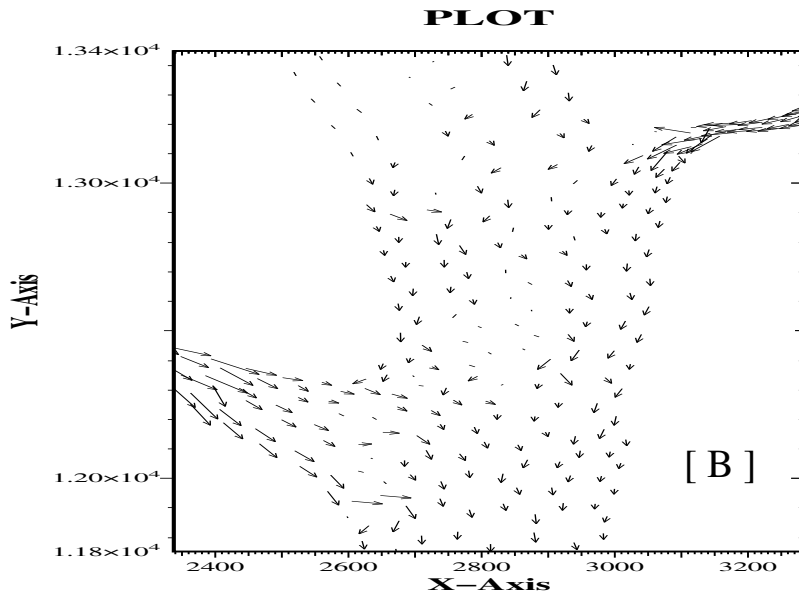


Figure 7.16: Flow pattern at the free surface in a zone of the domain of study in Po River Estuary at: A) during ebbing; B) during flooding

evolution, by taking into account the salt and temperature distribution with the related buoyancy effects on the fluid flow. A wet spring current was chosen for one-year simulation period.

At first, the initial temperature $T_0 = 22.5^\circ\text{C}$ and zero sediment and salt concentration were set in the entire modeled area as respectively the initial sediment concentration and salinity (see [56]). An equilibrium distribution is achieved after about one month simulation, and these values were re-applied as initial sediment, temperature and salinity to predict seabed evolution. Figure 7.17 shows the predicted profiles of respectively the density, temperature and salinity distribution at the selected gauge stations. Figure 7.18 shows the overall channel temperature distribution at 3 month simulation. These figures indicate that the steady state is reached after 3 month simulation. The upper the layer the smaller the density and salinity, as the higher the temperature. The density profile at the river inlet station North-Venezia (see fig. 7.4) is quit constant over the water depth. Moreover the maximum difference between pore water density (ρ) and water density, ρ_0 , is about 19 [kg/m³] in the channel. This suggests that the Po River Estuary is a stable and fairly stratified estuary (see [41]). Figures 7.19 shows the predicted salinity distribution in the overall channel after one year simulation at the layers respectively near to the free-surface and bottom. This figure indicates that the salinity is maximum near the open sea boundary and minimum at the river inlet. The bottom liolayers are more saline than free-surface layers, as the sea-water is encounter in the lower part of the channel (towards the open sea boundaries). This is in good accordance with the field observation.

Figures 7.20 shows the predicted contours of the suspended sediment concentration distribution at layer level of $z = 0.2H$ after one year simulation using: (A) a single pick-up and deposition function; (B) two mutually exclusive functions for deposition and re-suspension proposed by Krishnappan and Engel in Eqs. (7.24), (7.25) and (7.30); (C) the analytical function in Eq. (7.13) at the reference level $a = 0.01h$. It indicates that the two-function solution is closer to the analytical solution, while the single function over-predicts the suspended sediment at the bottom. This relies on the fact that the two-function algorithm accounts for the fraction of deposited *bed-load* sediment and the re-suspended one in addition to the updating process in Eq. (7.31). Figure 7.21 shows the suspended sediment concentration (SSC) distribution respectively after six months and one year simulation. It indicates that most of suspended sediment stand at the upper layers, while the sediment distribution is influenced by the climate and season (dry or wet season). The one year simulation is conducted from May 1999 to April 2000, when the river flow is lower during dry season, with the higher precipitation leading to higher pick-up of sediment. The addition of a depth-varying shear stress from energetic waves ($H_s = 2$ [m]) and higher precipitation significantly increased dispersal of both the unflocculated and flocculated material, with the flocculated material being confined to the shallowest sites near the coastline. The observed suspended sediment discharge is about 16×10^6 . The computed mean suspended sediment discharge using a single function was found to be about 22×10^6 tonnes/year. While using the two-function the suspended sediment discharge was found to be about 18×10^6 tonnes/year with mean SSC of about 250-420 [mg/l] in the main channel (Panaro-Pilla) and about 120-340 [mg/l] in the secondary distributaries (South-Pilla and South-Tolle). Thus two-function SSE is found to agree with the field observations. Figure 7.22 shows the bed deformation due to deposition-re-suspension and erosion from the river upstream boundary toward the PRE mouth branches progressively. It is found that when using the single function [see Eq. (7.18)], the bed delta is over-predicted of about 8 to 15% compared to the two-mutually exclusive power-law functions proposed by Krishnappan and Engel [see Eqs. (7.24)-(7.25)]. It should be emphasized that the single function accounts only for the simultaneous deposition and erosion process. This is the characteristic behavior of coarse sand particles, which is found to be different from that of fine cohesive sediment particles. The point is that by assuming the

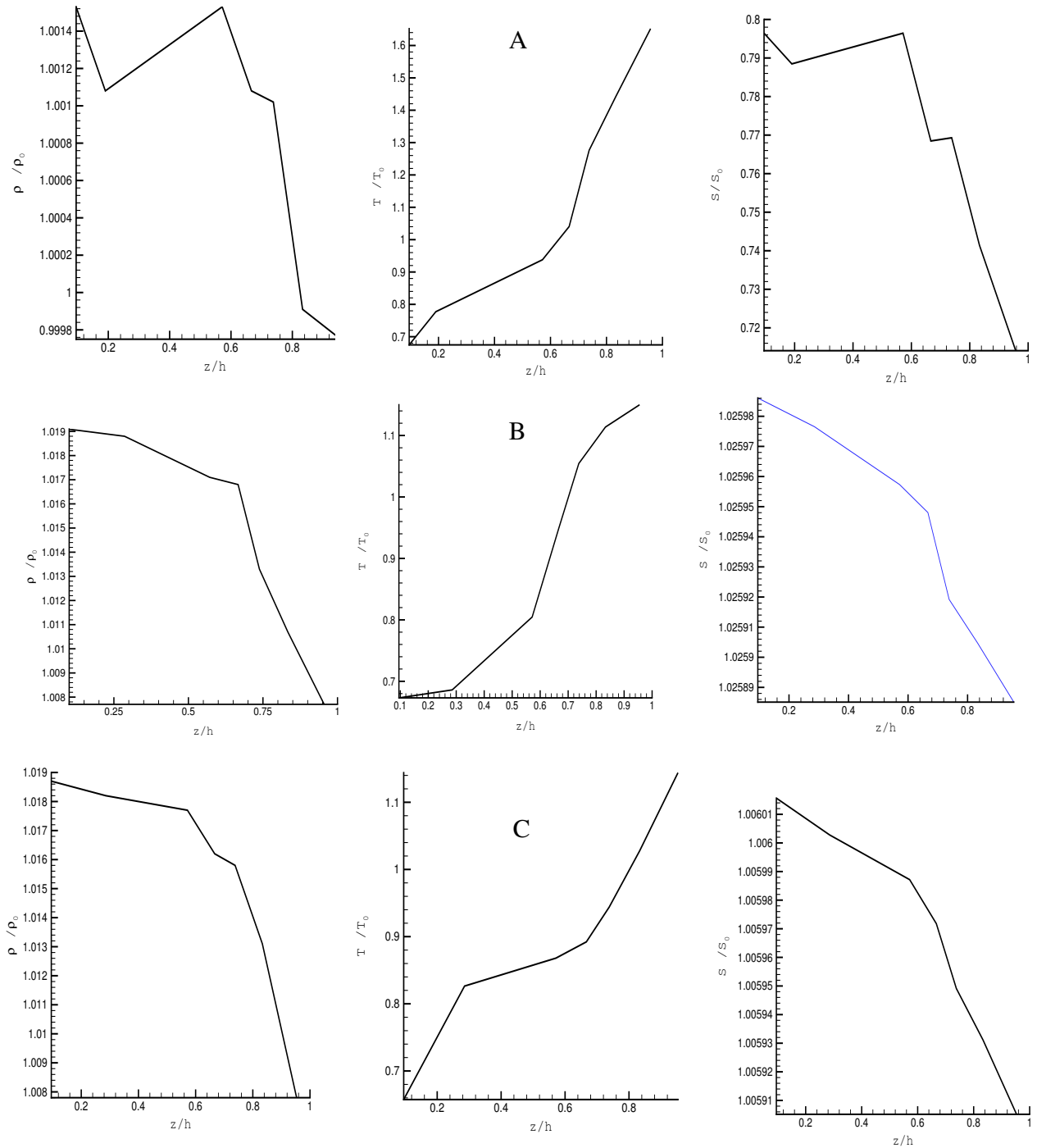


Figure 7.17: Profiles of predicted density, temperature and salinity after 3 months simulation at the selected gauges stations in Po River Estuary (see fig. 7.4): A) North-Venezia (NV) ; B) south-Tolle1 (ST1); C) south-Pilla1 (SP1)

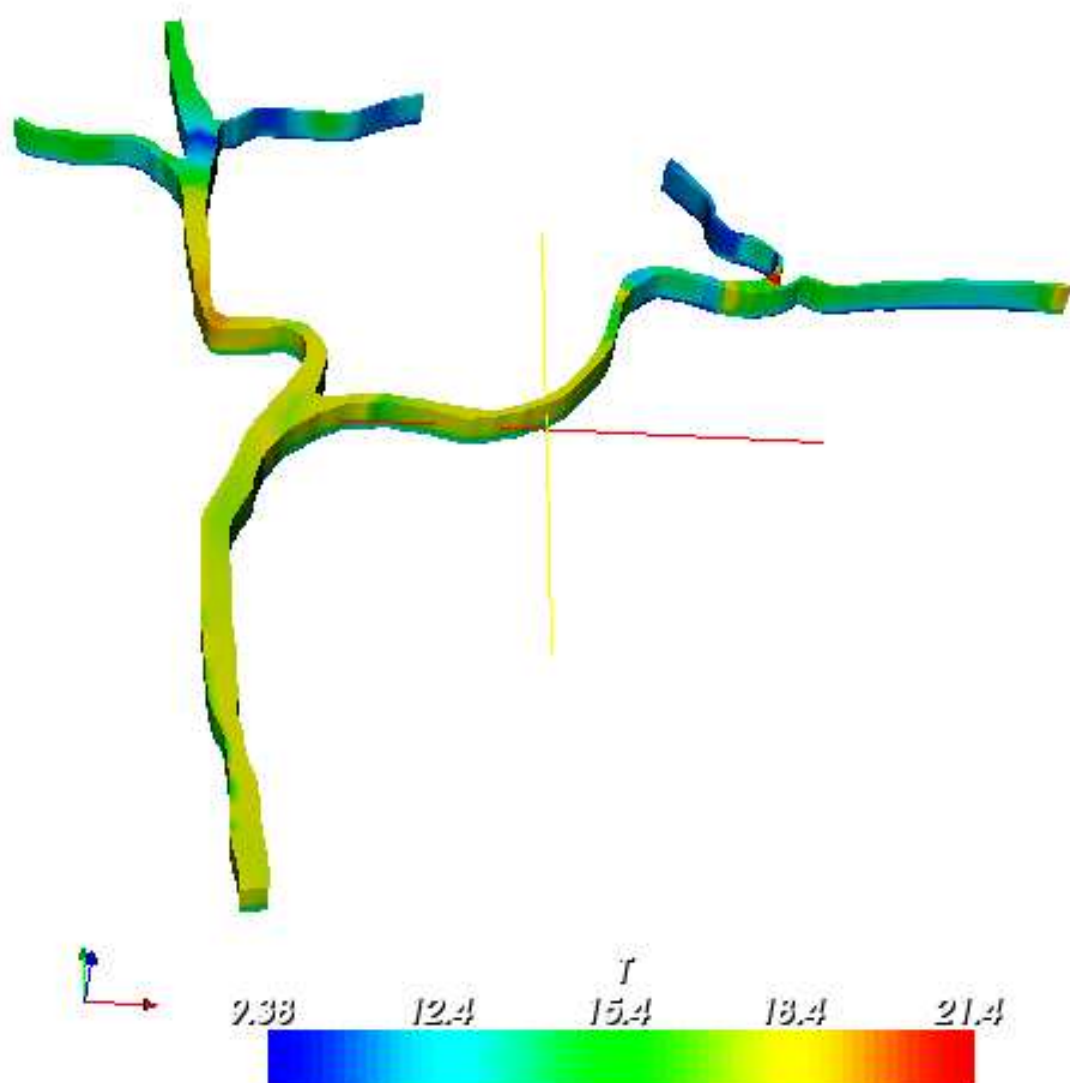


Figure 7.18: Prediction of temperature [$^{\circ}\text{C}$] after 3 months of simulation in Po River Estuary

same behavior between these two different kinds of particles, prediction does not fulfill the field observations and experiments (see Chapter 2). Indeed, the fine cohesive sediment behavior is quite different from the common coarse sand particles. The power-law two functions accounts for the mutually exclusive processes between the fraction of re-suspended or eroded sediment and the fraction of deposits which stands over the bed. This is very important and more useful for good prediction of the bed consolidation and/or fluidization.

In the sequel we will use the two-mutually exclusive functions of re-suspension/deposition in the framework of simulating the consolidation and/or fluidization processes. Figures 7.23, 7.24 and 7.25 show respectively the predicted contours of the bed-mud layer, the partially consolidated and the complete consolidated bed thicknesses after three-month and one-year simulation. These figures indicate that the bed deformation (deposition) moves progressively from the river upstream toward the PRE mouth branches (open-sea boundaries). The mean bed-mud layer thickness is about $4 \sim 13$ [cm/year], the partially consolidated one is about $2 \sim 4$ [cm/year] and the fully consolidated is found to be about $4 \sim 9$ [cm/year]. The mean deposition rate in the main channel is about $8 \sim 20$ [cm/year]. The amount of bed load (i.e. fresh deposits mud) being about 9×10^5 tonnes/year, which is about 7% of the total suspended sediment discharge. This confirms the experiments of Li and Zhang [72] and Van Rijn [119] who have found that the rate of suspended load transport is much larger than the rate of bed-load transport for fine particles, the ratio of the bed load compared to the suspended sediment discharge is found to be closer to the field observations. The prediction of deposition/re-suspension using two different approaches leads to a non-negligible difference in the results. The analysis showed that the consolidation/fluidization process may have important influence on the prediction of bed morphology, while the simulation of bed morphology using three-layer approach is a first attempt to model these processes in detail within a numerical model.

7.7 Concluding remarks

A novel 3D numerical model has been built for the cohesive sediment transport and applied for simulating temporal behavior of stratified water bodies with environmental forcing, by solving the SWE for incompressible flow using the hydrostatic assumption for pressure. Processes modeled include heat, salt and sediment distribution, tidal forcing, surface wind forcing, inflows and outflows as well as the turbulence modeling for multiphase fluid-solid flow. The effects of salinity, temperature and sediment concentration are most dramatically seen during periods of simulation, leading to the stratification of the fluid flow. The micro-tidal PRE (i.e. tidal elevation < 2 [m]) is found to be a fairly stratified estuary, with the estuarine turbidity maximum (ETM) i.e. near bed concentrations of 200 up to 420 [mg/l]. An investigation of the Hawkesbury River [52], has verified that turbidity maxima can occur in micro-tidal estuaries, despite the concentrations of suspended sediment being significantly lower (i.e. ETM of 100 and 220 [mg/l]) in the Swan [51] and Hawkesbury River [52], respectively compared with 26000 [mg/l] in the Tamar River, UK. This suggests that in micro-tidal estuaries the dominant processes contributing to the generation and maintenance of the ETM could change. The insight gained through the present study agrees well with such arguments. In the present model, silty sediment erosion, deposition, re-suspension and seabed evolution have been taken into account as well as the consolidated bed layer. The new set of equations and algorithm proposed by Krishnappan and Engel [58] and the model developed by Chen *et al.* [20] have been applied for computing erosion and deposition of cohesive sediment transport in the Po River Estuary in Italy.

The performance of a composite model for cohesive sediment transport has been analyzed. This model accounts for the differences in the critical conditions for erosion or re-suspension and

deposition of fine sediment, as well as the *three bed-layers* at the bottom. The power laws used in this model allow to simultaneous erosion and deposition to occur only in a limited range of bed shear stresses at the bed. For the good representation of the estuary, the natures of silt movement from study works including field measurement, theoretical analysis and simulation tests have been introduced in the model. The water elevation, velocity field, temperature, salinity and sediment concentration profiles computed from the numerical models were compared successfully to the experiments and analytical solution. It is found that, by assuming the common coarse non-cohesive sediment behavior when modeling the fine cohesive sediment, the fresh-mud layer prediction is found to be over-estimated of about 8-15%. This suggests that the transport characteristics of the common coarse non-cohesive sediment is very different with respect to the fine cohesive sediment one. This agrees well with experiments found in the literature. The present model accounts for the three-component of the bed morphology (i.e. mud-bed layer, partially consolidated bed and the complete consolidated bed), from the fluidization and/or consolidation of the cohesive sediment on the channel bed. The prediction of deposition/re-suspension using two different approaches leads to a non-negligible difference in the results. The analysis showed that the consolidation/fluidization process may have important influence on the prediction of bed morphology.

This suggests that a realistic prediction must account for the bed fresh mud re-suspension into the model. Finally, the prediction of bed morphology using three-layer approach is a first attempt to model these processes in detail within a numerical model. This *three bed-layers* modeling sheds new light on a phenomenon not yet modeled in the existing numerical models for the cohesive transport in the estuaries.

The present model is found to predict realistically the fine sediment transport modeling in the PRE.

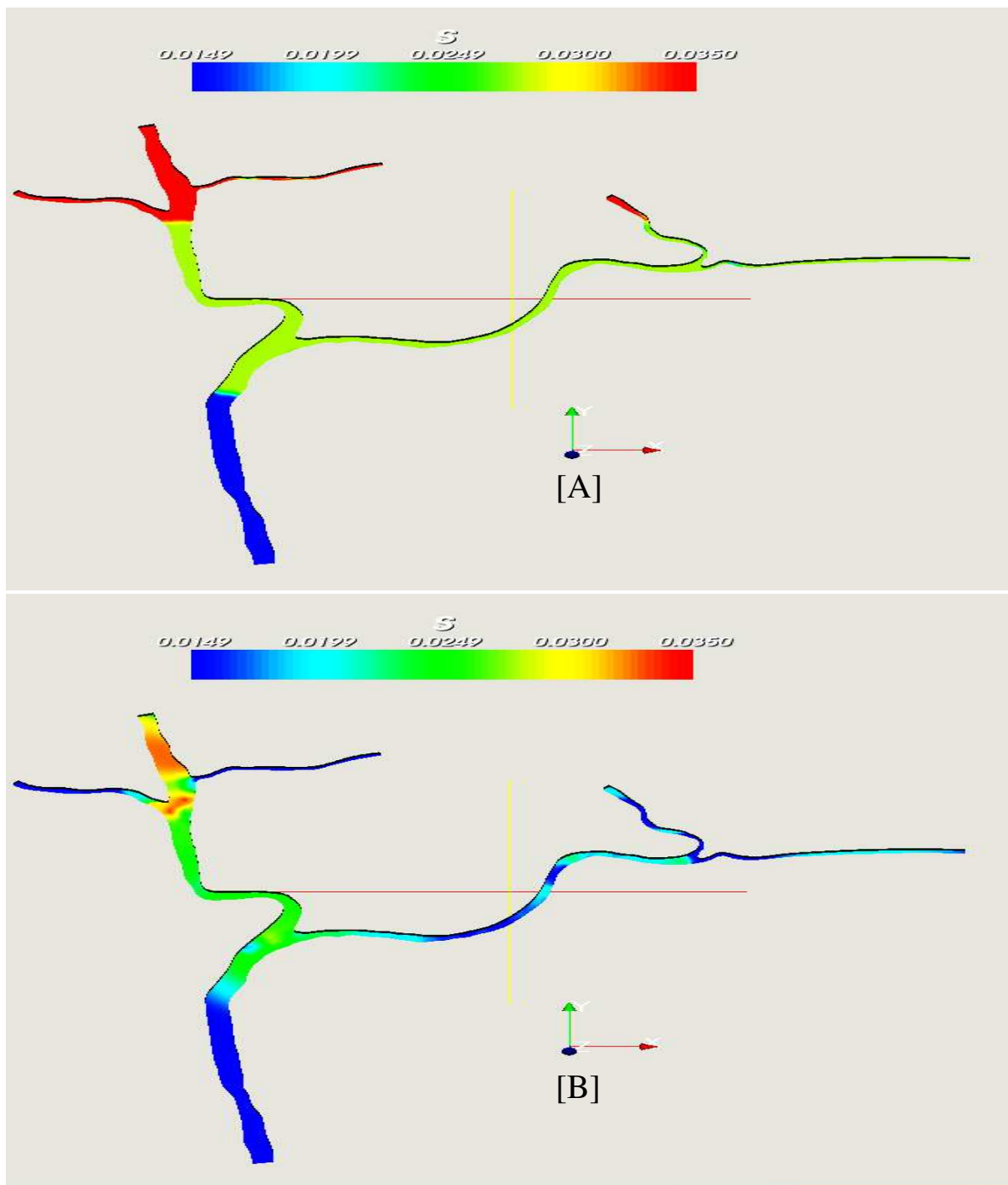


Figure 7.19: Prediction of salinity after three-months simulation in Po River Estuary : A) at layer level $z = 0.8H$; B) at layer level $z = 0.2H$

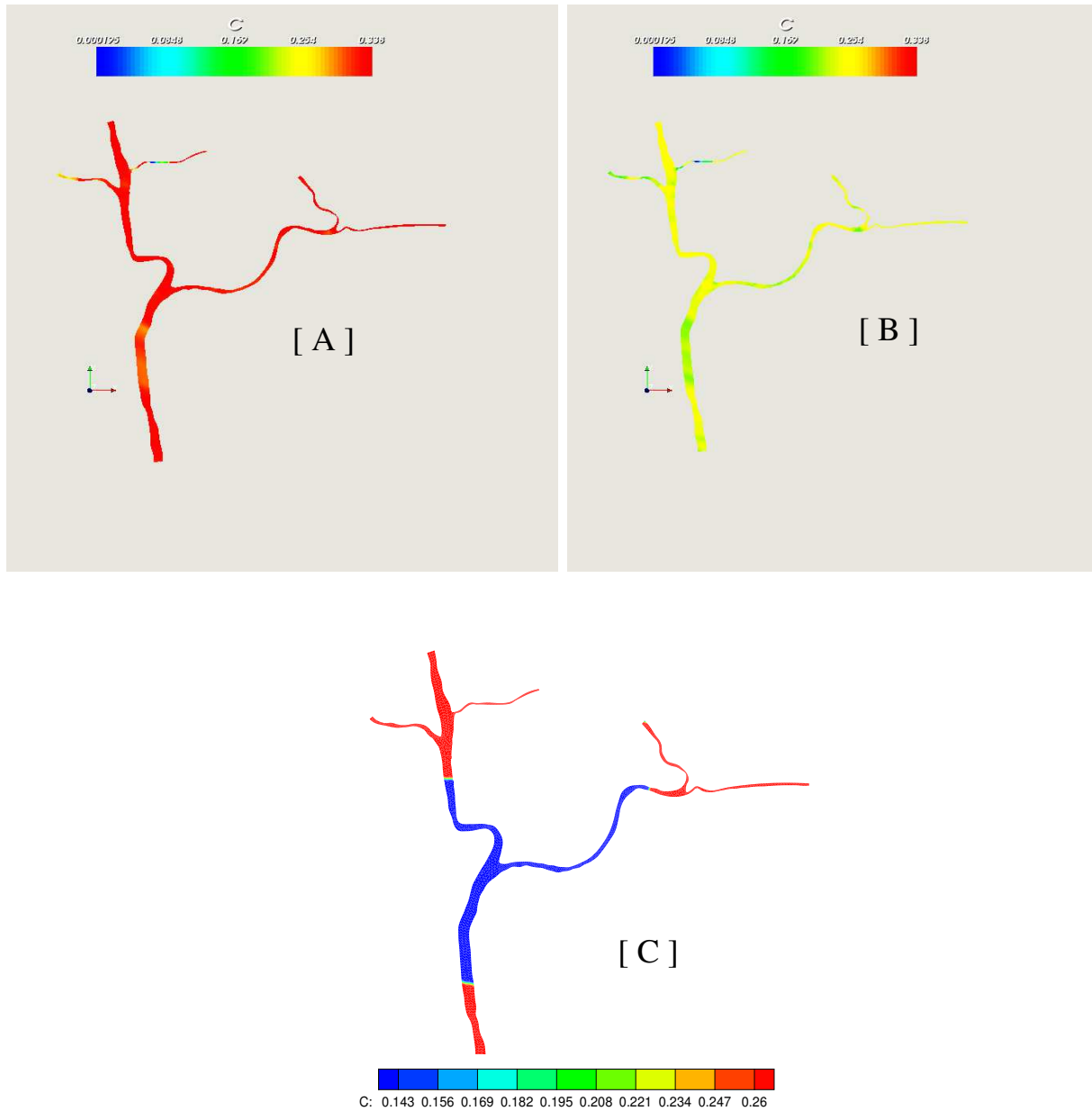


Figure 7.20: Suspended sediment concentration in $[\text{kg}/\text{m}^3]$ after one-year simulation in Po River Estuary at layer level $z = 0.2H$, using: A) single bed function Eq. (7.18); B) Mutually exclusive power-laws functions Eqs. (7.24)-(7.25); C) analytical solution Eq. (7.13)

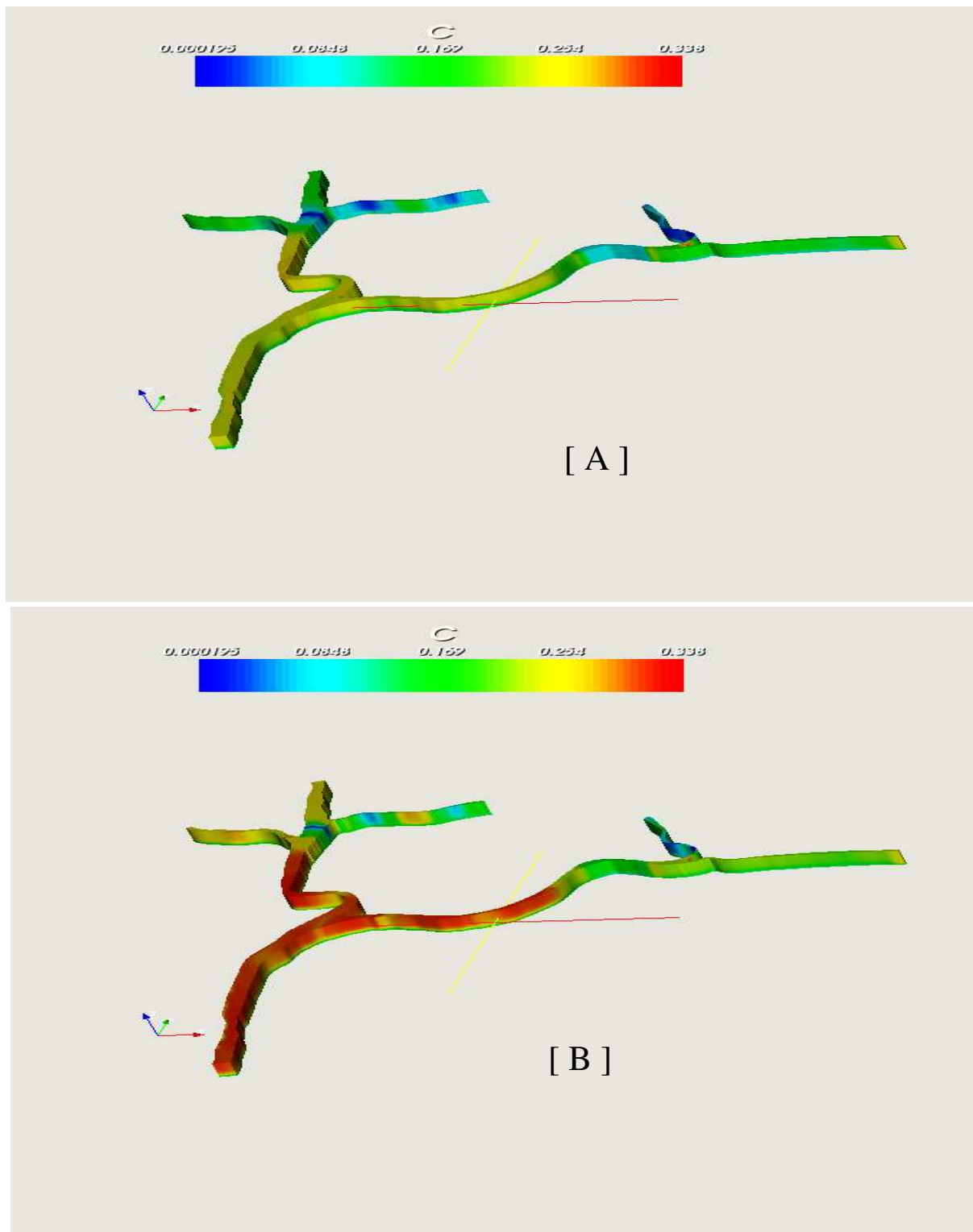


Figure 7.21: Predicted Suspended sediment concentration in [kg/m³] in Po River Estuary using the mutually exclusive power-laws functions Eqs. (7.24)-(7.25)

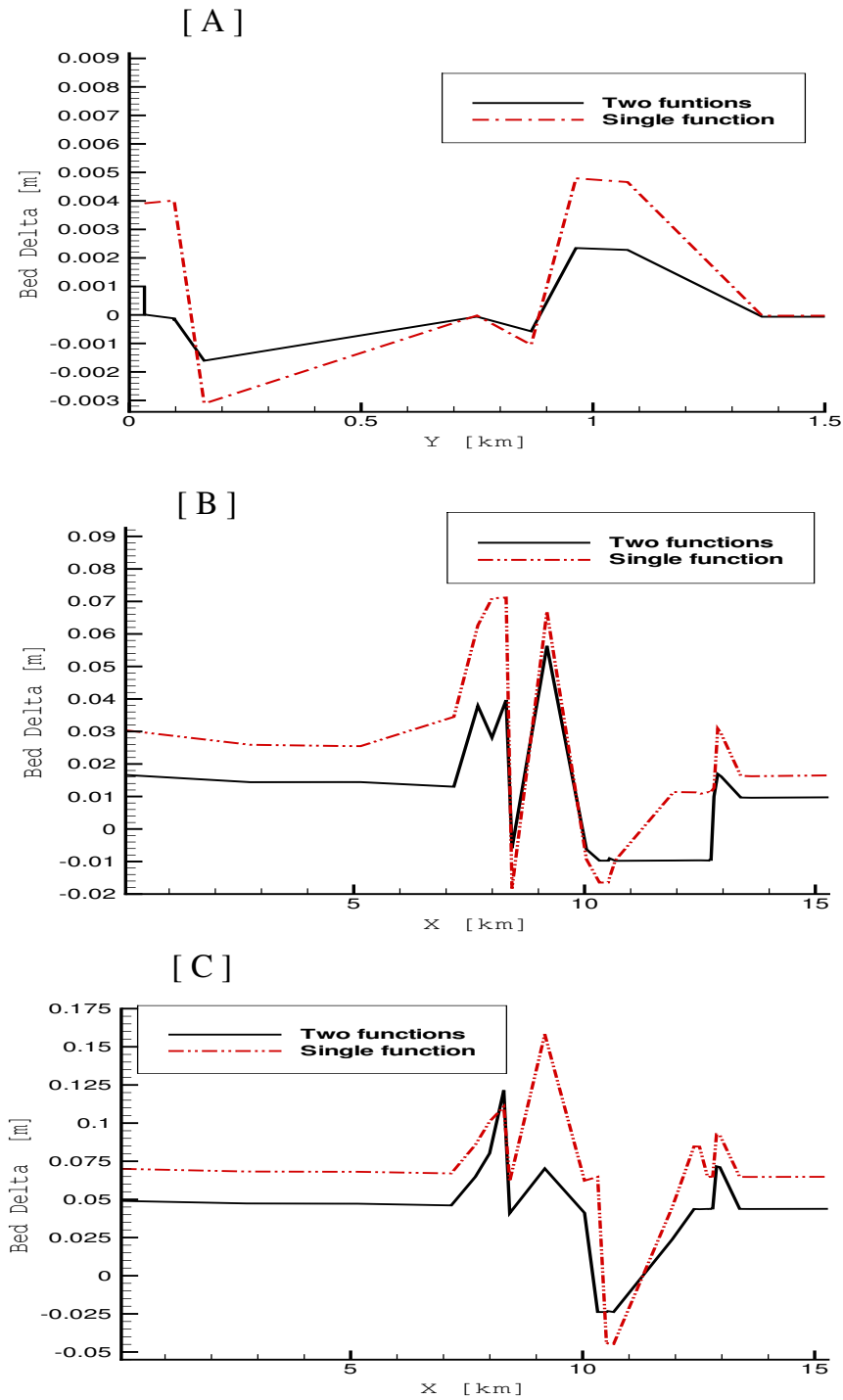


Figure 7.22: Simulated fresh mud-bed in Po River Estuary using power-law functions Eqs. (7.24)-(7.25): A) one month; B) three months; C) one year

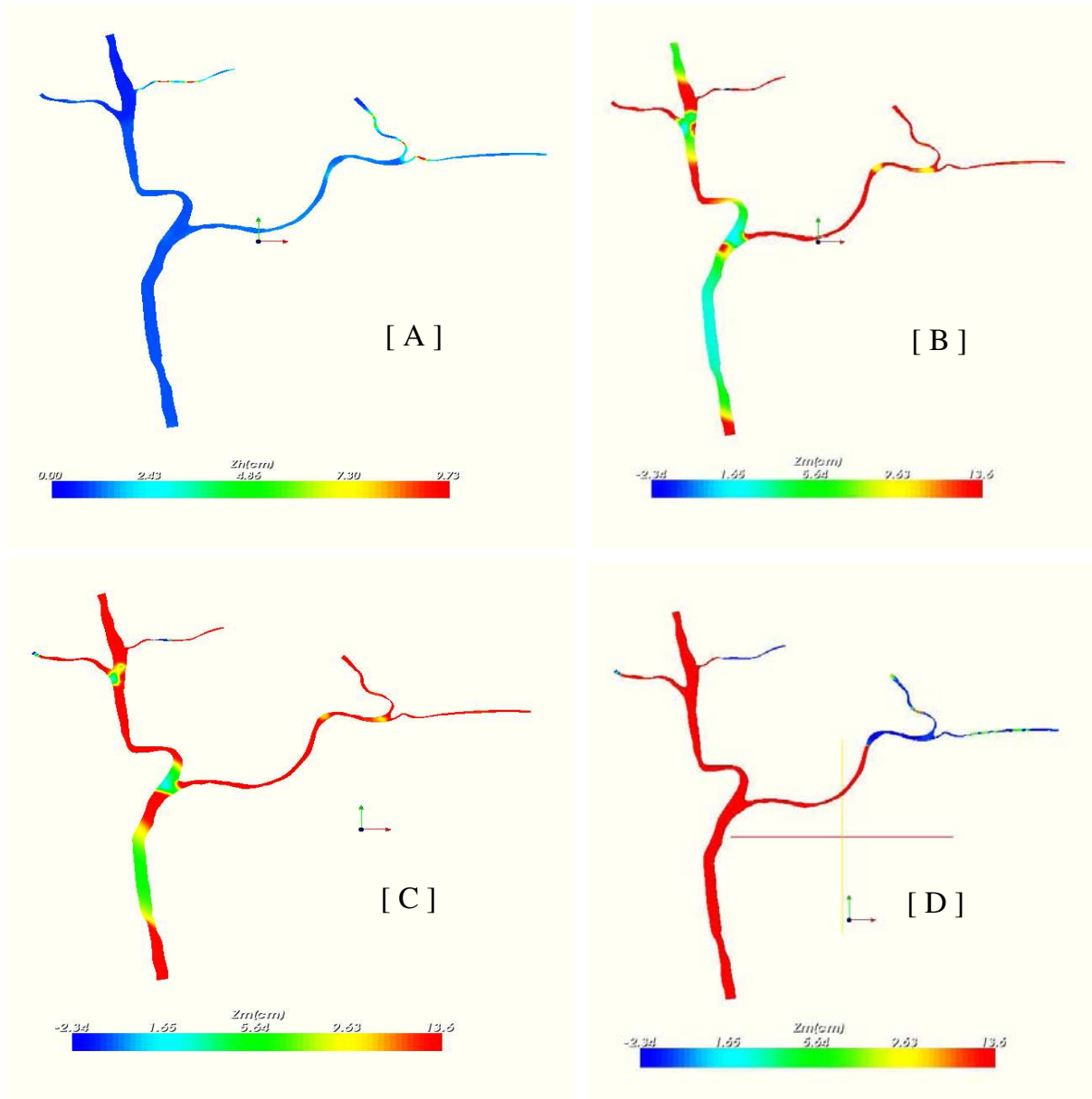


Figure 7.23: Contours of the fresh-mud bed in Po River Estuary using power-law functions: A) one month; B) three months; C) six months; D) one year

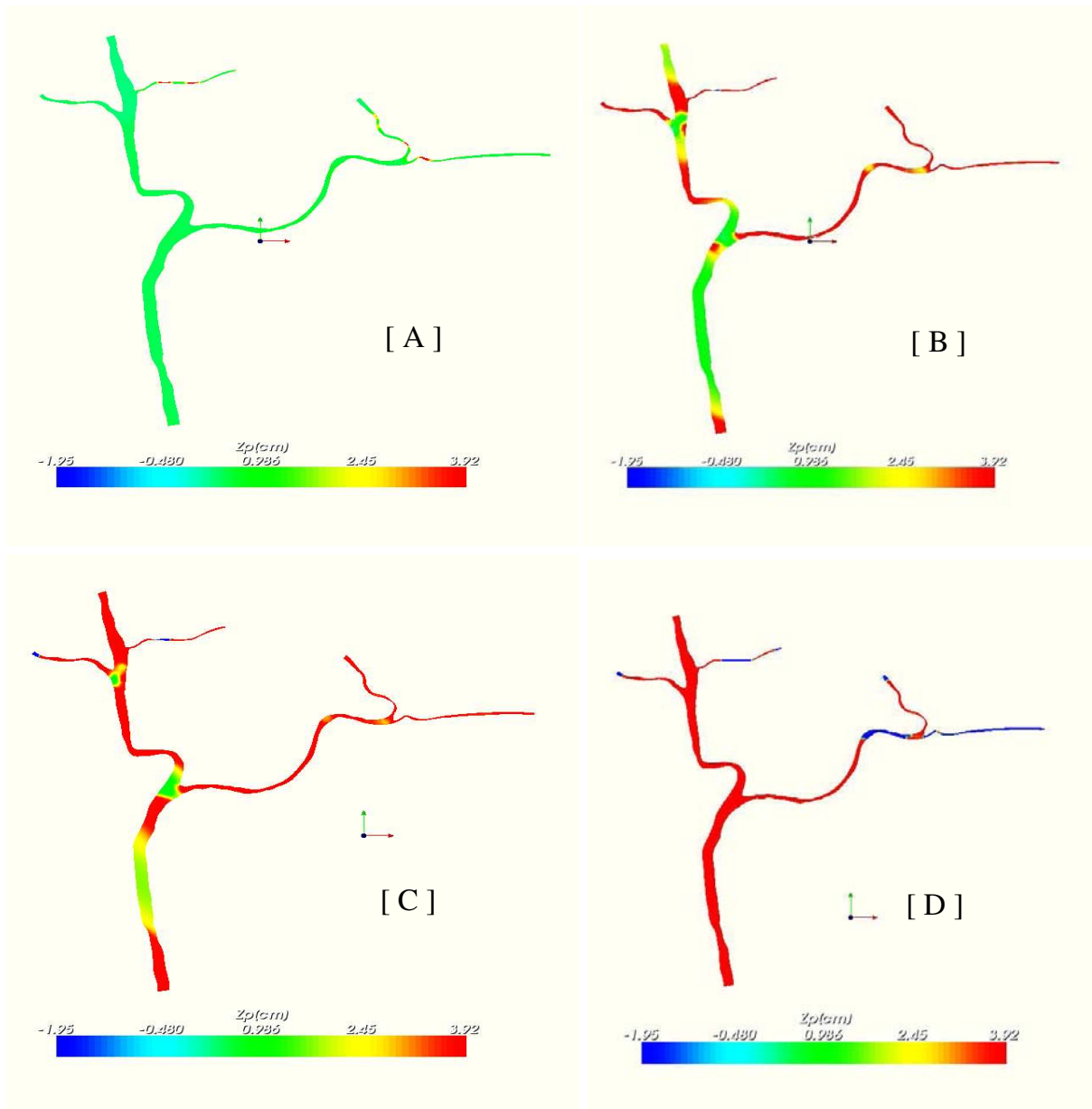


Figure 7.24: Contours of the partially consolidated bed in Po River Estuary 7.35: A) one month; B) three months; C) six months; D) one year

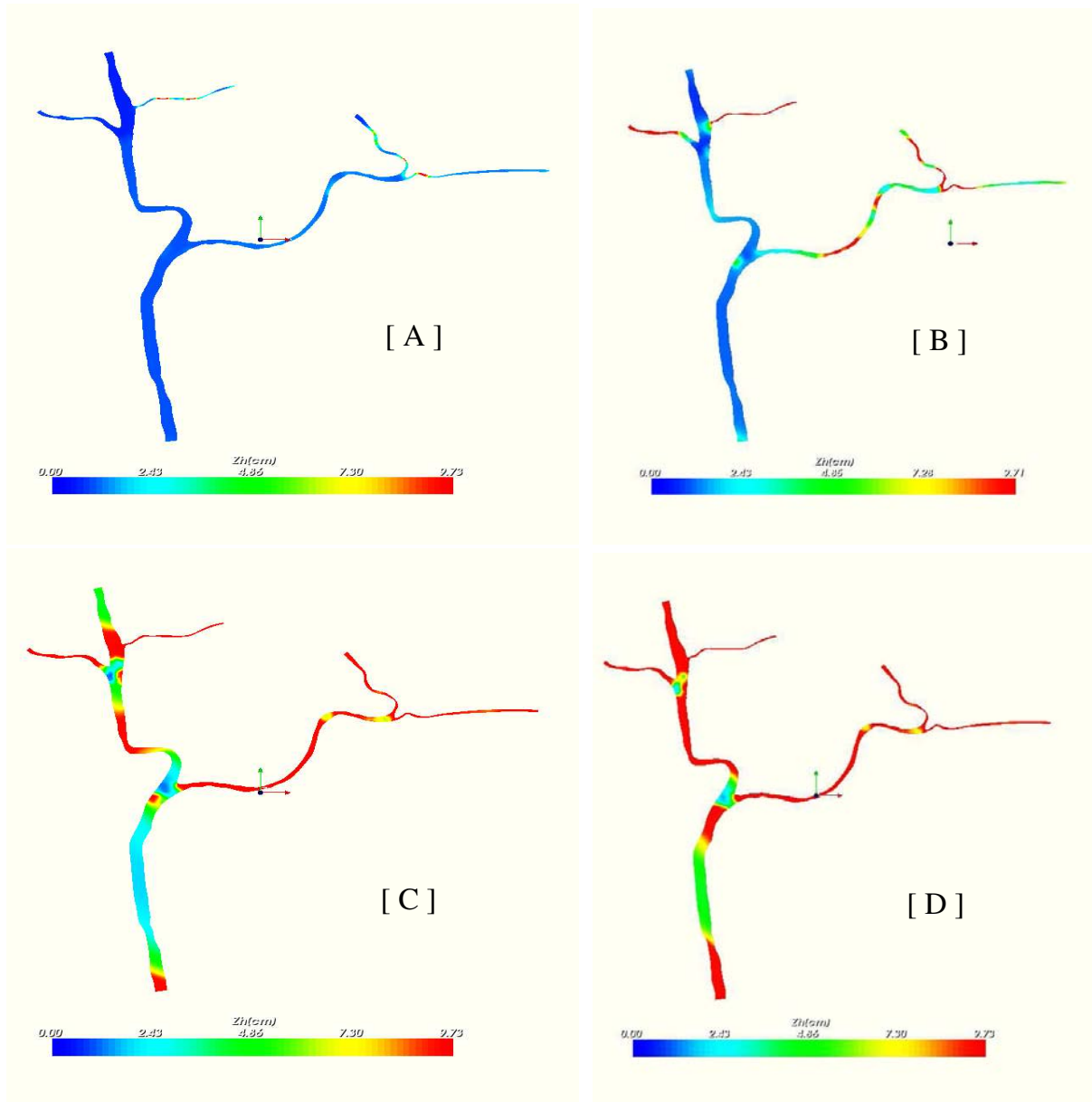


Figure 7.25: Contours of the fully consolidated bed in Po River Estuary using Eq. 7.34: A) one month; B) three months; C) six months; D) one year

Chapter 8

General conclusions

8.1 Achievements

A new 3D cohesive transport model has been developed, incorporating both the mud in suspension and fluid mud at bottom with the consolidation, and the efficient turbulence closure model. Two major lines of investigation have been pursued in this thesis. (i) More efficient, robust and realistic numerical techniques have been designed for the simulation of complex turbulent fluid flows; (ii) New algorithm and its analysis is performed in the context of multiphase fluid flow for the cohesive sediment transport in the estuarine channels.

8.2 Turbulence modeling of variable density fluid flows

Major sources of lack of robustness of numerical algorithms for the turbulence closure computation for multiphase fluid flows in estuary are : (i) the undesired occurrence of negative values for quantities that should always be positive (e. g, the turbulent kinetic energy and its rate of dissipation); (ii) the lack of stability of the scheme (due to new additional driving and/or stabilizing forces, when the density is no longer constant); (iii) generally turbulence models need a small time step with respect to the *Courant-Friedrichs-Lewy* (CFL) stability condition. On the other hand the transport of sediment needs the large time scale for the bed morphology prediction.

In this work, we have proposed a designed strategy for enhancing positiveness (monotonicity of the temporal scheme) to achieve and to preserve the positivity during the iterations, and we have used an efficient fractional step algorithm that preserves positivity of relevant turbulent quantities. We have shown how to implement such a technique, by taking into account the buoyancy and the time sub-scaling scheme (i. e. the time scale for solid phase flow that is longer than the hydrodynamic one) for the stability issues. The resulting computational scheme is very robust, flexible, stable and the procedure is well suited for treatment of complex flows (for variable and stratified or constant density fluid flow) with good overall first order accuracy in time and second order accuracy in space.

8.3 Cohesive sediment transport and bed morphology

Major sources of lack of reliability of numerical algorithms for the cohesive sediment transport can be summarized as follows : (i) most of the existing models in the available literature for

transport and fate of fine sediment in water columns assume the analogous transport characteristics with that of the coarse sediment and adopt sediment transport that were developed for the latter to treat the former; (ii) most of the existing models assume a constant settling velocity, whereas in reality it strongly depends on flocculation influenced by turbulence intensity, salinity and temperature distribution; (iii) almost all the existing models assume only one fresh-mud layer at bottom using continuous modeling concept to the highly concentrated suspended sediment.

In the present study we have shown (in conformity with recent researches and experiments analysis) that there are fundamental differences in the transport characteristics between the common coarse non-cohesive sediment and the fine cohesive sediment behavior. Novel realistic empirical relationships have been proposed for deposition and erosion or re-suspension of fine sediment, from experiments and in-situ observations. In the present work a derived function for sediment settling velocity combined with water temperature, settling distance, particle size and sediment concentration has been introduced.

The analysis in the present study showed that by using two different transport characteristics of coarse sediment and for the fine cohesive sediment modeling, there is a difference between results. This suggests that for a realistic prediction, numerical model must account for the fresh mud re-suspension capability on the bed.

Thus the present model accounts for the differences in the critical conditions between erosion or re-suspension and deposition of fine sediment and allows simultaneous erosion and deposition to occur only for a limited range of bed shear stresses. For bed shear stresses outside of this range, either erosion or deposition is allowed reflecting the cohesive nature of the sediment. The up-to-date algorithms used in the present model, lead to a realistic prediction of the cohesive sediment transport process as well as the turbulence modeling for the multiphase fluid-solid flow. A derived function for sediment settling velocity combined with water temperature, settling distance, particle size and sediment concentration has been introduced. Therefore, different parameters such as sediment settling velocity, incipient shear stress of cohesive (and/or non-cohesive) sediments, the Coriolis force, tidal forcing, wind action, resistance to flow at the bed, buoyancy effects due to temperature, salinity of sea-water and sediment concentration, bed-level changes due to deposition and erosion have been modeled satisfactorily for a realistic representation of the real world phenomena by simulating the Po River Estuary which is found to be one of the main estuary in Europe.

From the point of view of scientific appreciation, the present model investigates the cohesive sediment transport with the three-bed layers component at the bed which are: (i) the mud-bed layer, (ii) the partially consolidated bed, (iii) the complete consolidated bed. This bed morphology relies on the fluidization and/or consolidation process of the cohesive sediment on the channel bed. The prediction of bed morphology using three-layer approach is a first attempt to model these processes in detail within a numerical model. This *three bed-layers* modeling sheds new light on an phenomenon not yet modeled in the existing numerical models for the cohesive transport in the estuaries.

The point is that without accounting of the fluidization and/or consolidation process, this could obviously in the long term endanger the security and navigation in the channel.

The performance of a composite model for cohesive sediment transport has been analyzed, and the water elevation, velocity field, temperature, salinity and sediment concentration profiles computed from the numerical models were found to be in good agreement with the field measurements. Hence this composite model can be considered as an innovative, realistic and robust tool for predicting fine sediment transport modeling in the estuary.

The main scientific contributions of this study have been in determining the influence of the

estuary hydrodynamics on the water quality, the mutual influence of the flocculation and turbulence processes, the evolution of bed morphology and the benthic boundary layer components at the bottom. In estuarine and coastal areas, sediments and water quality are exposed to short term (e. g. tidal) and long term (e.g. seasonal rainfall-river flow) changes in salinity as well as temperature. The effects of salinity are most dramatically seen during periods of stratification. When a water body becomes stratified, vertical mixing is reduced, limiting interaction between river water inputs on the surface and denser, more saline waters on the bottom. Knowledge of the hydrodynamics, water and sediments quality and discharge acquired through intensive field studies including theoretical analysis and simulation tests being carried out in the Po River Estuary , enable validation of the model predictions. Due consideration is made of the properties of sediment and the relevant bed morphology. The micro-tidal Po River Estuary (i.e. tidal elevation $< 2[m]$) is found to be a fairly stratified estuary , with the estuarine turbidity maximum, ETM, (i.e. near bed concentrations) ranging from 200 to 420mg/l. It is shown that turbidity maxima can occur in micro-tidal estuaries, despite the concentrations of suspended sediment being significantly lower (i.e. ETM ranging from 100mg/l to 220mg/l; see Hughes et al. [52], [51]). Thus in micro-tidal Po River Estuary the dominant processes contributing to the generation and maintenance of the ETM could also change. The insight gained through the present study are in accordance with such arguments.

Investigations of a so-called *bed three-layers* from consolidation and/or fluidization have been undertaken in the present model using semi-empirical relationships collected from field observations and experiments, to evaluate temporal variability of estuarine circulation patterns as well as the bed morphology evolution in the Po River Estuary . A better understanding of circulation patterns and the interaction of physical and biochemical processes will be very important for refining current remediation strategies and provide further information for designing appropriate management strategies.

This was a first attempt to put together many semi-empirical equations in a numerical model. The composite model using the stabilization function and strategies, behaves well and remains stable during computations.

8.4 Future prospects

This work has led to a better understanding of several important issues related to the design and assessment of numerical models for simulating fine cohesive sediment in the estuaries. It has also opened new tracks for the rational development of turbulence two-equation closures as well as the bed morphology evolution. Many of these ideas have still to be investigated further. For instance, the models proposed in this work (composite equilibrium model) need additional testing and development. In this optic, computations on more practical configurations and systematic investigation would be necessary and the model must account for the importance of the vertical stratification on the up-welling and down-welling motions which are modulated by the tide, which generates in combination with the vertical density gradient, an internal tide. The meteorological conditions should be taken into account for enhancing the free-surface boundaries conditions for the temperature and salinity (i.e solar and non solar and long wave radiation flux for the heat, evaporation and precipitation rates for the surface salinity and water flow discharge).

Concerning the new strategy to solve turbulence equations, the context of coupling hydrodynamic and turbulence must be investigated, whereas the full 3D model (i.e. without Shallow Water assumption) should be assessed to be well suited for the deep estuaries. Also the proposed implementation of the three-layers bed morphology by introducing in this model a suitable re-

stricted developed SWE for the bed evolution which includes the effect of wave action and a multi-layer model of the muddy bed with the process of consolidation, should be evaluated [120]. More information on the flow properties of fluid mud at various concentrations might lead to an improved model. Some investigation of the ideas [92] for the estuary bed evolution modeling has to be performed [70] and opens interesting perspectives. The application of the non-equilibrium models in inhomogeneous flows and their characterization still remains a task to be performed. This model should be coupled to aquatic ecological module for simulating the dynamic ecosystems.

The parallel version of numerical model will be an asset to reduce computational effort and cost when simulating cohesive sediment transport and bed morphology.

Finally, the model should be applied to many real life harbor channels, for example the case of the Wouri estuary in Cameroon (which is the main entrance of one of the most important harbor in central Africa) for prediction of the movement of the sediments and for determining the optimal strategy for the maintenance of the navigation channel.

Some implementation issues

Array storage

The square and rectangular arrays used during computations, have many null elements and hence to save memory space they are stored using the so-called Compact Sparse Row (CSR) format. Given an array $A(n \times m)$ with nz non-zero elements the CSR format consists of 3 vectors called IA , JA and \tilde{A} (see figure 8.1):

- \tilde{A} is a vector of length nz and it contains the non-zero floating point numbers entries of the matrix, stored row-wise;
- JA is a vector of length nz . for entry $\tilde{A}(i)$, its corresponding column number is found $JA(i)$;
- IA is a vector of length $n + 1$: since entries of the same row are stored consecutively in \tilde{A} , we only need to know the index of the first entry row and the index of the last entry. The index of the first element of row i is stored in $IA(i)$, while the index of its last elements is $IA(i + 1) - 1$. The vector IA has length $n + 1$ since we need to know the index of the last element of row n .

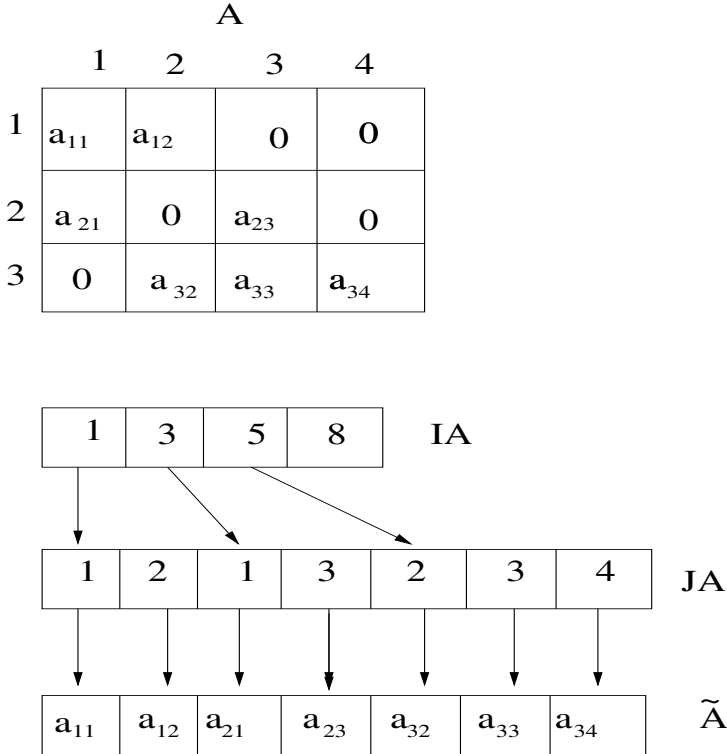


Figure 8.1: CSR format

Bibliography

- [1] A. H Arthington. Interactions between hydrology and environment. In *Proc. of 3rd Int. Conf. Hydrology and Water Ressources Symposium of the Institution of Engineers*, 3, 759-764, IEAust., Australia, 2000.
- [2] J. M. Ashish and E. Partheniades. An investigation of the depositional properties of flocculated sediments. *J. Hydr. Res., IAHR*, 13:361–381, 1975.
- [3] P. Bassoulet, P. Le Hir, D. Gouleau, and S. Robert. Sediment transport over an intertidal mudflat: field investigations and estimation of fluxes within Baie de Marennes-Oleron (France). *Continental Shelf Res.*, 20:1635–1653, 2000.
- [4] J. P. Benqué, G. Lagadie, and J. Rona. A new finite-element method for Navier Stokes equations coupled with temperature equation. In *Proc. 4th Int. Conf. on Finite Element Methods in Flow Problem, 295-301*, Amsterdam, Netherland, 1982.
- [5] K. Blanckaert. *Flow and turbulence in sharp open-channel bends*. PhD thesis, Ecole Polytechnique Fédérale de Lausanne-EPFL, No. 2545, 2002.
- [6] K. Blanckaert and W. H. Graf. Momentum transport in sharp open-channel bends. *ASCE, J. Hydr. Engrg.*, 130:186–198, 2004.
- [7] I. Brenon and P. Le Hir. Modélisation de la dynamique des sédiments fins dans l’Estuaire de la Gironde. Technical Report C R IV èmes Journées Génie Civil-Génie Côtier, Toulon, 13-15 Mai, pp.171-181., Paralia ed. Soec., 1998.
- [8] I. Brenon and P. Le Hir. Modelling fine sediment dynamics in the Seine Estuary : interaction between turbidity patterns and sediment balance. In Donkers and Scheffers, editors, *Physics of estuaries and costal seas*, pages 103–114, 1998.
- [9] I. Brenon and P. Le Hir. *Simulation du bouchon vaseux dans l’estuaire de la Seine : capacités et limites d’un modèle bidimensionnel horizontal*. Sciences de la terre et des planètes. C.R. Acad. Sci. Paris, 1999.
- [10] G. L. Browning, W. R. Holland, H. O. Kreiss, and S. J. Worley. An accurate hyperbolic system for approximately hydrostatic and incompressible oceanographic flows. *Dyn. Atmos. Oceans*, 14:303–332, 1990.
- [11] V. M. Canuto. Large eddy simulation of turbulence: A subgrid scale model including shear, vorticity, rotation, and buoyancy. *Astrophys. J.*, 428:729–752, 1994.
- [12] V. M. Canuto and Minotti F. Stratified turbulence in atmosphere and oceans: A new subgrid model. *J. Atmos. Sci.*, 1993.

- [13] V. M. Canuto, F. Minotti, C. Ronchi, M. Ypma, and O. Zeman. Second-order closure PBL model with new third-order moments : Comparison with LES data. *J. Atmos. Sci.*, 51:1605–1618, 1994.
- [14] X. Casamitjana and G. Schladow. Vertical distribution of particles in stratified lake. *J. Env. Engrg.*, 119:443–462, 1993.
- [15] A. Cattaneo, A. Correggiari, L. Langone, and F. Trincardi. The late-holocene gargano subaqueous delta, adriatic shelf: Sediment pathways and supply fluctuations. *Marine Geology*, 193:61–91, 2003.
- [16] T. Cebeci and P. Bradshaw. *Momentum Transfer in Boundary layers*. Hemisphere publi. Co., Washington, USA, 1977.
- [17] C. Cencini. Physical processes and human activities in evolution of the Po delta, Italy. Technical report, Universita of Bologna, Italy, http://freeweb.supereva.com/cencini1/Po_delta.htm.
- [18] S. Chandrasekhar. *Hydrodynamic and Hydromagnetic Stability*. International Series of Monograph on Physics. Dover Publications, Inc., New York, N. Y. 10014, 1981.
- [19] P. Chassaing, A. Antonia, F. Anselmet, L. Joly, and S. Sarkar. *Variable Density Fluid Turbulence*, volume 69 of *Fluid Mechanics and its Applications*. Kluwer Academic Publishers, The Netherlands, 2002.
- [20] Y. Chen, O. W. H. Wai, Y. S. Li, and Q. Lu. Three-dimensional numerical modeling of cohesive sediment transport by tidal current in Pearl River Estuary. *Int. J. Sediment Res.*, 14:107–123, 1999.
- [21] Y. Cheng and V. M. Canuto. Stably stratified shear turbulence: A new model for the energy dissipation length scale. *J. Atmos. Sci.*, 51:2384–2396, 1994.
- [22] D. Cokjlat and B. A. Younis. Second-order closure study of open channel flows. *ASCE, J. Hydr. Engrg.*, 121:94–105, 1995.
- [23] N. L. Coleman. Flume studies of the sediment transfer coefficient. *Water Resources Research*, 6, 3, 1970.
- [24] B. Cushman-Roisin, M. Gacic, P. Poulain, and A. Artegiani. *Physical Oceanography of the adriatic sea; Past, Present and Future*. Kluwer Academic Publishers, Dordrecht ; Boston, USA, 2001.
- [25] H. J. de vriend. Steady flow in shallow channel bends. Technical report, Rep. 81-3, Laboratory of Fluid Mechanics, Dept. of Civil Engrg., Delft univ. of Technology, Delft, The Netherlands, 1981.
- [26] R. G. Dean and R. A. Dalrymple. *Water Wave Mechanics for Engineers and Scientists*. World Scientific, Singapore, 1991.
- [27] D. M. Deeley and E. I. Paling. Assessing the ecological health of Estuaries in Australia. Technical report, Marine and fresh water Research Laboratory, Institute for Environmental Science, Murdoch University, LWRDC occasional paper 17/99 (Urban Sub-program, Report Number 10, 1999.

- [28] G. R. Dou. A suspended sediment numerical modelling under wave and tidal current. Technical Report Workshop 17th, Ocean Engineering in chinese, 1995.
- [29] J. K. Dukowicz and A. S. Dvinsky. Approximate factorization as a high order splitting for the implicit incompressible flow equations. *J. Comput. Phys.*, 102:336–347, 1992.
- [30] D. R. Durran. *Numerical Methods for Wave Equations in Geographical Fluid dynamics*. Springer-Verlag, New York, USA, 1999.
- [31] D. R. Durran. *Numerical Methods for Waves Equations in Geophysical Fluid Dynamics*. Springer-Verlag, New York, 1999.
- [32] K. R. Dyer. Sediment processes in estuaries : future research requirements. *J. Geophys. Res.*, 94:14327–14339, 1989.
- [33] J. W. Elder. The dispersion of marked fluid in turbulent shear flow. *J. Fluid Mech.*, 5:540–560, 1959.
- [34] ENDEAVOUR. Salt intrusion control: Pô Di Gnocca river project-Italy. Technical report, ENDEAVOUR-44030 Fossaltat Ferrara/Italia, 1986.
- [35] E. D. Estevez. A review and application of literature concerning freshwater flow management in riverine estuaries. Note marine laboratory technical report, South Florida Water Management District, Florida, 2000.
- [36] C. A. J. Fletcher. *Computational Techniques for Fluid Dynamics, vol I*. Springer-Verlag, Berlin-Heidelberg, 1988.
- [37] L. Fontana, E. Miglio, A. Quarteroni, and F. Saleri. A finite element method for 3D hydrostatic water flows. *Comput. Visual. Sci.*, 2:85–93, 1999.
- [38] G. Gabianelli. Marina di Ravenna Lido Adriano (Italy): IAHS publication No. 151. CE-NAS project. Technical report, Interdepartmental Centre for Environmental Sciences, Bologna University, 1997.
- [39] T. B Gatski, M. Y. Hussaini, and J. Lumley. *Simulation and Modeling of Turbulent Flows*. Oxford University Press, New York 10016, 1996.
- [40] W. H. Graf and M. S. Altinakar. *Hydraulique Fluviale, Tome I*. Presses Polytechniques et Universitaires Romandes, CH-1015 Lausanne, Switzerland, 1993.
- [41] W. H. Graf and M. S. Altinakar. *Hydraulique Fluviale, Tome II*. Presses Polytechniques et Universitaires Romandes, CH-1015 Lausanne, Switzerland, 1996.
- [42] C. Grenz, J. Cloern, S. Hager, and B. Cole. *Marine Ecology*. Marine Ecology-Progress series. Inter-Research, Oldendorf/Luhe, 2000.
- [43] W. B. Guan, E. Wolanski, and L. X. Dong. Cohesive sediment transport in Jiaojiang River Estuary, China. *Estuarine, Coastal and Shelf Science*, 46:861–871, 1998.
- [44] R. C. Gularte, W. E. Kelly, and V. A. Nacci. Rheological methods for predicting cohesive erosion. In *Proc. Ann. Conf. Marine Technological Soc.*, 251-258, 1979.
- [45] K. Hanjanlić and B. E. Launder. A Reynolds stress model of turbulence and its applications to thin shear flows. *J. Fluid Mech.*, 56:609–638, 1972.

- [46] F. Harlow and E. Welch. Numerical calculation of time dependent viscous incompressible flow of fluids with free surface. *Phys. Fluids*, 8:2182–2189, 1965.
- [47] E. J. Hayter. Mathematic modelling of cohesive sediment transport. In S. Y. Wang, H. W. Shen, and L. Z. Ding, editors, *Proc., Int. Symp. River Sedimentation*, School of Engineering, University of Mississippi, USA, 1986.
- [48] C. Hirt and B. Nichols. Volume of fluid (vof) method for dynamics of free boundaries. *J. Comp. Phys.*, 34:390–400, 1980.
- [49] J. W. Huang. The experimental study of the scouring and settling properties of cohesive sediment. *The Ocean Engrg.*, 7:61–70 in chinese, 1989.
- [50] S. Huang and Q. M. Lu. *Estuarine dynamics*. Water Conservancy and Electricity Press, Beijing, 1995.
- [51] M. G. Hughes, J. B. Keene, and R. Joseph. Hydraulic sorting of heavy mineral grains by swash on a medium-sand beach. *J. Sediment. Res.*, 70:1002–1012, 2000.
- [52] M.G. Hughes, P. T. Harris, and T. C. T. Hubble. Dynamics of the turbidity maximum zone in a micro-tidal estuary: Hawkesbury river, australia. *Sedimentology*, 45:397–410, 1998.
- [53] A. Iafrati, A. Di Mascio, and E. F. Campana. A level set technique applied to unsteady free surface flows. *Int. J. Numer. Meth. Fluids*, 35:281–297, 2001.
- [54] I. Istiarto. *Flow around a cylinder on a mobile bed*. PhD thesis, Ecole Polytechnique Fédérale de Lausanne- EPFL, NO. 2368, 2001.
- [55] W. P. Jones and B. E. Launder. The prediction of laminarization with a two-equation model of turbulence. *Int. J. Heat Mass Transfer*, 15:301–314, 1972.
- [56] A. J. Kettner and J. P. M. Syvistki. Predicting discharge and sediment flux of the Pô river, Italy since the late glacial maximum. Technical Report CO 80309-0450, University of Colorado, 2004.
- [57] B. G. Krishnappan. A new model of fine-sediment transport for the Fraser river. In *INTERCOH 2000*, Delft, Netherland, 2000.
- [58] B. G. Krishnappan and P. Engel. Critical shear stress for erosion and deposition of fine suspended sediments in the Fraser River. In *Proc., INTERCOH 94, Wallingford*, England, 1994.
- [59] R. B. Krone. Flume studies of the transport of sediments in estuarine shoaling processes. Technical Report SERL., University of California, Berkeley, 1963.
- [60] L. D. Landau and E. M. Lifshitz. *Fluid Mechanics*. Pergamon Press, New York, 1987.
- [61] Y. L. Lau and B. G. Krishnappan. Does reentrainment occur during cohesive sediment settling? *J. Hydr. Engrg., ASCE*, 120:236–244, 1994.
- [62] B. E. Launder and D. B. Spalding. The numerical computation of turbulent flows. *Comput. Methods in Appl. Mech. and Engrg.*, 3:269–289, 1974.

- [63] B. E. Launder and D. B. Spalding. *The numerical computation of turbulent flows*. Springer-Verlag, New York/Berlin, 1990.
- [64] P. Le Hir. Fluid and sediment integrated-modelling. Application to fluid mud flows in estuaries. In Wallingford, editor, *Paper 41 in Proc. 4th Nearshore and Estuarine Cohesive Sediment Transport Conference, INTERCOH'94*, J. Wiley, Chichester., 1994.
- [65] P. Le Hir. Modélisation des accumulations turbides dans l'estuaire de la Loire (France). Technical Report Rapports de synthèse de l'APEEL 1984-199, vol. I : hydrosédimentaire (Migniot & Le Hir), 63-83, Estuaire de la Loire, 1997.
- [66] P. Le Hir, P. Bassoulet, and H. Jestin. Application of the continuous modeling concept to the simulation of highly concentrated suspended sediment: comparison with measurements in a macrotidal estuary. In INTERCOH98, editor, *Proceedings of the 5th International Conference on Cohesive Sediment Transport*, volume 5, Ansan (Corée), 2000.
- [67] P. Le Hir, W. Roberts, O. Cazaillet, M. C. Christie, P. Bassoulet, and C. Bacher. Characterization of intertidal flat hydrodynamics. *Continental Shelf Res.*, 20:1433–1459, 2000.
- [68] P. Le Hir and B. Thouvenin. Mathematical modeling of cohesive sediment and particulate contaminants transport in the Loire. In K. R. Dyer & Robert R. J. Orth (eds), editor, *Estuary Proc. ECSA22/ERF Symp. - Plymouth, 71-78*, Olsen & Olsen, 1994.
- [69] M. A. Leschziner and W. Rodi. Calculation of annular and twin parallel jets using various discretization schemes and turbulence-model variations. *ASME, J. Fluid Engrg.*, 103:352–360, 1981.
- [70] C. Leupi. Modélisation mathématique en 3D du transport de sédiments de type cohésifs et formation du lit dans un canal estuarien. État de l'art sur le transport solide dans les estuaires, Juin 2000.
- [71] C. Leupi, E. Miglio, M. Altinakar, A. Quarteroni, and M. Deville. Quasi-3D finite element shallow-water flow with $k-\epsilon$ turbulence model. In Altinakar M. S., Wang S. S. Y., Holz K. P., and Kawahara M., editors, *Proc. of 6th Int. Conf. Hydro-Science and Engrg, 6, 400-402 & on CD-Rom*, Brisbane, Australia, May 31, June 03 2004. ICHE, SWang S. Y., NCCHE, University of Mississippi, Carrier Hall, University, MS38677, USA.
- [72] Y. S. Li and M. Y. Zhang. Dynamic coupling of wave and surge models by Eulerian-Lagrangian method. *J. Waterway Port. Coastal and Ocean Engrg.*, 123:1–7, 1997.
- [73] B. I. Lin and R. A. Falconner. Numerical modeling of three-dimensional suspended sediment for estuarine and coastal waters. *J. Hydr. Res.*, 34:435–456, 1996.
- [74] J. L. Lions, R. Temam, and S. Wang. On the equations of large-scale ocean. *Nonlinearity*, 5:1007–1053, 1992.
- [75] J. L. Lions, R. Temam, and S. Wang. On mathematical problems for the primitive equations of the ocean: the mesoscale midlatitude case. *Nonlinear Anal.*, 40:439–482, 2000.
- [76] J. J. Liu. Solitation calculation and forecasting at Lian Yuan harbourg. *J. of Nanjing Hydr. Res. Inst.*, 4, 1980.

- [77] W. L. Longley. Freshwater inflows to Texas bays and estuaries: ecological relationships and methods for determination of needs. Technical report, Water Development Board and Texas Park and Wildlife Department, Austin, Texas, 386 pp., 1994.
- [78] L. Lucas, J. Koseff, J. Cloern, S. Monismith, and J. Thompson. Marine ecology. *Marine Ecology-Progress series*, 1999.
- [79] P. J. Luyten, E. Deleensnijder, J. Ozer, and K. G. Ruddick. Presentation of a family of turbulence closure models for stratified shallow water flows and preliminary application to the Rhine outflow region. *Continental Shelf Res.*, 16:101–130, 1996.
- [80] P. J. Luyten, P. J. Jones, R. Proctor, A. Tabor, P. Tett, and K. Wild-Allen. Coherens—a coupled hydrodynamical-ecological model for regional and shelf seas, Belgium. Technical Report MUMM report, Management unit of the Mathematical Models of North Sea, 914pp, COSINUS, 1999.
- [81] A. Malcherek, M. Markofsky, and W. Zielke. Numerical modelling of the particle size distribution in estuaries. In *Proc. Of Int. Symp. Part*, Reinbek, 1993.
- [82] C. Mallet, H. Howa, T. Garlan, A. Sottolichio, and P. Le Hir. Utilisation of numerical and statistical techniques to describe sedimentary circulation patterns in the mouth of the Gironde estuary. Technical Report 331, Acad. Sci. Paris, 2000.
- [83] E. Marchi, G. Roth, and F. Siccardi. The Pô: Centuries of river training. *Phys. Cem. Earth*, 20:475–478, 1996.
- [84] A. G. Marchuk, L. B. Chubarov, and Y. I. Shokin. *Numerical Simulations of Tsunamis*. Mathematics and Mechanics series. MIR, Moscow, 1984.
- [85] J. Marshall, C. Hill, L. Perelman, and A. Adcroft. Hydrostatic, quasi-hydrostatic and nonhydrostatic ocean modeling. *J. Geophys. Res.*, 102:5733–5752, 1997.
- [86] A. J Mehta. Lectures notes on coastal and estuarines studies. In R. T. Barber and N. K. Mooers, editors, *Proc., Work Cohesive Sediment Dynamics*, Florida, USA, 1986.
- [87] A. J. Mehta and R. Srinivas. Observations on the entrainment of fluid mud by shear flow. In A. J. Mehta, editor, *Nearshore and estuarine cohesive sediment transport*, 224–246, AGU, Washington, 1992.
- [88] C. Michler, S. J. Hulshoff, E. H. van Brummelen, and R. de Borst. Monolithic approach to fluid-structure interaction. *Comput. Fluids*, 33:839–848, 2004.
- [89] E. Miglio. *Mathematical and Numerical Modelling for Environmental Applications*. PhD thesis, Department of Mathematics, University of Milano, 2000.
- [90] E. Miglio, A. Quarteroni, and F. Saleri. Finite element approximation of quasi-3D shallow water equations. *Comput. Methods Appl. Mech. Engrg.*, 174:335–369, 1999.
- [91] E. Miglio, A. Quarteroni, and F. Saleri. On the coupling of free-surface and groundwater flows. *Comput. Fluids*, 32:73–83, 2003.
- [92] C. Migniot. A study of the physical properties of various forms of very fine sediment and their behaviour under hydrodynamics action. *La Houille Blanche*, 7:591–620, 1968.

- [93] C. Migniot. Dynamique sédimentaire. *Oceanis*, 6:433–441, 1980.
- [94] C. Migniot. Etude des accès du port de Douala. Technical Report 1348, Laboratoire de Construction hydraulique France (LCHF)/ Office National de Port du Cameroun (ONPC), 1985.
- [95] F. Milosvav. Mathematical methods in fluid dynamics. Technical Report 67, Pitman Monographs Surveys Pure Appl. Math., Harlow, Longman Scientific & Technical, 1993.
- [96] B. Mohammadi and O. Pironneau. *Analysis of $k-\epsilon$ Turbulence Model*. Research in Applied Mathematics. John Wiley & Sons, Chichester, 1994.
- [97] K. W. Morton, A. W. Priestley, and E. S'uli. Stability of the Lagrangian-Galerkin method with non-exact integration. *Math. Model. Numer. Analysis*, 22:625–653, 1998.
- [98] J. C. Muccino, W. G. Gray, and M. G. G. Foreman. Calculation of vertical velocity in three-dimensional, Shallow Water Equation, finite element models. *Internat. J. Numer. Methods Fluids*, 25:779–802, 1997.
- [99] D. Naot and W. Rodi. Numerical simulation of secondary currents in channel flow. *ASCE, J. Hydr. Engrg.*, 108:948–968, 1982.
- [100] N. V. M. Odd and J. G. Rodger. An analysis of the behaviour of fluid mud in estuaries. Technical report, HR Wallingford, 1986.
- [101] L. Y. Oey and G. L. Mellor. A Three-Dimensional Simulation of the Hudson-Raritan Estuary. part I: Description of the Model and Model Simulations. *J. Phys. Oceanogr.*, 15:1676–1692, 1985.
- [102] J. Oliger and A. Sundström. Theoretical and practical aspects of some initial boundary value problem in fluid dynamics. *SIAM J. Appl. Math.*, 35:419–446, 1978.
- [103] R. B. Olsen and M. Skoglund. Three-dimensional numerical modeling of water and sediment flow in a sand trap. *J. Hydr. Res.*, 36:833–844, 1994.
- [104] R. C. Pacanowski and S. G. H. Philander. Parameterization of vertical mixing in numerical models of tropical oceans. *J. Phys. Oceanogr.*, 11:1413–1451, 1981.
- [105] E. Partheniades, R. H. Cross, and A. Ayora. Further results on the depositional of cohesive sediments. In *Proc.*, 11th Conf. on Coastal Engrg., ICCE, London, England, 1968.
- [106] E. Partheniades and J. F. Kennedy. Depositional behaviour of fine sediment in turbulent fluid motion. In *Proc.*, 10th Conf. on Coastal Engrg., ICCE, Tokyo, JAPAN, 1966.
- [107] W. L. Pierson, K. Bishop, and D. Van Senden. Environmental water requirements to maintain estuarine processes. Technical report, National River Health Program, Australia, 2000.
- [108] O. Pironneau. On the transport of diffusion algorithm and its application to the Navier-Stokes equations. *J. Numer. Math.*, 38:309–332, 1982.
- [109] B. S. Pope. *Turbulent Flows*. Cambridge University Press, Cambridge, UK, 2000.
- [110] Z. Qu. *Unsteady Open-Channel Flow over a Mobile bed*. PhD thesis, Ecole Polytechnique Fédérale de Lausanne- EPFL, N0. 2688, 2002.

- [111] A. Quarteroni, F. Saleri, and A. Veneziani. Analysis of the Yosida method for the incompressible Navier-Stokes equations. *J. Math. Pures Appl.*, 78:473–503, 1999.
- [112] A. Quarteroni and A. Valli. *Numerical Approximation of Partial Differential Equations*. Series in Computational Mathematics. Springer-Verlag, New York/Berlin, 1994.
- [113] M. Rappaz, M. Bellet, and M. Deville. *Modélisation Numérique en Science et Génie des Matériaux*. Presses Polytechniques et Universitaire Romande, Ch-1015 Lausanne, Switzerland, 1998.
- [114] P. A. Raviart and J. M. Thomas. *A mixed finite element method for 2nd order elliptic problems*. Mathematical Aspects of Finite Element Methods, Lect. Notes 606. In Dold a. and Eckmann B. (eds), Berlin, Heidelberg, New York, 1977.
- [115] L. C. van Rijn. Mathematical modeling of suspended sediment in non uniform flows. *J. Hydr. Engrg.*, 112:433–455, 1986.
- [116] L. C. van Rijn. Mathematical modelling of morphological processes in the case of suspended sediment transport. Technical Report 382, Delft Hydraulic Laboratory, 1987.
- [117] L. C. van Rijn. Field verification of 2d and 3D suspended-sediment models. *J. Hydr. Engrg.*, 116:1270–1288, 1990.
- [118] L. C. van Rijn. *Principles of fluid flow and surface waves in rivers, estuaries, seas and oceans*. Aqua Publications, P. O. Box 9896, 1006 Amsterdam, The Netherlands, 1990.
- [119] L. C. van Rijn. Transport of fine sands by currents and waves. *J. Waterway Port. Coastal and Ocean Engrg.*, 121:113–133, 1993.
- [120] W. Roberts. Development of mathematical model of fluid mud in the coastal zone. In HR Wallingford, editor, *Proc. Instn. Civ. Engrs Wat. Marit. Energy*, Wallingford, 173-181, 1994.
- [121] W. Roberts, P. Le Hir, and R. J. S. Whitehouse. Investigation using simple mathematical models of the effect of the tidal currents and waves on the profile shape of intertidal mudflats. *Continental Shelf Res.*, 20:1079–1097, 2000.
- [122] W. Rodi. *Turbulence models and their applications in hydraulics*. 2nd ed. IAHR, Delft, Netherlands, 1984.
- [123] W. Rodi. Examples of calculation methods for flow and mixing in stratified fluids. *J. Geophys. Res.*, 92:5305–5328, 1987.
- [124] S. Roland. *Modélisation et simulation des écoulements turbulents*. Traité de Nouvelles Technologies, Mécanique. Guilford et King's Lynn, Paris, 1993.
- [125] J. Sander. Dynamical equations and turbulent closures in geophysics. *Continuum Mech. Thermodyn.*, 10:1–28, 1998.
- [126] J. A. Sethian. *Level Set Methods and Fast Marching Methods*. Cambridge univ. Press, Cambridge, U. K., 1996.
- [127] A. Shirou. Longitudinal and transverse mixing in open-channel flows. Technical report, Hydraulics Laboratory, Kyoto University, 1991.

- [128] J. R. Silva and P. Le Hir. Rheological response of stratified muddy beds to water waves. In *Proc. 5th Int. Conf. on Cohesive Sediment Transport, INTERCOH98*, Ansan(Corée), 2000.
- [129] F. Sixin, B. Lakshminarayana, and M. Barnett. Low-Reynolds number $k - \epsilon$ model for unsteady turbulent boundary-layer flows. *AIAA J.*, 10:1777–1784, 1993.
- [130] F. Sotiropoulos and V. C. Patel. Turbulence anisotropy and near-wall modelling in predicting three-dimensional shear-flows. *AIAA J.*, 33:504–514, 1995.
- [131] A. Sottolichio, P. Le Hir, and P. Castaing. Dynamique des sédiments fins dans l’estuaire de la Gironde. Mise en oeuvre d’un modèle mathématique. Technical Report Actes du colloque Bordomer 97, Aménagement et protection de l’environnement littoral, Bordeaux, 1997.
- [132] C. B. Tang. The law of sediment initiation. *Shuili Xuebao, in chinese*, 2:113–133, 1963.
- [133] C. Teisson, O. Simonin, J. C. Galland, and D. Laurence. Turbulence and mud sedimentation: a Reynolds stress model and a two-phase flow model. In ASCE, editor, *Proc. 23rd Int. Conf. on Coastal Eng., 2853-286*, 1992.
- [134] H. Tenekes and J. L. Lumley. *A first course in Turbulence*. MIT press, Cambridge, 2000.
- [135] B. Thompson, B. Anderson, J. Hunt, K. Taberski, and B. Phillips. Relationships between sediment contamination and toxicity in San Francisco bay. *Marine Env. Res.*, 48:285–309, 1999.
- [136] M. F. C. Thorn and J. G. Parsons. Erosion of cohesive sediments in estuaries: An engineering guide. Technical Report 3, Proc. 3rd Int. Symp. on Dredging Technology, Bordeaux, France, 1980.
- [137] E. A. Toorman. The thixotropic behaviour of dense cohesive sediment suspension. Technical Report Rep. HYD149, Hydraulics Laboratory, K.U. Leuven, 1995.
- [138] E. A. Toorman. Sedimentation and self-weight consolidation: general unifying theory. *Géotechnique*, 46:103–113, 1996.
- [139] M. P. Trimbak and A. J. Mehta. Erosion of soft cohesive sediment deposits. *J. Hydr. Engrg.*, 111:1308–1326, 1985.
- [140] F. Trivellato, E. Bertolazzi, and B. Firmani. Finite volume modelling of free surface draining vortices. *J. Comput. Appl. Math*, 103:175–185, 1999.
- [141] J. S. Turner. *Buoyancy effects in Fluids*. Cambridge University Press, Cambridge, UK, 1973.
- [142] R. E. Uittenbogaard and J. C. Winterwerp. 3D cohesive sediment transport. Technical Report Report Z1022, Delft Hydraulics, 1996.
- [143] L. Umlauf. *Turbulence Parameterisation in Hydrobiological Models for Natural Waters*. PhD thesis, Technical university of Darmstadt, Germany, 2001.
- [144] UNESCO. International Oceanographic Tables. *Unesco technical papers in marine science*, 40, 1987.

- [145] W. G. M. Van Kesteren, J. C. Wintwerp, C. Kuijper, and M. Cornelisse. A new theory for the erosion of cohesive sediments. In *ICCE'92 Book of Abstracts (23rd Int. Conf. Coastal Eng., Venice, Oct)*, 667-668, 1992.
- [146] W. Van Leussen and J. M. Corneliss. The determination of the sizes and settling velocities of estuarine flocs by an underwater video system. *Neth. J. Sea Res.*, 31:231-241, 1993.
- [147] K. K. Versteeg and W. Malalasekera. *Introduction to Computational Fluid Dynamics: The Finite Volume Method*. Longman Group, Essex, England, 1995.
- [148] L. Viganó. The sediment quality of the Pô river and the italian decree no. 152/99 for the protection of aquatic environments. *Ann Ist Super Sanità*, 32:137-141, 2002.
- [149] C. B. Vreugdenhil. *Numerical Methods for Shallow-Water Flows*. Kluwer Academic Press, Dordrecht, 1994.
- [150] F. Welch, F. Harlow, J. P. Shannon, and B. J. Daly. The MAC method: A computing technique for solving viscous, incompressible, transient fluid-flow problems involving free-surfaces. Technical Report Rep. LA-3425, Los Alamos Scientific Laboratory, 1966.
- [151] R. Whitehouse, P. Bassoullet, K. Dyer, H. Mitchener, and W. Roberts. The influence of bedforms on flow and sediment transport over intertidal mudflats. *Continental Shelf Res.*, 20:1099-1124, 2000.
- [152] G. B. Whitham. *Linear and nonlinear waves*. John Wiley and Sons, New York, 1974.
- [153] D. H. Willis and B. G. Krishnappan. Cohesive sediment transport. In *Int. Symp. On Interactions Between Sediments and Water. Int. Association for sediment water science, IASWS*, Canada, 2002.
- [154] C. A. M. E. Wilson, J. B. Boxall, I. Guymer, and N. R. B. Olsen. Validation of a three-dimensional numerical model using a high spatial resolution data set collected from a meandering channel with natural bed topography. *ASCE, J. Hydr. Engrg.*, 129:758-768, 2003.
- [155] J. C. Winterwerp. A simple model for turbulence induced flocculation of cohesive sediments. In ASCE, editor, *25th Int. Conf. Coastal Eng. (Florida)*, ASCE, Florida, 1996.
- [156] J. C. Winterwerp and C. Kranenburg. On the erosion of fluid mud layers due to entrainment. In Wallingford, editor, *Paper 21 in Proc. 4th Nearshore and Estuarine Cohesive Sediment Transport Conference, INTERCOH'94*, J. Wiley, Chichester., 1994.
- [157] J. C. Winterwerp and C. Kranenburg. Erosion of fluid mud layers. part 1, entrainment model. *ASCE, J. Hydr. Engrg.*, 123:504-511, 1997.
- [158] J. C. Winterwerp and C. Kranenburg. Fine sediment dynamics in the marine environment. In Elsevier Science B.V., editor, *Proceedings in Marine*, volume 5, P.O. Box 211, 1000 AE Amsterdam, The Netherlands, 2002.
- [159] W. Wu, W. Rodi, and T. Wenka. 3D numerical modeling of flow and sediment transport in open channels. *J. Hydr. Engrg.*, 126:4-15, 2000.

- [160] M. S. Yalin and G. D. Finlayson. On the velocity distribution of the flow-carrying sediment in suspension. Technical report, Symposium to Honour Professor H. A. Einstein, H. W. Shen, ed., 1972.
- [161] T. Yamamoto, H. L. Koning, H. Sellmeijer, and E. Van. On the response of a poro-elastic bed to water waves. *J. Fluids Mech.*, 87:193–206, 1978.
- [162] J. Ye and J. A. McCorquodale. Simulation of curved open channel flows by 3d hydrodynamic model. *J. Hydr. Engrg.*, 124:684–698, 1998.
- [163] J. Zhu, Q. Zeng, D. Guo, and Z. Liu. Optimal control of sedimentation in navigation channels. *J. Hydr. Engrg.*, 125:750–759, 1999.
- [164] C. K. Ziegler and B. Nisbet. Fine-grained sediment transport in Pawtuxet, Rhode Island. *J. Hydr. Engrg.*, 120:561–576, 1994.

Curriculum vitae

Family name: Leupi
First name: Célestin
Date of bear: April 24, 1966
Nationality: Cameroonian

Language

French: Mother tongue
English: fluent in writing, good in speaking
Nufi (or fe'efé): Native language.

Degree obtained

1998: DIPET II (Diplôme de Professeur de l'Enseignement Technique de Deuxième grade)- Master of Science in Engineering. Dept. of Mechanical Eng., Ecole Normale Supérieure de l'Enseignement Technique (ENSET), The University of Douala, Cameroon.

Thesis title: *Etude, conception et réalisation d'un banc d'essai pour études comparatives de différents types de transmission de puissance utilisés en construction mécanique*
price of excellence and the first of promotion.

1990: DIPCET (Diplôme de Professeur des collèges d'Enseignement Technique)- Bachelor of Science in Engineering. Dept. of Mechanical Eng., Ecole Normale Supérieure de l'Enseignement Technique (ENSET), The University centre of Douala, Cameroon.

Thesis title: *Etude, conception et fabrication d'un banc d'essai pour l'étude de torsion et de flexion des matériaux utilisés en construction mécanique*

Profession

2001-present: **Research assistant**, Laboratoire d'Ingénierie Numérique (LIN) at EPFL.

1999-2001: **Research assistant**, Laboratoire de Mécanique de Fluides (LMF) at EPFL, and Teaching assistant in Laboratoire d'Hydraulique Environnementale (LHE) at EPFL.

1998-1999: **Research assistant**
Dept. of Mechanical Eng., Ecole Normale Supérieure de l'Enseignement Technique (ENSET),

The University of Douala, Cameroon.

Consultant in industrial automatism, *Polyservices aux entreprises- de la Salle* , Douala-Cameroon.

1995-1996: **Teaching Inspector** of the academy in construction and mechanical manufacture at the MINEDUC (the Ministry for the National Education of Cameroon).

1990-1995: **Teacher of mechanics** to the Government Technical High School of Ngaoundéré.

Assistant of teaching and assistant of research at the department of mechanics of the National School Higher of Industries Agronomists and Agricultural (ENSIAAC)" of the university of the university Centre of Ngaoundéré-Cameroon.

Education

Oct. 2001-present: **Ph.D. student** Dept. of Mech. Eng., Ecole Polytechnique Fédérale de Lausanne (EPFL), Switzerland.

Advisors: Prof.M. O. Deville, Prof. M. Altinakar.

Sept. 1996-July 1998. Graduate Student (DIPET II - Master of Science in Engineering) Dept. of Mech. Eng., Ecole Normale Supérieure de l'Enseignement Technique (ENSET), The University of Douala, Cameroon. Prof. E. Njeugna and Dr. E. Kingue

Main subject: Mechanic construction and manufacturing, fluid mechanics.

Sept. 1987-July 1990 Graduate Student (DIPCET - Bachelor of Science in Engineering) Dept. of Mech. Eng., Ecole Normale Supérieure de l'Enseignement Technique (ENSET), The University of Douala, Cameroon.

Advisors: Prof. E. Njeugna, Dr. A. Ateba and Mr. J. B. Nyami.

Main subject: Mechanic construction and manufacturing.

publications

Scientific journals with referee

1. Leupi, C., and Altinakar, S. M. *Finite Element Modeling of Free-surface flows with Non-hydrostatic Pressure and $k - \varepsilon$ Turbulence model*. Int. J. Numer. Meth. Fluids, Accepted in March 2005.
2. C. Leupi, E. Miglio, M. Altinakar, A. Quarteroni and M. Deville. *3D Finite Element solver for Shallow-water free-surface Flows with $k - \varepsilon$ turbulence model*. Submitted for publication to J. Hydr. Res., 2005 (review in progress).
3. Leupi C., Miglio E., and Altinakar S. M. *Free-Surface Flows Solver with Non-hydrostatic pressure and Modified $k - \varepsilon$ turbulence model: Simulation of the Curved Open Channel*. Submitted for publication J. Hydr. Engrg., 2005, (review in progress).
4. Leupi, C., Deville, M.O., and Altinakar, S. M. *Three-dimensional Numerical Modeling of Turbulent Flow in a Curved Open Channel Free-surface flows*. ASCE, J. Hydr. Res., 2004.
5. Leupi, C., Deville, M.O., and Altinakar, S. M. *Three-dimensional Numerical Modeling of Cohesive Sediment Transport and Bed morphology in Po River Estuary*. Int. J. Sedim. Res., 2005.

Referee conference proceedings

1. C. Leupi, E. Miglio, M. Altinakar, A. Quarteroni, and M. Deville. *Quasi-3D Finite Element Shallow-water Flows with $k - \varepsilon$ turbulence model*. Proc. Int. Conf. On Advances in hydro-Science and Engineering, Brisbane, Australia, volume 6, 2004, p400 & CD-ROM.
2. C. Leupi, and M. S. Altinakar *3D Finite Element Modeling of free-surface flows with Efficient $k - \varepsilon$ Turbulence Model and Non hydrostatic pressure*. Proc. Int. Conference On Computational Science, ICCS, ATLANTA, USA, 22-25 May 2005, in press.
3. C. Leupi, E. Miglio, and M. S. Altinakar. *Three-dimensional Numerical Modeling of Curved open channel using Non hydrostatic Turbulent Finite Element Solver for free-surface flows*. 3rd Proc. Int. M.I.T conference, M.I.T, Massachussets, USA, 14-17 June 2005, in press.

Technical report

1. C. Leupi, (2000) *Modélisation Mathématique en 3D du transport de Sédiments Cohésifs et formation du Lit dans les canaux estuariens*. TR, EPFL/DGM/LM, June 2000, unpublished.